



A University of Sussex PhD thesis

Available online via Sussex Research Online:

<http://sro.sussex.ac.uk/>

This thesis is protected by copyright which belongs to the author.

This thesis cannot be reproduced or quoted extensively from without first obtaining permission in writing from the Author

The content must not be changed in any way or sold commercially in any format or medium without the formal permission of the Author

When referring to this work, full bibliographic details including the author, title, awarding institution and date of the thesis must be given

Please visit Sussex Research Online for more information and further details



**Search for the Electroweak Production of
Supersymmetric Particles in
Three-Lepton Events at the ATLAS
Detector with Focus on Compressed
Mass Spectra**

Yusufu Shehu

QUALIFICATION Submitted for the degree of Doctor of Philosophy
University of Sussex
DATE OF SUBMISSION: 30th June 2016

Declaration

I hereby declare that this thesis has not been and will not be submitted in whole or in part to another University for the award of any other degree.

Signature:

Yusufu Shehu

UNIVERSITY OF SUSSEX

YUSUFU SHEHU, DOCTOR OF PHILOSOPHY

SEARCH FOR THE ELECTROWEAK PRODUCTION OF
SUPERSYMMETRIC PARTICLES IN THREE-LEPTON EVENTSAT THE ATLAS DETECTOR WITH FOCUS ON COMPRESSED MASS SPECTRASUMMARY

This thesis presents a search for the electroweak production of supersymmetry using the dataset taken by the ATLAS detector at the Large Hadron Collider with $\sqrt{s} = 8$ TeV during 2012. Events with three leptons are selected and required to satisfy additional kinematic criteria that define optimised signal regions. In these signal regions, Standard Model processes are discriminated against, whilst retaining a large fraction of events produced by specified compressed supersymmetry scenarios. Compressed refers to near mass-degeneracy between the decaying gauginos and the final state gauginos. The expected number of Standard Model events are estimated using a combination of Monte Carlo and data-driven methods, where the predictions are tested against data in specifically designed validation regions. Exclusion limits are then set at 95% confidence level (CL) on via $\tilde{\ell}_L$ - and via WZ-decay scenarios for the decaying charginos and neutralinos. With the $\tilde{\ell}_L$ halfway between the decaying charginos and neutralinos and the final state neutralinos, there is a new sensitivity up to 250 GeV. In scenarios with large mass splitting, the decaying chargino and neutralino masses are excluded up to 740 GeV. Looking forward to the 13 TeV data-taking, a search for the electroweak production of supersymmetry with three-lepton final states is presented, with a first look at an optimisation strategy to improve sensitivity to charginos and neutralinos.

Acknowledgements

There are many people I would like to acknowledge for helping me bring my PhD endeavours to completion and I will do my best to list them. Firstly, I would like to thank my supervisor Antonella De Santo for providing guidance, encouragement and support every step of the way. Thanks to my second supervisor Fabrizio Salvatore for being a warm and welcoming presence and a pleasure to work with.

My student and post-doctoral colleagues within the Experimental Particle Physics group at the University of Sussex have all been there to lend to the friendly and fun environment I have been privileged to work in. I would like to mention and thank Stewart Martin-Haugh and Anthony Rose who have since moved on from the group and were there during the first year of my PhD, when I asked the most questions and was in need of the most guidance. Special thanks to Nicky Santoyo for all the help within the electroweak SUSY multilepton group. I would like to give special thanks to Zara Grout, James Waterfield, Ed Leming, James Sinclair, Fabrizio Miano and Nicola Abraham for moral support and countering stresses of analysis and deadlines with drink-breaks and great banter. Thanks to Daniel Gibbon, who has since moved on from the group, Giuseppe, Fabio, Olly, Tristan, Mark, Sam, Luke, Emma and Diana who have also made Sussex a great place to be. Thanks to Mark Pickering for the fun times at CERN and various conferences.

Thank you to all the friends I have made at University of Sussex and at CERN who have also helped make my PhD experience enjoyable and full of memories.

Finally I would like to thank my parents and my little sister for always encouraging me to achieve whatever I set my mind to.

Contents

1	Introduction	1
2	The Standard Model and Supersymmetry	2
2.1	Introduction	2
2.2	The Importance of Symmetries	3
2.3	The Particle Zoo	4
2.4	Forces of Nature	5
2.4.1	Quantum Electrodynamics	6
2.4.2	Electroweak Symmetry Breaking and the Higgs Mechanism	7
2.4.3	Quantum Chromodynamics	8
2.5	Limitations of the SM	9
2.5.1	Hierarchy Problem	9
2.5.2	Neutrino Masses	10
2.5.3	Dark Matter	11
2.6	Supersymmetry	12
2.6.1	Motivations for SUSY	13
2.6.2	The Minimal Supersymmetric Standard Model	14
2.6.3	Soft SUSY Breaking	15
2.6.4	MSSM Mass Spectra	17
2.6.5	Naturalness in SUSY	18
2.6.6	R-Parity	19
2.6.7	Models of SUSY	21
2.6.8	Simplified Models	22
2.7	Motivation for Compressed Spectra SUSY	23
3	The ATLAS Detector at the LHC	25
3.1	The Large Hadron Collider	25

3.2	The ATLAS Detector	27
3.3	ATLAS Detector Geometry and Nomenclature	28
3.4	Magnet System	29
3.5	Inner Detector	30
3.5.1	Pixel Detector	31
3.5.2	Semiconductor Tracker	32
3.5.3	Transition Radiation Tracker	32
3.6	Calorimeters	33
3.6.1	The Electromagnetic Calorimeter	34
3.6.2	The Hadronic Calorimeter	35
3.7	Muon Spectrometer	36
3.8	Trigger and Data Acquisition System in Run-1	38
3.8.1	The ATLAS Trigger System	38
3.8.2	Trigger Chains and Menus	41
3.9	ATLAS Run-2 Upgrades	43
3.9.1	Insertable B-layer	43
3.9.2	ATLAS TDAQ Upgrades for Run-2	43
4	The Generation, Simulation and Reconstruction of ATLAS Data	46
4.1	Event Generation	46
4.1.1	Parton Distribution Functions	48
4.1.2	Matrix Element Calculation	49
4.1.3	Parton Showers	49
4.1.4	Hadronisation	49
4.1.5	Underlying Event	50
4.2	Detector Simulation	50
4.3	Digitisation	51
4.4	Reconstruction	51
4.4.1	Pile-up in the Inner Detector	52
4.4.2	Inner Detector Track Reconstruction	52
4.4.3	Vertex Reconstruction	53
4.4.4	Electron Reconstruction	54
4.4.5	Electron Identification	55
4.4.6	Muon Reconstruction and Identification	57
4.4.7	Jet Reconstruction	60

4.4.8	Tau Reconstruction and Identification	61
4.4.9	Missing Transverse Energy	63
4.5	Object Selection for the Analysis	65
4.5.1	Baseline Light Lepton Selection	65
4.5.2	Baseline Jet Selection	65
4.5.3	Baseline Tau Selection	65
4.5.4	Overlap Removal	65
4.5.5	Signal Electrons	66
4.5.6	Signal Muons	67
4.5.7	Signal Jet Selection	68
4.5.8	Signal Tau Selection	68
4.6	MC Samples	68
4.6.1	MC Generators	68
4.6.2	SM Background MC Samples For Run-1	69
4.6.3	MC Signal Samples For Run-1	72
4.6.4	SM Background MC Samples For Run-2	72
4.6.5	MC Signal Samples For Run-2	72
5	The E/Gamma Signature Trigger on ATLAS	75
5.1	Trigger Efficiency	75
5.1.1	Determining Efficiencies with $Z \rightarrow ee$ events	77
5.2	Data-Driven Efficiency Measurement	77
5.2.1	Efficiency Measurement Results with Run-1 8 TeV Data	78
5.3	The E/Gamma Signature Trigger Efficiency with Early Run-2 Data	80
5.3.1	Likelihood-based (LH) Electron Identification for Run-2	80
5.3.2	Results and Trigger Performance	81
6	A Search for Electroweak SUSY in Three-Lepton Final States with Compressed Spectra in 8 TeV Data at ATLAS	86
6.1	Introduction	86
6.2	Analysis Overview	87
6.3	Dataset and Event Selection	88
6.3.1	Trigger Selection	88
6.3.2	Event Cleaning	89
6.4	Signal Region Optimisation	90

6.4.1	Optimisation Strategy	91
6.4.2	ISR Signal Region Procedure	96
6.4.3	Soft Lepton Signal Region Procedure	102
6.4.4	Signal Region Summary	102
6.4.5	Significance in Soft Lepton and ISR Signal Regions	105
6.5	Standard Model Background Estimation	110
6.5.1	Standard Model Background Model Overview	110
6.5.2	MC Background Estimation	111
6.5.3	Data Driven Background Estimation: The Matrix Method	112
6.6	Background Model Validation	117
6.6.1	Validation Regions	117
6.7	Systematic Uncertainties	124
6.7.1	MC Statistics	124
6.7.2	MC Cross Section	124
6.7.3	PDF	124
6.7.4	MC Background Uncertainties	125
6.7.5	Electrons	125
6.7.6	Muons	125
6.7.7	Jets	125
6.7.8	Missing Transverse Energy	126
6.7.9	B-tagging Efficiency	126
6.7.10	Trigger	126
6.7.11	Luminosity	126
6.7.12	Pile-up	126
6.7.13	Signal	127
6.7.14	MC Generator Systematic Uncertainties	127
6.7.15	Systematic uncertainties on the reducible background	132
6.7.16	Systematic Uncertainties Summary	132
7	Results and Interpretations for Run-1 Compressed Spectra SUSY Analysis	134
7.1	Statistical Procedure	134
7.1.1	The CL_s Method	134
7.1.2	Combination of Signal Regions	137
7.2	Observations in 8 TeV Data	137

7.2.1	Kinematic Distributions	138
7.3	Statistical Interpretation of Results	142
7.3.1	Model Independent Limits	142
7.3.2	Model Dependent Limits: Simplified Models	143
7.3.3	Summary of Electroweak SUSY Searches at 8 TeV	144
8	Looking Into the Future: A First Optimisation for an Electroweak SUSY Search with Three-Lepton Final States at 13 TeV	147
8.1	Introduction	147
8.2	Analysis Overview	148
8.3	SUSY Simplified Models Considered	148
8.4	Trigger Selection	149
8.5	Object Selection	149
8.5.1	Electrons	149
8.5.2	Muons	149
8.5.3	Jets	150
8.5.4	Missing Transverse Energy	150
8.6	Signal Region Optimisation	151
8.6.1	High Mass Signal Region - SR 3ℓ -H	152
8.6.2	Intermediate Mass Signal Region - SR 3ℓ -I	156
8.6.3	Signal Region Summary	158
8.7	Significance in Signal Regions	158
8.7.1	Significance in Intermediate Mass Signal Region	159
8.7.2	Significance in High Mass Signal Region	161
8.7.3	Combined Significance in Signal Regions	161
9	Conclusions	166
A	Multilepton Trigger Results	168
A.1	Introduction	168
A.2	Three-Lepton Trigger Efficiencies	169
B	Appendix B Systematic Uncertainties	181
B.1	Introduction	181
B.2	Glossary	181
B.3	Systematic Uncertainty Figures	183

Chapter 1

Introduction

The content of this thesis is taken from work carried out during the author’s PhD over the course of just under 4 years on the ATLAS experiment [1] at the Large Hadron Collider [2]. Two analyses are presented in this thesis, each searching for electroweak production of supersymmetric particles. The $\sqrt{s} = 8$ TeV analysis uses events containing three electrons or muons and an initial state radiation (ISR) from the ATLAS dataset taken in 2012. The $\sqrt{s} = 13$ TeV analysis uses events containing three electrons or muons with ATLAS Run-2 conditions. The results from the 8 TeV analysis were made public in the Physical Review D journal in March 2016 [3]. Chapter 2 provides an overview of the current status of particle physics theory, the unanswered questions of the current model and an introduction to supersymmetry as an extension to this model. The Large Hadron Collider and the ATLAS detector, which are used for producing and detecting the high energy data used by this analysis are described in Chapter 3. Chapter 4 discusses the electron/photon signature trigger in ATLAS, which is an essential signature for the analyses described in this thesis. Chapter 5 discusses the software required to process data collected at ATLAS and to produce simulated events. The 8 TeV three-lepton analysis is presented in Chapter 6 including the signal region optimisation, background estimation and systematic uncertainties. The results of this analysis are then presented in Chapter 7. The 13 TeV three lepton analysis is presented in Chapter 8 including the signal region optimisation and expected sensitivity to considered supersymmetry scenarios.

Chapter 2

The Standard Model and Supersymmetry

The Standard Model (SM) is an effective theory motivated to provide a general description of fundamental physical phenomena at the microscopic level. There are, however, some limitations to the theory and unknown entities that are not addressed by the SM. Supersymmetry (SUSY) provides explanatory power and solutions to the limitations which arise in the SM.

This chapter gives an overview of the most successful model in particle physics, the SM, starting with an introduction in Section 2.1 then the theoretical motivation, starting from its basis in gauge invariance in Section 2.2. A description of the fundamental particles and the forces that govern their behaviour in nature is presented in Sections 2.3 and 2.4 respectively, which includes the phenomenon of electroweak symmetry breaking and the proposal of the existence of a new fundamental scalar (the Higgs boson). The limitations of the SM are discussed in 2.5. SUSY as a theory beyond the SM is described and motivated in Section 2.6. Finally, compressed SUSY scenarios, which are targeted specifically in this thesis, are described and motivated theoretically in Section 2.7.

2.1 Introduction

During the 1960’s and 1970’s, through the combination of theory and experiment, a predictive model that describes many fundamental physical phenomena at the microscopic level was developed, known as the SM [4]. It is the most general renormalizable quantum field theory locally invariant under the transformations of the gauge symmetry $SU(3) \otimes SU(2) \otimes U(1)$, which describes interactions of three of the four fundamental forces

in nature (weak, electromagnetic (EM) and strong).

The SM predicts many measurable quantities that have been experimentally well verified, and has predicted the existence of particles prior to their discovery, for example the W boson, the Z boson and the τ lepton [5]. The most recent discovery was that of the Higgs Boson at the Large Hadron Collider (LHC) in 2012 [6, 7], with a mass of $125.09 \pm 0.21(\text{stat.}) \pm 0.11(\text{syst.}) \text{ GeV}/c^2$ (combined CMS and ATLAS result [8]) falling well within the SM predicted mass of a missing large spin 0 scalar.

However, there are some problems with the SM: there is no inclusion of gravity as a quantum field theory; dark matter and dark energy have been observed or inferred experimentally which is not consistent with the current model; neutrino oscillations are observed yet there is no mechanism to explain the mass generation of neutrinos; the mass hierarchy of the SM particles is not explained.

Several theories serving as extensions to the SM have been developed since the 1970's [9]. In these theories, the SM works as an effective theory in the low energy regime, whilst the extension has explanatory power in the higher energy regimes. A compelling theory for these regimes is SUSY, which is a proposed space-time symmetry that relates fermions (half integer spin) to bosons (integer spin). A new set of particles are postulated with masses much heavier (GeV-TeV scale) than those present in the SM, which could in principle be observed with high energy collider experiments. The search for SUSY will be the focus of most of the original work presented in later chapters.

2.2 The Importance of Symmetries

A symmetry is a property of a physical system, whether observed or intrinsic, which is preserved or remains unchanged under some transformation. The transformations describing physical symmetries typically form a mathematical group, thus group theory is used to describe the symmetries conserved in the SM. Within quantum field theory, if the Lagrangian is invariant under a continuous group of local transformation, this description of the Lagrangian is referred to as a gauge theory. Here gauge refers to the redundant degrees of freedom in the Lagrangian. Symmetries inherent in a gauge theory are known as gauge symmetries and these are the symmetries which exist in the SM. Gauge transformations refer to the transformations between possible gauges and collectively form a *Lie Group*, with an associated *Lie Algebra* of group generators. For each group generator therein arises a corresponding gauge field, which exists to ensure Lagrangian invariance under the local group transformations (gauge invariance). The quanta of the gauge fields are called

gauge bosons. Three of the four fundamental forces of nature can be described as gauge theories. Quantum electrodynamics is an Abelian gauge theory with the symmetry group U(1) [10], and has one gauge field, the electromagnetic four-potential, and a single gauge boson, the photon. The strong and weak forces are associated with *non-Abelian* gauge groups. These groups have non-vanishing commutators between the generators for their gauge fields, which consequently means the gauge bosons can self interact. Non-Abelian Lie groups are used to describe elementary particle behaviour in the Yang-Mills theory. Quantum chromodynamics (QCD) is mediated by gauge bosons invariant under the non-Abelian group SU(3) and the weak theory is mediated by gauge bosons invariant under the non-Abelian group SU(2).

2.3 The Particle Zoo

All particles that exist within the SM can be categorised into two groups based on the values of their spin. Fermions have half-integer spin values and are the matter particles, whilst bosons have integer-spin values. So-called gauge bosons form a subset of bosons with spin=1 and are the fundamental force mediators of the SM.

The six quarks of the SM are arranged into SU(2) doublets of three families:

$$\begin{pmatrix} u \\ d \end{pmatrix}, \begin{pmatrix} c \\ s \end{pmatrix}, \begin{pmatrix} t \\ b \end{pmatrix},$$

The up-type quarks (top half of the doublets shown above) have a fractional charge of $+\frac{2}{3}e$ and the down-type quarks (bottom half of the doublets shown above) have a fractional charge of $-\frac{1}{3}e$, where e is the magnitude of the electron charge. All quarks possess a quantum number as an analogue to electric charge, known as colour charge. It can have three different values, labelled as “red”, “green” and “blue”. Due to *confinement*, a property which will be discussed in more detail in Section 2.4.3 quarks do not exist in isolation. Instead they group together to form *hadrons*. Hadrons containing three quarks are referred to as baryons, with the most common examples being the proton and the neutron. Each quark has a baryon number of $\frac{1}{3}$. Quark and anti-quark pairs can be bound together to form mesons.

Particle	Charge (e)	Mass [MeV]
Up (u)	$+\frac{2}{3}$	$2.3^{+0.7}_{-0.5}$
Down (d)	$-\frac{1}{3}$	$4.8^{+0.5}_{-0.3}$
Charm (c)	$+\frac{2}{3}$	1275 ± 25
Strange (s)	$-\frac{1}{3}$	95 ± 5
Top (t)	$+\frac{2}{3}$	$173210 \pm 510 \pm 710$
Bottom (b)	$-\frac{1}{3}$	4180 ± 30

Table 2.1: Some properties of the three generations of quarks present within the SM [11].

There are three lepton generations: electron e , muon μ and tau τ , forming doublets with an electrically neutral neutrino ν_α and charged lepton of the same flavour.

$$\begin{pmatrix} \nu_e \\ e^- \end{pmatrix}, \begin{pmatrix} \nu_\mu \\ \mu^- \end{pmatrix}, \begin{pmatrix} \nu_\tau \\ \tau^- \end{pmatrix},$$

Each lepton generation possesses a characteristic quantum number, called the lepton number: the electron lepton number (L_e), muon (L_μ) and tau lepton number (L_τ). Some of the properties of the three lepton generations are summarised in Table 2.2.

Particle	Charge (e)	Mass [MeV]	L_e	L_μ	L_τ
ν_e	0	$< 2.25 \times 10^{-7}$	1	0	0
e^-	-1	0.51	1	0	0
ν_μ	0	$< 0.19 \times 10^{-7}$	0	1	0
μ^-	-1	105.66	0	1	0
ν_τ	0	$< 18.2 \times 10^{-7}$	0	0	1
τ^-	-1	1776.82	0	0	1

Table 2.2: Some properties of the three generations of leptons present within the SM [11].

2.4 Forces of Nature

The fermionic particles in the SM interact via the electromagnetic (EM), weak and strong forces. These interactions are mediated by vector gauge bosons. The EM force is associated with electric charge and therefore affects only charged leptons and quarks but not the electrically neutral neutrinos. The weak force is related to particle *chirality* or handedness, and only the left-handed components of particles experience the weak interaction. The lepton and quark doublets discussed in Section 2.3 are comprised of left-handed com-

ponents of the particles, which are accompanied by right-handed singlets: e_R^-, μ_R^-, τ_R^- ; and u_R, d_R, s_R, c_R, b_R and t_R ; in the lepton and quark sectors respectively. Only the left-handed component for neutrinos has been observed and only the right-handed component for anti-neutrinos. This exclusivity in action of the weak force on only left-handed particles violates parity conservation. Quark states which interact via the weak force are mixtures of the mass eigenstates of the SM, as defined by the CKM mixing matrix [11]. The strong force is associated with colour charge and only interacts with particles with colour charge, i.e. quarks and the strong force mediators, gluons g , of which there are eight.

The mathematical formulation of the fundamental forces will be covered in the following sections. Section 2.4.1 describes Quantum Electrodynamics (QED), the effective description of the EM force. The weak interaction is discussed in unification with the EM force, referred to as the electroweak interaction in Section 2.4.2. Finally, the strong interaction is described with the formalism of Quantum Chromodynamics (QCD) in Section 2.4.3.

2.4.1 Quantum Electrodynamics

QED was the first theory to be developed which merges quantum mechanics and special relativity. It is invariant under the unitary gauge group $U(1)_Q$, where Q refers to the electric charge, which is the conserved charge in this interaction [5]. The gauge field, which mediates the interaction between the charged spin- $\frac{1}{2}$ fields is the electromagnetic field. The QED Lagrangian [12] for a spin- $\frac{1}{2}$ field Ψ with mass m interacting with the EM field is given as:

$$\mathcal{L} = -\frac{1}{4}F_{\mu\nu}F^{\mu\nu} + \bar{\Psi}(i\gamma^\mu D_\mu - m)\Psi, \quad (2.1)$$

where γ^μ are the Dirac matrices. The electromagnetic field tensor $F_{\mu\nu}$ is defined in terms of the covariant four-potential of the EM field A_ν as:

$$F_{\mu\nu} = \partial_\mu A_\nu - \partial_\nu A_\mu, \quad (2.2)$$

where ∂_μ is the derivative in four dimensional space-time derivative $\frac{\partial}{\partial x_\mu}$. The gauge covariant derivative D_μ is defined as:

$$D_\mu = \partial_\mu + iqA_\mu, \quad (2.3)$$

where q is the electric charge of the spin- $\frac{1}{2}$ field. QED is an Abelian gauge theory, meaning that the generators of the group all commute with one another. The physical interpretation of this is the electrical neutrality of the photon and the fact that it does not self-interact.

2.4.2 Electroweak Symmetry Breaking and the Higgs Mechanism

The electroweak theory is an $SU(2)_L \otimes U(1)_Y$ gauge symmetric field theory. It has four gauge fields, three associated with weak isospin, these being the $W_\mu^{i=1,2,3}$ fields. The subscript on the $SU(2)_L$ indicates that these fields only couple to left-handed fermions. The remaining B_μ field couples to the weak hypercharge (Y) of particles. In order to obtain photon fields without coupling to neutrinos, the gauge bosons B_μ and W_μ^3 are required to mix as follows:

$$\begin{pmatrix} A_\mu \\ Z_\mu \end{pmatrix} = \begin{pmatrix} \cos \theta_W & \sin \theta_W \\ -\sin \theta_W & \cos \theta_W \end{pmatrix} \begin{pmatrix} B_\mu \\ W_\mu^3 \end{pmatrix}, \quad (2.4)$$

where θ_W is the *Glashow-Weinberg angle* and relates the coupling constants of the weak and EM interactions. It can be expressed in terms of the coupling strengths of the B_μ (g_1) and the W_μ^a (g_2) to the fermions:

$$\tan \theta_W = \frac{g_1}{g_2}. \quad (2.5)$$

The photon is identified with the field A_μ and the Z and W bosons are manifestations of the fields Z_μ and W_μ^\pm :

$$W_\mu^\pm = \frac{1}{\sqrt{2}}(W_\mu^1 \mp iW_\mu^2). \quad (2.6)$$

$$Z_\mu = W_\mu^3 \cos \theta_W - B_\mu \sin \theta_W, \quad (2.7)$$

and

$$A_\mu = W_\mu^3 \sin \theta_W + B_\mu \cos \theta_W. \quad (2.8)$$

The electroweak gauge symmetry forbids mass terms for the gauge bosons as well as fermionic masses as they are not invariant under gauge transformations. This how-

ever is clearly contradicted by the measurements of the massive W and Z bosons. This can be solved by introducing a Higgs field as a complex scalar Higgs doublet as shown in Equation 2.9 to the model for mass generation through spontaneous symmetry breaking [13, 14, 15].

$$\Phi = \begin{pmatrix} \phi^+ \\ \phi^0 \end{pmatrix} = \begin{pmatrix} G^+ \\ \frac{1}{\sqrt{2}}(v + H + iG^0) \end{pmatrix}, \quad (2.9)$$

where v is the vacuum expectation value of the Higgs field. Equation 2.9 introduces a complex scalar field G^+ and two real scalar fields H and G^0 . G^\pm and G^0 correspond to three spinless Goldstone bosons [16]. These massless scalars exist for each spontaneously broken, continuous symmetry and are absorbed due to the gauge transformations by the electroweak gauge bosons of the SM. The real scalar field H is referred to as the SM Higgs boson field, whose ground state has a non-zero v . This can be represented as:

$$\Phi_0 = \begin{pmatrix} 0 \\ \frac{1}{\sqrt{2}}v \end{pmatrix}, \quad (2.10)$$

where Φ_0 indicates the ground state. This representation is still invariant under $U(1)_{EM}$ guaranteeing electric charge conservation. As a result, the SM gauge symmetry $SU(3)_C \otimes SU(2)_L \otimes U(1)_Y$ is broken into $SU(2)_L \otimes U(1)_Y$. The interaction of the Higgs field at this VEV with the $SU(2)_L \otimes U(1)_Y$ gauge fields creates screening currents, which result in the three $W_\mu^{i=1,2,3}$ fields acquiring mass. The fourth gauge field B^0 remains massless. The Higgs field is reduced to a spinless scalar, corresponding to a massive Higgs boson particle. The fermions do not gain non-zero mass values as a result of electroweak symmetry breaking but afterwards due to interactions with the Higgs boson.

2.4.3 Quantum Chromodynamics

QCD is the gauge field theory that describes the strong interactions of coloured quarks and gluons and is the $SU(3)_C$ component of the $SU(3)_C \otimes SU(2)_L \otimes U(1)_Y$ SM. Here C refers to colour charge. Each quark in the SM has three associated fields corresponding to the different colour charges of red, green and blue. Quarks can be described as colour triplets i.e.:

$$\mathbf{q} = \begin{pmatrix} q_r \\ q_g \\ q_b \end{pmatrix}.$$

These triplets are invariant under $SU(3)_C$ transformations, which describe strong interactions. There are eight generators associated with this group, which correspond to the eight gluon gauge fields, each of which is defined by a linear combination of colour and anti-colour states. The group is non-Abelian. The physical interpretation of this is the self-interaction between gluons. The Lagrangian density of the strong force is:

$$\mathcal{L} = -\frac{1}{4} \sum_{a=1}^8 G_{\mu\nu}^a G^{a\mu\nu} + \sum_{f=1}^6 [\bar{\mathbf{q}}_f i\gamma^\mu (\partial_\mu + ig\mathbf{G}_\mu) \mathbf{q}_f - m_f \bar{\mathbf{q}}_f \mathbf{q}_f], \quad (2.11)$$

where

$$\mathbf{G}_\mu = \frac{1}{2} \sum_{a=1}^8 G_\mu^a \lambda_a, \quad (2.12)$$

is a sum over all the gluon states and λ_a are the *Gell-Mann matrices*. The index f refers to the quark flavours and \mathbf{q} are quark colour triplet states.

The coupling of strong interactions increases with increasing distance, corresponding to decreasing energy, and is smaller at short range, which corresponds to high energy. This is due to gluon self interactions and has two main consequences. Firstly, in nature, neither quarks nor gluons are observed as free particles. Only colourless “singlet” states are observed. This is referred to as confinement and results in coloured particles at collider experiments being observed as “jets” - collimated showers of hadronic particles which have formed in the detector. The second consequence is that at higher energy the strong interaction is weaker, which is referred to as *asymptotic freedom*, which allows the interaction to be calculated perturbatively, whereas at lower energies, non-perturbative methods must be used, which is discussed in detail in Section 4.1.1.

2.5 Limitations of the SM

2.5.1 Hierarchy Problem

The fermion masses are introduced via coupling terms with the Higgs boson. However the Higgs mass squared term receives corrections for each of these fermionic couplings due to

additional higher-order loops. The term due to fermionic loop coupling is given by:

$$\Delta m_H^2 = -\frac{|\lambda_f|^2}{8\pi^2} \Lambda_{UV}^2 + \dots, \quad (2.13)$$

where only quadratic terms have been considered in this case. Here $|\lambda_f|$ is the coupling between the fermion and the Higgs field and Λ_{UV} is the ultraviolet momentum cut-off which has been selected as the cut-off value for the loop integral. This cut-off choice is required to correspond to the energy scale at which higher energy physics processes occur. If this is set equal to the Planck mass $M_{Pl} \simeq 2.4 \times 10^{18}$ GeV, which is the scale at which a quantum field theory description of gravity becomes possible, then the one loop correction to m_H^2 would be more than 30 orders of magnitude larger than m_H^2 itself. Furthermore, this correction is independent of m_H^2 . This implies that, in the context of the SM, m_H^2 is an unnatural parameter. Even if the quadratic divergences are renormalised, a residual finite correction is left of the order of

$$\frac{m_f^2 \lambda_f^2}{8\pi}, \quad (2.14)$$

where m_f is the mass of the fermion. This correction is manageably small for a SM fermion like the electron but an unnatural amount of fine tuning would be required to cancel any contributions for any heavy fermions that couple to the SM Higgs.

It is observed that the EM and weak interaction unify at ≈ 100 GeV however there are no further unifications observed. This difference between the scale of electroweak physics $O(100$ GeV) and the Planck scale, with the absence of any new phenomena at any intermediate energy scale, which is manifested in the quantum corrections to the Higgs mass is known as the hierarchy problem [17].

2.5.2 Neutrino Masses

Within the SM, neutrinos do not couple to the Higgs boson as they are purely left-handed in nature, therefore there is no mechanism for mass generation for the neutrinos. However, measurements of the neutrino flux from solar and atmospheric sources as well as reactor and accelerator based experiments support the idea that neutrinos can oscillate between mass eigenstates, which is a feature that explicitly requires neutrinos to have mass [18]. Neutrino mass can be added to the SM in various ways. One approach involves adding Majorana mass terms for the neutrinos and/or adding additional right-handed neutrinos with a very heavy mass, known as the see-saw mechanism [19]. The addition of right-

handed neutrinos and other more exotic solutions involving new physics scales could reveal physics beyond the SM.

2.5.3 Dark Matter

In the 1930’s measurements of the orbital velocities of visible galactic matter in galaxies against radial distance was performed [20]. It was observed that galaxies rotate at speeds higher than expected given the amount of visible matter. To date there are only two possible explanations: either general relativity must be modified at galactic distance scales, or there is unseen matter that is responsible for the additional galactic mass. This would imply that there exists another form of “dark” matter that does not interact via the electromagnetic force, and therefore neither emits nor reflects light. Further indications for dark matter are measurements of the cosmic microwave background and the gravitational lensing of galaxy clusters [21], such as the bullet cluster. A possible candidate for dark matter would be a new type of particle without electromagnetic interactions, present throughout the universe, known as Weakly Interacting Massive Particles (WIMPs). Neutrinos have been proposed as dark matter candidates, but from the analysis of Cosmic Microwave Background anisotropies [22], combined with large-scale structure data, suggests that neutrinos are a sub-dominant component of non-baryonic dark matter. Even less is known about Dark Energy, which is a cosmological feature that arose from observations of the red-shift of supernovae in the universe as a function of distance [23]. It was seen that galaxies further away were expanding at a more rapid rate than what can be explained with particle physics and cosmology. It is accounted for in cosmological models with a cosmological constant but the explanation for the true nature of the phenomenon is still sought after.

There are other limitations to the SM. The generations of fermions are not explained, specifically, why there are three generations with apparently arbitrary mass differences; the matter dominance in the universe is not explained, as matter and anti-matter would be expected to be produced equally after the Big Bang, which would result in complete annihilation, with no matter in the universe. This can be explained by charge-conjugation violation, which allowed matter generating processes to occur at a higher frequency than anti-matter processes.

2.6 Supersymmetry

SUSY is a proposed space-time symmetry that relates fermions to bosons. A SUSY transformation transforms a bosonic state into a fermionic state and vice versa. The operator Q that generates transformations must be an anti-commuting spinor, with

$$Q|\text{Boson}\rangle = |\text{Fermion}\rangle, \quad Q|\text{Fermion}\rangle = |\text{Boson}\rangle. \quad (2.15)$$

Each SM particle has a supersymmetric partner, referred to as *sparticles*, with a difference in spin of $\Delta s = \frac{1}{2}$, and their symbols are identical to the SM convention but with an additional tilde. Spinors are intrinsically complex objects, so Q^\dagger is also a symmetry generator. The Coleman-Mandula theorem [24], implies that the generators Q and Q^\dagger must satisfy an algebra of anti-commutation and commutation relations as follows:

$$\{Q, Q^\dagger\} = P^\mu, \quad (2.16)$$

$$\{Q, Q\} = \{Q^\dagger, Q^\dagger\} = 0, \quad (2.17)$$

$$[P^\mu, Q] = [P^\mu, Q^\dagger] = 0, \quad (2.18)$$

where P_μ is the four-momentum generator of space-time translations. The first anti-commutator relation returns the generator of space-time translations, P_μ , which suggests SUSY is in fact a *space-time* symmetry. The Coleman-Mandula theorem states that no new space-time symmetries can exist with non-trivial Lorentz transformation properties, but this is ignoring the instance where conserved quantities can transform as spinors. Consequently, it is postulated that SUSY is the only possible extension of the known space-time symmetries of particle physics.

Each pair of partners is arranged in a *supermultiplet*, which is an irreducible representation of the SUSY algebra. Each supermultiplet contains both fermionic and bosonic states. Particles in the same supermultiplet must also be in the same representation of the gauge group, and so must have the same electric charge, weak isospin and colour degrees of freedom. The number of bosonic degrees of freedom n_B must equal the number of fermionic degrees of freedom n_F in each supermultiplet.

The first possible supermultiplet has a single Weyl fermion (with two spin helicity

states, so $n_F = 2$) and two scalars (each with $n_B = 1$), where the two scalars are grouped into one complex scalar field. This type of supermultiplet is called a *chiral supermultiplet*. The individual chirality states of the SM fermions are each in their own chiral supermultiplet with a corresponding complex scalar.

The second possible supermultiplet contains a spin-1 vector boson. In order for the theory to be renormalisable, this must be a massless gauge boson, in the instance that the gauge symmetry is not spontaneously broken. A massless spin-1 boson has two helicity states and so $n_B = 2$. Its superpartner is a massless spin-1/2 Weyl fermion, with two helicity states, so $n_F = 2$. Such a supermultiplet is called a *gauge* or *vector* supermultiplet.

2.6.1 Motivations for SUSY

2.6.1.1 Cancellation of Quadratic Divergences

The introduction of sparticles with $\Delta s = \frac{1}{2}$ compared to their SM partners elegantly provides a solution to the hierarchy problem. The Higgs mass squared potential receives corrections from a new scalar of mass m_s of the form:

$$\Delta m_H^2 = \frac{|\lambda_S|^2}{16\pi^2} \Lambda_{UV}^2 + \dots \quad (2.19)$$

Two scalar particles with Yukawa couplings equal to that of the top quark will exactly cancel the corrections to the Higgs mass provided the SM particle and the supersymmetric partner are mass degenerate. This applies for all SM fermions and has been shown to continue to all orders.

2.6.1.2 Running of Gauge Couplings

The SM predicts the running of gauge couplings, i.e. strength of the couplings as a function of energy is calculable given a value at some fixed scale. It was aforementioned that although the coupling strengths of EM and weak interaction unify at $\simeq 100$ GeV, that is not true for the strong force. Within the Minimal Supersymmetric Standard Model (MSSM), which is a supersymmetric extension to the SM which has minimal additional particle content and will be discussed in more detail in Section 2.6.2, different coefficients arise due to additional particles involved in the gauge interactions. This leads to an approximate unification of all three gauge couplings at the Planck scale as shown in Figure 2.1. This is indicative of a Grand Unified Theory that is attainable within a supersymmetric model.

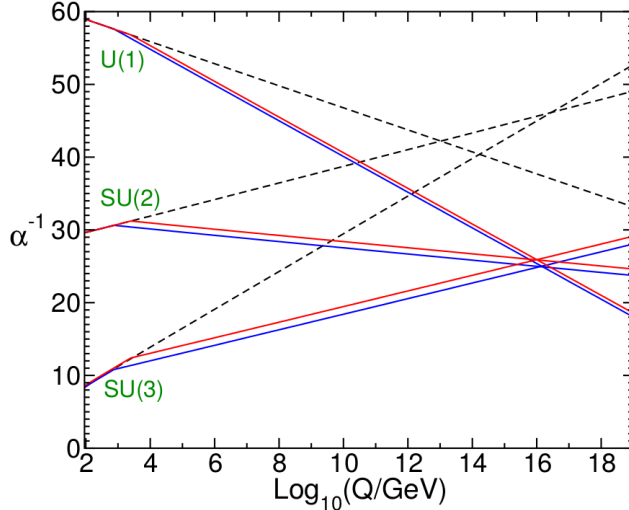


Figure 2.1: The running of the inverse gauge couplings of electromagnetic, weak and strong interactions with the SM (dashed lines) and for the MSSM with two possible sparticle mass scales at 500 GeV and 1.5 TeV (red and blue solid lines)

2.6.2 The Minimal Supersymmetric Standard Model

The Minimal Supersymmetric Standard Model (MSSM) is the model with supersymmetric theory that assumes the minimal particle content to solve the hierarchy problem, with no additional supermultiplets. The equations used to describe the behaviour of quantum fields within the SM can be modified to describe the supermultiplets using *chiral superfields*. The *superpotential* - supersymmetric equivalent of the potential - which describes the general non-gauge interactions of the chiral supermultiplets within the MSSM is as follows:

$$W_{MSSM} = \bar{u}y_u Q H_u - \bar{d}y_d Q H_d - \bar{e}y_e L H_d + \mu H_u H_d, \quad (2.20)$$

where y_u , y_d , μ is the Higgsino mass parameter term and y_e are Yukawa couplings and \bar{u} , Q , H_u , \bar{d} , H_d , \bar{e} and L are the chiral superfields corresponding to the supermultiplets described in Table 2.3 and Table 2.4.

All SM particles have supersymmetric versions with the inclusion of two Higgs doublets to generate mass terms for the up and down type quarks via the Yukawa interactions. Massive quarks and leptons are constructed from pairs of Weyl spinors with opposite chirality. This means that in a supersymmetric theory, every massive quark and lepton must be accompanied by a pair of scalar partners, which are known as squarks and sleptons respectively.

Though the scalar partners of the SM fermions are given the labels “right” and “left” they have no “handedness” themselves. Instead the labels refers to the helicity of their

Names		spin 0	spin $\frac{1}{2}$
squarks, quarks ($\times 3$ families)	Q \bar{u} \bar{d}	$(\tilde{u}_L \tilde{d}_L)$ \tilde{u}_R^* \tilde{d}_R^*	$(u_L d_L)$ u_R^\dagger d_R^\dagger
sleptons, leptons ($\times 3$ families)	L \bar{e}	$(\tilde{\nu} \tilde{e}_L)$ \tilde{e}_R^*	(νe_L) e_R^\dagger
Higgs, higgsinos	H_u H_d	$(H_u^+ H_u^0)$ $(H_d^0 H_d^-)$	$(\tilde{H}_u^+ \tilde{H}_u^0)$ $(\tilde{H}_d^0 \tilde{H}_d^-)$

Table 2.3: Particle content of the MSSM chiral supermultiplets. The left-hand column gives the type of particle and the symbols used for the supermultiplets containing them. The second and third columns contain the spin-0 and spin- $\frac{1}{2}$ components of each of these supermultiplets. The first generation of the quarks and leptons are included as an example and the other two generations follow the same convention. The Higgs fields are given a subscript label depending on whether they give mass to u -type or d -type quarks.

Names	spin $\frac{1}{2}$	spin 1
gluino, gluon	\tilde{g}	g
winos, W bosons bino, B bosons	$\tilde{W}^\pm, \tilde{W}^0$ \tilde{B}^0	W^\pm, W^0 B^0

Table 2.4: The gauge supermultiplet particle content of the MSSM. The left-hand column gives the names of the particles and the second and third columns contain the spin- $\frac{1}{2}$ and spin-1 components of the associated supermultiplets.

respective fermion partners, so for example the “right up squark” (\tilde{u}_R) is the scalar partner of the u_R Weyl fermion.

The gauge supermultiplets are the SUSY equivalent of the SM gauge bosons - the minimal additional fields necessary to create a theory at once supersymmetric and gauge invariant. In addition to a vector boson, each gauge multiplet contains a spin $\frac{1}{2}$, known as a gaugino. Those corresponding to unbroken $SU(3) \otimes SU(2) \otimes U(1)$ are called the gluinos, winos and bino respectively.

2.6.3 Soft SUSY Breaking

It has been previously shown in Section 2.6.1 that with the addition of sparticles in the MSSM, the quadratic divergent corrections can be cancelled provided the particle-sparticle pairs are mass degenerate. However there have been no discoveries of sparticles at the mass scale of their SM partners. This suggests there must be a spontaneous SUSY breaking mechanism to generate sparticle masses akin to the electroweak spontaneous symmetry breaking. The mechanism must be spontaneous and the symmetry breaking must be done by a non-zero VEV in order to preserve Lagrangian invariance under SUSY and providing

a solution to the hierarchy problem. If the relationship between the fermionic and bosonic couplings is altered, then the corrections to the Higgs mass squared parameter from SM fermions will not be cancelled by their SUSY partners correction terms. This equates to adding terms to the SUSY Lagrangian which are gauge invariant and violate SUSY, but contain only masses and couplings with positive mass dimension. The total Lagrangian is defined as:

$$\mathcal{L} = \mathcal{L}_{SUSY} + \mathcal{L}_{soft}, \quad (2.21)$$

where all additional terms are contained within \mathcal{L}_{soft} and the original SUSY invariant interaction terms are contained within \mathcal{L}_{SUSY} . New free parameters are introduced by the soft SUSY breaking, with the key parameters summarised in Table 2.5. These parameters determine the mixing between the flavour eigenstates and consequently the SUSY phenomenology. The phenomenology of supersymmetric theories will be discussed in Section 2.6.4. The actual mechanism for SUSY breaking is unknown, but there are several proposed ideas that have been studied in depth. The general approach involves a coupling to a separate *hidden sector* of fields, in which, spontaneous SUSY breaking occurs [24]. The hidden sector then communicates the SUSY breaking to the MSSM sector via *messenger fields* such that the soft SUSY-breaking terms are generated. There are several ways in which this communication occurs, including gauge mediation [25], gravity mediation [26], extra-dimensional [27] or anomaly-mediation [28]. This thesis considered scenarios in SUSY which specify gauge mediated SUSY breaking, where the soft terms are generated via electroweak and strong interaction loop diagrams with new messenger particles. The messengers are new chiral supermultiplets that are charged under $SU(3)_C \times SU(2)_L \times U(1)_Y$.

Parameters	Definition
M_1, M_2, M_3	Masses of the bino, wino and gluino
$m_{\tilde{Q}_L}, m_{\tilde{u}_R}, m_{\tilde{d}_R}, m_{\tilde{L}_L}, m_{\tilde{e}_R}$	Masses of the left-handed squarks, up-type and down-type right-handed squarks, left-handed sleptons and right-handed sleptons.
$m_{H_u^2}, m_{H_d^2}, \mu , B$	Up and down-type higgsino mass squared parameters, the higgs-higgsino mass and the bilinear higgs term.
A_u, A_d, A_e	Up and down-type squark and sfermion Higgs interaction trilinear couplings.
$\tan \beta$	Ratio of the VEVs of the two higgs doublet fields.

Table 2.5: Key free parameters introduced by soft SUSY breaking in the MSSM.

2.6.4 MSSM Mass Spectra

The general properties of the supersymmetric mass terms, mixing and the resulting phenomenology are discussed here.

2.6.4.1 Higgs Sector

The Higgs scalar fields in the MSSM consist of two complex $SU(2)_L$ -doublet, or eight real, scalar degrees of freedom. As a consequence of electroweak symmetry breaking ($SU(2)_L \times U(1)_Y \rightarrow U(1)_{EM}$), three of them are the Nambu-Goldstone bosons G^0 , G^\pm , which become longitudinal modes of the Z^0 and W^\pm massive vector bosons. The remaining five Higgs scalar mass eigenstates consist of two CP-even neutral scalars h^0 and H^0 , one CP-odd neutral scalar A^0 and a charge +1 scalar H^+ and its conjugate charge -1 scalar H^- . The masses of A^0 , H^0 and H^\pm are not bound by theory and can be arbitrarily large as their mass terms are proportional to $1/\sin\beta$. However the mass of h^0 is bounded from above, at tree level as follows:

$$m_{h^0} < m_Z |\cos(2\beta)|, \quad (2.22)$$

where, $\tan\beta$ is the ratio of the electroweak vacuum expectation values. The lightest Higgs mass is bounded below the Z mass without radiative corrections. The tree level formula for the squared mass of h^0 is subject to large radiative corrections. The largest corrections come from top and stop loops. However these can be tuned in order to match the observed SM Higgs mass of ≈ 126 GeV [29].

2.6.4.2 Gauginos

The neutral higgsinos (\tilde{H}_u^0 , \tilde{H}_d^0) and the neutral gauginos (\tilde{B}^0 , \tilde{W}^0) combine to form four mass eigenstates called *neutralinos*. These are denoted as $\tilde{\chi}_1^0$, $\tilde{\chi}_2^0$, $\tilde{\chi}_3^0$, $\tilde{\chi}_4^0$ and increase in mass from $1 \rightarrow 4$. The mixing can be represented by a matrix:

$$\begin{pmatrix} \tilde{\chi}_1^0 \\ \tilde{\chi}_2^0 \\ \tilde{\chi}_3^0 \\ \tilde{\chi}_4^0 \end{pmatrix} = \begin{pmatrix} M_1 & 0 & -c_\beta m_Z s_W & s_\beta m_Z s_W \\ 0 & M_2 & c_\beta m_Z c_W & -s_\beta m_Z c_W \\ -c_\beta m_Z s_W & c_\beta m_Z c_W & 0 & -\mu \\ s_\beta m_Z s_W & -s_\beta m_Z c_W & -\mu & 0 \end{pmatrix} \begin{pmatrix} \tilde{B}^0 \\ \tilde{W}^0 \\ \tilde{H}_u^0 \\ \tilde{H}_d^0 \end{pmatrix},$$

where $c_\beta = \cos \beta$, $s_\beta = \sin \beta$, $c_W = \cos \theta_W$ and $s_W = \sin \theta_W$.

The charged higgsinos (\tilde{H}_u^+ , \tilde{H}_d^-) and winos (\tilde{W}^+ , \tilde{W}^-) mix to form two mass eigenstates with charge \pm called *charginos*. These are denoted by $\tilde{\chi}_1^\pm$ and $\tilde{\chi}_2^\pm$ and increase in mass from $1 \rightarrow 2$. This mixing can also be represented by a matrix:

$$\begin{pmatrix} \tilde{\chi}_1^\pm \\ \tilde{\chi}_2^\pm \end{pmatrix} = \begin{pmatrix} M_2 & \sqrt{2}M_W s_\beta \\ \sqrt{2}M_w c_\beta & \mu \end{pmatrix} \begin{pmatrix} \tilde{W}^\pm \\ \tilde{H}^\pm \end{pmatrix}.$$

The gluino is colour charged, therefore it does not mix with the other gauginos. The gluino mass is given by a third gaugino mass parameter, M_3 .

2.6.4.3 Squarks and Sleptons

There is mixing of the slepton and squark states due to electroweak symmetry breaking, although this is considered negligible with the exception of the third generation particles which have large masses and Yukawa couplings. The $\tilde{\tau}_L$ and $\tilde{\tau}_R$ states mix to give the mass eigenstates $\tilde{\tau}_1$ and $\tilde{\tau}_2$, the \tilde{b}_L and \tilde{b}_R states mix to give the mass eigenstates \tilde{b}_1 and \tilde{b}_2 and the \tilde{t}_L and \tilde{t}_R states mix to give the mass eigenstates \tilde{t}_1 and \tilde{t}_2 . It is conventional for the eigenstate with lower mass to have the lower index as with the neutralinos and charginos. Mixing is also observed in the Higgs sector, with five mass eigenstates arising. The resulting mass eigenstates which differ from the gauge eigenstates are given in Table 2.6.

Names	Gauge Eigenstates	Mass Eigenstates
Higgs	$H_u^0 H_d^0 H_u^+ H_d^-$	$h^0 H^0 A^0 H^\pm$
Squarks	$\tilde{t}_L \tilde{t}_R \tilde{b}_L \tilde{b}_R$	$\tilde{t}_1 \tilde{t}_2 \tilde{b}_1 \tilde{b}_2$
Slepton	$\tilde{\tau}_L \tilde{\tau}_R \tilde{\nu}_\tau$	$\tilde{\tau}_1 \tilde{\tau}_2 \tilde{\nu}_\tau$
Neutralinos	$\tilde{B}^0 \tilde{W}^0 \tilde{H}_u^0 \tilde{H}_d^0$	$\tilde{\chi}_1^0 \tilde{\chi}_2^0 \tilde{\chi}_3^0 \tilde{\chi}_4^0$
Charginos	$\tilde{W}^\pm \tilde{H}_u^\pm \tilde{H}_d^\pm$	$\tilde{\chi}_1^\pm \tilde{\chi}_2^\pm$

Table 2.6: Mass eigenstates of the MSSM - only those which differ from the gauge eigenstates are listed.

2.6.5 Naturalness in SUSY

The concept of “natural SUSY” is understood as a supersymmetric scenario where the ad-hoc adjusting of relevant parameters (fine-tuning) is as minimal as possible and is taken as a useful guide for exploring supersymmetric phenomenology. The motivation is to discover SUSY in a region of the MSSM parameter space where the electroweak breaking is not fine-tuned. This is because the main phenomenological virtue of SUSY is precisely to avoid

the large fine-tuning which arises to deal with the hierarchy problem. If it is considered that the SM-like Higgs doublet, H , is a linear combination of two supersymmetric Higgs doublets, $H = \sin\beta H_u + \cos\beta H_d$ then the absence of fine tuning can be expressed as minimal contributions to the Higgs mass parameter squared, m^2 [30]. Given that the physical Higgs mass is $m_h^2 = 2|m|^2$ it follows that:

$$\tilde{\Delta} = \left| \frac{\delta m^2}{m^2} \right| = \frac{2\delta m^2}{m_h^2}. \quad (2.23)$$

For large values of $\tan\beta$ the value of m^2 is given by $m^2 = |\mu|^2 + m_{H_u}^2$. The higgsino mass is constrained as the μ parameter should not be too large to avoid large fine-tuning [31]. Constraints are also set on the particles which contribute radiative corrections to $m_{H_u}^2$. The most important contributions come from the stop and the gluino. Once a criteria for ranking models of naturalness is defined, the features of natural models can be used to draw conclusions about sparticle mass spectra. Assuming that the new Higgs-like boson discovered recently at the LHC is the lightest Higgs boson of the MSSM, and taking into account current experimental constraints, a summary of the minimal requirements for a natural SUSY spectrum is given as [31]:

- two stops and one (left-handed) sbottom, both below 500-700 GeV
- two higgsinos, i.e., one chargino and two neutralinos below 200 - 350 GeV. In the absence of other chargino/neutralinos, their spectrum is quasi-degenerate
- a not too heavy gluino, below 900 GeV - 1.5 TeV

These constraints, particularly for light higgsinos provide motivation for compressed spectra SUSY, which will be described and discussed in Section 2.7.

2.6.6 R-Parity

Within the MSSM there are terms that are gauge-invariant but violate either baryon number (B) or total lepton number (L). Taking the most general gauge-invariant and renormalisable superpotential includes terms not only from Equation 2.20 but also the terms

$$W_{\Delta L=1} = \frac{1}{2} \lambda^{ijk} L_i L_j \bar{e}_k + \lambda'^{ijk} L_i Q_j \bar{d}_k + \mu'^i L_i H_u \quad (2.24)$$

$$W_{\Delta B=1} = \frac{1}{2} \lambda''^{ijk} \bar{u}_i \bar{d}_j \bar{d}_k \quad (2.25)$$

where i, j, k refer to flavour and $\lambda^{ijk}, \lambda'^{ijk}, \lambda''^{ijk}$ and μ'^i are coupling constants for the interactions between the chiral superfields. Q_i have a baryon number of $+1/3$, \bar{u}_i, \bar{d}_i have a baryon number of $-1/3$, with $B=0$ for all other terms. L_i have a lepton number of $+1$ and \bar{e}_i have a lepton number of -1 with $L=0$ for all other terms. This means that the terms in Equation 2.24 violate total lepton number by 1 unit (as well as the individual lepton flavours) and the terms in Equation 2.25 violate baryon number by 1 unit. The presence of the λ' and λ'' couplings would result in an extremely short proton lifetime, i.e. much shorter than the current measurement of the proton lifetime of $\sim 10^{32}$ years [11]. This is due to the fact that the proton is only able to decay into lighter leptons which would violate baryon number by 1 unit and lepton number by 1 unit and can occur if the aforementioned couplings are non-zero. In order to remove the B and L violating terms in the renormalisable superpotential, a new quantum number is assumed within the MSSM, called “R-parity”. R-parity is a multiplicatively conserved quantum number defined as

$$R_P = (-1)^{3(B-L)+2S} \quad (2.26)$$

for each particle in the theory [24]. This will have a value of $+1$ for SM particles and -1 for SUSY particles. The imposed symmetry is that any additional candidate term in the Lagrangian (or in the superpotential) is allowed only if the product of R_P for all of the fields in it is $+1$. If R-parity is conserved, SUSY particles are forbidden from decaying only to SM particles as this would give $\Delta R_P = 2$. An important consequence of R-parity conservation is the lightest supersymmetric particle (LSP) will be stable, as there are no lighter particles with the same R_P number for it to decay into. As a weakly interacting, stable and massive particle this makes it a key potential candidate for dark matter. Another experimental consequence is that sparticles can only be produced in even numbers if the initial $R_p = +1$.

The MSSM will not be rendered inconsistent if R-parity conservation is not imposed. Furthermore the laws of baryon and lepton number conservation is accepted not as a consequence of any symmetry but because all observed interactions are seen to obey them. R-parity violating terms are permitted to exist but their coupling are limited by measurements like the proton lifetime. The MSSM can be extended to models that do not conserve R-parity, however within the scope of this thesis only R-parity conserving models are considered.

2.6.7 Models of SUSY

Within supersymmetric theory, there exist are different modes of production which can be explored experimentally. Strong production refers to the production of SUSY particles which interact via the strong interaction (squarks and gluinos). Electroweak production refers to the production of SUSY particles which interact by the electroweak interaction (charginos and neutralinos). Recent LHC limits place powerful constraints on the production of squarks and gluinos [32]. Depending on the SUSY breaking mechanism, squarks and gluinos may be too massive to be produced at the LHC. This motivates electroweak SUSY particle production, which may be the dominant SUSY production at the LHC, despite the comparatively low production cross sections to squarks and gluinos. The pair production cross section as a function of mass for the electroweak and strong processes are shown in Figure 2.2 to illustrate the difference in production cross sections between the electroweak processes $\tilde{\chi}_2^0 \tilde{\chi}_1^\pm$ and $\tilde{\chi}_2^0 \tilde{g}$ and the strong processes $\tilde{q}\tilde{g}$, $\tilde{q}\tilde{q}$ and $\tilde{q}\tilde{q}^*$.

Electroweak SUSY production can be searched for at the LHC through the detection of events with multiple charged leptons in the final state. This is because charginos and neutralinos can decay via intermediate sleptons, gauge bosons or Higgs bosons to charged leptons. Charged sleptons can be produced directly if they are sufficiently light. Chargino or slepton decays can produce one charged lepton in the final state. Neutralino decays can produce two charged leptons in the final state. Thus the combination of chargino and neutralino decays can yield three leptons in the final state. Leptonic decays of direct chargino and neutralino production is the electroweak SUSY production mode explored in this thesis.

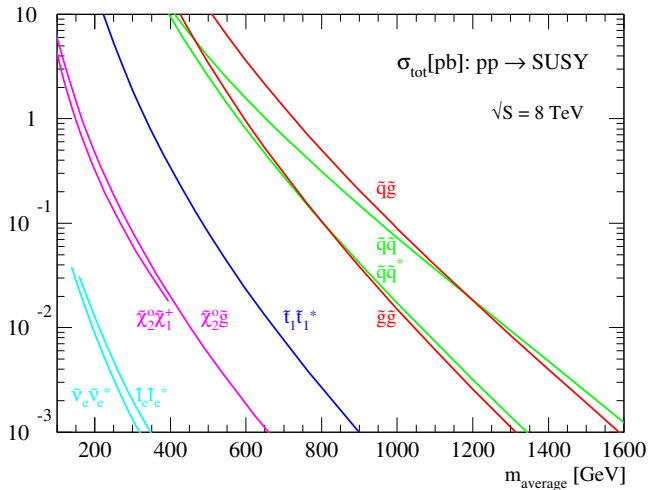


Figure 2.2: Production cross section for supersymmetric particles at the LHC energy of $\sqrt{s} = 8 \text{ TeV}$ as a function of mass

2.6.8 Simplified Models

Experimentally, SUSY can be explored by focusing on one or more SUSY production processes with a fixed decay chain and considering minimal particle content necessary to reproduce such events. This approach is referred to as *simplified models* [33]. The direct pair production of the lightest chargino ($\tilde{\chi}_1^\pm$) and the second-lightest neutralino ($\tilde{\chi}_2^0$) is considered in this analysis, producing three leptons and missing transverse energy in the final state. The masses of the relevant particles in the decay chain are the only free parameters in these models. The following assumptions are made for the considered simplified models: the $\tilde{\chi}_1^\pm$ and $\tilde{\chi}_2^0$ consist purely of the wino component and are degenerate in mass; the $\tilde{\chi}_1^0$ consists purely of the bino component; the squark and gluino masses are set as high as a few hundred TeV.

The different scenarios for the decay of $\tilde{\chi}_1^\pm$ and $\tilde{\chi}_2^0$ are classified according to the particles (or sparticles) in the intermediate step of the decay chain. Two simplified models are explored in the analysis discussed in this thesis and are described in the following sections.

2.6.8.1 Simplified Models with Three Lepton Final States via Sleptons

In this simplified model scenario, the left-handed charged sleptons and sneutrinos are assumed to be light, whereas the right-handed charged sleptons are assumed to have masses at the TeV scale. Therefore, the wino-like chargino and neutralino will dominantly decay through left-handed charged sleptons or sneutrinos as shown in Figure 2.3. For these models, the masses of $\tilde{\chi}_1^\pm$, $\tilde{\chi}_2^0$, $\tilde{\ell}_L$, $\tilde{\nu}$ and $\tilde{\chi}_1^0$ are the free parameters. Lepton universality requires that the branching ratios to e, μ and τ are equal. Mass degeneracy of $m_{\tilde{\ell}_L, \tilde{\nu}}$ for various flavours is assumed for simplicity, these are set such that $m_{\tilde{\ell}_L} = (m_{\tilde{\chi}_1^\pm} + m_{\tilde{\chi}_2^0})/2$. Both the branching ratio branching ratio of the $\tilde{\chi}_1^\pm$ into $\ell\tilde{\nu}$ and the branching ratio into $\tilde{\ell}_L\nu$ are set to equal 50%. Also, both the branching ratio of the $\tilde{\chi}_2^0$ into $\ell\tilde{\ell}_L$ and the branching ratio into $\tilde{\nu}\nu$ are set equal to 50%.

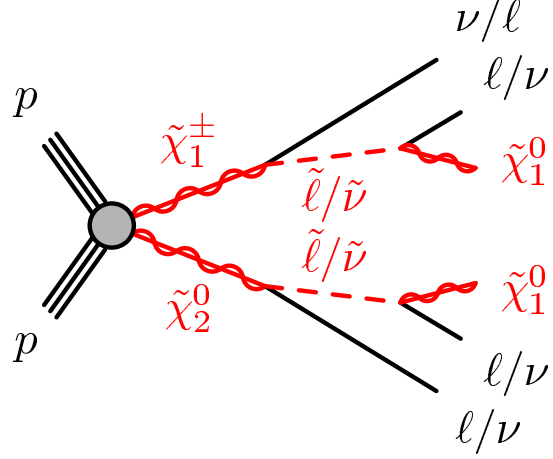


Figure 2.3: Schematic diagram for $\tilde{\chi}_2^0 \tilde{\chi}_1^\pm$ via sleptons, yielding three leptons in the final state [34].

2.6.8.2 Simplified Models with Three Lepton Final States via WZ

In the second simplified model scenario, all sleptons and sneutrinos are assumed to be at the TeV scale and the $\tilde{\chi}_1^\pm$ and $\tilde{\chi}_2^0$ dominantly decay via $W^{(*)}$ and $Z^{(*)}$ bosons, respectively, with a branching fraction of 100%, leading to three leptons and missing transverse energy in the final state. The decay chain for this process is shown in Figure 2.4.

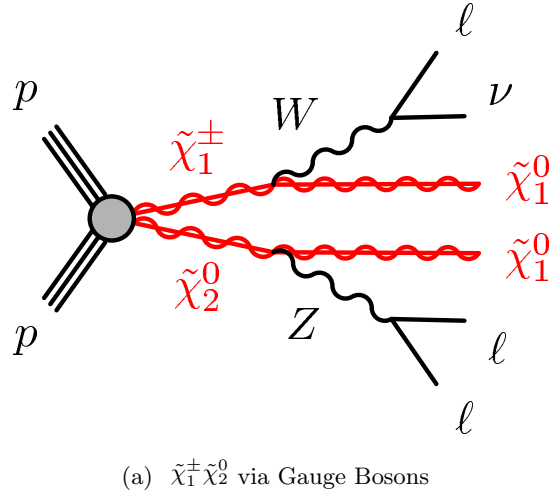


Figure 2.4: Schematic diagram for $\tilde{\chi}_2^0 \tilde{\chi}_1^\pm$ simplified models with intermediate WZ boson decays yielding three leptons in the final state [35].

2.7 Motivation for Compressed Spectra SUSY

Compressed spectra SUSY refers to the scenario where the final state sparticles are near mass degenerate with the heavier decaying sparticles. This scenario is well-motivated the-

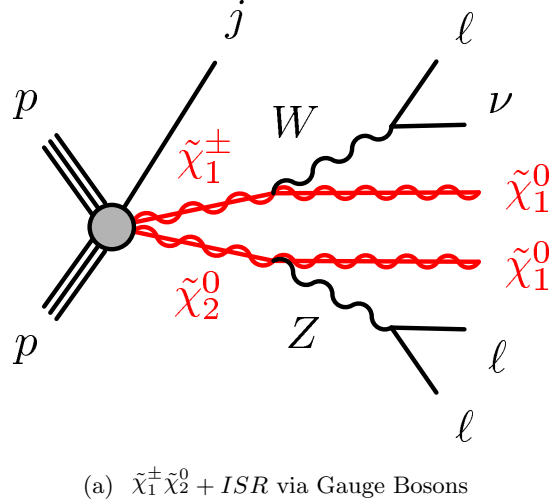


Figure 2.5: Schematic diagram for $\tilde{\chi}_2^0 \tilde{\chi}_1^0$ simplified models with intermediate WZ boson decays and an ISR jet yielding three leptons in the final state [36].

oretically due to the requirement of a low μ parameter and therefore low Higgsino mass for minimal fine-tuning in the MSSM. In the case of $\mu \ll M_1, M_2$, the three lightest neutralino and chargino mass eigenstates, $\tilde{\chi}_1^0$, $\tilde{\chi}_2^0$ and $\tilde{\chi}_1^\pm$ are quasi-degenerate and nearly pure higgsinos [37]. In this scenario the dark matter relic density is typically below the WMAP [38] and PLANCK [39] measurements due to the high rate of higgsino annihilation to SM gauge and Higgs bosons and the higgsino co-annihilation processes. Although the relic abundance would be below experimental constraints, this parameter space is not excluded, since the remaining relic abundance can be accounted for by other additional sources, e.g. axions [37]. If the mass gap between the $\tilde{\chi}_1^\pm \tilde{\chi}_2^0$ and $\tilde{\chi}_1^0$ is large enough to provide final states with leptons, this parameter space can be explored with the LHC. However the leptons produced will have diminishing p_T compared to non-compressed scenarios. One way to circumvent the challenges of compressed SUSY scenarios is to search for events with an energetic jet from initial state radiation (ISR) [40] [41] [42]. In such events the invisible particles can recoil against the jet such that $E_T^{\text{miss}} \sim p_T(j)$, and the signal event can at least be triggered. In addition, the lepton momenta receive a part of the boost, which increases the likelihood of passing the leptonic triggers. The topology of the event with an ISR present can be exploited to enhance signal sensitivity, where there will be large angular separation between the jet and the invisible decay products. This method is discussed in further detail in Section 6.4.1. The monojet decay chain considered in this analysis is illustrated in Figure 2.5, for this simplified model, the constraints on the relevant particles are the same as in Section 2.6.8.2.

Chapter 3

The ATLAS Detector at the LHC

This chapter discusses the experimental apparatus that was used to complete the analysis detailed in this thesis. The Large Hadron Collider (LHC), which supplies proton-proton (pp) collisions for the experiment and the ATLAS detector which is used to contain and measure the particles produced from these collisions. The scope of this thesis covers two distinct periods of data taking for the ATLAS detector, Run-1 and Run-2. During the transition from Run-1 to Run-2 referred to as the Long Shutdown 1 (LS1), upgrades were made to the ATLAS detector for continued optimal physics analysis. This chapter will discuss the LHC and the ATLAS detector to include Run-1 and Run-2 aspects as follows: The LHC is introduced in Section 3.1. The ATLAS detector is described from Section 3.2 to Section 3.7. The ATLAS trigger system during Run-1 is described in Section 3.8. The upgrades made to the ATLAS detector and trigger system for Run-2 is discussed in Section 3.9.

3.1 The Large Hadron Collider

The Large Hadron Collider (LHC) is a large scale circular particle accelerator and collider based in the former LEP [43] tunnel at the European Organisation for Nuclear Research (CERN). Located on the Franco-Swiss border, near Geneva, the LHC has been running since September 2008, although CERN has been conducting particle collision and nuclear physics experiments since the 1950s. The tunnel is 27 km in circumference and varies in depth between 40 - 170m below ground level.

The collider was designed to extend the frontiers of particle physics by utilising unprecedented beam energies and luminosity. Bunches of up to 10^{11} protons collide 40 million times per second to provide 8-13 TeV pp collisions at a design luminosity of $10^{34}\text{cm}^{-2}\text{s}^{-1}$.

The LHC also collides heavy ions, in particular lead nuclei at 5.5 TeV per nucleon pair [44], at a design luminosity of $10^{27} \text{ cm}^{-2}\text{s}^{-1}$. The luminosity is related to properties of the colliding beams and bunches:

$$L = \frac{f N_1 N_2}{4\pi\sigma_x\sigma_y}, \quad (3.1)$$

where N_1 and N_2 are the number of particles per bunch in each of the colliding beams, f is the frequency of the bunch collisions, and σ_x and σ_y are the horizontal and vertical dimensions of the beam.

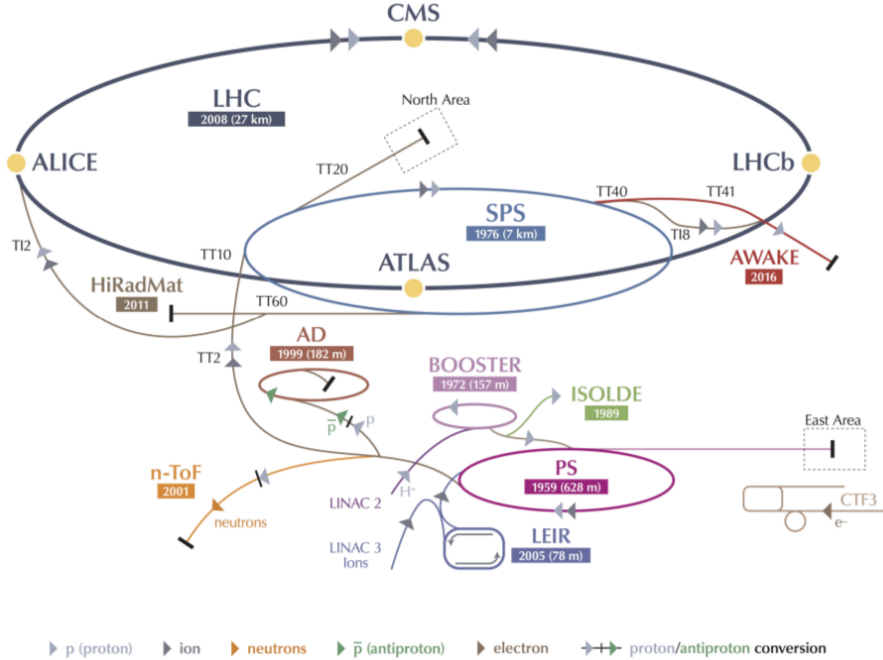


Figure 3.1: Diagram of the layout of the accelerators connected to and including the LHC at CERN, as well as the locations of the four major detector sites [45].

The LHC receives high energy protons that are supplied after passing through a chain of smaller accelerators. The energies of the protons are gradually increased through each step in the chain. The acceleration of the beams of protons begin at the linear accelerator LINAC 2, where they are accelerated to energies of 50 MeV. They are then passed to the Proton Synchrotron Booster where they reach energies of 1.4 GeV. Next in the sequence is the Proton Synchrotron, which pushes energies up to 25 GeV, and then the Super Proton Synchrotron, at energies up to 450 GeV. Finally the proton beams are injected in bunches into the LHC, which circulates them in opposite directions, accelerating them to energies of 8 TeV for Run-1 and 13 TeV for Run-2. Upon attaining these energies the bunches are made to collide at four key positions around the ring where the particle detector

experiments are based.

For the heavy ion collisions, the bunches are processed by LINAC 3 and the Low Energy Ion Ring (LEIR) before they are passed to the PS whereby they then follow the same path as the protons.

The four large detectors on the collision points are: the multi-purpose detectors A Toroidal LHC ApparatuS (ATLAS) and Compact Muon Solenoid (CMS) [46], Large Hadron Collider beauty (LHCb) [47], which focuses on flavour physics, and A Large Ion Collider Experiment (ALICE) [48], which specialises in heavy ion physics. In addition there are a number of smaller experiments located in the four caverns about the collision points, but this is beyond the scope of this thesis and will not be discussed any further.

3.2 The ATLAS Detector

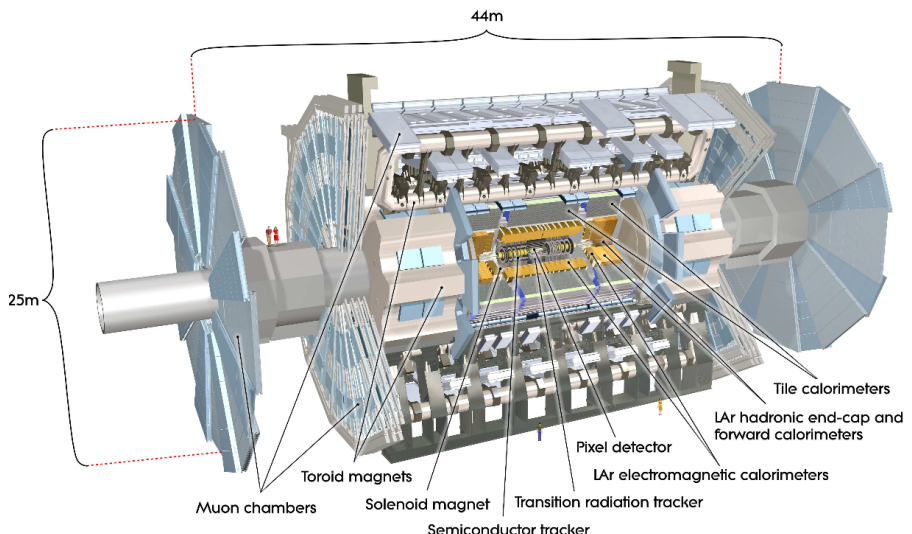


Figure 3.2: Cut-away view of the ATLAS detector. [1].

The ATLAS detector is a general purpose detector that sits on the LHC ring in the Point 1 cavern. It has cylindrical symmetry, measuring 45 m in length and 25 m in diameter. It is designed to reconstruct and measure physics objects, including electrons, muons, photons and hadronic jets that are created from the pp collisions supplied by the LHC. The detector was optimised for the discovery potential for the Higgs boson and beyond-the-Standard-Model (BSM) physics. The detector is composed of several sub-detector systems, which are designed to measure different particle properties, and will be discussed in more detail below.

3.3 ATLAS Detector Geometry and Nomenclature

The nominal interaction point is defined as the origin of the coordinate system, while the beam direction defines the z -axis and the x - y plane is transverse to the beam direction. The positive x -axis is defined as pointing from the interaction point to the centre of the LHC ring and the positive y -axis is defined as pointing upwards. The side-A of the detector is defined as that with positive z and side C is that with negative z . The azimuthal angle ϕ is measured around the beam axis, and the polar angle θ is the angle from the beam axis.

A special coordinate is defined to describe the angle of a particle with respect to the beam axis, known as the pseudorapidity. It is defined as

$$\eta = -\ln \left[\tan \left(\frac{\theta}{2} \right) \right]. \quad (3.2)$$

In the case of massive objects such as jets, the rapidity is defined as

$$y = \frac{1}{2} \left[\frac{E + p_z}{E - p_z} \right], \quad (3.3)$$

where E is the particle's energy and p_z is the z -component of its momentum. The distance ΔR in the pseudorapidity-azimuthal angle space is defined as

$$\Delta R = \sqrt{\Delta\eta^2 + \Delta\phi^2}, \quad (3.4)$$

where $\Delta\eta$ and $\Delta\phi$ are the distance in η and ϕ between the two considered objects. Requirements on spatial proximity between objects can be made by imposing conditions on ΔR . The boundary of a ΔR condition describes a cone around the considered object. The transverse momentum p_T and transverse energy E_T and the missing transverse energy E_T^{miss} are defined in the x - y plane. The transverse momentum is defined as:

$$p_T = \sqrt{p_x^2 + p_y^2}, \quad (3.5)$$

where p_x and p_y are the x and y components of the momentum. The initial momentum in the x - y plane of a proton-proton interaction is taken to be zero and therefore the final total transverse momentum is also zero as a consequence of momentum conservation. The total visible transverse momentum, p_T^{vis} can be used to infer the amount of missing transverse energy in the event if it is measured as non-zero. This indicates there were

additional undetected particles present in the event, resulting in an invisible p_T component, responsible for the perceived momentum imbalance. The missing transverse energy or E_T^{miss} is the magnitude of the momentum of all undetected particles in the event, defined as:

$$\vec{p}_T^{miss} = -\vec{p}_T^{vis} = -\Sigma \vec{p}_T, \quad (3.6)$$

where the p_T of all visible particles are summed.

3.4 Magnet System

A fundamental method of identification and measurements of charged particles is the direction and curvature of the particles' path in a magnetic field. These two parameters are related to the particles charge and momentum. The ATLAS detector features a hybrid system of four large superconducting magnets which deflect charged particles within the detector. The magnetic system is 22 m in diameter and 26 m in length, with a stored energy of 1.6 GJ. More specifically, the ATLAS magnet system consists of:

- A solenoid which is aligned on the beam axis and provides a 2 T axial magnetic field for the Inner Detector (ID), while minimising the radiative thickness in front of the barrel Electromagnetic Calorimeter (ECAL). It is located in between the ID and the ECAL. It has an axial length of 5.8 m, an inner radius of 2.46 m and an outer radius of 2.56 m.
- A barrel toroid and two end-cap toroids, which produce a toroidal magnetic field of approximately 0.5 and 1 T for the muon detectors in the central and end-cap regions, respectively. The magnetic field supplied is orthogonal to the trajectory of the particles in the muon spectrometer, allowing for measurements of the muon momenta. The barrel toroid has an axial length of 25.3 m, an inner diameter of 9.4 m and an outer diameter of 20.1 m. The endcaps are 5 m in length and have inner and outer diameters of 1.65 and 10.7 m respectively.

All components are made from NbTi, which is a superconducting material with a critical temperature of 10 K. The magnets are cooled to 4.5 K by liquid helium.

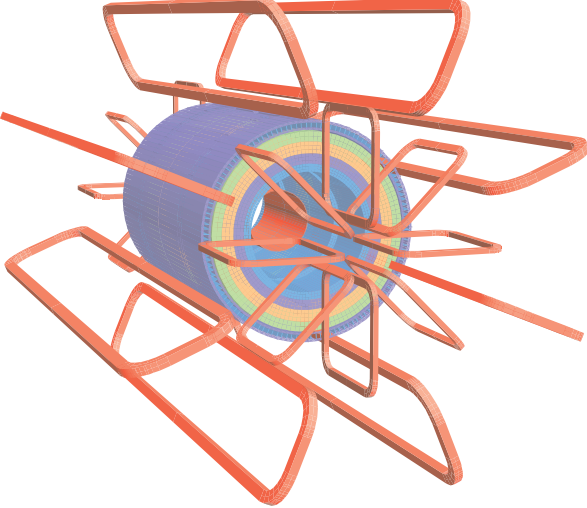


Figure 3.3: Geometry of magnet windings and tile calorimeter steel. The eight barrel toroid coils, with the end-cap coils interleaved are visible. The solenoid winding lies inside the calorimeter volume [1].

3.5 Inner Detector

The ATLAS Inner Detector [49] is designed to provide robust pattern recognition, momentum resolution and both primary and secondary vertex measurements, for charged tracks above a given threshold (nominally 0.5 GeV) and within $|\eta| < 2.5$. It also provides electron identification over $|\eta| < 2.0$ and a wide range of energies (between 0.5 GeV and 150 GeV).

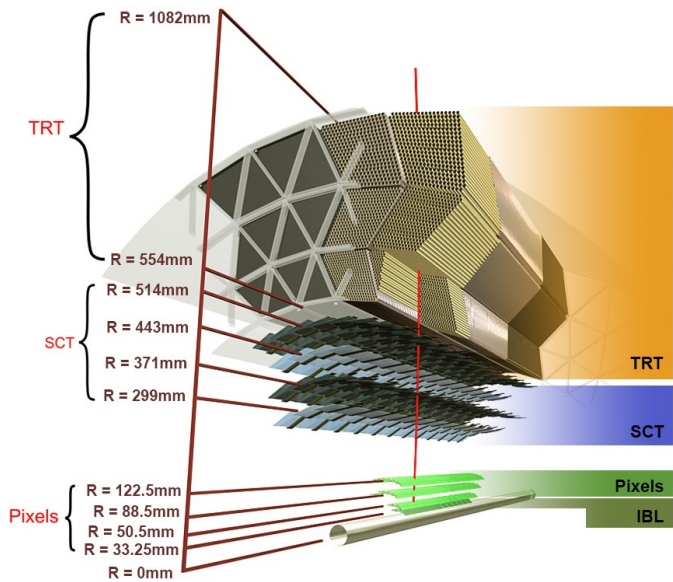


Figure 3.4: Diagram of the ATLAS inner detector and its components, including the new insertable B-layer (IBL) [50].

The ID is contained within a cylindrical envelope of length ± 3512 mm and a radius of 1150 mm, within a solenoidal magnetic field of 2T.

During Run-1, the ID was composed of three independent but complementary sub-detectors:

- The inner most component is the Pixel Detector, comprised of silicon pixel layers. It is utilised primarily in the reconstruction of both the primary interaction vertex and also secondary vertices in an event.
- The intermediate layer is the Semiconductor Tracker (SCT), comprised of silicon microstrip layers, focuses primarily on the accurate measurement of particle momenta.
- The final layer is the Transition Radiation Tracker (TRT), comprised of many layers of gaseous straw tube elements interleaved with transition radiation material. This layer contains average 36 hits per track, it provides continuous tracking to enhance the pattern recognition, and improve the momentum resolution over $|\eta| < 2.0$ and electron identification complementary to that of the ECAL over a wide range of energies.

All three sub-detectors have barrel and end cap components. The addition of the insertable B-layer for Run-2 is described in Section 3.9.1.

3.5.1 Pixel Detector

The pixel detector is composed of 1750 identical sensorchip-hybrid modules, each covering an active area of 16.4×60.8 mm 2 . The total number of modules correspond to approximately 80 million semiconductor silicon pixels ($50 \times 400 \mu\text{m}^2$ rectangular segments of silicon sensors). This large number of pixels is necessary to cope with the high luminosity of the ATLAS detector. Each pixel is read out with an independent electronics channel.

The silicon pixel detector forms a cylindrical envelope 48.4 cm in diameter and 6.2 m in length providing a pseudorapidity coverage of $|\eta| < 2.5$. The three concentric barrel layers of radii are at 50.5 mm, 88.5 mm and 122.5 mm and are shown in Figure 3.4. It also consists of a total of six disk layers, three at each forward region. Charged tracks produced by particles will cross these three layers, yielding at least three space points. The main feature of the pixel detector is the fine granularity or size of each pixel, which is essential for high resolution measurement and precise vertex information as it provides more detection area and therefore a more accurate position.

3.5.2 Semiconductor Tracker

The SCT is designed to measure four precision space points (corresponding to eight silicon layers) on the track of a charged particle over a range $|\eta| < 2.5$, which is mainly used for precise momentum reconstruction. Each module has an intrinsic resolution of $17 \mu\text{m}$ in the $R - \phi$ direction and $580 \mu\text{m}$ in the z direction.

The SCT consists of 4088 modules of semi-conducting silicon micro-strip detectors arranged in four concentric barrel layers, with radii ranging from 299 mm to 514 mm and nine layers in each of the end-caps, as shown in Figure 3.4. The silicon-strip sensors are read out by radiation hard front-end chips, with each chip reading out 128 channels. Due to the SCT being further away from the beam-pipe, there is reduced particle density expected within the SCT, which allows for reduced granularity compared to the pixel detector to maintain the same level of performance while using ≈ 6.3 million read-out channels (≈ 2 million fewer than the pixel detector).

3.5.3 Transition Radiation Tracker

The TRT [51] is the outermost of the three subsystems of the ID. It utilises layers polyimide straw tube elements, 4 mm in diameter. Transition radiation material surrounds, which is made of polypropylene fibres in the barrel or polypropylene foils in the end-caps. The tubes are filled with 70% Xe, 27% CO₂ and 3% O₂. As a charged particle goes through the TRT it will ionise the gase inside the straw tubes. It has an average of 36 hits per track in the central region, providing continuous tracking to enhance pattern recognition and improve the momentum resolution over the pseudorapidity range $|\eta| < 2.0$, which is important for electron identification. The TRT improves the p_T resolution for particles with longer track length. It also provides particle identification capability through the detection of transition radiation X-ray photons generated by high velocity particles traversing through various materials with different dielectric constants.

The TRT barrel section is arranged in three concentric layers with radii ranging from 544 mm to 1082 mm (as shown in Figure 3.4), each with 32 modules jointly containing approximately 50,000 straws, 1.44 m in length, which are aligned parallel to the beam direction with independent read-out at both ends. The two end-cap sections are each divided into 14 wheels, with approximately 320,000 straws that run in the R -direction.

3.6 Calorimeters

The ATLAS Calorimeter system is composed of a number of sampling detectors, which form the electromagnetic calorimeter (ECAL) and hadronic calorimeter (HCAL), which are designed to stop and measure the energy of electromagnetic and hadronic particles respectively. They provide full ϕ coverage and $|\eta| < 4.95$ about the beam axis. Sampling involves utilising layers which cause the particles to lose energy and slow down (absorber), which are alternated with layers which measure the energy of the resulting showers (sampler). All energy must be contained within the calorimeters, both to improve energy measurements and to avoid particles showers penetrating into the muon spectrometer.

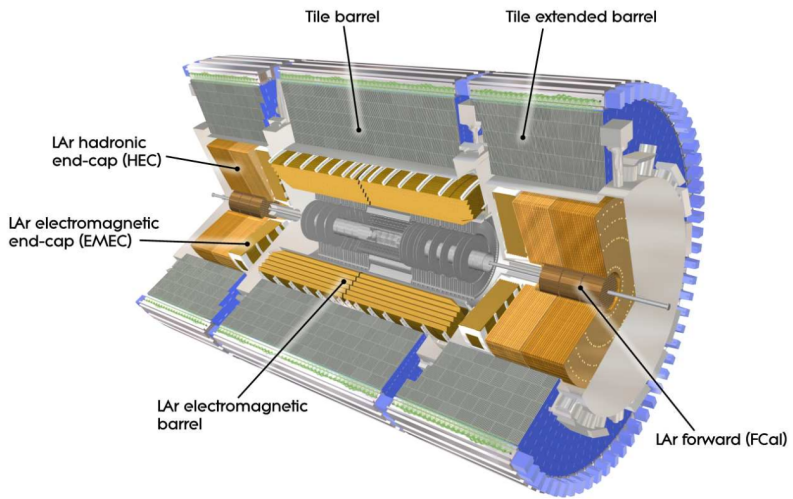


Figure 3.5: Cut-away view of ATLAS electromagnetic and hadronic calorimeter systems [1].

The lengths of barrel and endcap sections of the calorimeter systems can be defined in terms of radiation length (X_0) for the ECAL, which is defined as the distance over which an electron loses $1/e$ of its energy within a given material, and for strongly interacting particles in the HCAL, the equivalent is the nuclear interaction length (λ_I). The ECAL is at least $22 X_0$ thick in the barrel, and $24 X_0$ in the end caps. Although this can vary in some regions of $|\eta|$. The HCAL is $10 \lambda_I$ thick on average, this also varies with η . On average the nuclear interaction length is of the order of a factor ten larger than the average radiation length, hence hadronic particles are much more penetrating than electromagnetic particles. Figure 3.6 shows the simulated thickness of material from the interaction point up to and including the calorimeters for both radiation lengths and nuclear interaction lengths.

3.6.1 The Electromagnetic Calorimeter

The ECAL consists of modules alternating layers of lead absorber and liquid Argon (LAr) sampler, which are folded into an accordion geometry as shown in Figure 3.7. This design was used to provide full ϕ coverage without any regions of non-interactive material (cracks) and for fast extraction of the signal from the front or rear end of the electrodes. The calorimeter is divided in two half-barrel wheels covering in pseudorapidity up to $|\eta| < 1.475$, housed in the barrel cryostat and two end-cap detectors ($1.375 \leq |\eta| \leq 3.20$) in two end-cap cryostats. There is a region defined as the crack region at the junction of the barrel and end cap components. Signal from this region is discarded in analysis due to the large volume of material in this region, which makes it particularly obscure. In the barrel, the accordion layers are axial and run in ϕ , the folding angles of the layers vary with radius to keep the liquid-argon gap constant. In the end-caps the layers are parallel to the radial direction and run axially. The LAr is ionised by electromagnetic showers. The read-out circuits are made of three copper layers insulated by two layers of polyimide. The two outer layers, split in sectors, are connected to high-voltage sources and polarize the LAr gap to the absorber. The inner layer is where the signal is collected through capacitive coupling and is then segmented into read-out pads.

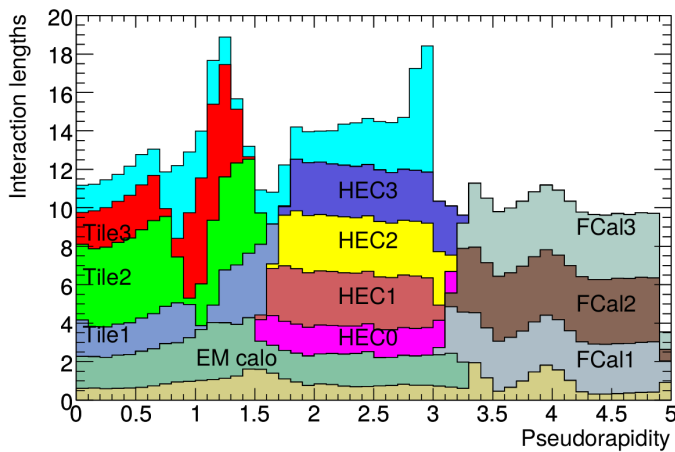


Figure 3.6: Cumulative amount of material, in units of interaction length, as a function of $|\eta|$, in front of the electromagnetic calorimeters, in the electromagnetic calorimeters themselves, in each hadronic layer, and the total amount at the end of the active calorimetry. Also shown for completeness is the total amount of material in front of the first active layer of the muon spectrometer (up to $|\eta| < 3.0$) [1].

In the region of $|\eta| < 1.8$ there is an additional presampler layer. This consists of a thin (0.5 cm in the end-cap and 1.1 cm in the barrel) LAr layer with no absorber. This is placed at the front of the calorimeter [52]. This is to correct for the energy lost at the front of the calorimeter, by taking a measurement just before the ECAL is reached and the majority

of the showering occurs. The granularity of the barrel presampler is very fine in η (0.003) to allow precise pointing of photons. The first layer of the calorimeter is designed for precision measurements, in particular distinguishing between prompt photons and neutral pion decays. By necessity it has the smallest measurable segment size of the three layers with $\Delta\eta \times \Delta\phi = 0.025 \times 0.025$. The second layer will contain the largest fraction of energy deposited by an EM shower and is designed mainly for energy measurements. Because of this it is used to distinguish between EM showers and hadronic showers which are much more penetrating. As a discriminatory layer, it can have a coarser granularity at $\Delta\eta \times \Delta\phi = 0.05 \times 0.025$.

The depth of the three sampling layers has been subject to thorough optimisation, mostly based on the criterion of π^0 rejection. The depth of the first layer is $6 X_0$ (including dead material and presampler). The end of the second (main) layer was chosen to be $24 X_0$. The depth of the last layer varies between 2 to $12 X_0$ (for η less than 0.6). The depth of the second sampling is limited to $22 X_0$, in order to have at least $2 X_0$ in the third sampling.

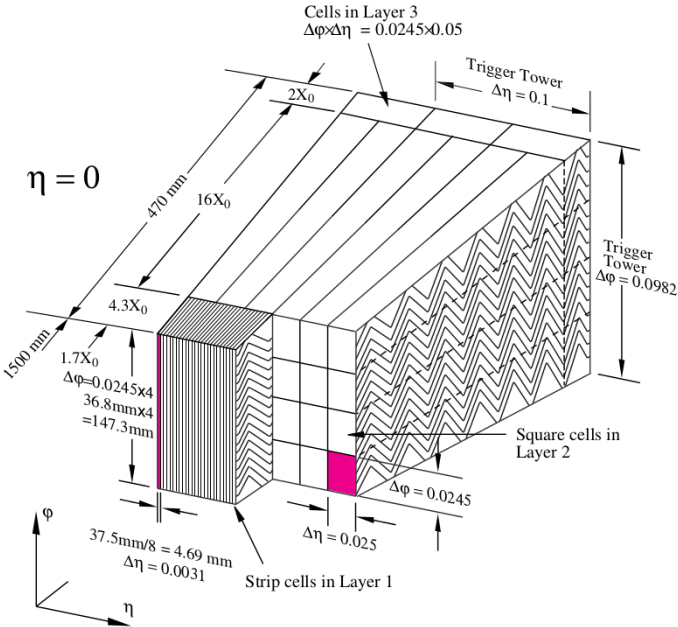


Figure 3.7: Sketch of a barrel module where the different layers are clearly visible with the ganging of electrodes in ϕ . The granularity in η and ϕ of the cells of each of the three layers and of the trigger towers is also shown [1].

3.6.2 The Hadronic Calorimeter

The HCAL uses slightly different materials and techniques to the ECAL, which also vary between the tile calorimeter, end-cap (HEC) and forward calorimeter (FCal) components.

The barrel section at $|\eta| < 1.0$ and extended barrel sections at $0.8 < |\eta| < 1.7$ make up the tile calorimeter, which uses steel absorber layers and plastic scintillating tiles as the active medium [1]. These are read out from both sides by wavelength-shifting fibres to photo-multiplier tubes (PMTs). There are three layers of modules in each barrel section, which are 1.5 -, 4.1 - and $1.8\lambda_I$ thick in the barrel, and 1.5 -, 2.6 - and $3.3\lambda_I$ thick in the extended barrels. Module layers are offset with respect to the layers of their neighbours for increased granularity, which is $\Delta\eta \times \Delta\phi = 0.1 \times 0.1$ in the first two layers and $\Delta\eta \times \Delta\phi = 0.1 \times 0.2$ in the final layer. The electronics are contained with girder plastic rings, which also provide flux return for the central solenoidal magnetic field.

The HEC consists of two wheels, each consisting of two layers of wedge-shaped modules which use copper absorber layers alternated with LAr with a flat plate design. The end-caps provide $1.5 < |\eta| < 3.2$ coverage, overlapping slightly with both the tile calorimeter and the FCAL in η .

The FCAL is located in the same cryostats as the end-cap calorimeters and provide coverage over $3.1 < |\eta| < 4.9$ and uses an absorber metal matrix combined with rod and tube electrodes, where LAr fills all of the small gaps in between. It is comprised of three modules, the first using copper as the shower-initiating metal, which is focused on EM measurements and the last two, which both use tungsten as the absorber and are primarily for the measurement of hadronic energy and to provide containment and minimise lateral spread of hadronic showers.

3.7 Muon Spectrometer

The Muon Spectrometer (MS) [53] is the outermost part of the ATLAS detector, which surrounds the calorimeters and measures the muon tracks in conjunction with the charged tracks in the ID and small energy deposits in the calorimeters for muon reconstruction. It is divided into the barrel, containing three layers at radius 5, 7.5 and 10 m in the region $|\eta| < 10$, and two end-caps, comprised of wheels at 7.4, 10.8, 14 and 21.5 from the origin and covering the range $1.0 < |\eta| < 2.7$. A cut-away showing the structure and individual components can be seen in Figure 3.8 and examples of muon trajectories in the barrel and end-cap are shown in Figure 3.9.

The magnetic field used to bend particle trajectories is provided by the barrel toroids for $|\eta| < 1.4$, by the end-cap toroids for $1.6 < |\eta| < 2.7$, and a combination of the two in the “transition” region $1.4 < |\eta| < 1.6$. In the barrel region, the toroidal field is produced by eight very large superconducting coils arranged in an open geometry, with a B -field

varying from 0.5 to 2T.

The components of the muon system are: resistive plate chambers (RPCs), thin gap chambers (TGCs), cathode strip chambers (CSCs), and monitored drift tube chambers (MDTs). The MDTs and CSCs are used to precisely measure the muon tracks. The MDTs provide a precise momentum measurement. They cover the pseudorapidity range $|\eta| < 2.7$ in each layer except the innermost end-cap layer where their coverage is limited to $|\eta| < 2.0$. Each chamber consists of three to eight layers of 29.970 mm drift tubes, each filled with Ar/CO₂ gas and with a tungsten-rhenium wire through the centre. The wire is kept at a potential to collect gas ionised by charged particles passing through. They achieve an average resolution of 80 μm per tube, or about 35 μm per chamber.

The CSCs are placed at high pseudorapidity ($2.0 < |\eta| < 2.7$) in the inner-most tracking layer. They possess a high rate capability and time resolution. They are comprised of multiwire proportional chambers filled with AR/CO₂/CF₄ gas. There are cathode planes segmented into strips in orthogonal directions, which allows both coordinates to be measured from the induced charge distribution. The solution of a chamber is 40 mm in the bending plane (η) and approximately 5 mm in the transverse plane.

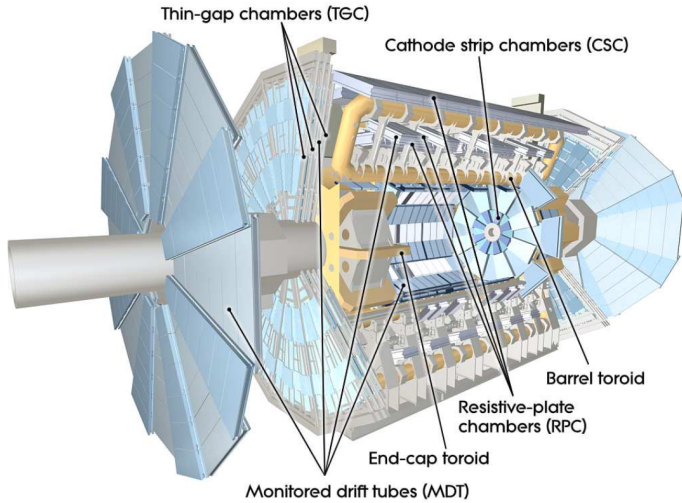


Figure 3.8: Cut-away view of ATLAS muon system [1].

The trigger chambers are operational in the region $|\eta| < 2.4$, with two different types of chamber employed to handle the increased rates in the forward region. The RPCs are located in the barrel and cover the region $|\eta| < 1.05$ and the TGCs are in the end-caps covering $1.05 < |\eta| < 2.4$. As well as providing a fast enough read-out (less than 50 ns) for triggering, these also determine a second reading of the muon coordinate which is orthogonal and complementary to that taken by the precision chambers. The RPCs consist of gaseous (C₂H₂F₄/Iso-C₄H₁₀/SF₆) parallel electrode-plate detector. The resistive plastic

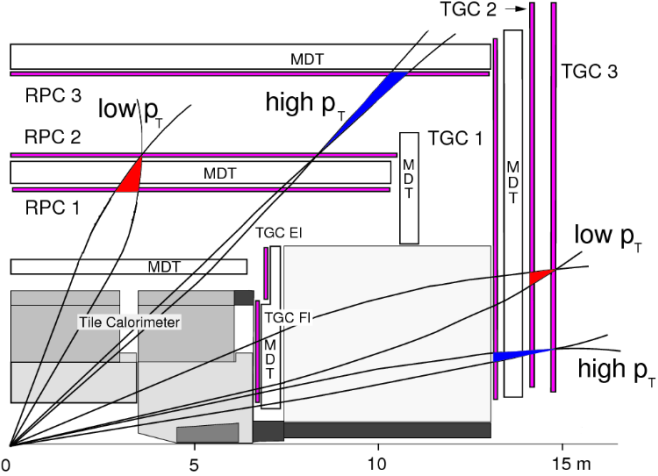


Figure 3.9: Muon trajectories exemplified for the barrel (RPCs) and the end-cap (TGCs) [1].

plates used are at a spacing of 2 mm and with a voltage of 4.9 kV/mm across them. The gas mixture forms ionising avalanches when a charged particle passes through. These are read off by metallic couplings on the outside of the resistive plates. The TGCs are multi-wire proportional chambers similar to the CSCs, with a higher granularity than the RPCs.

3.8 Trigger and Data Acquisition System in Run-1

The Trigger and Data Acquisition (TDAQ) system is designed with the purpose of reducing the event rate taken from the LHC at 40 MHz (during Run-1) to a recordable size of approximately 200 Hz, which corresponds to an average data rate of ≈ 300 MB/s. However the actual recordable event rate during Run-1 was between 0.5 - 1 kHz. It consists of two subsystems: the trigger and data acquisition, which handle the event selection and data flow respectively.

3.8.1 The ATLAS Trigger System

The trigger consists of three levels of event selection: Level 1 (L1), Level 2 (L2) and the Event Filter (EF). The L2 and event filter form the High-Level Trigger (HLT). The L1 trigger searches for signatures from high- p_T muons, electrons, photons, jets, hadronically decaying τ -leptons and large missing transverse energy. It selects a region of interest (RoI) in η and ϕ based on these signatures using reduced granularity information from the calorimeters and the muon spectrometer. During the decision making process, the event

information from the detectors is stored in front-end pipelines and is then passed to the Read Out Buffers (ROBs) if the decision is positive along with RoI information from the L1. The maximum L1 accept rate which the detector read-out systems can handle is 75 kHz (For Run-2 100 kHz). The L1 decision must reach the front end electronics with 2.5 μ s after the bunch crossing with which it is associated. The L2 trigger is “seeded” by RoIs, which contain possible trigger objects within the event. The L2 takes RoI information from the ROBs for co-ordinates, energy and signature type combined with tracking information from the ID to limit the amount of data transferred from the detector read-out. In doing so, the L2 trigger reduces the rate to below 3.5 kHz, with an average event processing time of \approx 40ms. If the event is accepted, the data is passed to the Event Builder and stored in the Full Event Buffer. The EF then accesses the fully built event using offline algorithms, with access to full detector granularity, maximum calorimeter and muon chamber precision to refine trigger selection. Improved information on energy deposition improves the threshold cuts, while the track reconstruction in the ID vastly improves particle identification, particularly for electrons and photons. A higher latency is utilised to achieve a more accurate reconstruction. Nominally, the EF was designed to reduce the event rate to approximately 200 Hz with an average event processing time of the order of four seconds. Figure 3.10 shows a flowchart representing this process.

3.8.1.1 Level 1 Trigger

The L1 trigger uses custom fast electronics to perform the initial event selection based on detector information. It then passes its decision to the Central Trigger Processor (CTP). The L1 Calorimeter (L1Calo) seeks to identify high- E_T objects, in addition to the objects highlighted in the introduction, a trigger on the scalar sum of the jet transverse energies is also available and for the electron/photon triggers, isolation can be required. The isolation requirement implies that the energetic particle must have a minimum angular separation from all other significant energy deposits within the same trigger.

To identify RoIs for electrons, photons, taus and jets, coarse granularity segments of the HCAL and ECAL, referred to as trigger towers are used. They cover blocks of size $\Delta\eta \times \Delta\phi = 0.1 \times 0.1$ in the central calorimeters and up to $\Delta\eta \times \Delta\phi = 0.4 \times 0.4$ in the forward calorimeters.

The L1 Muon trigger is based on signals in the muon trigger chambers using the three layers of RPCs and TGCs in the barrel and end-cap of the muon spectrometer. The trigger searches for patterns of hits consistent with high p_T muons originating from the point of

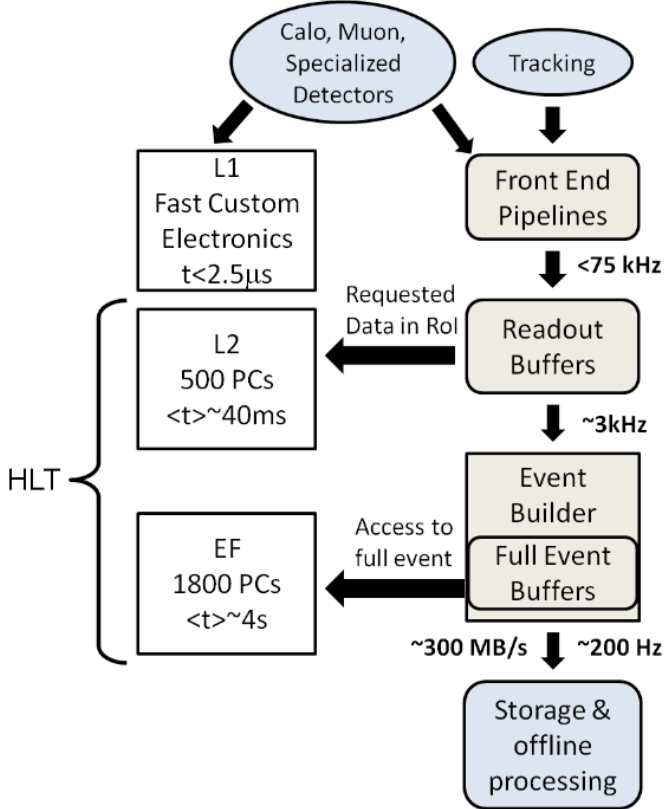


Figure 3.10: Schematic of the ATLAS Trigger System. Numbers quoted are the design goals taken from [54] and in some cases differ from those for 2011 and 2012.

interaction.

If an event passes the L1 trigger requirements, an accept signal (L1A) is sent to the CTP. The CTP then sends information about the trigger decision for all trigger items to the L2 trigger (RoI builder) and the data acquisition (ROS). To prevent an overwhelming rate of data flow through the front-end buffers, the CTP enforces two types of dead-time; simple and complex. The simple dead time requires a given period has to pass after an L1A decision from the L1 before another is allowed. For Run-1 during 2011 and 2012 this was five bunch crossings. The CTP vetoes any L1A signals within this time period. The complex dead time sets a limit on the number of L1A allowed within a given period, which, for Run-1 during 2011 and 2012 was set to 8 accepts per 416 bunch crossings. Part of the read-out data of the CTP is the number of the corresponding luminosity block. A luminosity block is defined as the shortest time interval for which the integrated luminosity, corrected for dead time and pre-scale effects, can be determined. A luminosity block should be small enough such that, in the event of detector failures, the data can be rejected with unnecessary data loss. However, a luminosity block should contain enough data such that the uncertainty on the luminosity is only determined by systematics and

by the available statistics. For ATLAS this is of the order of minutes.

3.8.1.2 High Level Trigger

The High Level Trigger (HLT) consists of the L2 and EF triggers. Both are implemented in software and run mostly on commodity hardware (farms) [55]. The L2 trigger uses signature-based algorithms, which have a limited precision in order to operate on a short timescale. It uses the RoI information (type, position and p_T of the highest trigger threshold passed) from the L1 trigger seed. This keeps the amount of raw data passed to the L2 trigger at a few percent of the total event information. In addition to the muon detector and calorimeter data, the L2 also has access to the tracking information from the ID.

Two separate algorithm strategies were used during Run-1. Both strategies start by identifying a primary vertex, using the hit occupancy for the event in the pixel and SCT sub-detectors as a function of the z co-ordinate. The point with the highest hit occupancy is taken as the primary vertex for the event. The algorithms generate final tracks from the space points using a Kalman filter [56], which is a general type of linear filtering algorithm that iteratively compensates for the effect of noise on a signal. In the case of tracking algorithms, the signal is the true trajectory of the particle and the noise is the effect of associating incorrect space points to the true trajectory. If an event passes the L2 Trigger, the information from the RoI is sent to the final trigger layer, the Event Filter. This has access to the full granularity data from the whole event and is not restricted to the RoIs. It uses standard ATLAS offline reconstruction algorithms. The average rate after the EF decision was approximately 400 Hz in 2011 and approximately 1 kHz in 2012 (higher than design rates).

3.8.2 Trigger Chains and Menus

Physics events of interest can contain a multitude of important physics signatures, to achieve full information on these events, a sequence of algorithms for the L1, L2 and EF triggers must be satisfied. The combination of these algorithms forms a specific trigger selection, which is referred to as a chain. For each signature used for triggers there are a set of chains defined. Each chain is composed of a Feature Extraction (FEX) algorithms, which create the objects (like calorimeter clusters) and Hypothesis (HYPO) algorithms that apply selection criteria to the objects (for example $p_T > 20$ GeV). Caching in the trigger system allows features extracted from one chain to be recycled in another chain. This reduces both the data access and processing time of the trigger system.

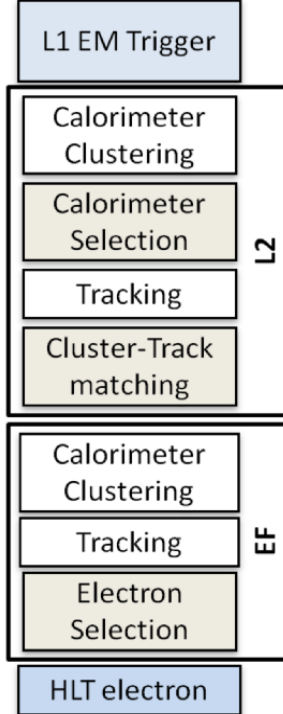


Figure 3.11: Schematic example of an electron trigger chain [54] .

To illustrate, take the example of the single electron trigger, *e24_medium*. This chain is built on the L1EM18 trigger, which has a threshold of 18 GeV and uses the EM trigger tower to determine this threshold is passed. The detector information in the RoI provided by the L1EM18 trigger is seeded to the *L2_e24_medium* trigger, which has a 25 GeV threshold, lastly the full detector information is sent to the *EF_e24_medium* trigger, which also has a 25 GeV threshold. Primary chains are physics-based and used for analyses. Backup chains have a higher threshold than the primary chains and can be used if the detector malfunctions or the luminosity increases unexpectedly, supporting chains provide support for physics analyses, for example background estimation methods and the monitoring chains are used to monitor data performance.

Events which have passed the EF are classified into streams. An event can be contained in more than one stream, and the type of stream is dependent on the category of chain that accepted the event. The four physics streams are muon, electron/photon, jet/tau/ E_T^{miss} and minimum bias. Data from these streams are recorded separately, to allow analyses to focus only on events containing objects of interest. In addition to the physics streams 10% of events are written to the express stream for fast reprocessing to validate the recorded data and data collections for calibration.

The full collection of all trigger chains for all signatures is referred to as the trigger

menu. These menus may change depending on the running conditions. Changes in collision energy or pile-up has an effect on the I/O rates of the various triggers, which would in turn require a change to the trigger menu. The trigger menu was updated for Run-2 to account for the higher centre-of-mass energy and increase in pile-up.

3.9 ATLAS Run-2 Upgrades

The LHC during Run-2 of its planned schedule will attain its design energy and nominal luminosity with a centre of mass energy of $\sqrt{s} = 13\text{-}14 \text{ TeV}$, $\mathcal{L} = 1 \times 10^{34} \text{ cm}^{-2}\text{s}^{-1}$, a bunch spacing of 25 ns and a pile up $\langle \mu \rangle$ of ≈ 40 . It is essential for the ATLAS detector and the TDAQ system to be upgraded in order to cope with the increased event rate at higher energies to continue with physics analysis. This section will discuss the main changes to the ATLAS detector in preparation for Run-2, which took place during Long Shutdown 1 (LS1).

3.9.1 Insertable B-layer

The Insertable B-Layer [57] is the fourth layer added to the Pixel Detector between a new beam pipe and the current innermost pixel layer (*B*-layer), as shown in Figure 3.4. The IBL improves the overall performance of the Pixel Detector and the ATLAS experiment by enhancing the quality of impact parameter reconstruction of tracks. This is done by improving vertexing and tagging of *b*-quark containing jets (*b*-tagging, see Section 4.4.7). Furthermore, in case of a complete *B*-layer failure, the IBL can restore the full *b*-tagging efficiency. The addition of a fourth layer also helps to mitigate luminosity effects such as the increase in event pile-up, which leads to high occupancy and read-out inefficiency. Detailed simulations of the ID performance with and without the IBL have been performed. The IBL detector has been fully integrated into the ATLAS ID software and its response is based on the existing pixel digitisation algorithm [58].

3.9.2 ATLAS TDAQ Upgrades for Run-2

With beam energies of 13-14 TeV and up to 80 pp interactions per bunch crossing, to access physics events of interest under these conditions required improvements to the Run-1 trigger system. In particular:

- Make the HLT code more robust and faster to compensate for increased processing time due to high pile up and allow for use of slower offline reconstruction algorithms.

- Harmonise trigger and offline analysis selections to increase trigger selection efficiency.
- Introduce specialised, selective triggers to help reduce trigger rates.

3.9.2.1 L1 Topological Trigger

Previously, the L1 trigger system was only able to look for single objects or apply simple combinations of such single objects to be present in the event. The L1 topological trigger (L1-Topo) [59] has been designed to extend the functionality of the L1 trigger. It receives energy and direction information about the objects found by the L1 calorimeter and the muon trigger. This information is then processed by dedicated algorithms implemented in its FPGAs. Signatures that will be looked for include a muon close to a jet, an object with a certain transverse mass or an event with an effective mass above a certain threshold. However the L1-Topo will only be able to send limited information to the HLT due to the 100 kHz read-out rate. The HLT has the challenge of using the specific L1 object combination with the correct topological criteria to seed the RoI-guided HLT reconstruction. In answer to this challenge, the L1 topological trigger hardware is simulated, i.e. the FPGA code will also be implemented in C++ and validated against the hardware response and run online in the HLT.

3.9.2.2 Fast TracKing Trigger System (FTK)

As the LHC luminosity approaches its design luminosity, the combinatorial problem arising from charged particle tracking becomes increasingly difficult, resulting in lower signal efficiencies for larger pile up and constant rates of fake physics objects. The Fast TracKer [60] or FTK is a proposed system of electronics which will perform global track reconstruction after each L1 trigger decision to enable the L2 trigger to have early access to tracking information. The FTK will use data from the pixel and semiconductor tracker detectors as well as the new IBL pixel detector. The necessity for improved track reconstruction performance at higher luminosities is essential for identifying heavy particles such as b -quarks and τ leptons.

The FTK will receive all the SCT and pixel detector data from the inner detector charged particle tracker at each L1A signal, with up to 100 kHz rate. The hardware then finds and reconstructs charged track candidates using pattern matching on specially pre-processed data in an associative memory. In this sense the hardware provides tracking information for the whole detector very quickly, with no need for HLT processing time

or read-out bandwidth. This information can be used to: calculate the isolation of identified leptons from other charged particles, find the primary vertices of the event using all reconstructed tracks, seed the HLT track reconstruction to reconstruct charged tracks with high precision in a large area of the detector. The reconstructed tracks may be used directly in the b-tagging and tau reconstruction algorithms to improve their performance with the additional tracking information.

3.9.2.3 The Merged High Level Trigger

In Run-1 the ATLAS trigger system had distinct L2 and EF farms. For Run-2, these farms were merged into a single farm running a unified HLT process, that retains the on-demand data read-out of the old L2 and uses offline based algorithmic code from the EF. This new system reduces code and algorithm duplication and results in a more flexible HLT. The majority of the trigger selections were reoptimised during LS1 to minimize differences between the HLT and the offline analysis selections, which in some cases reduced trigger inefficiencies by more than a factor of two. The HLT tracking algorithms also were prepared for the inclusion of the FTK system. The average output rate of the HLT has been increased from 400 Hz to 1 kHz. The HLT processing performed within RoIs has been augmented for some triggers to also allow for merging of RoIs into a single object, referred to as a super-RoI. This reduces the trigger processing for events with a large multiplicity of partially overlapping RoIs.

The upgraded ATLAS trigger system has been commissioned using cosmic ray data and early 13 TeV collisions. It works efficiently allowing ATLAS to efficiently select events for physics analysis in Run-2.

Chapter 4

The Generation, Simulation and Reconstruction of ATLAS Data

Monte Carlo (MC) simulation is used in ATLAS to mimic particle interactions or decays, with each referred to as an “event”. These events are used to understand SM and beyond the SM processes and are validated with events from real data taken by the detector. The process of generating an event using MC simulation can be categorised into two parts: event generation and detector simulation. Data which has been recorded by the ATLAS detector requires processing to reconstruct physics objects to be used in analysis. The Athena software framework [61], which is based on the GAUDI [62] framework developed by LHCb [47] is used to do this. This framework is implemented for all aspects of the experiment software including the triggering of events, event reconstruction and event processing for simulated data. This chapter discusses event generation in Section 4.1, event simulation in Section 4.2 and digitisation in Section 4.3. Reconstruction algorithms are the same for both real data and MC simulated events and are described in Section 4.4. The objects used for the analysis in this thesis are selected from the reconstructed objects based on a set of criteria, which are described in Section 4.5. Finally the MC simulated samples used for the SM and SUSY processes are described in Section 4.6.

4.1 Event Generation

All SM and beyond the SM physics processes are simulated by MC event generators [63]. These generators use a combination of perturbative and phenomenological calculations to produce randomly distributed “events” of a given type with stable final state particles. The ATLAS detector collects information from proton-proton collisions, which essentially

involves the collisions of the constituent *partons*. These partons include the three valence quarks (uud); the gluons mediating the strong interactions between the valence quarks; and the sea quarks which are produced in virtual $q\bar{q}$ pairs by interactions of the gluons. These interactions are collectively known as Deep Inelastic Scattering (DIS) processes. They are called as such because the substructure of the proton is probed by an incoming particle (deep), for example another proton, and the proton's momentum is not conserved in the scattering (inelastic) as shown in Figure 4.1.

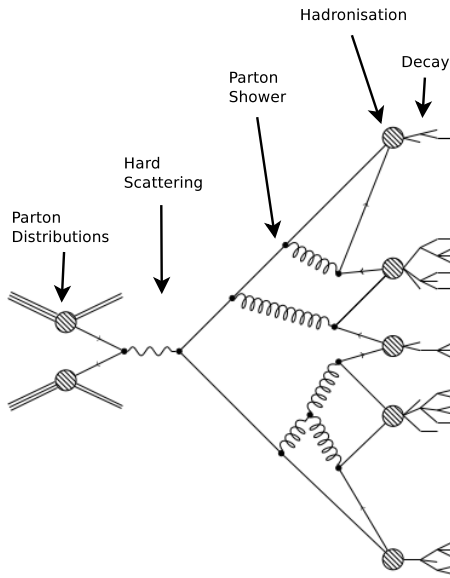


Figure 4.1: Diagram of a simulated high energy proton-proton collision process.

If Q^2 represents the squared 4-momentum-transfer vector q of the exchanged virtual photon. The interacting parton carries a fraction of the proton's momentum x , known as the Bjorken scaling variable.

The measure of momentum transfer in the event Q^2 is related to the momentum transferred by the exchanged boson q by:

$$Q^2 = -q^2. \quad (4.1)$$

To effectively describe partons within the protons colliding at the LHC, parton distribution functions (PDFs) are used, this will be discussed in Section 4.1.1.

Scattering interactions involving protons at the LHC can be grouped into two categories: Hard processes, which can be described with perturbation theory, or soft processes, which involve non-perturbative QCD effects. Hard processes involve large momentum transfer and soft processes involve low momentum transfer, with inelastic interactions at

the LHC being dominated by soft processes [64]. Each pp collision will typically contain a hard scattering process between two colliding partons, and a number of soft processes, which can include Initial State Radiation (ISR), Final State Radiation (FSR) and the Underlying Event (UE). ISR refers to the particles radiated by the partons which will interact in the hard process prior to scattering. Additional parton interactions in hard processes due to beam remnants and the rest of the proton constituents form the UE. The particles radiated from the final state products of the hard scatter form the FSR. Coloured particles in the event are capable of radiating gluons and/or producing $q\bar{q}$ pairs, resulting in a cascade of radiation in the detector, known as parton showering.

The following sections will briefly describe the techniques used to model the hard process, parton shower (PS) and hadronisation within the event, in addition to the modelling of the UE.

MC generated samples are categorised on the basis of the hard-process specified before generation, which allows analysers to choose samples with relevant processes.

4.1.1 Parton Distribution Functions

PDFs [65] describe the probability density of constituent partons of the interacting protons to have proportion x of the overall momentum. PDFs, denoted $f_a(x, Q^2)$ are functions of the momentum fraction, parton species a and momentum transfer Q^2 . The factorisation theorem [66] states that the differential cross section $d\sigma$ of any hard process can be written in the form

$$d\sigma = \sum_{i,j} \int_0^1 dx_i \int_0^1 dx_j \quad d\sigma_{i,j}^{part} f_i(x_i, Q^2) f_j(x_j, Q^2). \quad (4.2)$$

Here i and j are the indices of the interacting partons with momentum fractions x_i , x_j and the $d\sigma_{i,j}^{part}$ is the differential cross section of the hard process between partons i and j with momentum fractions x_i , x_j . The PDFs are functions of the momentum fraction and are thus independent of the hard process. They are also dependent on the parton type (valence quark, gluon or sea quark). It is not possible to calculate the PDFs perturbatively, but their evolution as a function of Q^2 for a given parton can be obtained using the DGLAP evolution equations [67], using a range of hard scattering data from both fixed target and collider experiments. These equations describe the evolution of the structure functions of the proton's constituent quarks and gluons as a function of the “running” strong coupling α_s , where running refers to Q^2 dependence. A range of PDF

sets are used by the MC samples considered by this analysis.

4.1.2 Matrix Element Calculation

The hard process involves a large momentum transfer ($Q^2 > \mathcal{O}(1 \text{ GeV})$), the simulation of this process can be calculated using quantum field theory techniques - this is known as the matrix element calculation. PDFs simulate partons coming into the hard scatter process using matrix elements to leading order (LO) or next-to-leading order (NLO) in an expansion in α_s to calculate a probabilistic distribution of the outgoing partons. Additions can be made to the matrix element to include *hard emission*, which refers to the production of high momentum quarks and gluons in the event. This includes several processes; a gluon splitting into two gluons ($g \rightarrow gg$), a gluon decaying to a quark-antiquark pair ($g \rightarrow q\bar{q}$), and a quark radiating a gluon ($q \rightarrow gq$).

4.1.3 Parton Showers

The processes mentioned in the Matrix Element section can also occur at lower energies, but cannot be modelled by the matrix element calculation due to their non-perturbative nature. They are handled with the PS phenomenological modelling, which is valid for Q^2 values above $\mathcal{O}(\text{GeV})$, the QCD scale. PS models have been developed by the HERWIG [68], PYTHIA [69] and SHERPA [70] collaborations. The algorithms used to simulate PS are based on a Markov chain [71], using probabilities that a gluon is radiated or a $q\bar{q}$ pair is produced. The decision of whether or not these processes will occur is made at each point in the chain. At intermediate Q^2 , gluon/quark radiation may be treated as a hard emission or part of the PS, which can lead to double-counting of the total radiation in a given event. The CKKW [72] and MLM [73] schemes are used to determine whether emissions form part of the matrix element or PS. Eventually the energy of the partons will decrease below 1 GeV and undergo hadronisation, which is modelled separately.

4.1.4 Hadronisation

Free partons are not observed directly in nature due to confinement. Resulting partons produced in showering from pp collisions hadronise at low energy scale. At this scale perturbation theory is not valid, so modelling is used to simulate what occurs. The two common approaches are the Lund string model [74] used by the PYTHIA MC and the Cluster model used by the HERWIG MC program [75].

4.1.5 Underlying Event

The “spectator” partons, which are the partons not involved in the hard process of an event are referred to as the underlying event (UE) [76]. These partons hadronise to form colour-singlet state. This hadronisation is described by phenomenological models developed by the JIMMY [77], PYTHIA and SHERPA collaborations. The modelling involves many additional free parameters, which are tuned to data and are described in further detail in Section 4.6.1.

4.2 Detector Simulation

The MC generated events need to be passed through an accurate simulation of the ATLAS detector, which mimics the response of the real detector to the physics processes. This is done by the GEANT4 framework [78]. It is the only officially supported software for the ATLAS detector simulation and is integrated into the ATLAS offline software. The detector simulation involves the interaction of particles within the detector volume, this includes particle ionisation, energy deposition in the calorimeters and intermediate particle decays, radiation and scattering. These interactions are recorded as GEANT4 “hits”. Output files containing data of the detector simulation, known as “hit files”, are generated. These are then “digitised” to produce voltages and currents in the detector. The simulation of electronic noise, pile-up and other effects from the detector electronics are factored in at the digitisation stage. It is vital to mention the detector geometry and simulation infrastructure remains the same for simulation, digitisation and reconstruction to ensure agreement between simulation and reconstruction. With the completion of the detector simulation, the simulated data (in the form of digits) are in an equivalent format to the data recorded with the ATLAS detector.

Fully simulating each event traversing the detector can be very time consuming, with some events taking up to ten minutes. A faster simulation process can also be performed using the ATLFASTII package [79], which does not run all of the aforementioned stages for full simulation. Instead, the energy of single particle showers is deposited directly using parameterisations of their longitudinal and lateral energy profile and a simplified geometry is applied. The calorimeter is simulated using FastCaloSim [80]. Scattering of particles within the inner detector is simulated using a simplified model. The GEANT4 simulation time can be reduced by more than one order of magnitude by using the ATLFASTII. A fast simulation is important in cases when the total number of events simulated is a limiting

factor for analysis, for example SUSY “signal” processes. In this case, samples can be generated with a large number of events given that this fast simulation is well validated against the full simulation samples.

4.3 Digitisation

The hits produced during simulation are passed through a simulation of the detector in order to produce digitised values for voltages, associated times etc. Any noise within the detector is included. Soft collisions, beam halo, cosmic rays and the cavern background are independent of the event itself, therefore are not simulated each time. These hits can be overlaid at this stage. The MC is then output in a raw data object (RDO) format, which contains the equivalent information to the real data recorded by the detector. A *truth* record for the simulated events is stored in a simulated data object (SDO) format, which contains the information on the true identity of particles at each vertex and the corresponding tracks left behind and consequent decays. The truth objects do not necessarily correspond exactly to the objects reconstructed from the RDO, for example a lepton can be mistakenly identified as a photon. The truth record is stored to study detector behaviour, for example potential misreconstruction rates of various particles. Truth objects can be “matched” to reconstructed objects by requiring a minimum spatial requirement between the objects. In addition, matching can be used to trace back the decay chain and identify the “parent” of a particle, using the particle identifier and vertex information.

4.4 Reconstruction

Both the data and the simulated MC events are passed through the same reconstruction algorithms. At this stage, the electronic pulses from the digitisation stage are reconstructed into tracks and calorimeter deposits, which are in turn reconstructed into physics objects, such as jets, electrons, muons, taus, photons and missing transverse energy or E_T^{miss} . Loose definitions for physics objects are made initially for most analyses to use. More stringent requirements can be applied on top to focus on the needs of particular analyses. The benefit of this approach is the increased purity of selected objects. The definitions for the physics objects relevant to the analysis presented in this thesis are described in the following sections.

4.4.1 Pile-up in the Inner Detector

Characterisation of pile-up is an important step in event reconstruction. The number of proton-proton interactions per bunch crossing follows a Poisson distribution with mean value μ . During a bunch fill, μ decreased with decreasing intensity and increasing emittance, such that the peak value, or μ^{peak} , is the highest value in a single bunch crossing at the start of the stable beam period of the fill. The number of interactions per bunch crossing also varies between bunches. The number of interactions per bunch crossing averaged over a specific luminosity block and over all colliding branch crossing IDs (BCIDs) is referred to as $\langle\mu\rangle$.

In data, μ is calculated using the following formula [81]:

$$\mu = \frac{L \times \sigma_{inel}}{n_{bunch} f_r}, \quad (4.3)$$

where L is the luminosity, σ_{inel} is the total inelastic cross-section, n_{bunch} is the number of colliding bunches and f_r is the LHC revolution frequency. The uncertainty on μ depends on the uncertainties on the luminosity and the total inelastic cross-section. Figure 4.2 shows the luminosity-weighted mean number of interactions per bunch crossing μ for the 7 TeV and 8 TeV centre-of-mass luminosities. The inelastic cross section was taken to be 71.5 mb for 7 TeV collisions and 73.0 mb for 8 TeV collisions.

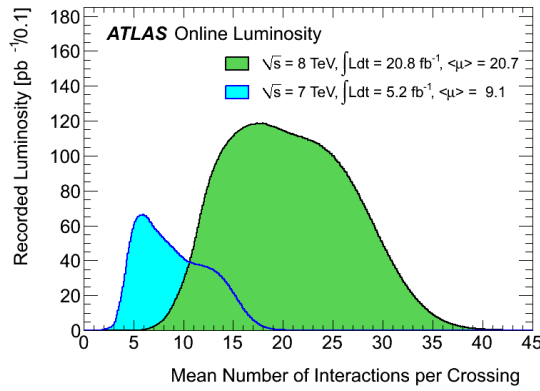


Figure 4.2: Luminosity-weighted distribution of the mean number of interactions per crossing for the 7 and 8 TeV data [82].

4.4.2 Inner Detector Track Reconstruction

Charged particles leave tracks in the ID, they are reconstructed using three different algorithms. The main track reconstruction strategy is the “inside-out” strategy, which starts by finding a track candidate in the pixel and SCT detectors and then extends the trajec-

tories of successfully fitted tracks to the TRT to reconstruct a full inner detector track. It starts from 3-point seeds in the silicon detectors and adds hits moving away from the interaction point using a combinatorial Kalman filter [56]. Primary particles are defined as particles with a mean lifetime of greater than 3×10^{-11} s directly produced in a pp interaction or from the subsequent decays or interactions of particles with a lifetime shorter than 3×10^{-11} s. The tracks reconstructed by the inside-out algorithm are required to have transverse momentum $p_T > 400$ MeV. This track reconstruction strategy is complemented by an “outside-in” strategy, which starts from unassigned TRT segments and looks for matching hits in the pixel and SCT detectors. This type of track reconstruction targets the late decays of neutral particles and photon conversions to e^+e^- pairs and is also able to recover the remaining trajectory after a catastrophic energy loss. Finally there are tracks with a TRT segment but no extension to the silicon detectors are referred to as TRT-standalone tracks. There are several quality cuts applied to the tracks. The tracks are assigned values of η and ϕ using their direction with respect to the origin in the right-handed co-ordinate system described in Section 3.3, where the origin is taken to be the position of the primary interaction, as illustrated in Section 4.1. Two parameters are defined for the track quality: d_0 is defined as the distance of closest approach between the track and the origin, and z_0 is defined as the z -plane component of d_0 , with $z_0\sin\theta$ defined as the projection of d_0 onto the z -axis. The transverse momentum p_T of a track is related to the magnetic field B , and the bending radius R , which quantifies the bending of the track trajectory due to B . The relationship is given as $p_T = 0.3 \times B \times R$. The following cuts are applied to all track referred to after this point, unless specified otherwise:

- $p_T > 1$ GeV,
- $|\eta| < 2.5$,
- $d_0 < 1.5$ mm,
- $z_0\sin\theta < 1.0$ mm,
- Number of hits in the pixel detector ≥ 2 ,
- Number of hits in the SCT detector ≥ 7 .

4.4.3 Vertex Reconstruction

A *vertex* is defined as the point in space at which two particles interact or a single particle decays. They are extrapolated with sufficient accuracy using at least five ID tracks back to a common interaction point. The primary vertex, which is supposed to be the source of the hardest interaction, is defined by finding the vertex with the largest summed track

p_T . Primary vertices are reconstructed using an iterative vertex finding algorithm. Vertex seeds are obtained from the z -position at the beam-line of the reconstructed tracks. An iterative χ^2 fit is made using the seed and nearby tracks. Each track is assigned a weight which is a measure of its compatibility with the fitted vertex depending on the χ^2 of the fit. Tracks that are displaced by more than 7σ from the vertex are used to seed a new vertex and the procedure is repeated until no additional vertices can be found. Secondary vertices can be reconstructed from particles with sufficient lifetime for the decay length to be measurable at ATLAS, for example b -quarks, which can travel a few millimetres. These secondary vertices will be displaced with respect to the primary vertex.

4.4.4 Electron Reconstruction

The electron-reconstruction algorithm used in the central region of the detector where the ID is operational ($|\eta| < 2.5$) identifies energy deposits in the EM calorimeter and associates these clusters of energy with reconstructed tracks in the inner detector. This process is a three-step reconstruction:

4.4.4.1 Cluster reconstruction

The EM clusters are seeded by energy deposits with total transverse energy $E_T > 2.5$ GeV by using a sliding-window algorithm [83]. The window size is 3×5 in units of 0.025×0.025 in (η, ϕ) space.

4.4.4.2 Track association with the cluster

Within the tracking volume, tracks with $p_T > 0.5$ GeV are extrapolated from the last point of measurement to the middle layer of the EM calorimeter. The extrapolated η and ϕ co-ordinates of the impact point are compared to a corresponding seed cluster position in that layer. The match between the track and a cluster is successful if the distance between the track impact point and the EM cluster barycentre is $|\Delta\eta| < 0.05$. To account for the bremsstrahlung losses on the azimuthal distance, the size of the $\Delta\phi$ track-cluster matching window is 0.1 on the side where the extrapolated track bends as it traverses the solenoidal magnetic field. An electron candidate is considered to be reconstructed if at least one track is matched to the seed cluster.

4.4.4.3 Reconstructed electron candidate

After successful track-to-cluster matching, the cluster sizes are optimised to take into account the overall energy distributions in the different regions of the calorimeter. In the EM barrel region, the energy of the electron cluster is collected by enlarging its size to 3×7 in units of 0.025×0.025 in the (η, ϕ) space. In the EM end-caps the size is changed to 5×5 . The electron energy is calculated as the energy deposited the energy deposited within the cluster plus a factor to account for energy deposited outside of the cluster, which is referred to as leakage. This includes contributions deposited prior to the ECAL, within the ECAL but outside the cluster (lateral leakage) and beyond the ECAL (longitudinal leakage).

4.4.5 Electron Identification

Electrons in the central region of the detector are identified based on sequential cuts on the calorimeter, tracking and combined track-cluster variables. Three sets of reference selection criteria are used [84], labelled LOOSE++, MEDIUM++ and TIGHT++ are designed for use in analyses. These criteria are hierarchical as to provide increasing background-rejection power at the cost of losing some identification efficiency moving from LOOSE++ to TIGHT++. The efficiency for each of the three electron identifications can be seen in Figure 4.3 as a function of the number of primary vertices (which is a measure of pile-up) for 2011 and 2012 data.

4.4.5.1 Loose++

This selection uses shower-shape variables in both the first and second layers of the EM calorimeter. Hadronic leakage information is used in addition to requirements on the quality of the electron track and track-cluster matching to improve the rejection of hadronic backgrounds by a factor of five in the E_T range 30-40 GeV while maintaining a high identification efficiency. The loose ID variables are summarised in Table 4.1.

4.4.5.2 Medium++

This selection builds on the LOOSE++ selection by requiring the presence of a measured hit in the innermost layer of the pixel detector (to reject electrons from photon conversions), applying a LOOSE++ selection requirement on the transverse impact parameter $|d_0|$ and

Category	Description	Variable
Loose++		
Acceptance	$ \eta < 2.47$	-
Hadronic leakage	In $ \eta < 0.8$ and $ \eta > 1.37$, ratio of E_T in the first layer of the hadronic calorimeter to E_T of the EM cluster	$R_{had,1}$
	In $0.8 < \eta < 1.37$: ratio of E_T in whole hadronic calorimeter to E_T of the EM cluster	R_{had}
Middle layer of the EM	Ratio of energies in 3×7 cells over 7×7 cells	R_η
	Lateral width of the shower	$w_{\eta 2}$
Front layer of the EM	Total shower width Energy difference of the largest and second largest energy deposits in the cluster divided by their sum	w_{stot} E_{ratio}
Track quality and track-cluster matching	Number of hits in the pixel detector (> 0) Number of hits in the silicon detectors (≥ 7) $ \Delta\eta $ between the cluster position in the first layer and the extrapolated track (< 0.015)	- - $\Delta\eta_1$

Table 4.1: LOOSE++ ID variables [85].

identifying the transition radiation in the TRT (to reject charged-hadron background), when available. All common discriminating variables with the loose selection are tightened, improving the background rejection by an order of magnitude with respect to LOOSE++. The medium variables are summarised in Table 4.2.

Category	Description	Variable
Medium++ (includes Loose++ with tighter requirements on shower shapes)		
Track quality and track-cluster matching	Number of hits in the b-layer > 0 for $ \eta < 2.01$ Number of hits in the pixel detector > 1 for $ \eta > 2.01$ Transverse impact parameter $ d_0 < 5$ mm Tighter $ \Delta\eta_1 $ cut (< 0.005)	- - d_0 -
TRT	Loose cut on TRT high-threshold fraction	-

Table 4.2: MEDIUM++ ID variables [85].

4.4.5.3 Tight++

This selection uses all particle-identification tools available for electron ID. Tighter requirements are placed on the existing MEDIUM++ selection discriminating variables, as well as stricter requirements on the track quality in the presence of a track extension in the TRT detector, on the ratio of the EM cluster energy to the track momentum and a veto on reconstructed photon conversion vertices associated with the cluster are applied. The

background rejection power is increased by a factor of two with respect to the MEDIUM++ selection. The efficiency for each of the three identifications can be seen in Figure 4.3 as a function of the number of reconstructed primary vertices (a measure of the aforementioned pile-up), for 2011 and 2012 data. The tight variables are summarised in Table 4.3.

Category	Description	Variable
Tight++ (includes Medium++)		
Track quality and track-cluster matching	Tighter transverse impact parameter cut ($ d_0 < 1$ mm)	-
	Asymmetric cut on $\Delta\phi$ between the cluster position in the middle layer and the extrapolated track	$\Delta\phi$
	Ratio of the cluster energy to the track momentum	E/p
TRT	Total number of hits in the TRT	-
	Tighter cut on the TRT high-threshold fraction	-
Conversions	Reject electron candidates matched to reconstructed photon conversions	-

Table 4.3: TIGHT++ ID variables [85].

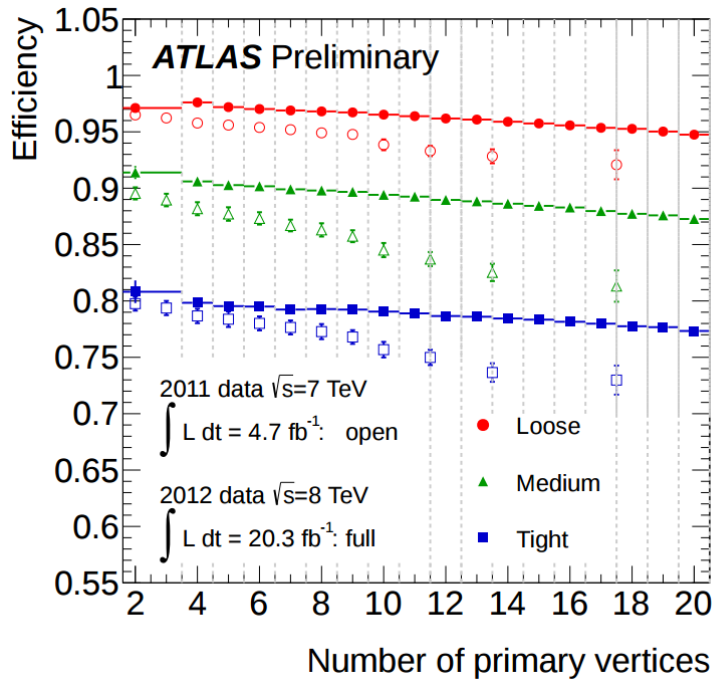


Figure 4.3: Electron identification efficiency in data for the various cut-based selections measured with 2011 and 2012 datasets as a function of the number of reconstructed primary vertices. Taken from [86].

4.4.6 Muon Reconstruction and Identification

Muon identification is performed according to several reconstruction criteria, which lead to different “types” of muon, taking into account the available information from the ID,

the MS and the calorimeter sub-systems. The different types are:

- Stand-alone (SA) muons: The muon trajectory is reconstructed only in the MS. The direction of flight and the impact parameter of the muon at the interaction point are determined by extrapolating the track left in the MS back to the point of closest approach to the beam line, taking into account the energy loss of the muon in the calorimeters.
- Combined (CB) muons: the track reconstruction is performed independently in the ID and the MS, a combined track is formed from the successful combination of a SA track with an ID track.
- Segment-tagged (ST) muons: A track in the ID is identified as a muon if the track extrapolated to the MS is associated with at least one track segment in the MDT or CSC.
- Calorimeter-tagged (CaloTag) muons: a track in the ID is identified as a muon if the track can be associated to an energy deposit in the calorimeter corresponding to a minimum ionising particle. Although this type has the lowest purity of all muon types it recovers acceptance in the uninstrumented region of the MS. The identification criteria of this muon type are optimised for a region of $|\eta| < 0.1$ and a momentum range of $25 \lesssim p_T \lesssim 100$ GeV.

The following quality requirements are applied to the ID tracks used for CB, ST or CaloTag muons:

- At least 1 Pixel hit;
- At least 5 SCT hits;
- At most 2 active Pixel or SCT sensors traversed by the track but without hits;
- In the region of full TRT acceptance, $0.1 < |\eta| < 1.9$ at least 9 TRT hits.

The number of hits required in the first two points is reduced by one if the track traverses a sensor known to be inefficient according to a time-dependent database. The above requirements are dropped in the region $|\eta| > 2.5$, where the short ID track segments can be matched to SA muons to form a CB muon.

The muons used in this analysis are reconstructed using the statistical combination (STACO) algorithm [87], complemented by the tagging algorithm MuTAG [87], which uses a χ^2 procedure for tagging. STACO reconstructs straight track segments in the MS chambers using pattern recognition algorithms on the hits, beginning in the outer layer and working inwards. All tubes crossed by a segment must contain a hit for the track to be considered. The hits are then extrapolated back to the ID, where they are geometrically

matched to independently reconstructed ID tracks, provided that their kinematic properties, e.g. p_T , are compatible. Statistically combining the parameters of both tracks takes advantage of the momentum sensitivity of both the ID and MS systems. The MuTAG algorithm works from the ID tracks which are extrapolated to the MS and then matched to straight track segments. This algorithm heavily relies on the hits in the MS. The energy lost between ID and MS is applied as a correction to the reconstructed muons in data, the simulated muons have their energy distributions smeared using random numbers to reflect how well the ID and MS can measure the momentum of any given muon.

Figure 4.4 shows the reconstruction efficiency for muons using the methods described in this section over most of the covered phase space ($|\eta| < 2.7$ and $5 \lesssim p_T \lesssim 100$ GeV). The combination of all the muon reconstruction types (for CB, ST and CaloTag muons) gives a uniform muon reconstruction efficiency of about 99% over most of the detector regions.

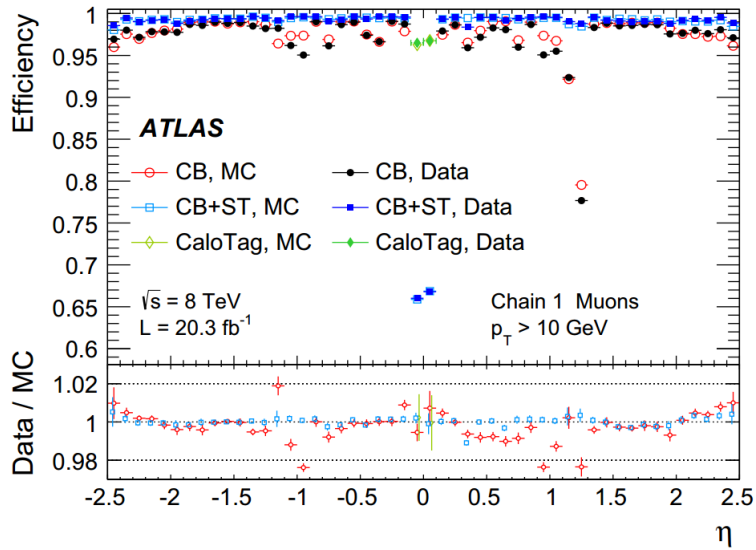


Figure 4.4: Muon reconstruction efficiency as a function η measured in $Z \rightarrow \mu\mu$ events for muons with $p_T > 10$ GeV and different muon reconstruction types. The uncertainties considered here are statistical only. The error bars on the ratios are combined statistical and systematic uncertainties. CB muons refer to STACO muons, CB+ST refer to MuTAG muons and CaloTag muons are not considered in this analysis. Taken from [88].

Muons only have one set of identification criteria available. The backgrounds considered comes mostly from charged pions, which usually leave larger energy deposits in the electromagnetic and hadronic calorimeters and tend not to reach the MS. Muons must pass the STACO requirements, although those in the region $|\eta| < 1.05$ can also pass the MuTAG requirements.

4.4.7 Jet Reconstruction

Jets are reconstructed beginning with the formation of *topological* clusters in the hadronic calorimeter using the topological algorithm [89]. The topo-cluster formation algorithm [83] is an iterative procedure which starts from a seed cell with a signal to noise ratio $S/N \geq 4$, where S is the energy measured in the seed cell and N is defined as the root mean squared (RMS) of the cell energy measured in random bunch crossings. Any neighbouring cells with $S/N \geq 2$ are then added to form a cluster. This cluster is then used in an additional splitting step: every calorimeter cell with energy > 500 MeV is tested for a local maximum, and any cell passing this criterion is used as a trial seed for a new topo-cluster. Topo-clusters are defined to have zero mass, with energy equal to the sum of the energy of the constituent calorimeter cells.

The topological clusters need to be calibrated before being used as input for the anti- k_T recombination algorithm. For this analysis, local cluster weighting (LCW) calibration was used, which uses an algorithm to determine whether topological clusters originate from a hadronic or EM shower. The energy measured in the hadronic topological clusters is then corrected according to the simulated response of single hadrons in the cells. Corrections for energy deposition in dead material and noise effects are applied.

In the next step, the LCW calibrated topological clusters are provided as input to the anti- k_T jet algorithm [90] with a distance parameter $R = 0.4$, which determines the size of the reconstructed jets and a four momentum recombination scheme. The anti- k_T algorithm works iteratively, in the first step the distance parameter d_{ij} is calculated, which is defined as

$$d_{ij} = \left(\frac{1}{k_{T_i^2}}, \frac{1}{k_{T_j^2}} \right) \frac{\Delta R_{ij}}{R^2}, \quad (4.4)$$

where i and j are topo-cluster indices, k_T is the transverse momentum of each topo-cluster, $\Delta R_{ij} = \sqrt{\Delta\phi_{ij}^2 + \Delta\eta_{ij}^2}$ is the distance between the two topological clusters. The topological clusters i and j which minimise d_{ij} are then combined to form larger individual clusters. The next iteration takes into account the larger individual clusters as well as the remaining initial topological clusters and combines them according to the same procedure. This process is repeated until all remaining topo-cluster pairs satisfy the criterion $\Delta R_{ij} > R$.

After cluster calibration and jet reconstruction, additional corrections are needed to calculate the jet energy properly. The jet energy scale corrections are determined using

MC, where the truth jet energy is compared to the reconstructed value. The results from this comparison are then validated by comparing with in-situ methods such as di-jet and γ -jet balancing method [91].

Jet reconstruction can be affected by the presence of pileup events. Pileup interactions can increase the total energy deposited in the calorimeters, which then affects the energy calibration of the jets. To correct for this problem, an offset pileup contribution to the energy density is subtracted, which is parameterised by the number of vertices in the event [92]. Pileup interactions can also introduce additional jets. These jets do not originate from the interaction of interest, therefore it is useful to suppress them. Pileup jets can be effectively suppressed using the jet-vertex-fraction (JVF) variable. It is a quantification of how much of a jet’s energy is associated with the primary vertex of interest in the event. The JVF for a jet is defined as

$$\text{JVF} = \frac{\sum_{\text{tracks}_{\text{jet}, \text{PV}}} p_T}{\sum_{\text{tracks}_{\text{jet}}} p_T}, \quad (4.5)$$

where the sums are taken over the tracks matched to the jet and PV denotes the tracks associated to the primary vertex. Jets that have no associated tracks are assigned $\text{JVF} = -1$. Pileup jets will have a higher fraction of jet energy associated with pileup vertices, making this variable a good discriminator.

B -hadron jets have a displaced secondary vertex due to the long lifetime of the b -quark. There are different jet origins: those from b -quarks, c -quarks and light flavour quarks or τ leptons. Several algorithms are used to “tag” jets as b -jets. The algorithm which is most commonly used with 2012 data is the MV1 algorithm, which is based on a neural network. The input algorithms used are described in [93].

4.4.8 Tau Reconstruction and Identification

The reconstruction and identification of τ leptons is a challenging task, as purely leptonic τ decays are virtually impossible to distinguish from prompt electrons or muons in ATLAS. The τ identification algorithms are developed to reconstruct and identify the visible part of the hadronic decay modes, referred to by the term $\tau_{\text{had-vis}}$ [94]. However the hadronic τ decay signatures in the detector are very similar to quark- or gluon-initiated jets from QCD processes. Leptonic decays are treated as indistinguishable from the prompt production of light leptons in this analysis. The hadronic decays can be divided into modes, “1-prong” and “3-prong” decays, where the number corresponds to the charged particles produced in the decay.

These signatures produce relative narrow clustering of tracks and energy deposits in the calorimeters, which is useful for discriminating against the multi-jet background. Decays producing more than three charged particles are not considered by ATLAS due to their very small branching ratios and the increased difficulty of reconstructing them into taus.

The $\tau_{had-vis}$ reconstruction algorithm is seeded from jets reconstructed using the anti- k_T algorithm, with a distance parameter $R = 0.4$. LCW calibrated topological clusters are used as an input for the jet algorithm. All jets with $p_T > 10$ GeV and $|\eta| < 2.5$ seed the reconstruction algorithm. The reconstructed four-momentum of the $\tau_{had-vis}$ candidate is defined in terms of three degrees of freedom: p_T, η and ϕ . The η and ϕ are taken from the seed jet, which is determined by calculating the sum of the four vectors of the constituent topological clusters, assuming zero mass for each of the constituents. The mass of the $\tau_{had-vis}$ candidate is defined to be zero, consequently the p_T and the E_T are identical. Due to the specific mixture of charged and neutral pions in hadronic τ decays, the energy scale of hadronic τ candidates is calibrated independent of the jet energy scale. The reconstructed energy of $\tau_{had-vis}$ candidates is corrected to the final energy scale by an MC based calibration procedure using clusters, within $\Delta R < 0.2$ of the seed jet barycentre axis.

For a track to be associated with a $\tau_{had-vis}$ candidate they must lie within the *core cone*, defined as the region with $\Delta R < 0.2$ of the axis of the seed jet and satisfy the track quality criteria outlined in Section 4.4.2.

The identification of taus is based on a boosted decision tree (BDT) which takes many different track and calorimeter based variables as input to discriminate against the hadronic jet background. Tracks within the *isolation annulus* of $0.2 < \Delta R < 0.4$ are useful for the discrimination. Additional quantities used in the BDT include shower shape variables, the proportion of energy deposited in the ECAL and HCAL, the ratio of normal to high threshold TRT deposits and coordinates of the τ decay vertex. Full details of all variables used in these selections can be found in [95].

Three working points, *loose*, *medium* and *tight* corresponding to the different τ identification efficiency values are provided. The corresponding signal efficiency values, defined with respect to 1-prong or 3-prong reconstructed $\tau_{had-vis}$ candidates matched to true $\tau_{had-vis}$ are shown in Figure 4.5.

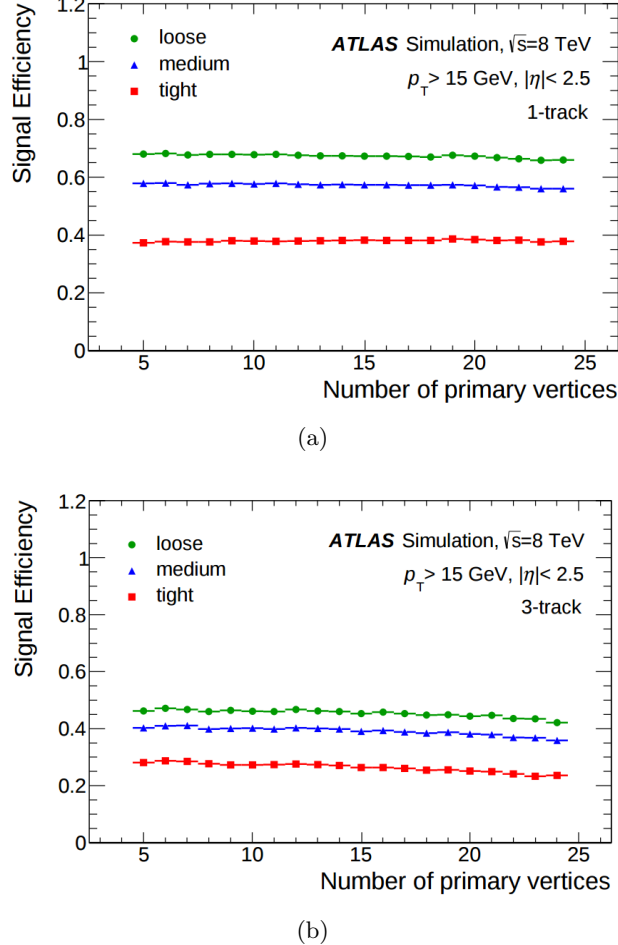


Figure 4.5: Offline τ reconstruction efficiency dependence on the number of reconstructed primary vertices for (a) 1-track and (b) 3-track $\tau_{had-vis}$ decays matched to true $\tau_{had-vis}$ from $Z \rightarrow \tau\tau$, $Z' \rightarrow \tau\tau$ and $W \rightarrow \tau\nu$ simulated samples. Taken from [94].

It is observed that the signal efficiencies for taus are significantly lower than for electrons, muons and jets, due to the difficulty in distinguishing real taus from the QCD background.

4.4.9 Missing Transverse Energy

Stable neutral particles produced in ATLAS that are relevant to this analysis such as neutrinos or the SUSY LSP in R-parity conserving models will escape the detection and lead to an imbalance of momentum. The missing transverse energy refers to the magnitude of the momentum imbalance in the plane transverse to the beam axis. It is reconstructed by taking the vector sum of all energy deposits in the detector calorimeters and muon spectrometer [96]. This is a measure of the total momentum of all the visible particles in order to infer the remaining invisible momentum. These are summed in the following

order for the x and y axes:

$$E_{x(y)}^{miss} = -(E_{x(y)}^e + E_{x(y)}^\gamma + E_{x(y)}^\tau + E_{x(y)}^{jets} + E_{x(y)}^{soft jets} + E_{x(y)}^{calo\mu} + E_{x(y)}^{cellout} + E_{x(y)}^{MS\mu}). \quad (4.6)$$

The first three terms give the energies from topological clusters associated to electrons, photons and hadronically decaying taus respectively. The energy term for jets includes all deposits for jets with $p_T > 20$ GeV, whilst *soft jets* with $10 < p_T < 20$ GeV are added separately as they are calculated from topological clusters and tracks not associated to high- p_T objects. Energy lost by muons within the calorimeters is included in the “calo μ ” term. All clusters not associated to reconstructed objects are also summed and included in the “cell out” term. These terms together give the total energy deposited in the calorimeter subsystems. Finally, the sum of transverse momenta of all muons in the muon spectrometer is added. The terms included for electrons, muons, taus and jets are calibrated and no calibration is required for the soft jet or cell out terms. The missing transverse energy is calculated using the energy in the x and y axes:

$$E_T^{miss} = \sqrt{(E_x^{miss})^2 + (E_y^{miss})^2}. \quad (4.7)$$

An optimised reconstruction and calibration of E_T^{miss} was developed by the ATLAS Collaboration [96]. The E_T^{miss} measurement is significantly affected by pile-up, so methods were devised to suppress pile-up. Event samples used to assess the quality of the E_T^{miss} reconstruction are minimum bias events, events with leptonically decaying W and Z bosons and simulated events with large jet multiplicity and/or large missing transverse momentum, such as $H \rightarrow \tau\tau, t\bar{t}$ and simulated SUSY events. These test the detector capability in the reconstruction and calibration of different physics objects, the optimisation of the E_T^{miss} calculation and the methods of pile-up suppression. An important requirement on the measurement of E_T^{miss} is maximising detector coverage and reducing the effect of finite detector resolution, the presence of dead regions and different sources of noise as well as cosmic-ray and beam-halo muons that cross the detector can produce fake E_T^{miss} .

The ATLAS calorimeter coverage extends to large pseudorapidities to reduce the impact of high energy particles escaping in the very forward direction. However, there are transition regions between different calorimeters containing inactive material which lead to increased fake E_T^{miss} . Selection criteria are applied to reduce the impact of these sources of fake E_T^{miss} . Full details on the reconstruction of E_T^{miss} is discussed in [97].

4.5 Object Selection for the Analysis

The reconstructed objects read from data storage files are not used directly by analysers, instead they are subjected to further selection criteria. “Baseline objects”, which provide a general description of the particle are defined first. These then undergo the “overlap removal” procedure that is applied before more stringent cuts are applied to define “signal objects”. Taus are an exception to this ordering, where signal taus are used as the input to overlap removal, rather than baseline taus.

4.5.1 Baseline Light Lepton Selection

Electrons are required to have $p_T > 7$ GeV and muons $p_T > 5$ GeV. The ECAL cluster of an electron must have $|\eta| < 2.47$ and muons must have $|\eta| < 2.5$. Electrons are required to pass the MEDIUM++ identification criteria described in Section 4.4.5. Muons are required to pass a loose identification criteria with the STACO algorithm as described in Section 4.4.6 and have specific hits present in the ID, as well as requests based on the number of normal hits in the TRT compared to outliers. The total number of hits n is defined as the sum of the normal and outlier hits and the condition $n > 5$ must be satisfied. In addition the proportion of outliers must be less than 90%.

4.5.2 Baseline Jet Selection

Baseline jets must have $p_T > 20$ GeV and $|\eta| < 4.5$ and are reconstructed as described in Section 4.4.7.

4.5.3 Baseline Tau Selection

Baseline taus are seeded from jets which must have $p_T > 10$ GeV and $|\eta| < 2.5$ as described in Section 4.4.8. The taus themselves are then required to satisfy $p_T > 20$ GeV and $|\eta| < 2.5$. They must also have either one or three tracks associated with them, corresponding to a one or three prong tau decay. No identification criteria are required at this stage.

4.5.4 Overlap Removal

Objects that are geometrically close (i.e. within a ΔR cone of a given size) can pose issues for reconstruction due to spatial resolution. Selections are placed on the spatial (η, ϕ) proximity of objects, corresponding to the type of object to improve the accuracy of

Object	η	p_T [GeV]	Identification	Other
Electron	$ \eta ^{cl} < 2.47$	$p_T > 7$	MEDIUM++	
Muon	$ \eta < 2.5$	$p_T > 5$	STACOloose	$n_{b-layer} \geq 1, n_{pixel} \geq 1,$ $n_{SCT} \geq 6, n_{holes(pix+SCT)} < 3$ $n_{TRT}^{total} > 5, \frac{n_{outliers}}{n_{TRT}^{total}} < 0.9$
Jet	$ \eta < 4.5$	$p_T > 20$	-	-
Tau	$ \eta < 2.5$	$p_T > 20$	-	$n_{tracks} = 1$ or $3,$ $charge = \pm 1$

Table 4.4: Summary of cuts used to define baseline objects in this analysis.

identification. The overlap removal procedure is performed between baseline objects and is applied in the order shown in Table 4.5.

Overlap Removal Cuts	Overlap Removal Criterion
$\Delta R_{e1,e2} < 0.05$	Discard the lowest E_T electron to remove duplicated electrons with different clusters and shared tracks.
$\Delta R_{e,j} < 0.2$	Discard jet to remove electrons duplicated in jet container.
$\Delta R_{e,\tau} < 0.2$	Discard τ to remove electrons duplicated in τ container.
$\Delta R_{\mu,\tau} < 0.2$	Discard τ to remove muons duplicated in τ container.
$\Delta R_{e,j} < 0.4$	Discard electron to remove electrons within jets.
$\Delta R_{\mu,j} < 0.4$	Discard muon to remove muons within jets.
$\Delta R_{e,\mu} < 0.01$	Discard both electron and muon due to muons undergoing bremsstrahlung.
$\Delta R_{\mu,\mu} < 0.05$	Discard both muons due to shared tracks.
$\Delta R_{signal\tau,j} < 0.2$	Discard jets to remove taus duplicated among the jets.

Table 4.5: Overlap removal criteria for objects used in the analysis presented in this thesis. The indices refer to the object pair being evaluated.

4.5.5 Signal Electrons

Signal electrons are required to pass the TIGHT++ identification criteria, in addition to isolation and d_0 and $z_0 \sin\theta$ conditions:

$$\frac{|d_0|}{\sigma(d_0)} < 5, \\ z_0 \sin\theta < 0.4\text{mm}. \quad (4.8)$$

The isolation conditions for the leading electron require one for the track and one for the cluster in the calorimeter. The track isolation requires that:

$$\frac{p_T^{cone30}}{p_T} < 0.16, \quad (4.9)$$

where p_T is the transverse momentum of the electron, and p_T^{cone30} is the combined p_T of all tracks with $\Delta R \leq 0.3$ of the electron track, where tracks satisfy the requirements given

in Section 4.4.2. The cluster isolation requires:

$$\frac{E_T^{cone30corr}}{E_T} < 0.18, \quad (4.10)$$

where the energy-density corrected isolation, $E_T^{cone30corr}$, is defined as:

$$E_T^{cone30corr} = E_T^{cone30} - A \times N_{vtx}. \quad (4.11)$$

N_{vtx} is the number of vertices with at least 5 associated tracks and A is a scale factor to account for energy leakage in the calorimeter and additional deposits from pile-up conditions. Values of 20.15 MeV for data and 17.97 MeV for MC simulation are used, due to differences between the modelling and data measurement. E_T^{cone30} is defined equivalently to p_T^{cone30} , as the combined E_T of all tracks within $\Delta R \leq 0.3$ of the electron track.

If the electron is not the leading lepton in p_T , it must satisfy tighter isolation requirements than those prescribed above in order to remove fake contributions introduced with lower lepton p_T thresholds. The track and cluster isolation requirements in this case are as follows:

$$\begin{aligned} \frac{p_T^{cone30}}{p_T} &< 0.07, \\ \frac{E_T^{cone30corr}}{E_T} &< 0.13. \end{aligned} \quad (4.12)$$

4.5.6 Signal Muons

Signal muons do not require any additional identification criteria. Cuts on $|d_0|$ and $|z_0 \sin \theta|$ are as follows:

$$\begin{aligned} \frac{|d_0|}{\sigma(d_0)} &< 3, \\ z_0 \sin \theta &< 1\text{mm}. \end{aligned} \quad (4.13)$$

The track isolation condition for the leading muon is:

$$\frac{p_T^{cone30corr}}{p_T} < 0.12, \quad (4.14)$$

where

$$p_T^{cone30corr} = p_T^{cone30} - A \times N_{vtx}, \quad (4.15)$$

and for muons the values used for A are 10.98 MeV for data and 6.27 MeV for MC

simulation.

If the muon is not the leading lepton in p_T , it must satisfy tighter isolation requirements than those prescribed above similarly to electrons. The track isolation requirements in this case are:

$$\frac{p_T^{cone30cor}}{p_T} < 0.06,$$

$$\frac{E_T^{cone30corr}}{E_T} < 0.14. \quad (4.16)$$

4.5.7 Signal Jet Selection

Baseline jets are identified using criteria which aim to efficiently reject background jets while keeping the highest efficiency selection for jets produced in pp collisions. All selected jets must $p_T > 20$ GeV and be within pseudorapidity coverage of the calorimeters, $|\eta| < 4.5$.

Signal jets are selected from baseline jets and are required to cover a pseudorapidity range of $|\eta| < 2.5$ and have a $JVF > 0.5$. Large JVF values suppress jets from a different (not primary) interaction in the same beam crossing.

4.5.8 Signal Tau Selection

Signal taus are required to pass additional medium identification criteria. This requires the muon veto to be passed, in addition to the loose definition of the electron BDT selection, and the medium jet BDT selection, all of which are described in Section 4.4.8. All baseline taus passing these criteria are defined as signal taus, and these are then used as input for the overlap removal described in Section 4.5.4.

4.6 MC Samples

4.6.1 MC Generators

The main choices regarding the different types of MC generators employed in this thesis are described below.

4.6.1.1 General Purpose MC Generators

PYTHIA [69], HERWIG [68], and HERWIG++ [98] are general purpose MC event generators that use Matrix Element (ME) calculations to Leading Order (LO), which include the simulation of both hard and soft interactions. For the simulation of the UE, HERWIG is interfaced with JIMMY [77]. Both PYTHIA and JIMMY simulate the UE as a scattering between proton remnants using matrix elements at LO. SHERPA [99] is another multi-purpose event generator, which is interfaced with PYTHIA for simulation of the PS. A multiple parton scattering model is used for the UE simulation.

4.6.1.2 Matrix Element MC Generators

The ALPGEN [100], MADGRAPH [101] and ACERMC [102] generators simulate the hard process of a proton-proton collision using calculations at fixed order in perturbation theory. Events are generated with different multiplicities of outgoing partons. The cross sections are calculated at LO for the PS and hadronisation. These generators are interfaced with PYTHIA or HERWIG because they can only provide generation of events to parton-level. The addition of PS introduces a double-counting of events. This is due to the additional jets which can be produced in a sample with n-partons from PS that are already taken into account in the n+1-partons sample. When more than two generators are interfaced, matching techniques such CKKW and MLM are used to remove double counting the matrix element and PS emissions.

4.6.1.3 Next-to-Leading Order MC Generators

MC@NLO [103] and POWHEG [104] provide alternative simulation methods by combining lowest-multiplicity Next-to-Leading Order (NLO) matrix elements with PS without double counting. MC@NLO and POWHEG produce hard scattering processes at NLO, where the former includes negative weighted events in the method to prevent double counting. The MC@NLO generated events are typically used as input to HERWIG for the PS and hadronisation, and to JIMMY for the UE. POWHEG events are interfaced with PYTHIA to include PS and UE effects.

4.6.2 SM Background MC Samples For Run-1

Several background samples have been considered in the Run-1 analysis and can be grouped into different categories, as detailed in the following.

Diboson

The WW, WZ and ZZ processes are generated with the NLO generator POWHEG. These samples correspond to all SM diboson processes leading to $\ell\nu\ell'\nu'$, $\ell\ell\ell'\nu'$ and $\ell\ell\ell'\ell'$, respectively, with $\ell, \ell' = e/\mu/\tau$ and $\nu, \nu' = \nu_e/\nu_\mu/\nu_\tau$. The SHERPA generator is used for the Z/W + γ processes.

Triboson

The $pp \rightarrow WWW \rightarrow \ell\nu\ell\nu\ell\nu$, $pp \rightarrow ZWW \rightarrow \ell\ell\ell\nu\ell\nu$ and $pp \rightarrow ZZZ \rightarrow \ell\ell\ell\nu\nu$ processes (collectively referred to as VVV) were generated with MADGRAPH to LO in QCD.

Top and Anti-top with Associated Vector Boson

The $t\bar{t}+Z(+\text{jets})$ and $t\bar{t}+W(+\text{jets})$ processes were generated using the LO generator ALPGEN, while the $t\bar{t}+\text{WW}$ and tZ processes were generated using MADGRAPH. All $t\bar{t}+\text{boson}$ samples are collectively referred to as $t\bar{t}V$ where at least one of the top quarks is decaying semi-leptonically ($t \rightarrow Wb \rightarrow b\ell\nu$).

Top

The top pair-production process, $t\bar{t}$, was generated with POWHEG (+PYTHIA for simulating the PS, hadronisation and the UE); single top production in the t -channel ($bq \rightarrow tq'$ and $b\bar{q}' \rightarrow t\bar{q}$) was generated with MC@NLO (+HERWIG for simulation of PS and hadronisation); and single top processes in the s -channel ($q\bar{q} \rightarrow W^* \rightarrow t\bar{b}$) and the associated production of a top quark and a W boson, Wt , was generated with ACERMC (+PYTHIA). All samples are produced using a top quark mass of 172.5 GeV and have been renormalised to Next-to-Next-to Leading Order (NNLO).

Boson+jets

Z/γ^* production and W production in association with jets (light and heavy flavour jets are taken into account) are produced with ALPGEN (+PYTHIA). For simplicity, these samples are referred to as “V+jets”. The W and Z/γ^* ALPGEN LO cross sections are renormalised to NNLO.

4.6.2.1 Standard Model Higgs

Samples where the Higgs decays are via taus or via W/Z bosons are generated with PYTHIA. $H \rightarrow \tau\tau$, $H \rightarrow WW^*$ and $H \rightarrow ZZ^*$ decaying into leptonic final states are considered, as these are expected to be the most important sources of Higgs background in this analysis. Five production mechanisms are included: gluon Fusion (ggF), Vector Boson Fusion (VBF), associated production with a W (WH) or Z boson (ZH), and associated production with $t\bar{t}$ pair ($t\bar{t}H$). All cross sections are calculated at NNLO, except $pp \rightarrow t\bar{t}H$, which is calculated at NLO QCD precision.

4.6.2.2 Low-Mass Drell-Yan

The $Drell-Yan \rightarrow ee$, $Drell-Yan \rightarrow \mu\mu$ processes are generated with SHERPA to NLO.

4.6.2.3 J/Ψ

The $pp \rightarrow J/\Psi \rightarrow ee$, $pp \rightarrow J/\Psi \rightarrow \mu\mu$ $pp \rightarrow J/\Psi \rightarrow \mu\mu Z\mu\mu$, $pp \rightarrow J/\Psi \rightarrow \mu\mu Zee$ $bb \rightarrow J/\Psi \rightarrow ee$, $bb \rightarrow J/\Psi \rightarrow \mu\mu$ processes are generated with PYTHIA to LO.

4.6.2.4 Υ

The $\Upsilon \rightarrow \mu\mu Z\mu\mu$ $\Upsilon \rightarrow \mu\mu Zee$ $pp \rightarrow \Upsilon \rightarrow \mu\mu$ processes are generated with PYTHIA to LO.

For all simulated processes, the propagation of particles through the ATLAS detector is modelled with GEANT4 using the full ATLAS detector simulation, except for the $t\bar{t}$ POWHEG sample, for which ATLFast-II simulation is used.

Simulated events are weighted to match the distribution of the number of interactions per bunch crossing observed in data.

There are free parameters for the different PS, UE and hadronisation models, which are tuned to data. The three different parameter tunes used for the UE generation in all MC samples are the ATLAS UE Tune 2B (AUET2B), AU2 and PERUGIA2011C, which are discussed in detail in [105].

Dedicated calculations are used to provide a renormalisation of the total cross sections for each SM process at NLO or NNLO, which have been specified in Table 4.7. The choice of PDF depends on the generator and for this analysis the CTEQ6L1 PDFs are used with MADGRAPH, ALPGEN, ACERMC, PYTHIA and the CT10 [106] PDFs with MC@NLO, POWHEG and SHERPA.

The choice of the generator type and the order of cross section calculations used for yield normalisation for the SM processes are summarised in Table 4.7.

4.6.3 MC Signal Samples For Run-1

Signal samples referring to the models considered in this analysis (Section 2.6.8) are generated with HERWIG++, using the CTEQ6L1 PDFs. Signal cross sections are calculated to NLO+NLL using PROSPINO2 [107]. Lepton filters are applied during event generation to enhance decays into a particular final state. A “light lepton filter” (electrons/muons) with the additional requirement of an electron/muon with $p_T > 5$ GeV, $|\eta| < 2.7$ is applied. The list of signal samples used in the analysis presented in this thesis can be found in Table 4.6.

Signal Grid	Generator	Cross section
Simplified Model via sleptons	HERWIG++ [68]	NLO+NLL
Simplified Model via WZ	HERWIG++ [68]	NLO+NLL

Table 4.6: MC signal samples used in this analysis.

4.6.4 SM Background MC Samples For Run-2

The MC samples used for the Run-2 analysis are described briefly in the following. The use of generators for several of the processes are different to those used in Run-1 for improved simulation and greater accuracy. Comparisons can be made between Table 4.7 and Table 4.8 for Run-1 and Run-2 respectively.

4.6.5 MC Signal Samples For Run-2

The samples are generated from LO matrix elements with up to two extra partons, using the MG5_AMC@NLO v2.2.3 generator [101] interfaced with PYTHIA with the A14 tune for the modelling of the SUSY decay chain, PS, hadronisation and the description of the UE. Parton luminosities are provided by the NNPDF23LO PDF set. Jet-parton matching has been done following the CKKW-L prescription [108], with a matching scale set to one quarter of the pair-produced superpartner mass. Signal cross sections are calculated to NLO in the strong coupling constant, adding the resummation of soft gluon emission at NLO+NLL accuracy [109]. The nominal cross section and the uncertainty are taken from an envelope of cross section predictions using different PDF sets and factorisation and

renormalisation scales, as described in [110]. All the signal MC samples were generated using a 25 ns bunch spacing configuration and simulated with ATLFast-II. To reduce the amount of statistics per point and to target specific final states to the analysis, a generator filter was applied to these samples. For the $\tilde{\chi}_1^\pm \tilde{\chi}_2^0$ production at least two leptons with $p_T > 5$ GeV and $|\eta| < 2.8$ in the event is required.

Process	Generator	Cross section
Dibosons		
$WW, WZ, ZZ, W/Z\gamma$	POWHEG + PYTHIA 8	NLO QCD with MCFM [111] [112]
Tribosons		
WWW, ZZZ, WWZ	MADGRAPH + PYTHIA	NLO [113]
Top+Boson		
$t\bar{t}W/Z$	ALPGEN + HERWIG	NLO [113] [114]
$t\bar{t}WW$	MADGRAPH + PYTHIA	NLO [114]
tZ	MADGRAPH + PYTHIA	NLO [115]
Top-quark pair-production		
$t\bar{t}$	POWHEG + PYTHIA	NNLO+NNLL [116]
Single top		
t -channel	ACERMC + PYTHIA	NNLO+NNLL [117]
s -channel, Wt	MC@NLO + HERWIG	NNLO+NNLL [118] [119]
W/Z+jets	ALPGEN + PYTHIA	DYNNLO [120]
Higgs		
via gluon fusion	POWHEG + PYTHIA 8	NNLL QCD, NLO EW [121]
via vector-boson fusion	POWHEG + PYTHIA 8	NNLL QCD, NLO EW [121]
associated W/Z production	PYTHIA 8	NNLL QCD, NLO EW [121]
associated $t\bar{t}$ production	PYTHIA 8	NNLO QCD [121]
Low-Mass Drell-Yan	SHERPA	NLO [122]
J/Ψ	PYTHIA 8	LO [123]
Υ	PYTHIA 8	LO [123]

Table 4.7: MC samples used in the Run-1 analysis for signal optimisation and background estimation, the generator type and the order of cross section calculations used for yield normalisation are also reported.

Process	Generator	Cross section
Dibosons $WW, WZ, ZZ, W/Z\gamma$	SHERPA [124]	0 jets @ NLO + 1,2,3 jets @LO [124] 0 jets @ NLO + 1,2,3 jets @ LO 0 jets @ NLO + 2,3 jets @ LO 0 jets @ NLO + 1,2 jets @ LO [124] 0,1,2 jets @ LO 0 jets @ NLO + 1,2 jets @ LO 0 jets @ NLO + 1,2 jets @ LO
Tribosons WWW, WWZ, ZZW, ZZZ	SHERPA [124]	0 jets @ NLO + 1,2 jets @ LO [124] 0 jets @ NLO + 1,2 jets @ LO 0 jets @ NLO + 1,2 jets @ LO
Top+Boson $t\bar{t}W/Z$ $t\bar{t}WW$ tZ	MADGRAPH + PYTHIA [125]	LO [125]
Top-quark pair-production $t\bar{t}$	POWHEG + PYTHIA [126]	NNLO + NNLL [126]
Single top t -channel s -channel, Wt	POWHEG + PYTHIA [126]	NLO+NNLL [126]
W/Z+jets Higgs via gluon fusion via vector-boson fusion associated W/Z production associated $t\bar{t}$ production	SHERPA [127] POWHEG + PYTHIA [128] POWHEG + PYTHIA POWHEG + PYTHIA aMC@NLO + HERWIG++	0,1,2 jets @ NLO + 3,4 @ LO [127] NNLO+NNLL QCD and NLO EW [128] NNLO QCD and NLO EW NNLO QCD and NLO EW NLO QCD

Table 4.8: MC samples used in the Run-2 analysis (Section 8 for signal optimisation, the generator type and the order of cross section calculations used for yield normalisation are also reported.

Chapter 5

The E/Gamma Signature Trigger on ATLAS

This chapter will address the electron-photon signature trigger (E/gamma), served as the author’s “technical task” whilst working on ATLAS. This particular signature also is important for the analysis discussed in this thesis as electrons, like other leptons are vital physics objects for electroweak SUSY searches. The concept of trigger efficiency and its uncertainty will be introduced in Section 5.1. The method of efficiency measurement of electron triggers using data, referred to as the Tag and Probe method is described in Section 5.2. The efficiencies of the Run-2 E/gamma trigger menu was assessed with early Run-2 data with 50 ns bunch crossings, the results are discussed in Section 5.3.

5.1 Trigger Efficiency

In order for a measurement on the number of electrons observed with the ATLAS detector to be related to physics analysis, the efficiency of ATLAS to select and reconstruct these electrons needs to be known. This efficiency is a convolution of the geometric acceptance of the detector, the efficiency of the trigger system and the efficiency of the offline reconstruction. The studies in this thesis focus specifically on the efficiency of the trigger system. A combination of electron and muon triggers are used in the analysis discussed in this thesis, but for the discussion in this chapter, single electron triggers will be used. The principles of trigger efficiencies discussed here can be generalised to all leptonic triggers.

The efficiency of the single electron trigger, ϵ , is interpreted as the probability, P , that an electron e , will pass the trigger given certain conditions, I , that describe the electron and the event it is present within:

$$\epsilon = P(\text{ pass the electron trigger } | I, e). \quad (5.1)$$

This probability is estimated with data. This estimation is done assuming the true efficiency, ϵ , is a real number between zero and one, to which the measured probability of selection tends in the limit of an infinite number of measurements. In a binomial model of efficiency, the measured probability, or efficiency estimator, $\hat{\epsilon}$, is given by:

$$\hat{\epsilon} = \frac{k}{n}, \quad (5.2)$$

where n is the total number of electrons, and k is the number of electrons which pass the trigger. The estimator of the variance on this efficiency estimator, $\hat{V}[\hat{\epsilon}]$, is then defined by:

$$\hat{V}[\hat{\epsilon}] = \frac{\hat{\epsilon}(1 - \hat{\epsilon})}{n}. \quad (5.3)$$

The standard deviation is defined as:

$$\sigma = \sqrt{\hat{V}}, \quad (5.4)$$

and is used to define the uncertainties on efficiencies. These uncertainties are statistical only, systematical sources of error on the trigger efficiency are not discussed in this thesis.

Differential trigger efficiency, as a function of a given variable, can be measured by binning k and n in the appropriate variable and then computing the $\hat{\epsilon}$ and $\hat{V}[\hat{\epsilon}]$ for each bin. For example, the one-dimensional efficiency estimator as a function of transverse energy defined in each bin i of transverse energy as:

$$\hat{\epsilon}_i = \frac{k(E_T^i)}{n(E_T^i)}, \quad (5.5)$$

where $k(E_T^i)$ is the number of electrons with transverse energy in the i -th E_T bin that pass the trigger, and $n(E_T^i)$ is the total number of electrons with transverse energy in the same bin. This concept of differential efficiency can be extended to higher dimensions. For example, two-dimensional efficiencies can be defined as a function of E_T and η .

5.1.1 Determining Efficiencies with $Z \rightarrow ee$ events

The process $Z \rightarrow e^+e^-$, as shown in Figure 5.1, is an example of a well understood SM process, which produces energetic isolated leptons. The NLO cross section for this process at an LHC centre of mass energy of 14 TeV is expected to be around 2,069 pb [129]. This would result in the production of around 206,900 events with an integrated luminosity of only $\mathcal{L} = 100 \text{ pb}^{-1}$ of data. The relative abundance and simple topology of this process means that is an excellent benchmark process for the evaluation of trigger efficiencies in a realistic detector environment.

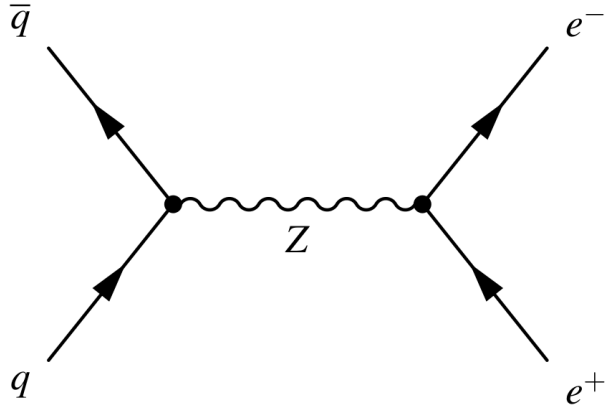


Figure 5.1: An example Feynman diagram of the $Z \rightarrow e^+e^-$ process.

To determine the efficiency of lepton triggers in MC, the samples produced for Z/γ^* production as described in Section 4.6.2, specifically the $Z \rightarrow e^+e^-$ samples for electron triggers and $Z \rightarrow \mu^+\mu^-$ for muon triggers.

5.2 Data-Driven Efficiency Measurement

The trigger efficiencies are measured relative to a well-defined offline electron passing one of the identification criteria described in Section 4.4.5. When computing the efficiency of the trigger on collision data recorded by ATLAS, the sample of events needs to be defined carefully to avoid a bias, since all events in data were already triggered by one or more triggers. To obtain an unbiased measurement of the trigger efficiencies on real data, the Tag and Probe method (TP) is used.

This method utilises $Z \rightarrow ee$ events. The strategy is to use a single trigger signature which selects one of the electrons from the final state as a reference (the tag) and to compute the efficiency using the other electron (the probe).

The events are selected using a single electron trigger with an E_T threshold of 24 GeV

and MEDIUM++ (see Section 4.4.5.2) identification requirements. These events are then required to have at least two reconstructed electron candidates in the central region of the detector $|\eta| < 2.47$, with opposite charges. One of the two electrons, the tag, must have $E_T > 25$ GeV in order to be above the trigger threshold, be matched to a trigger electron object within $\Delta R < 0.07$ and be outside the transition region between the barrel and the end-cap of the EM calorimeter, $1.37 < |\eta| < 1.52$. The tag must satisfy an identification requirement, nominally TIGHT++ (see Section 4.4.5.3). The probes, meanwhile, are required to pass the track quality criteria (see Section 4.4.2) and pass the trigger requirements for the trigger being studied.

The overall trigger efficiency estimator, as computed by the TP method, is defined as the number of probes that pass the trigger selection, k^p , divided by the total number of probes, n^p :

$$\hat{\epsilon} = \frac{k^p}{n^p}. \quad (5.6)$$

This efficiency can also be measured as a function of one or more kinematic variables by binning in the appropriate variable of the probe.

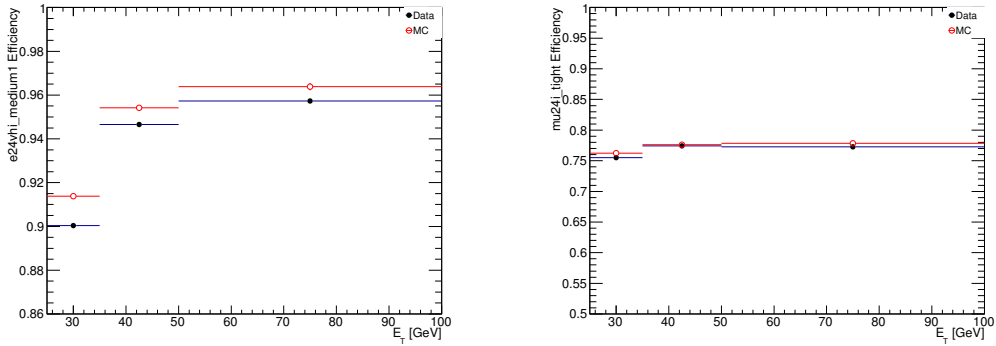
5.2.1 Efficiency Measurement Results with Run-1 8 TeV Data

The efficiency of the leptonic triggers used in the Run-1 analysis was assessed. The results were calculated from the data produced by the LHC at a centre of mass energy of $\sqrt{s} = 8$ TeV. This amounts to 20.3 fb^{-1} after good data quality requirements. The tag and probe leptons are required to pass signal lepton requirements as outlined in Section 4.5. The tag is matched to one of the single lepton triggers EF_mu24i_tight or EF_e24vhi_medium1. The tag and probe lepton must form a same-flavour opposite-sign (SFOS) lepton pair with an invariant mass with ± 10 GeV of the on-shell Z boson mass of 91.2 GeV. For the testing of multi-lepton triggers, the probe is tested against the given leg of the trigger. For example EF_e24vh_medium1_e7_medium1, has two legs: e24vh_medium1 and e7_medium1, which are tested individually. To avoid event overlap and to target events specific to the electron-photon signature, the e/ γ data stream is used for the electron trigger efficiencies and the Muon stream for the muon trigger efficiencies (refer to Section 3.8.2). In this chapter, a selection of efficiency distributions are discussed for two triggers, the efficiency distributions of all the triggers used in the Run-1 analysis are contained in Appendix A.

Figures 5.2, 5.3 and 5.4 show the efficiencies of two single lepton triggers, e24vhi_medium1

and mu24i_tight, which were the primary triggers in the analysis discussed in this thesis.

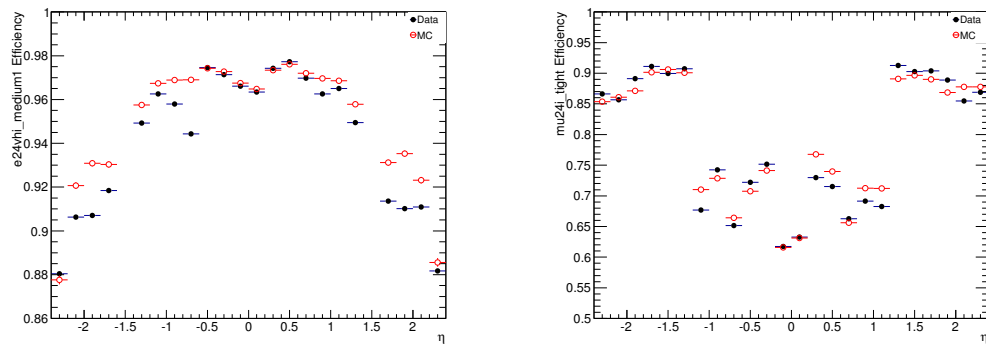
Figure 5.2 shows the efficiency as a function of E_T . As the electron or muon E_T reaches the energy threshold of the trigger, the efficiency increases sharply from zero to nearly one over the space of a few GeV. This is the *turn-on* region. Above the turn-on the efficiency is observed to be very high and almost flat. This is known as the *plateau* region.



(a) e24vhi_medium1 efficiency as a function of E_T (b) mu24i_tight efficiency as a function of E_T

Figure 5.2: Efficiencies of single lepton triggers as a function of E_T .

Figures 5.3 shows the efficiency as a function of η . Figure 5.3(a) shows the efficiency for e24vhi_medium, the barrel region $|\eta| < 1.5$ shows the highest efficiency, with slight degradation in efficiency in the end-caps due to the inhomogeneities in the online and offline cuts in the end-cap regions. This distribution includes electrons from the turn-on region, which contributes to the decrease in efficiency.

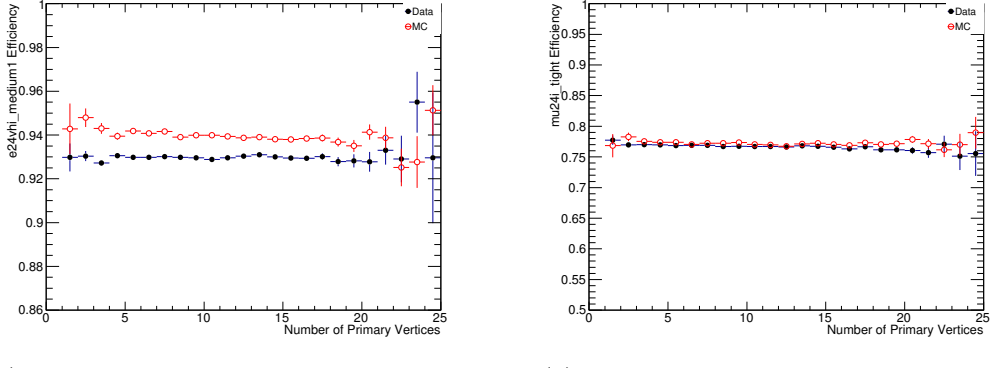


(a) e24vhi_medium1 efficiency as a function of η (b) mu24i_tight efficiency as a function of η

Figure 5.3: Efficiencies of single lepton triggers as a function of η .

Figure 5.3(b) shows the efficiency for mu24i_tight, the barrel region shows a degradation in efficiency in the barrel region, which is due to the limited geometric coverage of the Level-1 muon trigger, which is about 99% in the end-cap regions and about 80% in the barrel region. The limited geometric coverage in the barrel region is due to gaps around

$\eta = 0$ to provide space for services to the ID and calorimeters [130].



(a) e24vhi_medium1 efficiency as a function of Nvtx (b) mu24i_tight efficiency as a function of Nvtx

Figure 5.4: Efficiencies of single lepton triggers as a function of Nvtx.

Figure 5.4 shows the efficiency as a function of the number of primary vertices (Nvtx). Both Figures 5.4(a) and (b) show no dependency on Nvtx and therefore, increasing pile-up does not reduce the performance of these triggers.

5.3 The E/Gamma Signature Trigger Efficiency with Early Run-2 Data

Selection of events in real time based on electron and photon signatures is more challenging in Run-2 of the LHC due to the higher centre-of-mass energy and higher luminosity, which include a larger pile-up. These changes to the LHC beam conditions correspond to more difficult signal-to-background discrimination and higher trigger rates. The upgrades made to maintain performance is discussed in Section 3.9.2. This section will discuss the transition to likelihood based electron identification, the electron trigger efficiencies with early Run-2 data and the agreement in efficiency between data and MC simulated events.

5.3.1 Likelihood-based (LH) Electron Identification for Run-2

During Run-1, the electron triggers utilised a cut-based ID, as described in Section 4.4.5, while LH and cut-based electron ID both existed offline. In a cut-based ID, fixed requirements are imposed on quantities that discriminate between signal and background. The LH ID, by contrast, is based on PDFs of these various quantities for electrons and background processes. These PDFs are then used to determine the probability for a given electron candidate to be signal or background, and these probabilities are combined to

form a likelihood discriminant. Finally, a requirement is imposed on the likelihood discriminant to select signal-like objects and reject background-like objects [86]. These were both designed to have the same signal efficiency for a given operating point, which result in a background rejection that was approximately a factor of two better for the LH than the cut-based ID as shown in Figure 5.5(a), where the ratio of background efficiencies in Run-1 for LH operating points with respect to corresponding cut-based operating points, where each ratio compares operating points which have approximately the same signal efficiency. Therefore, for a given signal efficiency, the LH operating points reduce backgrounds by about a factor of two on average with respect to the cut-based operating points.

5.3.2 Results and Trigger Performance

The LH signal efficiency is about 6% higher than that of the cut-based triggers as shown in Figure 5.5(b), where the efficiency is measured with respect to reconstructed electrons originating from the $Z \rightarrow ee$ decay in simulation. This is because the Run 2 operating points were not designed to have the same absolute signal efficiency between the LH and cut-based operating points, due to rate requirements. The triggers in this figure require an electron candidate to have $E_T > 24$ GeV, to satisfy the appropriate cut-based or LH identification criteria for the MEDIUM operating point and to pass a loose isolation requirement. The trigger efficiencies measured with respect to the corresponding offline ID for the LH and cut-based triggers are similar, with slight improvements seen in both MC and data as shown in Figure 5.6. Here the offline reconstructed electron is required to pass cut-based *medium* or likelihood-based *lhmedium* identification.

The HLT_e24_(lh)medium_iloose_L1EM18VH triggers are two of the primary electron triggers used for the early Run-2 data taking and were used to provide data to MC scale factor recommendations for physics analysis groups. They require an electron candidate with $E_T > 24$ GeV satisfying the cut-based *medium* or likelihood-based *lhmedium* identification and a requirement $p_T^{iso}/E_T < 0.1$ on the relative track isolation calculated within a cone of $R = 0.2$. Both triggers are seeded by a level-1 trigger L1_EM18VH that applies an E_T dependent veto against energy deposited in the hadronic calorimeter behind the electron candidate's electromagnetic cluster. The efficiencies were measured with no background subtraction applied and are compared to the expectation from $Z \rightarrow ee$ simulation. The error bars show the statistical uncertainties only.

The components of Figure 5.6 are split up for comparison in Figures 5.7 and 5.8, which show cut-based and likelihood compared for MC simulation, data, then MC simulation and

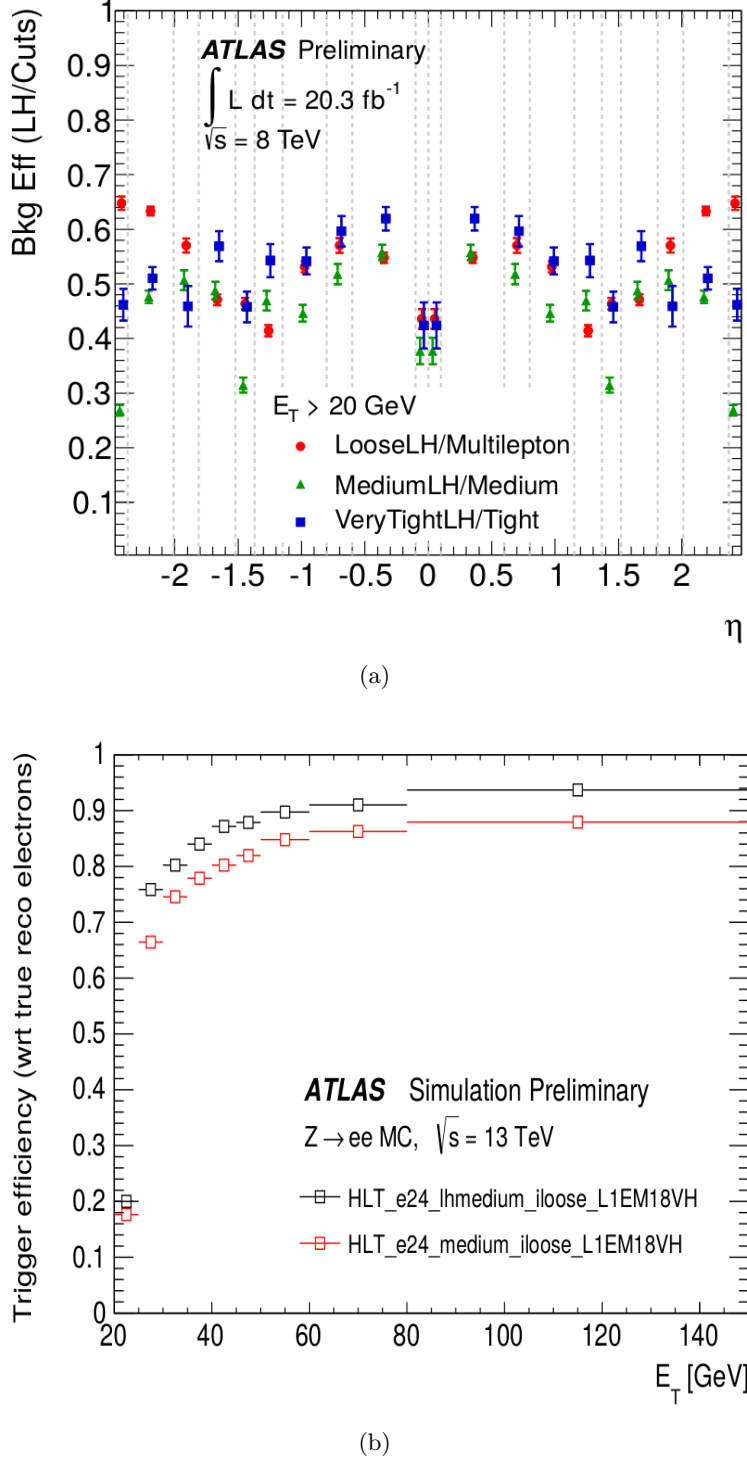


Figure 5.5: (a) Ratio of background efficiencies in Run-1 for LH operating points with respect to corresponding cut-based operating points. Taken from [131]. (b) Run-2 absolute trigger efficiencies expected for HLT_{e24}_(lh)medium_iloose_L1EM18VH triggers as a function of E_T of the offline electron candidate.

data are compared for likelihood then cut-based identification respectively. Figure 5.7(a) shows that the LH based trigger has a higher overall performance with less fluctuation than the cut-based trigger in data. Figure 5.7(b) shows that the LH- and cut-based triggers

perform almost identically with MC simulation. Figures 5.8(c) and (d) show that the LH-based trigger has better agreement between MC simulation and data than the cut-based trigger, as there is greater fluctuation in the central region of the efficiency plot with respect to η for the cut-based trigger. The inefficiency in data that can be observed in the plateaus of the distributions primarily arises at the last step of the High Level Trigger selection that requires tracking related track-cluster matching criteria. These results show that the TP method is a reliable method for measuring trigger efficiencies and there is overall good agreement seen between early 2015 data and MC across the E_T and $|\eta|$ spectra using the TP method. Many improvements have been made for the leptonic triggers since Run-1 in order to ensure rates remain manageable without degrading signal efficiencies. With the early Run-2 data, the ATLAS TDAQ system is shown to be performing well, allowing for analyses to be conducted using the leptons collected during this period.

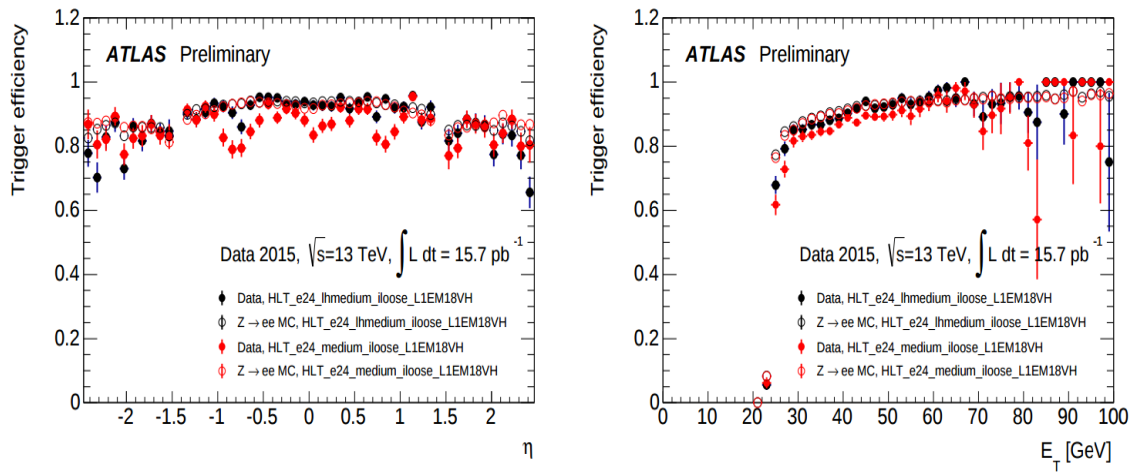
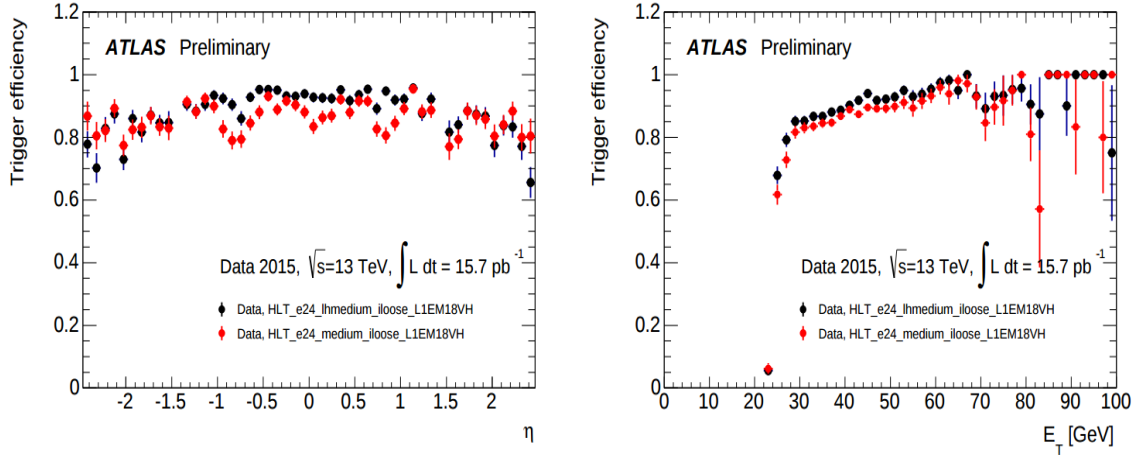
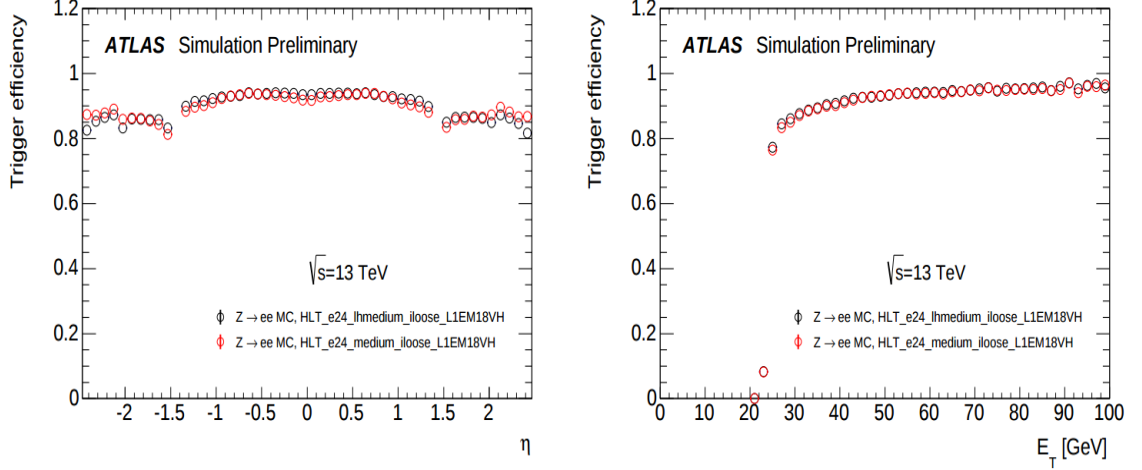


Figure 5.6: Single-electron trigger efficiencies for HLT_e24_(lh)medium_iloose_L1EM18VH triggers as a function of the offline electron candidate's E_T and η , measured with respect to the corresponding offline electron ID using data collected in June and July 2015.



(a) Electron efficiencies in data taken from Figure 5.6 for cut-based *medium* or likelihood-based *lhmedium* identification



(b) Electron efficiencies in $Z \rightarrow ee$ simulation, taken from Figure 5.6 for cut-based *medium* or likelihood-based *lhmedium* identification

Figure 5.7: Single-electron trigger efficiencies for HLT_e24_(lh)medium_iloose_L1EM18VH triggers as a function of the offline electron candidate's E_T and η , measured with respect to the corresponding offline electron ID using data collected in June and July 2015. Data (a) and simulation (b) are split for comparison with cut-based and likelihood identification.

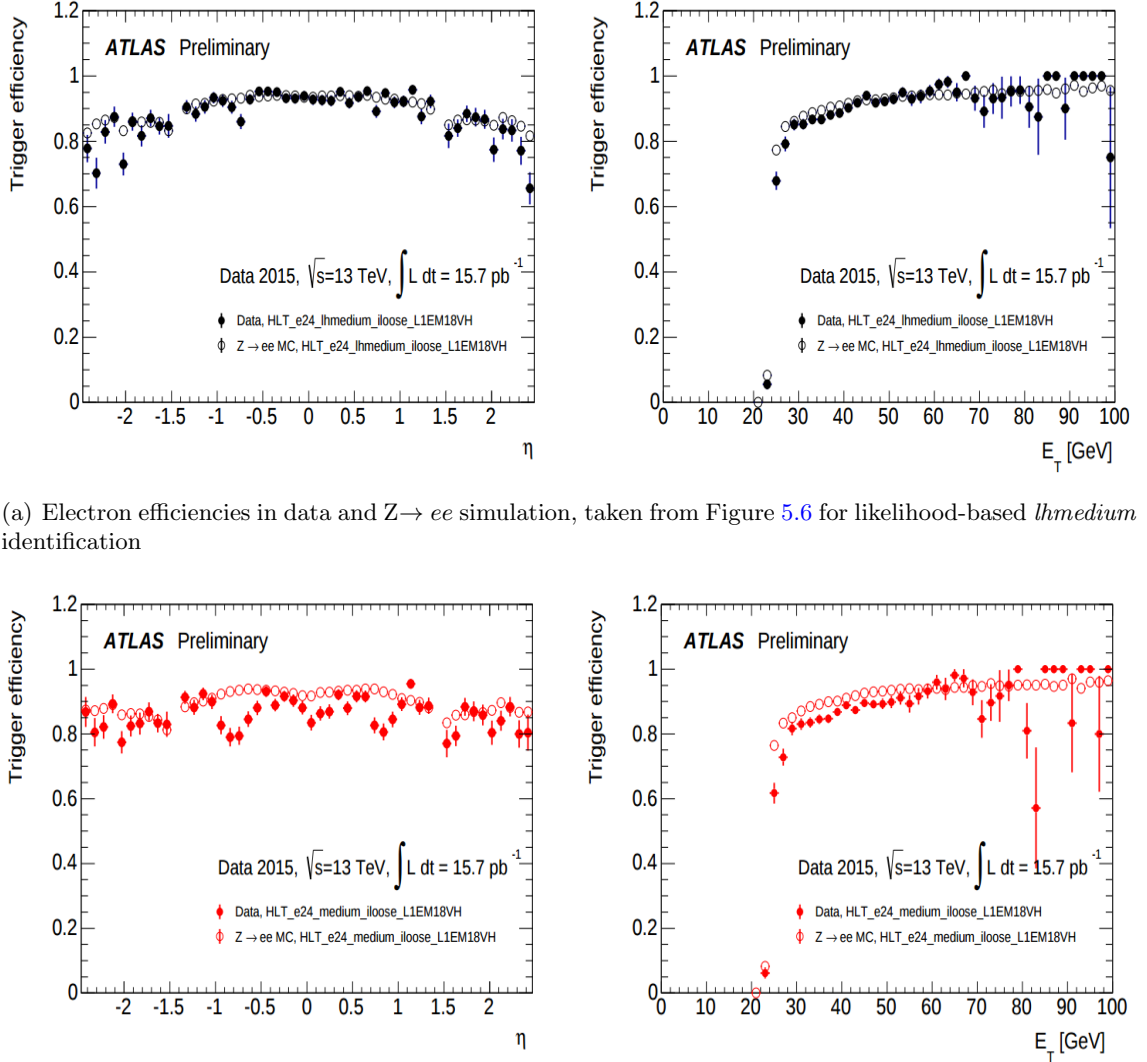


Figure 5.8: Single-electron trigger efficiencies for HLT_e24_(lh)medium_iloose_L1EM18VH triggers as a function of the offline electron candidate's E_T and η , measured with respect to the corresponding offline electron ID using data collected in June and July 2015. Data and simulation are compared with LH- (c) and cut-based-identifications (d).

Chapter 6

A Search for Electroweak SUSY in Three-Lepton Final States with Compressed Spectra in 8 TeV Data at ATLAS

6.1 Introduction

This chapter presents the search for electroweak SUSY, in particular direct $\tilde{\chi}_1^\pm \tilde{\chi}_2^0$ production and decay via SM gauge bosons or left-handed sleptons, $\tilde{\ell}_L$. The current limits on gluino and first- and second-generation squark masses are in the region of 1 TeV. If strongly interacting particles are heavy, then direct gaugino production may be the dominant SUSY cross-section at the LHC. Direct gaugino production can produce large lepton multiplicities through expected gaugino decays. The final state of three leptons and significant E_T^{miss} from the two escaping $\tilde{\chi}_1^0$ s is a particularly distinctive signature; no hadronic activity comes from the hard process, making it hadronically quiet. A previous search was conducted with 20.3 fb^{-1} of 8 TeV proton-proton collision data delivered by the LHC and recorded with the ATLAS detector in 2012 [132]. No significant excess of events was found in data above SM expectations. Limits were placed on the gaugino masses; for simplified SUSY models with intermediate slepton decays, degenerate $\tilde{\chi}_1^\pm/\tilde{\chi}_2^0$ masses up to 600 GeV were excluded for large mass differences with the $\tilde{\chi}_1^0$. For simplified SUSY models with gauge boson decays, degenerate $\tilde{\chi}_1^\pm/\tilde{\chi}_2^0$ masses up to 315 GeV were excluded for large mass differences with the $\tilde{\chi}_1^0$. However, this search was not sensitive to scenar-

ios where the mass difference between the $\tilde{\chi}_1^\pm/\tilde{\chi}_2^0$ and $\tilde{\chi}_1^0$ is less than 50 GeV. This near mass-degeneracy between the decaying gauginos and the final state gauginos is known as compressed scenarios and results in low p_T leptons and less significant E_T^{miss} than would otherwise be seen with large mass differences. For more details on compressed spectra SUSY, refer to Section 2.7.

This chapter describes a search for direct gaugino production with three leptons with compressed spectra in the final state. In order to explore $\tilde{\chi}_2^0 - \tilde{\chi}_1^0$ mass splittings below 50 GeV, this analysis utilises low- p_T leptons and the emission of a hard jet coming from initial state radiation (ISR), which in turn boosts the E_T^{miss} in the event and provides interesting event topology. By requesting an ISR jet however, the level of hadronic activity in the final state increases, therefore hadronically quiet scenario of the previous search does not apply in this case. The intent of this search is to provide improved sensitivity to the compressed scenarios not covered by the previous 3ℓ searches.

The author has contributed significantly to this analysis, including the development of the trigger strategy, signal region optimisation, track isolation studies, validation region optimisation and systematic uncertainty evaluation.

This chapter will highlight the general analysis strategy in Section 6.2; the event selection is detailed in Section 6.3. The signal sensitivity is discussed in Section 6.4.4. The method of SM background estimation is described in Section 6.5, which includes both MC background estimation and data-driven estimation methods. The validation of the background modelling is explored in Section 6.6. Finally, the systematic and theoretical uncertainties are discussed in Section 6.7.

6.2 Analysis Overview

Events from SM background processes can produce three lepton final states that can mimic the final state of the SUSY scenarios considered. These events are suppressed using sets of discriminatory cuts on kinematic variables, which highlight the behaviour of the SUSY signal events. The combination of these cuts form dedicated “Signal Regions” (SRs), as described in Section 6.4. The cuts are optimised using MC simulation only to maximise the expected sensitivity to the signal model. The background contributions in these SRs are estimated using a combination of MC and data-driven methods. The performance of these estimation methods are then “validated” with data in separate dedicated validation regions (VRs), which are adjacent to but orthogonal to the SRs. They are designed such that the contamination from the signal model is low and such that they are dominated by

the background process under consideration.

Several sources of systematic uncertainty are considered for the SM background estimates and signal yield predictions. Regions are designed to be enhanced in a particular SM process in order to assess the differences between data and MC. Both MC simulation and data-driven techniques are used to estimate different components of the background and are discussed in more detail in Section 6.5. The control regions (CRs) are defined with kinematic properties similar to the SRs, yet are disjoint from the SRs to avoid signal contamination. In this analysis, the CR are used to estimate the theoretical uncertainty on the simulation of specific samples, which is discussed in further detail in Section 6.7.14.

SRs are designed with MC estimation only. Data is not included as this could potentially bias the signal region strategy. This method of optimisation is denoted as “blinded”. Once the SRs are finalised, the uncertainties are effectively quantised and the agreement between data and MC is sufficient in the VRs, the signal regions are then “unblinded”, meaning the data is included in the signal regions to see if there is any excess above SM expectations. The statistical interpretation of the results are described in detail in Chapter 7.

6.3 Dataset and Event Selection

The data used for the analysis presented in this chapter was collected during 2012, with a centre-of-mass energy $\sqrt{s} = 8$ TeV, giving a total integrated luminosity of $\mathcal{L} = 20.3 \text{ fb}^{-1}$, which satisfied the ”Good Runs List” (GRL) data quality criteria.

6.3.1 Trigger Selection

The set of trigger chains used to select events for this analysis requires signatures containing up to and including three light leptons, applying the lowest p_T thresholds possible to the lepton p_T . The event selection requires data to have passed a logical OR of all the leptonic triggers summarised in Table 6.1. For any event passing one of these trigger chains, the leptons in the event must also pass the corresponding offline p_T thresholds in order to be accepted. The thresholds are set such that the lepton p_T is within the plateau efficiency for the trigger it has fired. These offline values vary depending on the trigger chain and are listed in Table 6.1 for all chains considered. The signal leptons are also required to be within $\Delta R < 0.15$ from the relevant trigger object. When a specific trigger lists “loose”, “medium” or “tight”, this applies to the type of offline lepton identification used in the

trigger algorithm - see Section 4.4.5. The “vh” label is used to identify triggers where electrons are vetoed at the L1 stage if they have left significant energy deposits within the hadronic calorimeter. The “i” label identifies an additional isolation requirement for the trigger, where the sum of the track p_T ’s within a cone of $\Delta R < 0.2$ of a candidate lepton must be less than 10% (12%) of the lepton p_T if it is an electron (muon).

Table 6.1: Summary of leptonic triggers used in this analysis and the offline threshold used ensuring that the lepton(s) triggering the event are in the plateau region of the trigger efficiency.

Trigger Type	Trigger Name	Offline p_T threshold [GeV]
Single Isolated e	EF_e24vh_medium1	25
Single Isolated μ	EF_mu24i_tight	25
Double e	EF_2e12Tvh_loose1 EF_e24vh_medium1_e7_medium1	14,14 25,10
Double μ	EF_2mu13 EF_mu18_tight_mu8_EFFS	14,14 18,10
Combined $e\mu/\mu e$	EF_e12Tvh_medium1_mu8 EF_mu18_tight_e7_medium1	14(e),10(μ) 18(μ),10(e)
Triple e	EF_e18vh_medium1_2e7T_medium1	20,9,9
Triple μ	3mu6 mu18_tight_2mu4_EFFS	7,7,7 19,5,5
Combined $e\mu$	EF_2e7T_medium1_mu6 EF_e7T_medium1_2mu6	9(e),9(e),7(μ) 9(e),7(μ),7(μ)

To avoid overlap between data streams, it is required that events that only pass the e , ee , eee or $e\mu$ triggers are in the Egamma stream, while events in the Muon stream must fail these triggers and pass the μ , $\mu\mu$ or $\mu\mu\mu$ triggers.

6.3.2 Event Cleaning

Event cleaning is a process whereby events are removed prior to data analysis if the quality of the reconstruction is lowered or partial due to the malfunction of part of the detector, or any other condition that would render the event invalid for physics analysis. These events are removed based on the ATLAS recommended procedures before the analysis specific cuts are made.

The procedure removes events where a timing, trigger and control processing (TTC) has restarted, which results in missing detector information. Events where bursts of noise have been reported in the LAr calorimeters are rejected as well as events where data from the Tile calorimeter has become corrupted. Any events with jets pointing to the Tile calorimeter “hot spot”, which is a problematic (η, ϕ) region (these regions are described

as $-0.2 < \eta < 0.1$ and $2.65 < \phi < 2.75$) are rejected. Events with jets potentially originating from detector effects are rejected. In order to suppress background from cosmic muons, events are rejected if they contain muons which have either an impact parameter d_0 satisfying $|d_0| > 0.2$ mm, or a projection of the impact parameter onto the z axis denoted as $z_0 \sin\theta$ satisfying $z_0 \sin\theta > 1$ mm. Furthermore events are rejected if muons have been poorly reconstructed due to mis-measurement. To be rejected they are required to satisfy:

$$\frac{\sigma_{q/p}}{|q/p|} \geq 0.2, \quad (6.1)$$

where q is the muon charge, p is muon momentum and $\sigma_{q/p}$ is the uncertainty on the measurement of q/p .

Events with fake E_T^{miss} due to non operational cells in the TileCal and the HCAL are rejected. There are calorimeter modules which are either temporarily or permanently masked throughout all data taking periods. High- p_T jets which fall within a masked module are usually overcorrected, while jets in modules adjacent to a masked module are undercorrected [133]. As the jet p_T is increased, this becomes a much more important contribution. Therefore it becomes important to reject events where such jets fall into masked regions, otherwise the jet will be poorly reconstructed. This is also important for E_T^{miss} reconstruction as these masked regions can create large amounts of fake E_T^{miss} .

6.4 Signal Region Optimisation

With the events that survive the event cleaning and quality requirements, the SRs are defined to discriminate for specific SUSY scenarios and against SM processes. These regions request a set of selections or cuts on various kinematic properties of interest, which are optimised using the statistical significance Z_N . This variable is a statistical measure of the relevance of an observation for a given region and is defined as:

$$Z_N = \sqrt{2}\text{erf}^{-1}(1 - 2p(S + B, B, \delta B)), \quad (6.2)$$

where erf is the error function, p gives the probability to observe more data than the background-only hypothesis prediction (See Section 7.1.1), S is the number of expected signal events, B is the number of expected background events and δB is the uncertainty on the background MC estimation. The uncertainty on the background is assumed to be 30% based on statistical uncertainties for previous three-lepton analyses. The background-only hypothesis is the SM, modelled by the MC samples. As the number of signal events

increases beyond the number of SM events the significance increases. The observed number of events is set by summing the number of expected background and signal events. Using this p-value estimate to calculate the significance gives a measure of how strong a statistical statement could be made if there was a signal observation in a given SR. The aim of the signal optimisation, is to maximise this property for each signal region as a function of the number of MC background and signal samples. This is done using MC prediction in a blind analysis strategy, which means the data in the signal regions is not observed until the SRs have been finalised based on expectation only. Data is used in other areas of the analysis: for the background estimation (control regions) and background validation (validation regions). The data contained in these regions must not overlap with data in the SRs.

6.4.1 Optimisation Strategy

Events are selected to satisfy a selection of cuts that highlight the most distinct features from direct gaugino production and decay via SM gauge bosons or $\tilde{\ell}_L$, this is defined as the “baseline” selection and will be explained in detail in the following sections. For the models considered, a total of exactly three leptons is always required. The baseline events are separated into channels depending on the request or veto of at least one ISR jet, defined as a jet in the event with transverse momentum above 50 GeV. The ISR signal regions request an ISR jet, while the soft lepton signal regions veto them. This is to ensure the events do not overlap between the signal regions. This condition is known as *orthogonality*. In these two channels, the events are further split according the minimum possible invariant mass of the SFOS pair of leptons in the event m_{SFOS}^{min} . For the ISR SRs, two channels are considered $5 < m_{SFOS}^{min} < 15$ GeV and $15 < m_{SFOS}^{min} < 25$ GeV. For the soft lepton SRs, $4 < m_{SFOS}^{min} < 15$ GeV and $15 < m_{SFOS}^{min} < 25$ GeV are considered. These channels are considered to target scenarios based on the mass difference between the $\tilde{\chi}_1^\pm/\tilde{\chi}_2^0$ and $\tilde{\chi}_1^0$. The mass difference corresponds to the kinematic endpoint of the m_{SFOS}^{min} distribution. This leads to a total of four signal regions, with each channel requesting additional criteria in order to target scenarios individualised by a range of properties. A detailed description of the signal optimisation will be covered from Section 6.4.1.1 to Section 6.4.3.

6.4.1.1 Baseline

In this analysis, baseline refers to a list of common cuts that are set before further optimisation is performed. The benchmark signal points shown in the baseline distributions

correspond to simplified models via WZ with masses: $m_{\tilde{\chi}_1^\pm/\tilde{\chi}_2^0} = 100$ GeV, $m_{\tilde{\chi}_1^0} = 87.5$ GeV and $m_{\tilde{\chi}_1^\pm/\tilde{\chi}_2^0} = 100$ GeV, $m_{\tilde{\chi}_1^0} = 75$ GeV. These cuts are as follows:

Transverse momentum of the leading lepton ($p_T^{1^{st}\ell}$): The compressed scenarios explored in this analysis produce low p_T leptons in the final state. This is shown in Figure 6.1. The tails of the signal distributions in p_T tend to zero around 100 GeV, whilst the SM background extends beyond 300 GeV. An upper cut of $p_T^{1^{st}\ell} < 30$ GeV is applied to preserve the signal events and remove the tails from the SM background. The optimisation for an upper cut on this variable is done using the N-1 method, where all signal region cuts are applied except one. The cut which is removed is optimised to maximise the significance whilst retaining signal and background statistics. Background statistics need to be maintained to reduce the statistical uncertainty in the signal regions and to see the distributions of the SM processes. The distributions are shown in Figure 6.2.

B-veto To reduce top-containing backgrounds and heavy flavour Z-boson decays all events containing b -jets are vetoed. Although the request of an ISR means the final state is not “hadronically quiet”, the expected jet to be produced in compressed spectra will not be heavy flavour. Figure 6.3 shows the b -jet multiplicity of events with three leptons and a SFOS pair request. The majority of the signal events have zero b -jet multiplicity, while Higgs and $t\bar{t}$ -V have a larger spread, with some events containing as many as 5 b -jets.

E_T^{miss} In order to discriminate against the Low Mass Drell-Yan processes and the Z+jets processes, which dominate in the low E_T^{miss} region a cut of $E_T^{\text{miss}} > 50$ GeV is applied. Figure 6.4 shows the E_T^{miss} distribution for events with three leptons a SFOS request and a b -jet veto. Z+jets, J/Ψ and Υ populate the E_T^{miss} below 60 GeV. The optimisation for this cut was done using the N-1 method and is shown in Figures 6.6(a) - (d). The cut was selected to reduce the Drell-Yan, Z+jets and diboson backgrounds.

m_{SFOS} The Υ meson has an invariant mass of 9.46 GeV. It can decay to a SFOS pair of leptons whose invariant mass would be within 1 GeV of the meson mass. This analysis has a lower threshold on the m_{SFOS} variable than the previous 3ℓ analysis, at 4 GeV for the “soft lepton” signal regions and 5 GeV for the ISR signal regions, and therefore would accept this background in the signal selection. To cleanly reject this background process a veto window of 1 GeV is applied on the m_{SFOS} distribution between 8.4 and 10.4 GeV. Figure 6.5 shows the m_{SFOS} distribution for events with three leptons, a SFOS request

and a b -jet veto. The peak from the Υ decays appears in the second bin of the distribution.

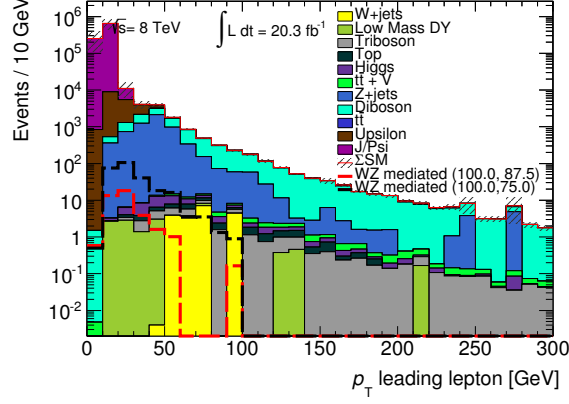


Figure 6.1: The leading lepton p_T distribution for 3ℓ events with a SFOS request and b -jet veto requirement applied.

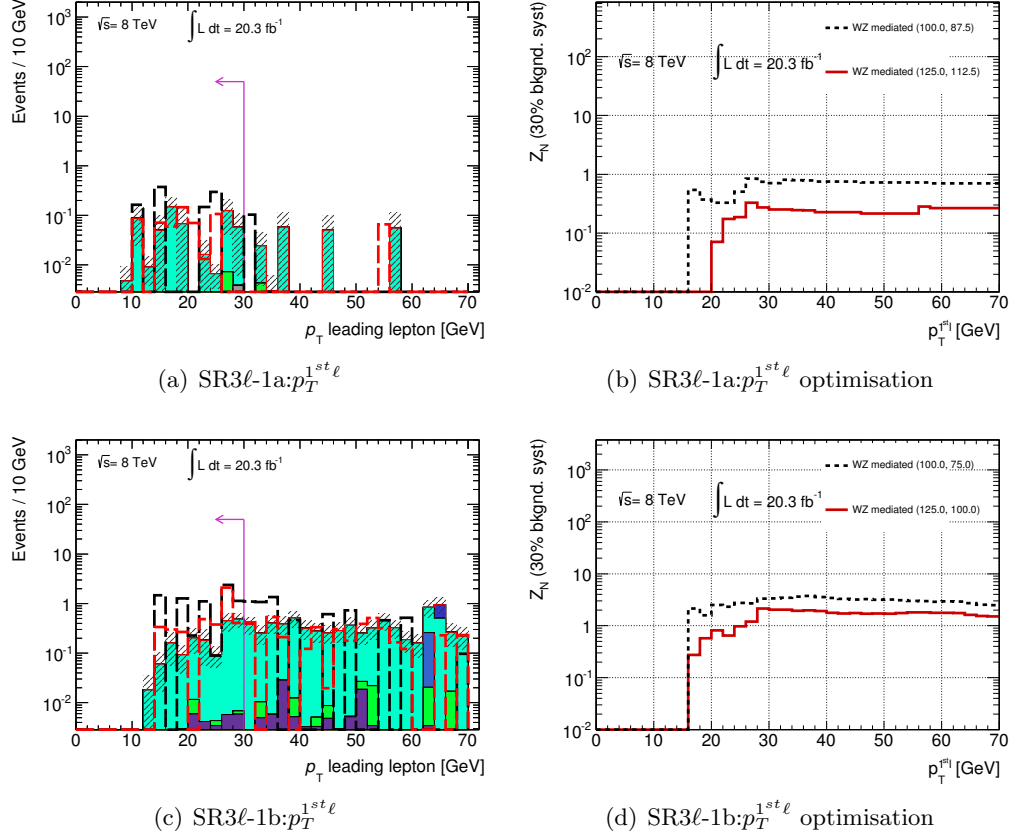


Figure 6.2: N-1 Distributions for $p_T^{1st \ell}$: All SR definition cuts applied except for the $p_T^{1st \ell}$ cut. The colours assigned to the SM processes are the same as Figure 6.1.

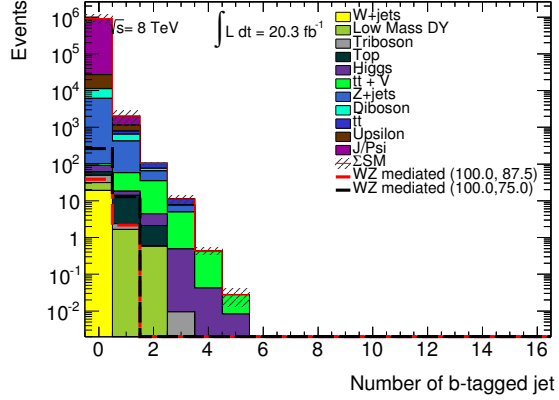


Figure 6.3: The b -jet multiplicity distribution for 3ℓ events with a SFOS request applied.

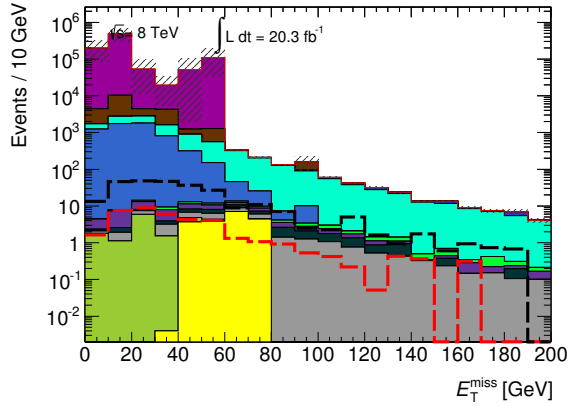


Figure 6.4: The E_T^{miss} distribution for 3ℓ events with a SFOS request and b -jet veto requirement applied. The colours assigned to the SM processes are the same as Figure 6.1.

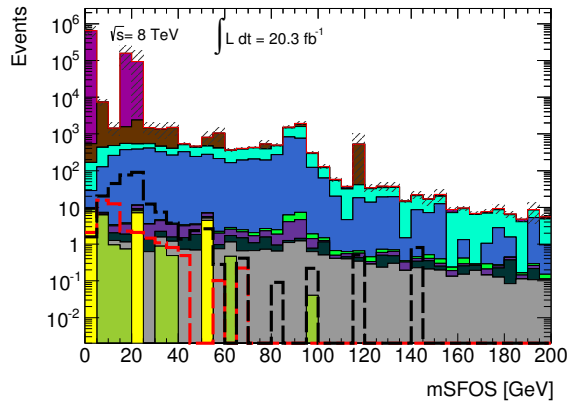


Figure 6.5: The m_{SFOS} distribution for 3ℓ events with a SFOS request and b -jet veto requirement applied. The colours assigned to the SM processes are the same as Figure 6.1.

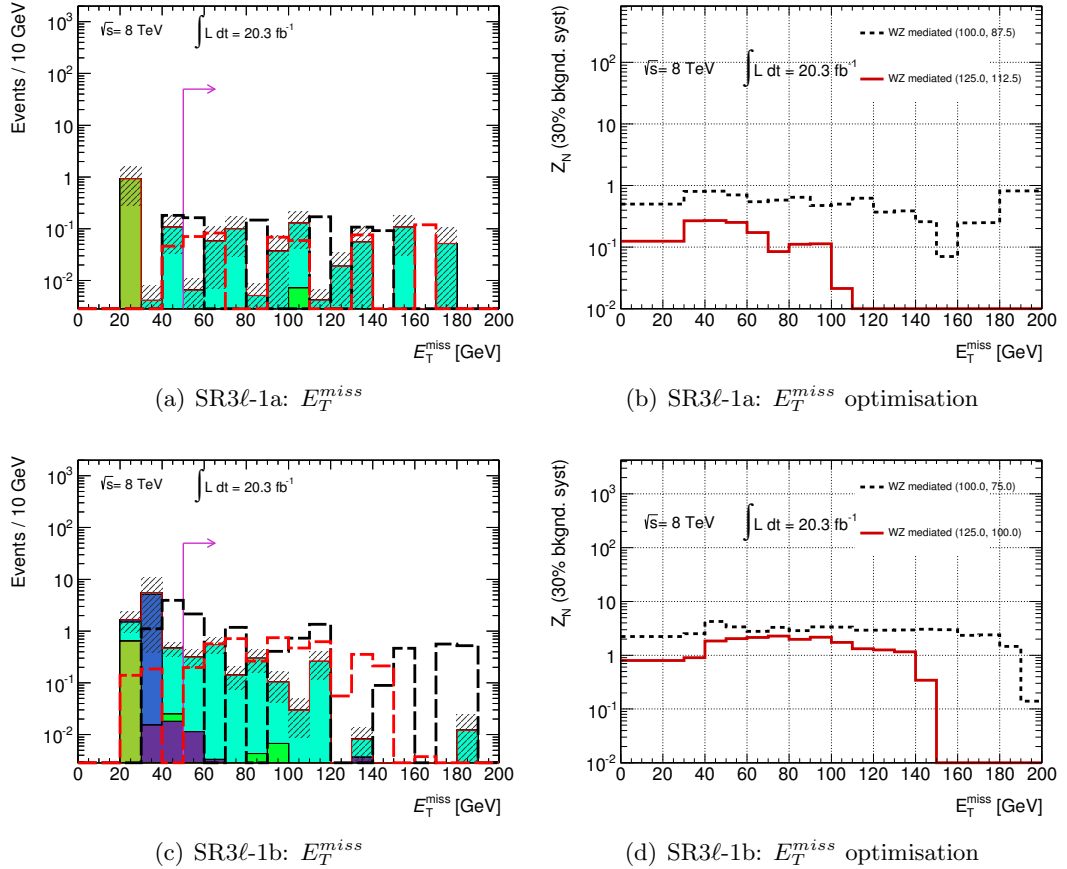


Figure 6.6: N-1 Distributions for E_T^{miss} : All SR definition cuts applied except for the E_T^{miss} cut. The colours assigned to the SM processes are the same as Figure 6.1.

6.4.1.2 Binning in $m_{\text{SFOS}}^{\text{min}}$

The leptons produced from compressed $\tilde{\chi}_1^\pm \tilde{\chi}_2^0$ decays are soft, consequently the invariant mass of the SFOS pair will be typically softer than the equivalent for the SM background processes which produce harder leptons in the final state. The kinematic endpoint of the $m_{\text{SFOS}}^{\text{min}}$ distribution corresponds to the mass difference between $\tilde{\chi}_1^\pm$ and $\tilde{\chi}_1^0$. The signal regions are binned in this variable to target different mass $\tilde{\chi}_1^\pm - \tilde{\chi}_1^0$ mass splittings. SR3 ℓ -1a selects events with $5 < m_{\text{SFOS}}^{\text{min}} < 15$ GeV to target the smallest mass splittings. SR3 ℓ -1b selects events with $15 < m_{\text{SFOS}}^{\text{min}} < 25$ GeV to target the larger mass splittings. Binning also preserves orthogonality, allowing for the signal regions to be statistically combined for optimal sensitivity to new physics. Figure 6.7 shows the $m_{\text{SFOS}}^{\text{min}}$ for events with three leptons, a SFOS request and a b -jet veto. The signal points shown correspond to simplified models via WZ with masses: $m_{\tilde{\chi}_1^\pm \tilde{\chi}_2^0} = 100$ GeV, $m_{\tilde{\chi}_1^0} = 87.5$ GeV and $m_{\tilde{\chi}_1^\pm \tilde{\chi}_2^0} = 100$ GeV, $m_{\tilde{\chi}_1^0} = 75$ GeV. The distinct kinematic endpoints are at 12.5 GeV for the former point and 25 GeV for the latter point. By binning in this variable two approaches can be applied to

signal optimisation. For the most compressed scenario, more stringent cuts can be used including the angular distributions of the ISR jet. For the less compressed scenario, there will still be sensitivity in the most compressed signal region. However, the optimisation cuts can be loosened as the production cross-section is higher for these points, resulting in higher initial yields, with longer tails in the considered kinematic variables than the most compressed points. The optimisation of the m_{SFOS}^{min} variable was performed using the N-1 method. Figure 6.8 shows the optimal upper cuts, indicated by the event distribution and the one-dimensional Z_N curves. An optimal Z_N is achieved in SR3 ℓ -1a with an upper cut of 15 GeV, using benchmark signal points, which correspond to simplified models via WZ with masses: $m_{\tilde{\chi}_1^\pm \tilde{\chi}_2^0} = 100$ GeV, $m_{\tilde{\chi}_1^0} = 87.5$ GeV and $m_{\tilde{\chi}_1^\pm \tilde{\chi}_2^0} = 125$ GeV, $m_{\tilde{\chi}_1^0} = 112.5$ GeV. An optimal Z_N is achieved in SR3 ℓ -1b with an upper cut of 25 GeV, using benchmark signal points, which correspond to simplified models via WZ with masses: $m_{\tilde{\chi}_1^\pm \tilde{\chi}_2^0} = 100$ GeV, $m_{\tilde{\chi}_1^0} = 75$ GeV and $m_{\tilde{\chi}_1^\pm \tilde{\chi}_2^0} = 125$ GeV, $m_{\tilde{\chi}_1^0} = 100$ GeV. These signal points are used in the following optimisation stages.

6.4.2 ISR Signal Region Procedure

ISR Jet Request Compressed signal production can be targeted by requesting at least one jet in the event with a sizeable transverse momentum minimum requirement. Figure 6.9 shows the leading jet p_T distribution with a SFOS request, a b -jet veto and at least one jet request in the $5 < m_{SFOS}^{min} < 15$ GeV bin. The optimal value is 50 GeV for both regions as shown in Figure 6.10. This value is also chosen to be identical to the E_T^{miss} cut due to the ISR jet recoiling against the invisible decay products as discussed in Section 2.7. The ISR jet definition is common to both signal regions SR3 ℓ -1a and SR3 ℓ -1b, to maintain consistency in object definition. The next sections will address the individual cuts for each region.

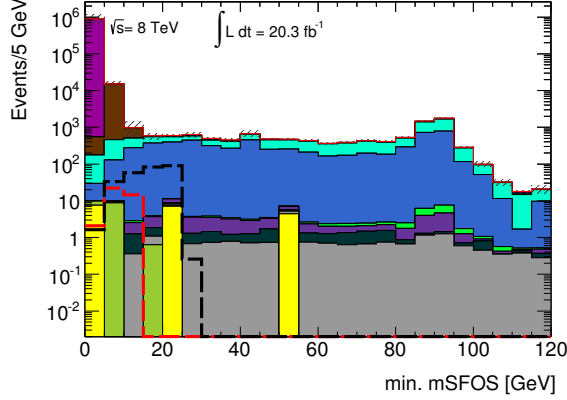


Figure 6.7: The m_{SFOS}^{min} distribution for 3ℓ events with a SFOS request and b -jet veto requirement applied. The colours assigned to the SM processes are the same as Figure 6.1.

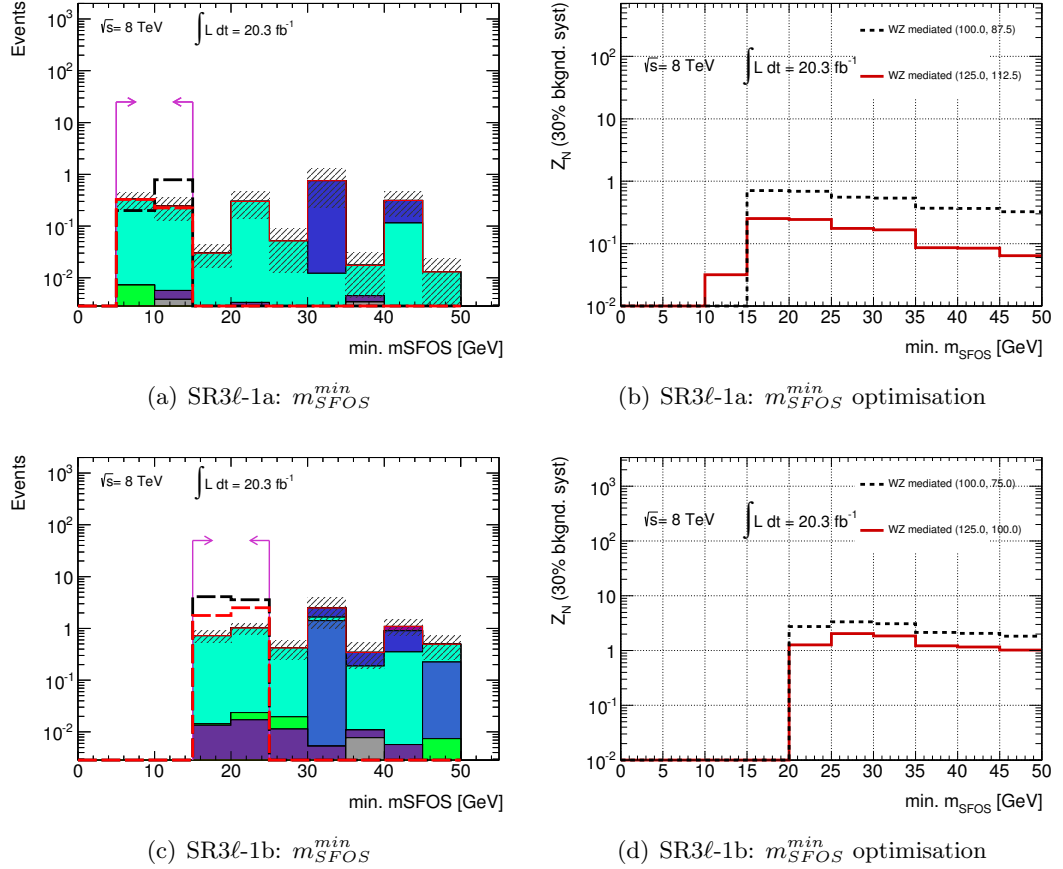


Figure 6.8: N-1 Distributions for m_{SFOS}^{min} : all SR definition cuts applied except for the upper cut on m_{SFOS}^{min} . The one-dimensional Z_N distributions show the effect of an upper cut on the m_{SFOS}^{min} variable. The colours assigned to the SM processes are the same as Figure 6.1.

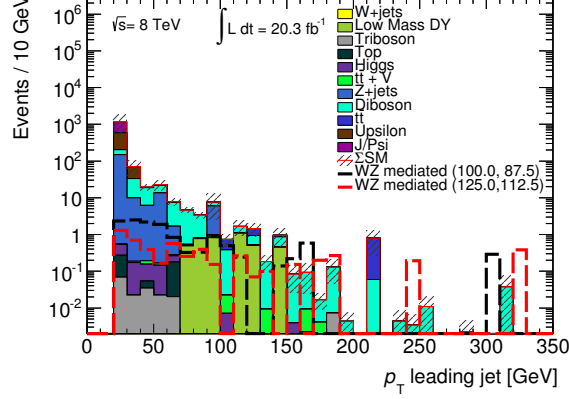


Figure 6.9: The leading jet p_T distribution for 3ℓ events with a SFOS request and b -jet veto applied in the SR 3ℓ -1a m_{SFOS}^{min} bin. At least one jet is requested in the event selection.

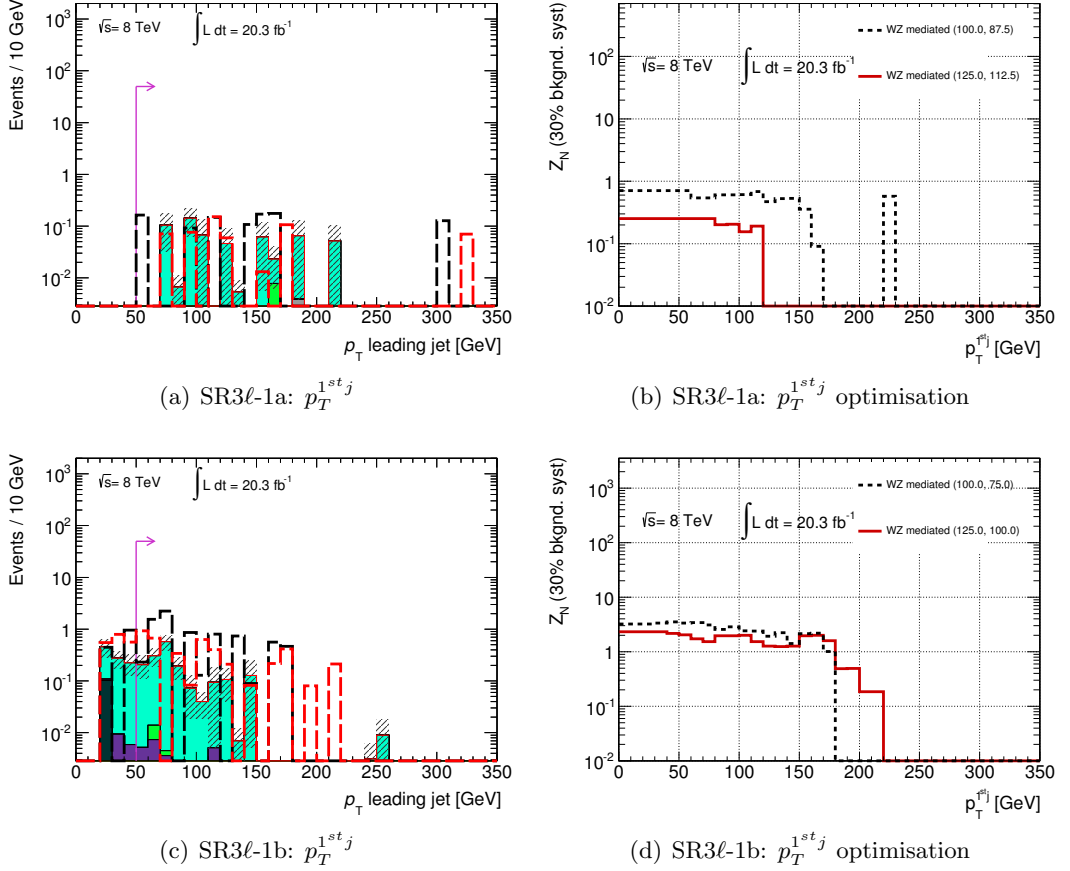


Figure 6.10: N-1 Distributions for $p_T^{1st j}$: all SR definition cuts applied except for the $p_T^{1st j}$ cut. The colours assigned to the SM processes are the same as Figure 6.1.

6.4.2.1 SR 3ℓ -1a Cuts

Polar angle between E_T^{miss} and ISR Jet ($\Delta\phi(E_T^{\text{miss}}, \text{Jet1})$): In the final state, the p_T of the leptons can be assumed negligible compared to the E_T^{miss} and the ISR jet. The

initial state momentum of a proton-proton collision is assumed to be zero. To conserve final state momentum, the ISR jet and the E_T^{miss} , both assumed to be carrying the majority of the final state momentum, will be produced back to back. This can be quantified by taking the angular distribution - $\Delta\phi$ - between E_T^{miss} and the ISR jet in the event. The signal events should have $\Delta\phi$ close to π , this is shown in Figure 6.11, where the signal events populate the bins close to π , whereas the SM background has a flat distribution from 0 to π . Using the N-1 optimisation method a cut above 2.7 rad was selected, which obtains optimal Z_N for the benchmark signal points shown in Figure 6.12.

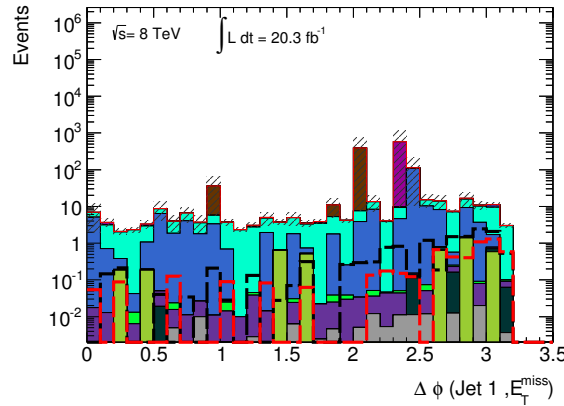


Figure 6.11: The $\Delta\phi(E_T^{miss}, \text{Jet1})$ distribution for 3ℓ events with a SFOS request and b -jet veto applied in the SR 3ℓ -1a m_{SFOS}^{min} bin. At least one jet is requested in the event selection. The colours assigned to the SM processes are the same as Figure 6.1.

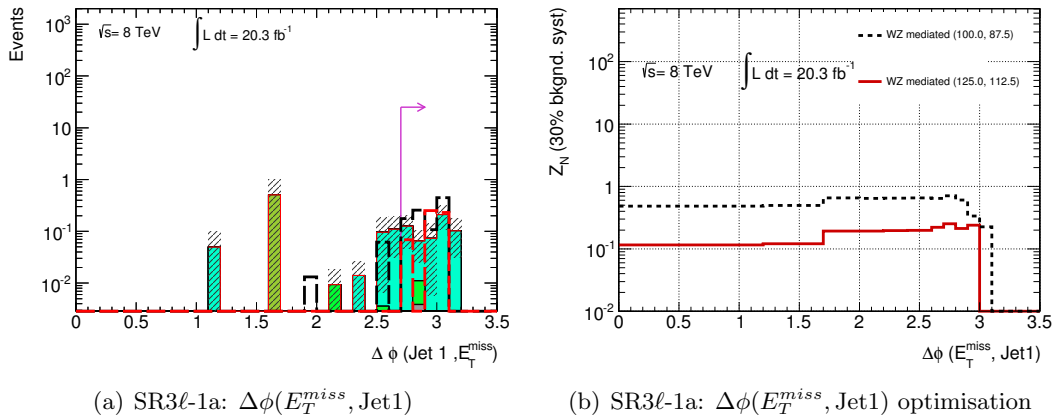


Figure 6.12: N-1 Distributions for $\Delta\phi(E_T^{miss}, \text{Jet1})$: all SR definition cuts applied except for the $\Delta\phi(E_T^{miss}, \text{Jet1})$ cut. The colours assigned to the SM processes are the same as Figure 6.1.

Ratio of the p_T of the leading lepton to ISR jet ($p_T^{1^{st}\ell}/p_T^{1^{st}j}$): The ISR jet together with E_T^{miss} carries the majority of the momentum in the final state. If the ratio of p_T between the leading lepton and the ISR jet is calculated, the ratio value should be less than

one for compressed scenario signal events and close to unity for SM background processes. This is shown in Figure 6.13, which shows the $p_T^{1^{st}\ell}/p_T^{1^{st}j}$ distribution for 3ℓ events with a SFOS request and b -jet veto applied in the SR3 ℓ -1a m_{SFOS}^{\min} bin. The signal events populate values below 1 whereas the SM backgrounds exhibits a flat distribution between 0 and 1.5. Using the N-1 method, the optimal cut lies at below 0.1, which is shown in Figure 6.14(b). However to maintain signal event statistics a slightly more conservative upper cut of 0.2 is applied.

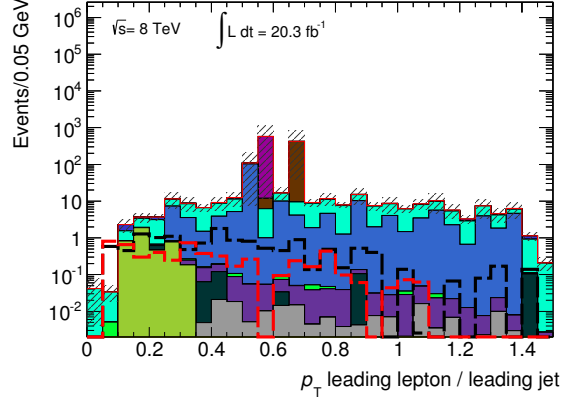


Figure 6.13: The $p_T^{1^{st}\ell}/p_T^{1^{st}j}$ distribution for 3ℓ events with a SFOS request and b -jet veto applied in the SR3 ℓ -1a m_{SFOS}^{\min} bin. At least one jet is requested in the event selection. The colours assigned to the SM processes are the same as Figure 6.1.

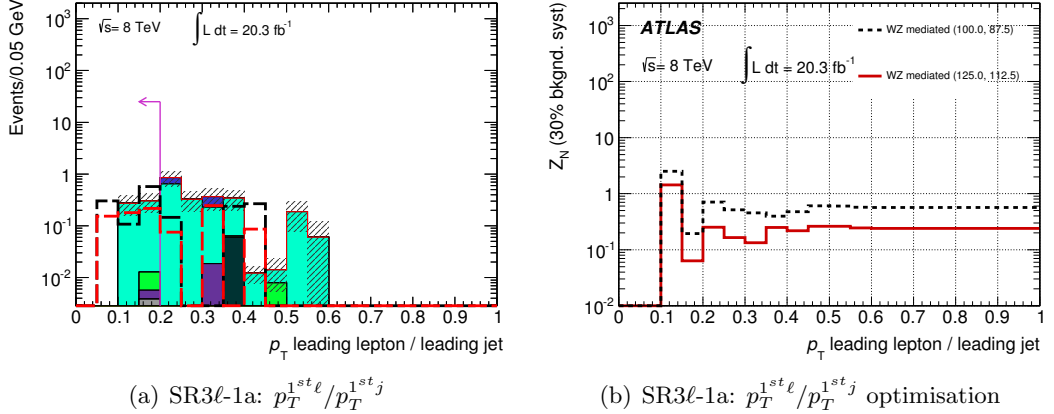


Figure 6.14: N-1 Distributions for $p_T^{1^{st}\ell}/p_T^{1^{st}j}$: all SR definition cuts applied except for the $p_T^{1^{st}\ell}/p_T^{1^{st}j}$ cut. The colours assigned to the SM processes are the same as Figure 6.1.

6.4.2.2 SR3 ℓ -1b Cuts

Polar angle between E_T^{miss} and the three leptons in the final state ($\Delta\phi(E_T^{\text{miss}}, 3\ell)$):
The topology between the E_T^{miss} and leading jet in the event has been exploited in Section 6.4.2.1. However, the leptons are not as strongly correlated with the direction of

the ISR jet or E_T^{miss} , and show a roughly flat distribution as shown in Figure 6.15. The $\Delta\phi(E_T^{miss}, 3\ell)$ distribution is shown for 3ℓ events with a SFOS request and b -jet veto applied in the SR3 ℓ -1b m_{SFOS}^{min} bin. The two $\Delta m_{\tilde{\chi}_1^\pm \tilde{\chi}_2^0 - \tilde{\chi}_1^0}$ benchmark signal points exhibit a flat distribution between 0 and π . Using the N-1 method for this variable, a cut of <2.2 rad removes the remaining $t\bar{t}$ process contribution as shown in Figure 6.16(b).

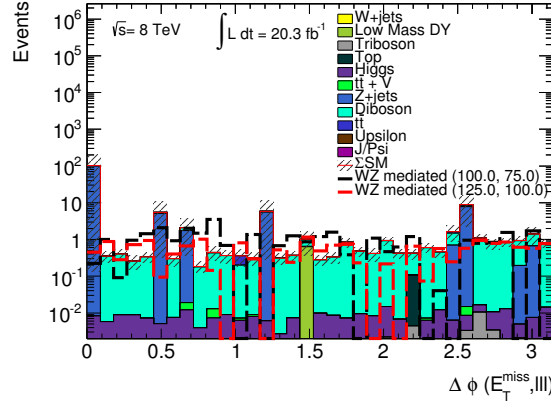


Figure 6.15: The $\Delta\phi(E_T^{miss}, 3\ell)$ distribution for 3ℓ events with a SFOS request and b -jet veto applied in the SR3 ℓ -1b m_{SFOS}^{min} bin. At least one jet is requested in the event selection.

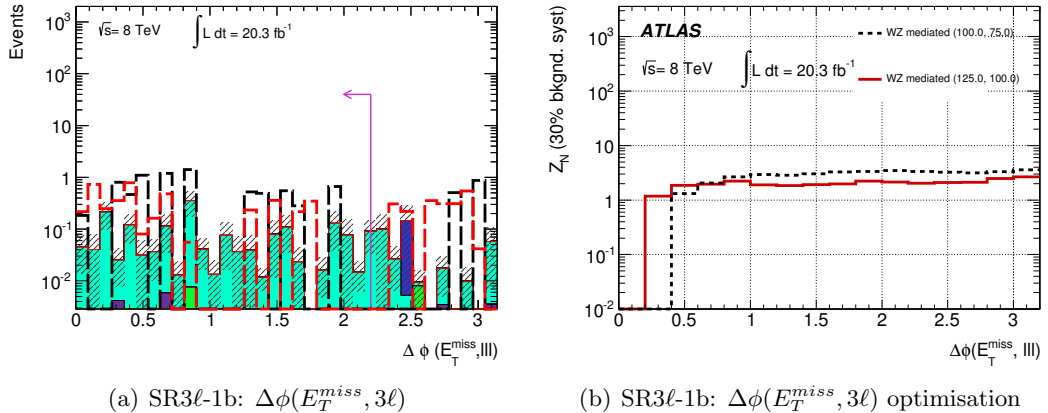


Figure 6.16: N-1 Distributions for $\Delta\phi(E_T^{miss}, 3\ell)$: all SR definition cuts applied except for the $\Delta\phi(E_T^{miss}, 3\ell)$ cut. The colours assigned to the SM processes are the same as Figure 6.1.

The soft lepton signal region procedure is discussed in Section 6.4.3. The focus of this thesis is the ISR signal regions, so only the N-1 optimisation distributions are shown and discussed for the soft lepton signal regions.

6.4.3 Soft Lepton Signal Region Procedure

Compressed signal production can be targeted by exploring the kinematic variables and angular distributions of the three low p_T leptons in the final state. These signal regions veto all jets in order to ensure all soft lepton signal region events do not overlap with the ISR signal region events. The baseline selection defined in Section 6.4.1.1 is used. The m_{SFOS}^{min} binning strategy is similar to the ISR signal regions with SR3 ℓ -0a targeting the smallest $\tilde{\chi}_2^0$ - $\tilde{\chi}_1^0$ mass splittings by selecting events with m_{SFOS}^{min} between 4 and 15 GeV and SR3 ℓ -0b targeting the slightly larger mass splittings by selecting events with m_{SFOS}^{min} between 15 and 25 GeV. Both SR3 ℓ -0a and SR3 ℓ -0b are defined with $E_T^{miss} > 50$ GeV and the invariant mass of the three-lepton system $m_{\ell\ell\ell}$ is between 30 and 60 GeV to reject diboson processes. The $m_{\ell\ell\ell}$ N-1 optimisation is shown in Figures 6.17(a) - (d), where the upper cut Z_N distribution is shown in Figures 6.17(b) and (d). SR3 ℓ -0a utilises the transverse mass variable, m_T , defined as:

$$m_T(\vec{p}_T^{\ell/\tau}, E_T^{miss}) = \sqrt{2p_T^{\ell/\tau}E_T^{miss} - 2\vec{p}_T^{\ell/\tau} \cdot \vec{E}_T^{miss}},$$

where the lepton used in the calculation is not used to form the SFOS lepton pair with mass closest to the Z boson mass. The transverse mass is required to be less than 20 GeV to reduce the WZ SM background. The N-1 optimisation for this variable is shown in Figures 6.18(a) and (b). The optimisation uses the same four $\tilde{\chi}_1^\pm$ - $\tilde{\chi}_2^0$ via WZ benchmark signal points described in Section 6.4.2.

6.4.4 Signal Region Summary

The final optimised cuts for each of the four signal regions are detailed in Table 6.2. The significance was calculated for the four regions. They were combined in quadrature to give an estimation of the performance of each signal region in both the $\tilde{\chi}_1^\pm$ - $\tilde{\chi}_2^0$ via WZ and via $\tilde{\ell}_L$ simplified models. The significance was calculated for each point in the simplified model grids and displayed on histograms with the significance as a function of the parameter space. The x and y axes display the $\tilde{\chi}_1^\pm$ - $\tilde{\chi}_2^0$ and $\tilde{\chi}_1^0$ masses respectively. Delaunay triangulation [134] is used to interpolate the significance values for bins in between the points where the signal samples exist in order to ensure the significance changes smoothly as a function of horizontal and vertical. A significance value of 1.64 or greater corresponds to an exclusion of the signal scenario considered with a 95% confidence level [135]. Refer to Section 7.1.1 for further explanation of exclusion of hypotheses.

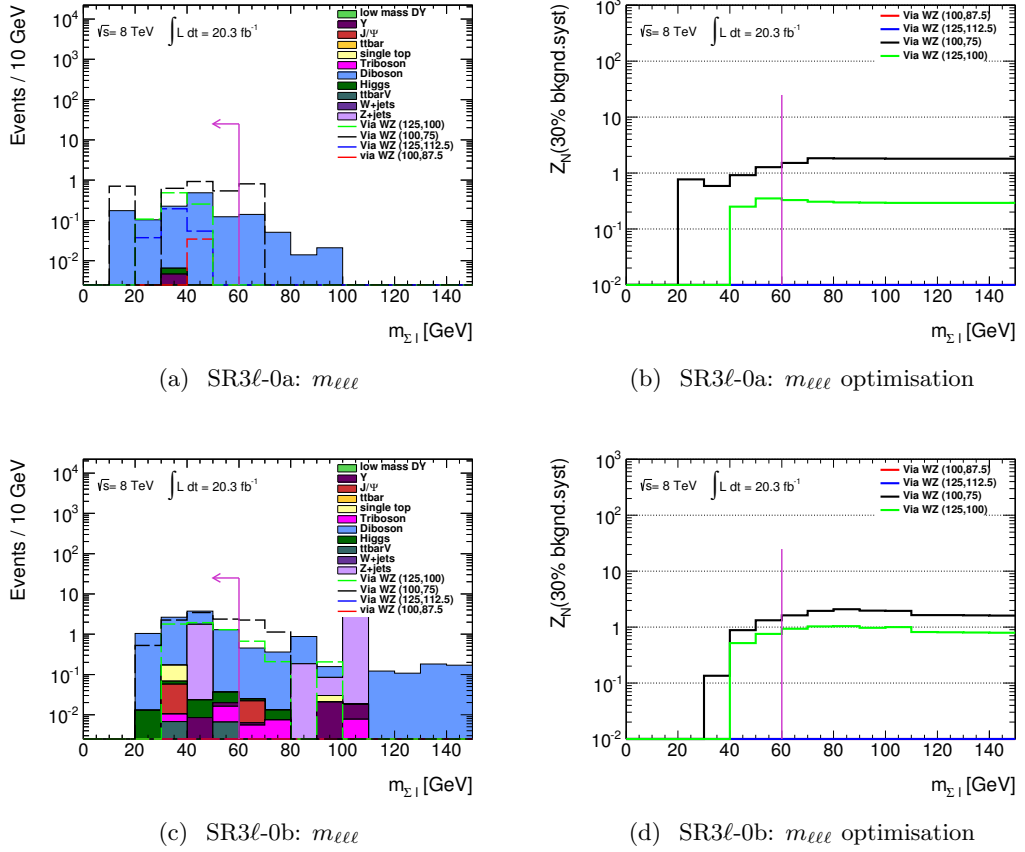


Figure 6.17: The N-1 $m_{\ell\ell\ell\ell}$ distributions for each bin in SR3ℓ-0: all SR definition cuts applied except for the $m_{\ell\ell\ell\ell}$ cut. The signal significance for WZ SUSY benchmark points is shown on the right plots as an upper cut on $m_{\ell\ell\ell\ell}$ is varied. (Produced by another analyser, taken from [136]).

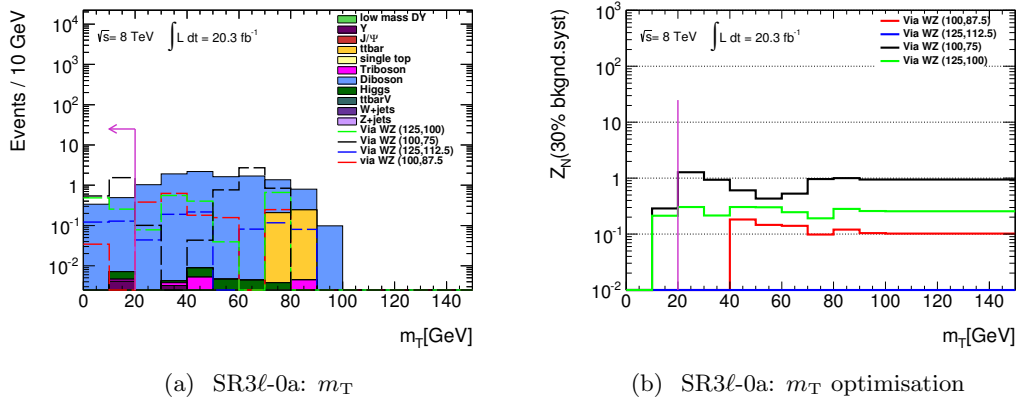


Figure 6.18: The N-1 m_T distributions for SR3ℓ-0a: all SR definition cuts applied accept m_T . The vertical black lines indicate bin edges. The signal significance for WZ SUSY benchmark points is shown on the right plots as an upper cut on m_T is varied (Produced by another analyser, taken from [136]).

Table 6.2: The selection requirements for the three-lepton signal regions, targeting $\tilde{\chi}_1^\pm \tilde{\chi}_2^0$ production with small mass splittings between the $\tilde{\chi}_1^\pm / \tilde{\chi}_2^0$ and $\tilde{\chi}_1^0$.

mSFOS	SR	Common			
		SR3 ℓ -0a	SR3 ℓ -0b	veto 8.4–10.4 GeV	veto 8.4–10.4 GeV
Central jets		no jets $p_T > 50$ GeV		≥ 1 jet $p_T > 50$ GeV	
$m_{\text{SFOS}}^{\text{min}}$	4–15 GeV	15–25 GeV		5–15 GeV	15–25 GeV
Other	$30 < m_{\ell\ell\ell} < 60$ GeV	$30 < m_{\ell\ell\ell} < 60$ GeV	$\Delta\phi(E_T^{\text{miss}}, \text{jet 1}) > 2.7$ rad	$\Delta\phi(E_T^{\text{miss}}, 3\ell) < 0.7\pi$ rad	
	$m_T < 20$ GeV		$p_T^{\text{lep } 1}/p_T^{\text{jet } 1} < 0.2$		

6.4.5 Significance in Soft Lepton and ISR Signal Regions

To determine the significance of the searches for new physics, the MC expected background is used. The significance is calculated for all four signal regions separately. The ISR signal regions SR3 ℓ -1a and SR3 ℓ -1b are in orthogonal bins of m_{SFOS}^{min} , therefore the calculated significances can be combined. The same applies for the soft lepton signal regions SR3 ℓ -0a and SR3 ℓ -0b. The calculation of the Z_N values for each of the simplified models considered are done for two scenarios: MC-based estimates for all SM backgrounds and combined MC-based and data driven matrix method estimates. The reasoning for different estimate methods is explained in Section 6.5. The uncertainty on the MC-based estimates is taken as a flat 30% while the uncertainty on the backgrounds estimated with the matrix method is taken directly from combined systematic uncertainties from the matrix method as described in Section 6.7.15. The MC-based scenario results are shown in Figures 6.19, 6.21, 6.23 and 6.25. The MC and data driven matrix method scenario results are shown in Figures 6.20, 6.22, 6.24 and 6.26. For reference, the compressed region in the parameter space is defined $\Delta m_{\tilde{\chi}_1^\pm \tilde{\chi}_2^0 - \tilde{\chi}_1^0} \leq 50$ GeV. Due to the stringent requirements in all signal regions, the background statistics are very low. This particularly applies to the background processes estimated by the matrix method. When the data driven matrix method estimate is included, the background statistics increase by 200-300%, which significantly reduces the expected sensitivity.

6.4.5.1 $\tilde{\chi}_1^\pm \tilde{\chi}_2^0$ via $\tilde{\ell}$

The significance Z_N was calculated for the $\tilde{\chi}_1^\pm \tilde{\chi}_2^0$ decay via intermediate sleptons simplified model in both the soft lepton and ISR signal regions. Starting with the ISR signal regions, for the MC-based only estimate $\tilde{\chi}_1^\pm / \tilde{\chi}_2^0$ masses can be excluded up to 350 GeV in the compressed region with a $\tilde{\chi}_1^0$ mass of 300 GeV. For the MC and data driven matrix method estimate $\tilde{\chi}_1^\pm \tilde{\chi}_2^0$ masses can be excluded up to 320 GeV in the compressed region with a $\tilde{\chi}_1^0$ mass 300 GeV. For the soft lepton regions, considering the MC-based only estimate $\tilde{\chi}_1^\pm \tilde{\chi}_2^0$ masses can be excluded up to 270 GeV with a $\tilde{\chi}_1^0$ mass of 230 GeV. Considering the MC and data driven matrix method estimate $\tilde{\chi}_1^\pm \tilde{\chi}_2^0$ masses can be excluded up to 200 GeV with a $\tilde{\chi}_1^0$ mass of 150 GeV. Improvements to the compressed region of the parameter space are seen for both signal regions compared to [132].

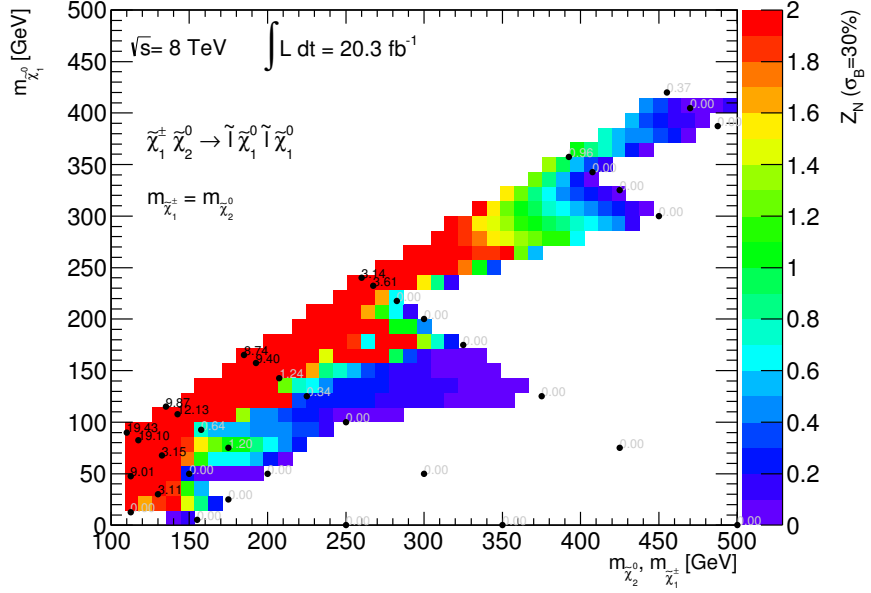


Figure 6.19: Combined expected significance for $\tilde{\chi}_1^\pm \tilde{\chi}_2^0$ production via $\tilde{\ell}$ in SR3 ℓ -1a and SR3 ℓ -1b. The overall values for the total systematic uncertainty are shown on the z-axis for each bin in SR3 ℓ -1.

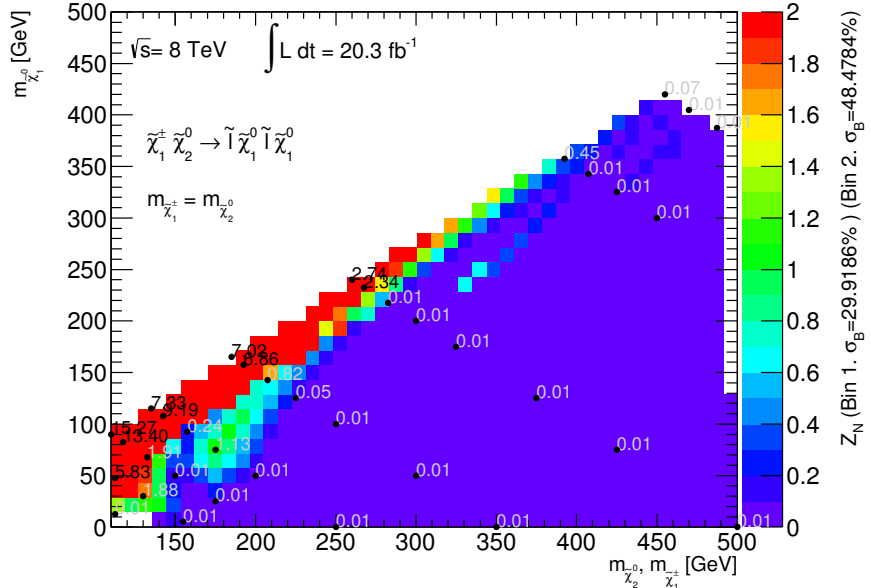


Figure 6.20: Combined expected significance for $\tilde{\chi}_1^\pm \tilde{\chi}_2^0$ production via $\tilde{\ell}$ in SR3 ℓ -1a and SR3 ℓ -1b. The overall values for the total systematic uncertainty are shown on the z-axis for each bin in SR3 ℓ -1.

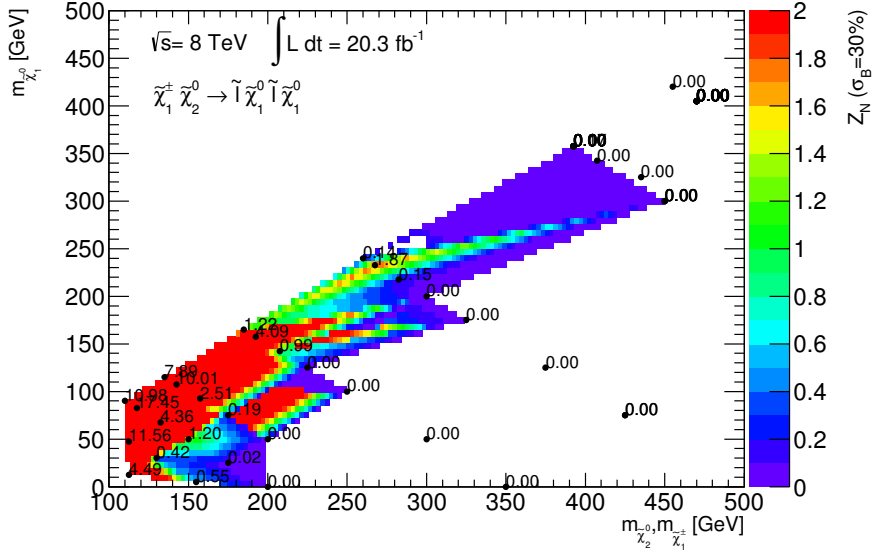


Figure 6.21: Combined expected significance for $\tilde{\chi}_1^\pm \tilde{\chi}_2^0$ production via \tilde{t} in SR3 ℓ -0a and SR3 ℓ -0b. The overall values for the total systematic uncertainty are shown on the z-axis for each bin in SR3 ℓ -0 (Produced by another analyser, taken from [136]).

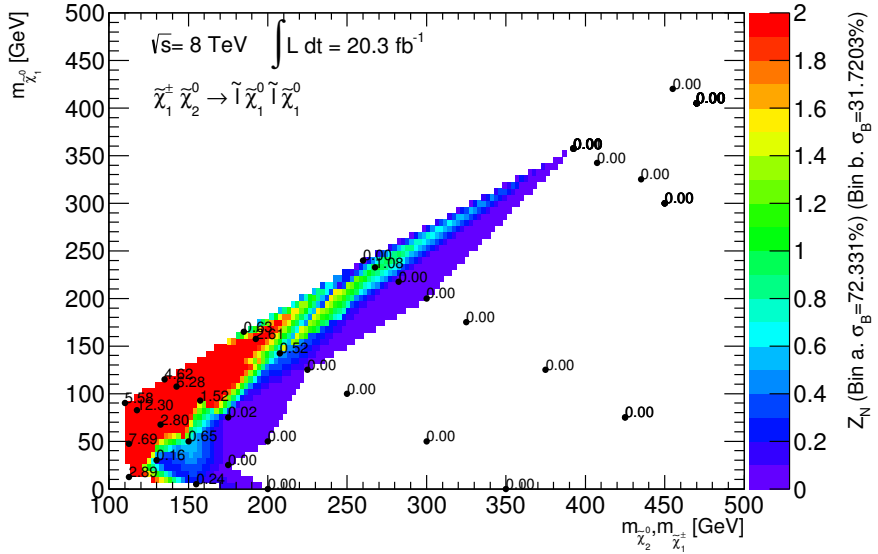


Figure 6.22: Combined expected significance for $\tilde{\chi}_1^\pm \tilde{\chi}_2^0$ production via \tilde{t} in SR3 ℓ -0a and SR3 ℓ -0b. The overall values for the total systematic uncertainty are shown on the z-axis for each bin in SR3 ℓ -0 (Produced by another analyser, taken from [136]).

6.4.5.2 $\tilde{\chi}_1^\pm \tilde{\chi}_2^0$ via WZ

The significance Z_N was calculated for the $\tilde{\chi}_1^\pm \tilde{\chi}_2^0$ decay via intermediate SM gauge bosons simplified model in the soft lepton and ISR signal regions. Starting with the ISR signal regions, for the MC-based only estimate $\tilde{\chi}_1^\pm / \tilde{\chi}_2^0$ masses can be excluded up to 150 GeV in the compressed region with $m_{\tilde{\chi}_1^0}$ of 125 GeV. For the MC and data driven matrix method estimate only one point in the compressed region is excluded with $\tilde{\chi}_1^\pm / \tilde{\chi}_2^0$ masses up to 100 GeV and a $\tilde{\chi}_1^0$ mass of 75 GeV. For the soft lepton regions, considering the MC-based only estimate $\tilde{\chi}_1^\pm / \tilde{\chi}_2^0$ masses can be excluded up to 100 GeV with a $\tilde{\chi}_1^0$ mass of 75 GeV. Considering the MC and data driven matrix method estimate no points in the compressed region are excluded. No significant improvement to the compressed region is observed for this simplified model, primarily due to the lower production cross sections compared to the via $\tilde{\ell}_L$ model.

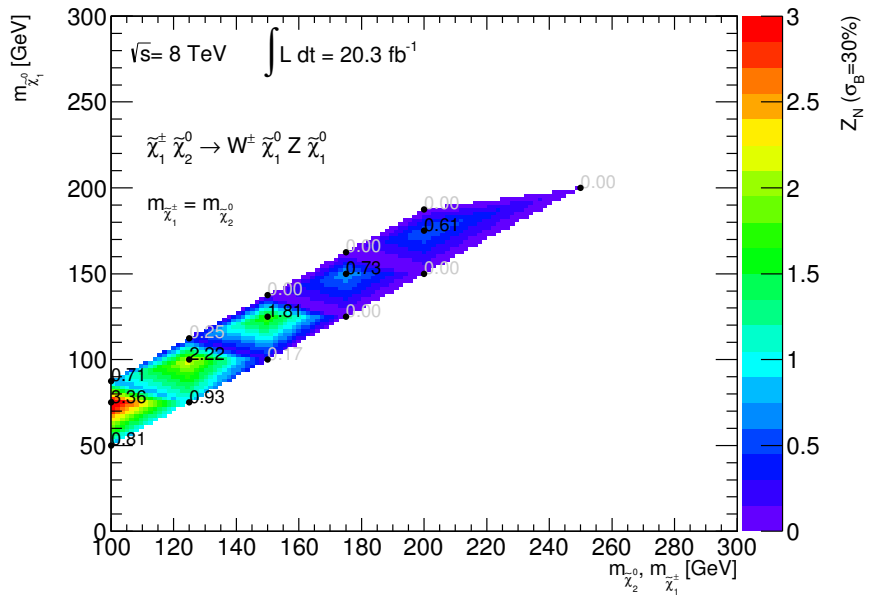


Figure 6.23: Combined expected significance for $\tilde{\chi}_1^\pm \tilde{\chi}_2^0$ production via WZ in SR3 ℓ -1a and SR3 ℓ -1b. The overall values for the total systematic uncertainty are shown on the z-axis for each bin in SR3 ℓ -1.

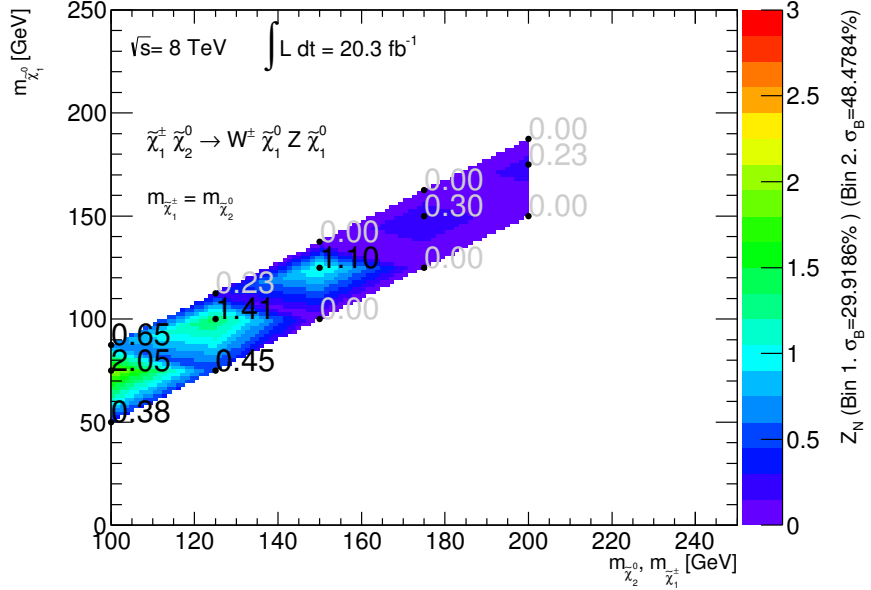


Figure 6.24: Combined expected significance for $\tilde{\chi}_1^\pm \tilde{\chi}_2^0$ production via WZ in SR3 ℓ -1a and SR3 ℓ -1b. The overall values for the total systematic uncertainty are shown on the z-axis for each bin in SR3 ℓ -1.

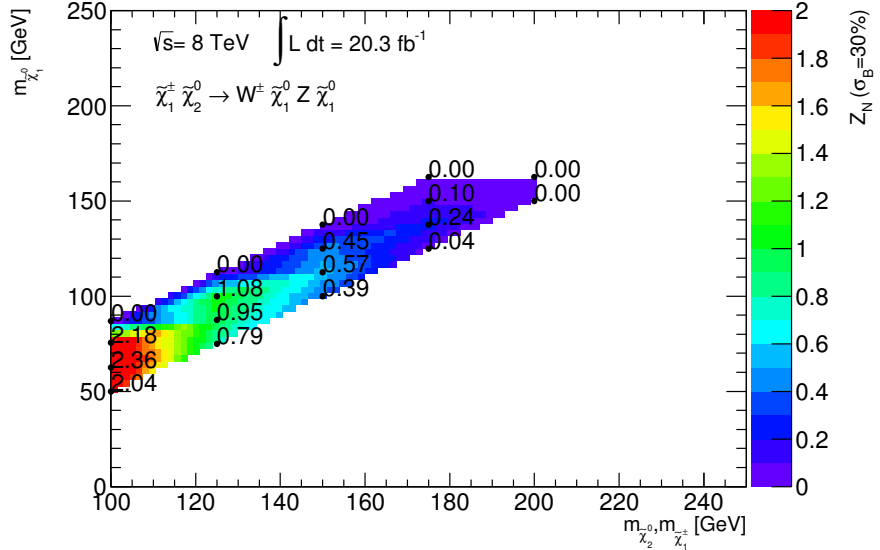


Figure 6.25: Combined expected significance for $\tilde{\chi}_1^\pm \tilde{\chi}_2^0$ production via WZ in SR3 ℓ -0a and SR3 ℓ -0b. The overall values for the total systematic uncertainty are shown on the z-axis for each bin in SR3 ℓ -0 (Produced by another analyser, taken from [136]).

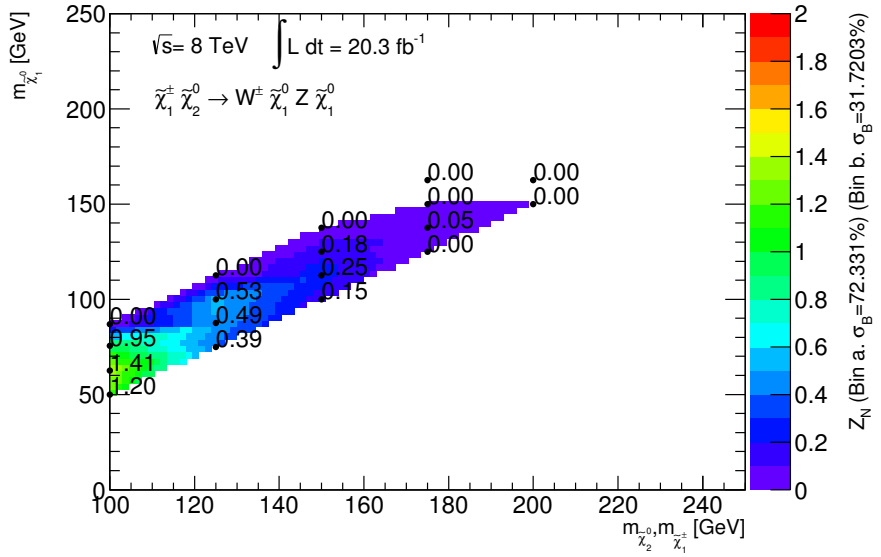


Figure 6.26: Combined expected significance for $\tilde{\chi}_1^\pm \tilde{\chi}_2^0$ production via WZ in SR3 ℓ -0a and SR3 ℓ -0b. The overall values for the total systematic uncertainty are shown on the z-axis for each bin in SR3 ℓ -0 (Produced by another analyser, taken from [136]).

6.5 Standard Model Background Estimation

6.5.1 Standard Model Background Model Overview

There are SM processes that can mimic the SUSY signature of three leptons and missing transverse momentum. These processes are classified into *irreducible backgrounds*, i.e. processes leading to events with three real leptons and *reducible backgrounds*, i.e. processes leading to events with at least one fake lepton. Here real lepton refers to a prompt - meaning originating from a primary vertex - genuinely isolated lepton and a fake lepton is a non-prompt or non-isolated lepton. The fake lepton object can arise from several sources:

- Mis-identification of light flavour jets
- Real but non-prompt leptons originating from semi-leptonic decays of heavy flavour decays (b - and c -quarks)
- Real electrons produced from Bremsstrahlung photon conversions

In addition to the identification of real, prompt leptons, there are processes that can mimic the E_T^{miss} signature due to mis-measurement of the momentum of a lepton or jet. This results in a large imbalance of momentum in the calculation for E_T^{miss} as shown in Equation 4.6.

The event selection outlined in Section 6.3.2 and Table 6.2 reduce the contributions from these background processes effectively, but not completely. Therefore the backgrounds need to be understood and estimated as accurately as possible in order to determine the compatibility of the observed data results with SM predictions. In order to construct an accurate and precise background estimate, a dedicated approach is assigned to each category of background. The list below provides an overview of all source of backgrounds considered in this analysis:

- Irreducible background:
 - 3 real leptons: WZ/γ^* , ZZ/γ^* , $t\bar{t} + Z/W/WW$, where the gauge boson can be off-shell;
- Reducible background:
 - 2 real and 1 fake lepton: $t\bar{t}$, single top (Wt), WW , Z/γ^* , accompanied by a heavy flavour jet, or a light flavour jet or a conversion
 - 1 real lepton and 2 fake leptons: single top, W accompanied by two fake leptons (from heavy flavour, light flavour, conversion)

There are some background processes estimated using MC predictions, which are then used for background composition studies and for comparing with results obtained with the data driven method. For example, the measurement of the weighted average efficiencies for the matrix method (Section 6.5.3) uses MC samples to model the fake lepton backgrounds.

6.5.2 MC Background Estimation

MC background estimation is vital for this analysis and is used in three distinct ways. First, they are primarily used to estimate the background processes that give three prompt leptons in the final state. Second, they are used in the matrix method to extract the efficiencies of real and fake leptons. Finally, they are used in the simulation-based optimisation of signal regions as discussed in Section 6.4. Therefore it is important that the samples used are well understood and describe ATLAS data as accurately as possible.

There are discrepancies that arise in the simulation of ATLAS data. Some are due to the lack of knowledge regarding the exact run conditions when the samples were simulated, for example the amount of pileup. Others discrepancies are corrected using data due to imperfect ATLAS detector simulation, for example reconstruction efficiencies. Corrections for these effects are derived from data-driven measurements and applied to the MC samples to improve their modelling of the data. The corrections applied to the MC is detailed below:

- Pileup is simulated by overlaying soft QCD interactions over SM events. The distribution in the number of pile up interactions in the MC is not an exact match to that found in data. This distribution in the MC is fixed before all the data is collected, consequently, reweighting is applied to the MC events to ensure the distributions are the same.
- Scale factors are applied to account for differences in electron reconstruction and identification efficiencies between MC and data. The scale factors are measured by the ATLAS Egamma performance group in $Z \rightarrow ee$ events with a tag-and-probe method and applied to events with electrons to correct the MC event weight as detailed in [86].
- Scale factors are applied to account for the differences in muon reconstruction efficiency between MC and data. The scale factors are provided by the ATLAS Muon performance group, which are measured in $Z \rightarrow \mu\mu$ and $J/\psi \rightarrow \mu\mu$ events as detailed in [88]. The scale factors are then applied to events with muons to correct the MC event weight.
- The muon p_T resolution is not in complete agreement between MC and data, therefore smearing is applied to the muon p_T in the MC events is done to give a closer agreement.
- Tau scale factors are applied to the MC to correct for the tau identification efficiency. These are provided by the ATLAS Tau performance group.
- Scale factors for b -tagging algorithms described in Sections 4.4.7 are used to correct for the b -tagging efficiency differences between MC and data. These scale factors take into account both the efficiency to tag b -jets as well as the mis-tag efficiency for non- b -jets.

6.5.3 Data Driven Background Estimation: The Matrix Method

The matrix method is a technique used for estimating the fake lepton background by exploiting the object characteristics between real and fake leptons on a statistical basis. Leptons are classified as “loose” (L) or “tight” (T) leptons according to the isolation and object reconstruction quality requirements. In this analysis, loose leptons are baseline leptons and tight leptons are signal leptons, as defined in Chapter 4. The principle of this method is that the number of events with varying L or T lepton composition can be expressed as a linear combination of the number of events with real and fake leptons in a given region. In the three-lepton final state, an 8×8 matrix is built to account for all

possible combinations of real and fake leptons. For processes that produce fake leptons in a three-lepton selection, the highest- p_T lepton will be real for the majority of the time ($> 95\%$ events) [132]. This is due to the fact that light lepton fakes tend to have a softer p_T spectrum than their real lepton counterparts. This is accounted for by ignoring the leading light lepton in the three-lepton matrix method. This simplifies the matrix from 8×8 to 4×4 , which can be rewritten in terms of the remaining sub-leading leptons (e/μ).

$$\begin{pmatrix} N_{TT} \\ N_{TL'} \\ N_{L'T} \\ N_{L'L'} \end{pmatrix} = \begin{pmatrix} \epsilon_1 \epsilon_2 & \epsilon f_2 & f_1 \epsilon_2 & f_1 f_2 \\ \epsilon_1 (1 - \epsilon_2) & \epsilon_1 (1 - f_2) & f_1 (1 - \epsilon_2) & f_1 (1 - f_2) \\ (1 - \epsilon_1) \epsilon_2 & (1 - \epsilon_1) f_2 & (1 - f_1) \epsilon_2 & (1 - f_1) f_2 \\ (1 - \epsilon_1) (1 - \epsilon_2) & (1 - \epsilon_1) (1 - f_2) & (1 - f_1) (1 - \epsilon_2) & (1 - f_1) (1 - f_2) \end{pmatrix} \cdot \begin{pmatrix} N_{RR} \\ N_{RF} \\ N_{FR} \\ N_{FF} \end{pmatrix}, \quad (6.3)$$

where:

- ϵ is the probability that a real-loose lepton is identified as a tight lepton referred to as “real efficiencies”;
- f is the probability that a fake-loose lepton is misidentified as a tight lepton, referred to as “fake rates” or “fake efficiencies”;
- N_{RR} is the number of events with two real leptons, $N_{RF} + N_{FR}$ is the number of events with one real and one fake lepton, and N_{FF} is the number of events with two fake leptons;
- N_{TT} , $N_{TL'}$, $N_{L'T}$ and $N_{L'L'}$ denote the number of events with two leptons with the first (second) index corresponding to the higher (lower) p_T lepton. Given that the leading lepton is always a real lepton, the matrix method only considers the other two leptons. L' indicates loose leptons that fail the tight requirement.

If the efficiencies (ϵ and f) are known, the matrix can be inverted to obtain the real composition (N_{RR}) and fake composition (N_{FF}) of loose leptons. The total number of events with fake-loose leptons is then given by:

$$\begin{aligned} N_{RF} + N_{FR} + N_{FF} = & \frac{1}{(\epsilon_1 - f_1)(\epsilon_2 - f_2)} [(\epsilon_1 \epsilon_2 - \epsilon_1 f_2 - f_1 \epsilon_2 + f_1 + f_2 - 1)N_{TT} \\ & + (\epsilon_1 \epsilon_2 - \epsilon_1 f_2 - f_1 \epsilon_2 + f_2)N_{TL'} \\ & + (\epsilon_1 \epsilon_2 - \epsilon_1 f_2 - f_1 \epsilon_2 + f_1)N_{LT} + (\epsilon_1 \epsilon_2 - \epsilon_1 f_2 - f_1 \epsilon_2)N_{LL}]. \end{aligned} \quad (6.4)$$

Since the analysis uses signal selection leptons (tight leptons), an extra step to extrapolate $LL \rightarrow TT$ is needed to estimate the fake-tight leptons selection:

$$\begin{aligned}
N_{Fake}^{LL \rightarrow TT} &= N_{RF}^{LL \rightarrow TT} + N_{FR}^{LL \rightarrow TT} + N_{FF}^{LL \rightarrow TT} \\
&= \epsilon_1 f_2 \times N_{RF} + f_1 \epsilon_2 \times N_{FR} + f_1 f_2 \times N_{FF}
\end{aligned} \tag{6.5}$$

with

$$\begin{aligned}
N_{RR}^{LL \rightarrow TT} &= \epsilon_1 \epsilon_2 \times N_{RR} \\
N_{RF}^{LL \rightarrow TT} &= \epsilon_1 f_2 \times N_{RF} \\
N_{FR}^{LL \rightarrow TT} &= f_1 \epsilon_2 \times N_{FR} \\
N_{FF}^{LL \rightarrow TT} &= f_1 f_2 \times N_{FF}.
\end{aligned} \tag{6.6}$$

The real lepton efficiencies and fake rates are measured in each SR and VR using MC and corrected to those measured in data using “scale factors”. These are measured for each lepton flavour as detailed below.

6.5.3.1 Weighted Average Fake Rates

Measuring the fake rates with the matrix method presents several challenges. The fake rate for a given lepton $\ell = \mu, e$ (labelled f in Equation 6.3) depends on the fake candidate (heavy flavour, light flavour and conversion) and on the originating process. For example, the fake rate of leptons from heavy flavour jets in top decays is smaller than the rate from heavy flavour jets from WZ production due to the harder b -quark spectrum in top decays. Consequently, the fake rates measured in a dedicated control region in data will not be directly applicable to another region where the fake type composition and originating processes are significantly different. In this analysis, the approach is to obtain the fake rate of each type from all MC simulated samples - properly weighted for luminosity - the rates are then corrected with type-dependent scale factors to account for the possible differences between data and simulation.

A weighted average fake rate to be used in the region $XR = SR, CR$ (where SR and CR stand for generic signal/control region) is therefore defined as:

$$f_{XR}^\ell = \sum_{i,j} (sf^i \times R_{XR}^{ij} \times f^{ij}), \tag{6.7}$$

where i indicates the fake type: light flavour (LF), heavy flavour (HF), or conversion

(CO); j indicates the process category the fake originates: Top (T) or Gauge Boson (V); the dependence on p_T and $|\eta|$ for electrons and on p_T for muons is implied for all terms as described below:

Scale Factor sf^i is the fake rate scale factor for the type i ; it is assumed to be independent of the process category j and of the region XR. No significant dependences on p_T and η are observed.

Fake Fraction R_{XR}^{ij} is the fraction of fake type i originating from process category j in the region XR; it is measured as the ratio of fake candidates of type i originating from the process category j with respect to the total number of all fake candidates from all processes. The fractions are obtained in each region XR summing over all relevant MC simulated samples properly weighted for their luminosity.

Fake Rate f^{ij} is the fake rate for the type i originating from the process category j ; it is measured as the ratio of the number of signal leptons over the number of baseline leptons for a given type and a given process. To be consistent with the matrix method, the rates are measured on the next-to-leading and next-to-next-to-leading leptons in events where the leading lepton is tight. Furthermore, the events must pass the quality cuts and the trigger requirements. The fake rates are parameterised in p_T for muons and p_T and η for electrons. A systematic uncertainty is assigned to cover for potential dependence on E_T^{miss} .

6.5.3.2 Fake Rates

The fake rates and fake fractions are measured in the three-lepton inclusive region with the truth information of all expected background MC samples. The fake origin fraction is measured in each region with the baseline leptons.

6.5.3.3 Scale Factors

The MC-based estimated fake rates require validation with data. To do this, control regions are defined to validate the MC truth fake rates and extract a data-MC scale factor for each fake type. Each control region is designed to enhance the purity of the respective fake sources: real efficiency (RE), conversion (CO), heavy flavour (HF) and light flavour (LF). Due to the difficulty in defining a region which has good enough purity for light flavour fakes with three-lepton events, the light flavour fakes scale factor is assumed to be

1.00 ± 0.10 . The scale factor measurements are outlined in the following paragraphs for the remaining fake types.

Real Lepton Identification Efficiency The measurement is carried out using the tag-and-probe method with $Z \rightarrow ee$ events (as outlined in Section 5.2.1). The tag-and-probe selection is applied as follows:

- exactly two SFOS leptons, passing the baseline selection
- at least one lepton should pass the trigger strategy outlined in Table 6.1 and the signal lepton object selection requirements
- $m_{\ell\ell}$ should be within 10 GeV of the on-shell Z-boson mass of 91.2 GeV

These cuts are chosen to target events with electrons originating from on-shell Z-boson decays, which are “standard candle” events used in the tag-and-probe selection.

There was no significant dependence on p_T , η and the number of vertices observed for the real lepton efficiency scale factor, therefore the final result is obtained without binning:

$$SF_e^{RE} = 1.00 \pm 0.01, SF_\mu^{RE} = 0.99 \pm 0.01.$$

Fake Rate Scale Factor for Electrons from Conversions The conversion fakes consist of misidentified leptons from photon radiation, which are mostly real leptons. For muons, this fake lepton contribution is negligible. Therefore, electrons are the sole focus for this measurement. The conversion control region is set to enhance the $Z/\gamma^* \rightarrow \mu\mu$ process with one radiated photon from one of the muons, as follows:

- an inclusive OR of the single & dimuon triggers, with at least one signal muon matching a trigger object and above the appropriate p_T threshold in data;
- exactly two opposite sign signal muons with $m_{\mu\mu} > 40$ GeV, to ensure the muons have sizeable p_T for straight-forward identification;
- exactly one baseline electron, which is selected as the probe;
- The invariant mass of the three leptons in the event composed of μ, μ and e must lie within 10 GeV of the on-shell Z mass, 91.2 GeV, such that the $\mu\mu e$ invariant mass is consistent with a Z boson.
- b -jet veto (MV1 @ 70% rejecting $t\bar{t}$)
- $E_T^{miss} < 40$ GeV (rejecting WZ)

There is no significant dependence on p_T , $|\eta|$ or number of good vertices observed, therefore the scale factor obtained without binning: $SF_e^{CO} = 1.41 \pm 0.06$.

This SF is particularly larger than the other scale factors due to underestimation of

the rate of electrons from conversions in MC at p_T values above 50 GeV.

Fake Rate Scale Factor for Leptons from Heavy Flavour If a b -quark decays leptonically and the resulting lepton is identified as a signal lepton, then heavy flavour jets can pass into the final selection as a fake contribution. The corresponding fake rate is measured in control regions enhanced for the $b\bar{b}$ or $c\bar{c}$ processes using a tag-and-probe method with a $b\bar{b}$ and $c\bar{c}$ selection. A requirement of $p_T > 20$ GeV is applied to all jets in all regions. The heavy flavour (HF) control region is defined as follows:

- satisfy the standard event quality criteria;
- contain exactly two baseline leptons;
- the event contains exactly one b -jet
- a tagged muon must have a $p_T > 20$ GeV being the one that fired the EF_mu18_tight leg of the EF_mu18_tight_mu8_EFFS trigger;
- the tagged muon is overlapped with a b -tagged jet within $\Delta R < 0.4$
- the probe lepton is separated from any jets by $\Delta R > 0.4$
- $E_T^{\text{miss}} < 60$ GeV to suppress the background to non heavy flavour leptons.
- The probe lepton $m_T < 50$ GeV to suppress W events

Despite the fact that tight selections are used, other backgrounds sources prove difficult to suppress due to the low lepton p_T requirement of this analysis. Therefore, all non-HF (i.e. light flavour, conversion, real) sources are subtracted from the data and MC fake rate estimates using the MC-truth information in this control region. With no scale factor dependency on the parameters, p_T , $|\eta|$ and number of good vertices, the central value of the scale factor is calculated without binning from the p_T distributions. The scale factors for heavy flavour fake rates are found to be: $SF_e^{\text{HF}} = 0.876 \pm 0.085$; $SF_\mu^{\text{HF}} = 0.878 \pm 0.062$

6.6 Background Model Validation

6.6.1 Validation Regions

To validate the background modelling, the MC estimates for irreducible backgrounds and the data-driven estimates for the reducible backgrounds estimated in VRs are compared to the observed data. Low- E_T^{miss} validation regions (“a” regions) are defined that are WZ , Z , J/ψ , and/or Υ rich, and high- E_T^{miss} + b -jet validation regions (“b” region) that are $t\bar{t}$ rich. The “a” regions remain orthogonal to the SRs by requesting $E_T^{\text{miss}} < 30$ or $E_T^{\text{miss}} < 50$ and the “b” regions remain orthogonal by requesting exactly one b -jet.

Two sets of validation regions are defined to validate the background modelling with or without the presence of an ISR jet. VR3 ℓ -0 vetoes the ISR jet and VR3 ℓ -1 requests the ISR jet. The explicit definitions are given in Table 6.3. The observed data counts and SM expectations are in good agreement within statistical and systematic uncertainties as shown in Table 6.4 and Figures 6.27 and 6.28. This indicates that the reducible background is well described by the matrix method and the irreducible background is well described by the MC. The following sections show the most interesting kinematic distributions relevant to each validation region.

Table 6.3: The selection requirements for the three-lepton validation regions.

Common				
ℓ flavor/sign	$\ell^\pm \ell^\mp \ell, \ell^\pm \ell^\mp \ell'$			
$m_{\text{SFOS}}^{\text{min}}$	> 4 GeV			
m_{SFOS}	veto 8.4–10.4 GeV			
SR	VR3 ℓ -0a	VR3 ℓ -0b	VR3 ℓ -1a	VR3 ℓ -1b
Central jets	no jets $p_T > 50$ GeV		≥ 1 jet $p_T > 50$ GeV	
$N_{b-\text{jets}}$	0	1	0	1
E_T^{miss}	< 30 GeV	> 30 GeV	< 50 GeV	> 50 GeV
Z boson	veto	–	veto	veto
$p_T^{\text{lep} 1}$	< 30 GeV	–	–	–
Target Process				
Irreducible	WZ	WZ	WZ	WZ
Reducible	$Z+\text{jets}, \Upsilon$	$t\bar{t}$	$Z+\text{jets}$	$t\bar{t}$

Table 6.4: Estimated and observed yields in the three-lepton validation regions. The uncertainties shown include both statistical and systematic components. The “Others” background category includes $t\bar{t}V$, VVV and SM Higgs boson production.

	VR3 ℓ -0a	VR3 ℓ -0b	VR3 ℓ -1a	VR3 ℓ -1b
WZ	108 ± 20	35 ± 7	36 ± 7	$9.7^{+2.0}_{-2.2}$
ZZ	63 ± 11	5.9 ± 1.3	5.2 ± 1.1	$0.33^{+0.08}_{-0.07}$
Reducible	990^{+300}_{-270}	159^{+40}_{-35}	56 ± 16	102^{+23}_{-19}
Others	1.0 ± 0.8	4.8 ± 1.7	1.5 ± 0.6	$9.9^{+3.4}_{-3.5}$
Total SM	1160^{+300}_{-280}	200 ± 40	99 ± 17	122^{+24}_{-20}
Data	1247	212	95	93

6.6.1.1 VR3 ℓ -1 Regions

Six kinematic distributions in validation region VR3 ℓ -1a with three light leptons and at least one ISR jet are shown in Figure 6.27: lepton 1,2,3 p_T (with index indicating p_T order from highest to lowest), $m_{\text{SFOS}}^{\text{min}}$, leading jet p_T and $\Delta\phi(E_T^{\text{miss}}, 3\ell)$. These variables are used

to define the ISR signal regions therefore must be correctly modelled. Two benchmark signal points are used with $\Delta m_{\tilde{\chi}_1^\pm - \tilde{\chi}_1^0} = 12.5$ and 25 GeV. The shapes of the distributions are seen to agree well with data. Six kinematic distributions in validation region VR3 ℓ -1b with three light leptons and at least one ISR jet are shown in Figure 6.28: lepton^{1,2,3} p_T , E_T^{miss} , m_T , $M_{\ell\ell\ell}$ and leading jet p_T . These variables are used to define the ISR signal regions therefore must be correctly modelled. Two benchmark signal points are used with $\Delta m_{\tilde{\chi}_1^\pm - \tilde{\chi}_1^0} = 12.5$ and 25 GeV. The shapes of the distributions are seen to agree well with data.

6.6.1.2 VR3 ℓ -0 Regions

Four kinematic distributions in validation region VR3 ℓ -0a with three light leptons and an ISR jet veto are shown in Figures 6.29: $m_{\text{SFOS}}^{\text{min}}$, $m_{\ell\ell\ell}$, m_T and jet multiplicity. These variables are used to define the soft lepton signal regions therefore must be correctly modelled. One benchmark signal points is used with $\Delta m_{\tilde{\chi}_1^\pm - \tilde{\chi}_1^0} = 25$ GeV. The shapes of the distributions are seen to agree well with data. Five kinematic distributions in validation region VR3 ℓ -0a with three light leptons and an ISR jet veto are shown in Figures 6.29: lepton^{1,2,3} p_T , E_T^{miss} , m_T and jet multiplicity. These variables are used to define the soft lepton signal regions therefore must be correctly modelled. One benchmark signal points is used with $\Delta m_{\tilde{\chi}_1^\pm - \tilde{\chi}_1^0} = 25$ GeV. The shapes of the distributions are seen to agree well with data.

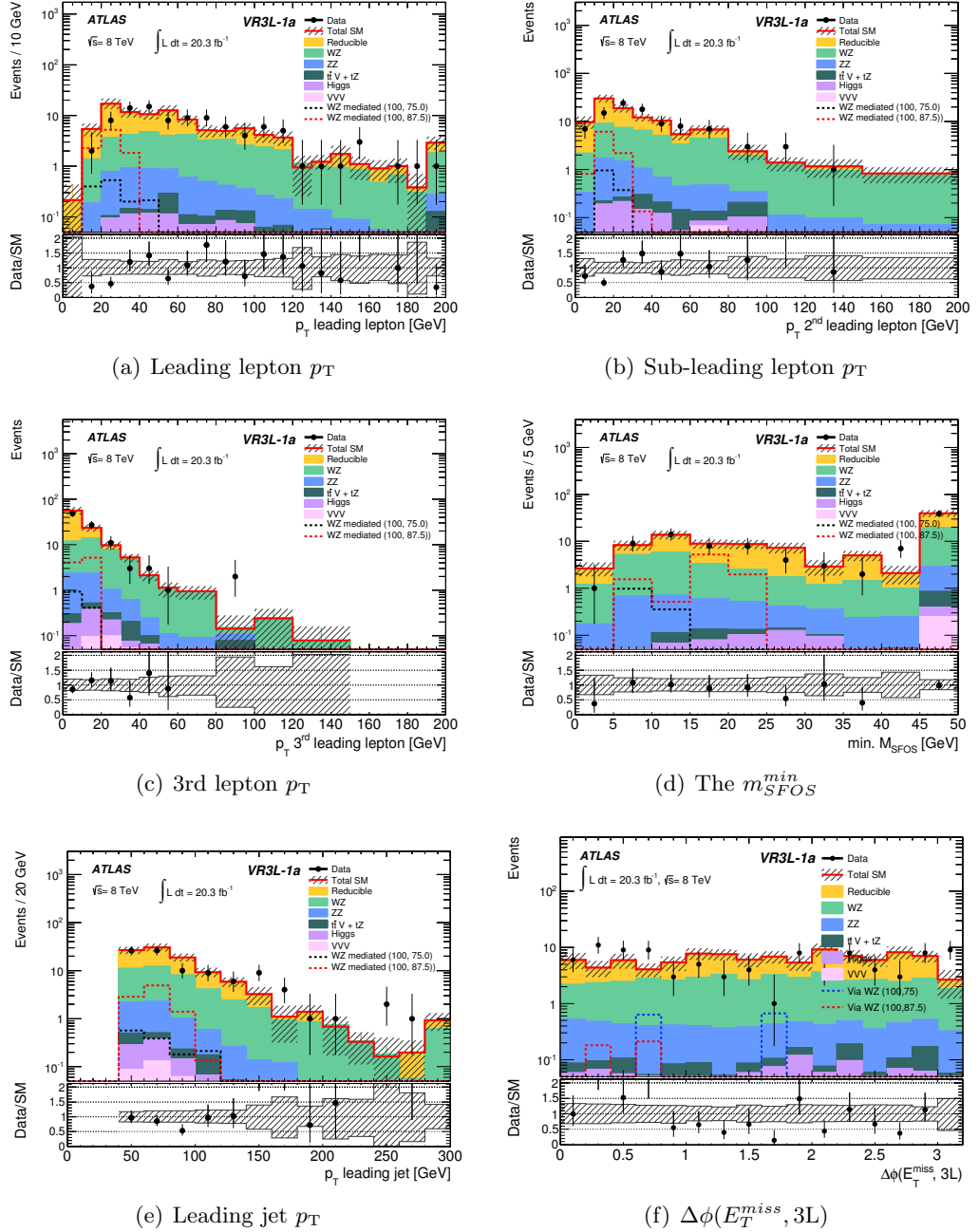


Figure 6.27: Kinematic distributions in VR3L-1a. The uncertainties are statistical and systematic.

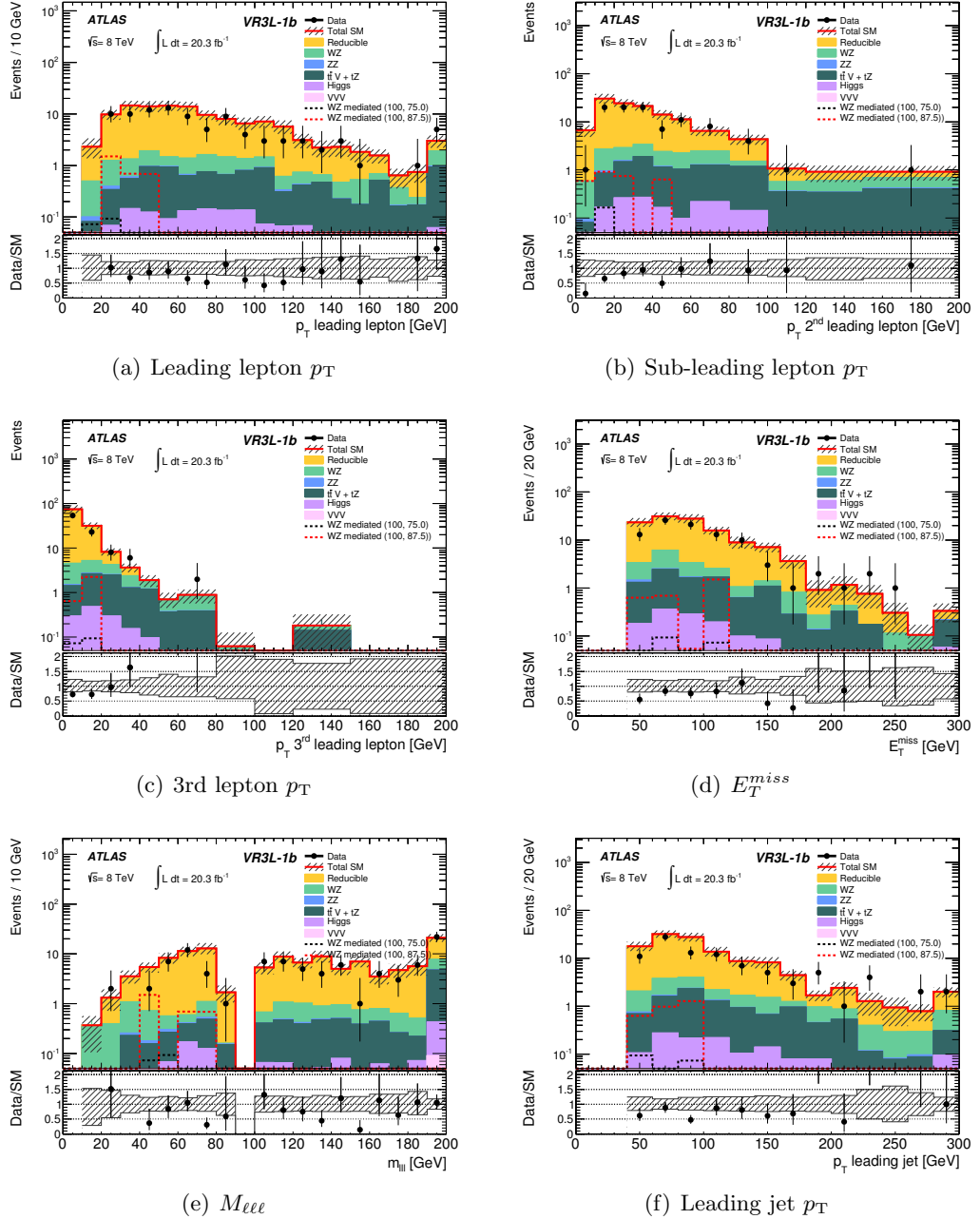


Figure 6.28: Kinematic distributions in VR3 ℓ -1b. The uncertainties are statistical and systematic.

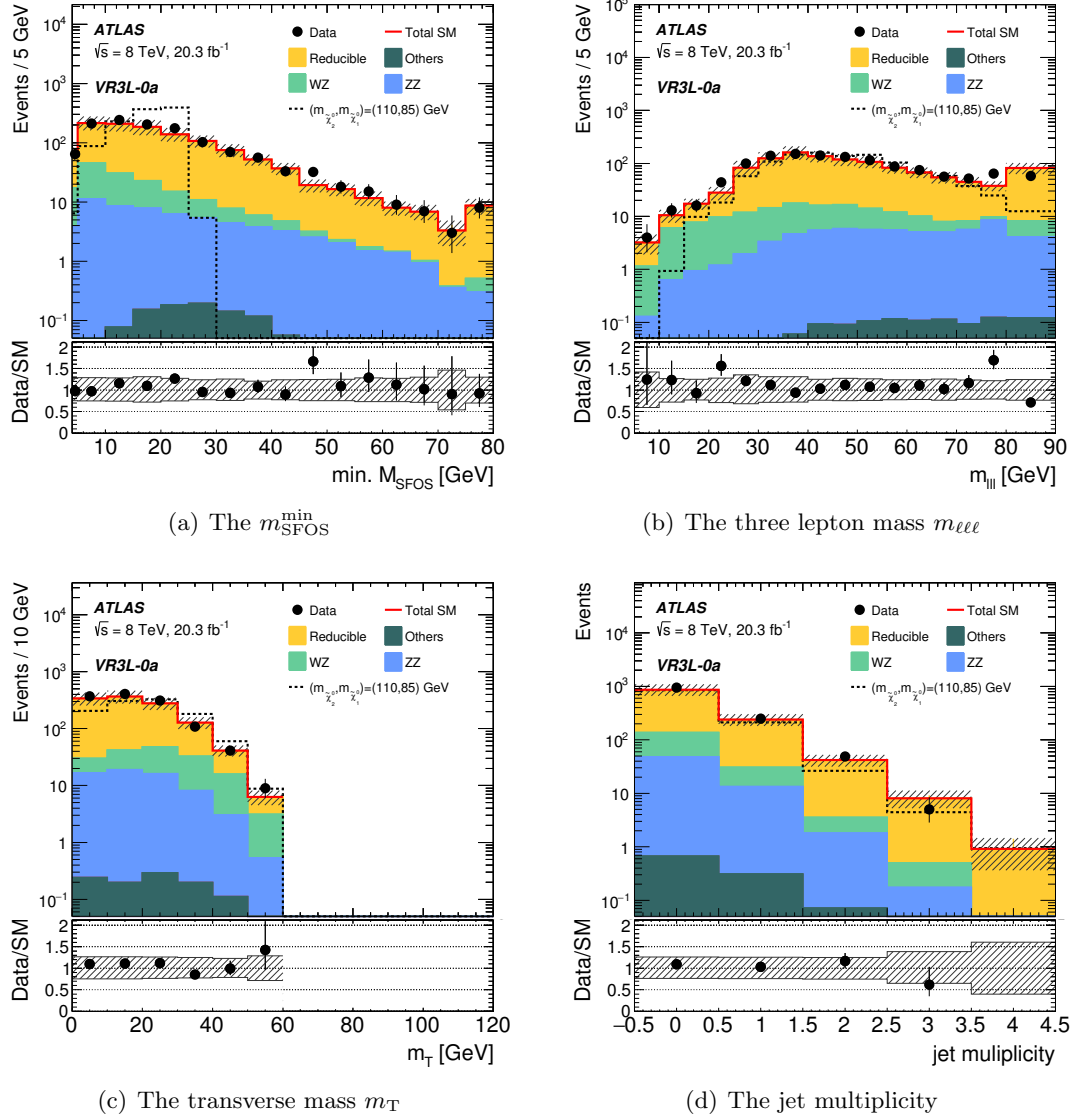


Figure 6.29: Kinematic distributions in VR3 ℓ -0a (Produced by another analyser, taken from [136]).

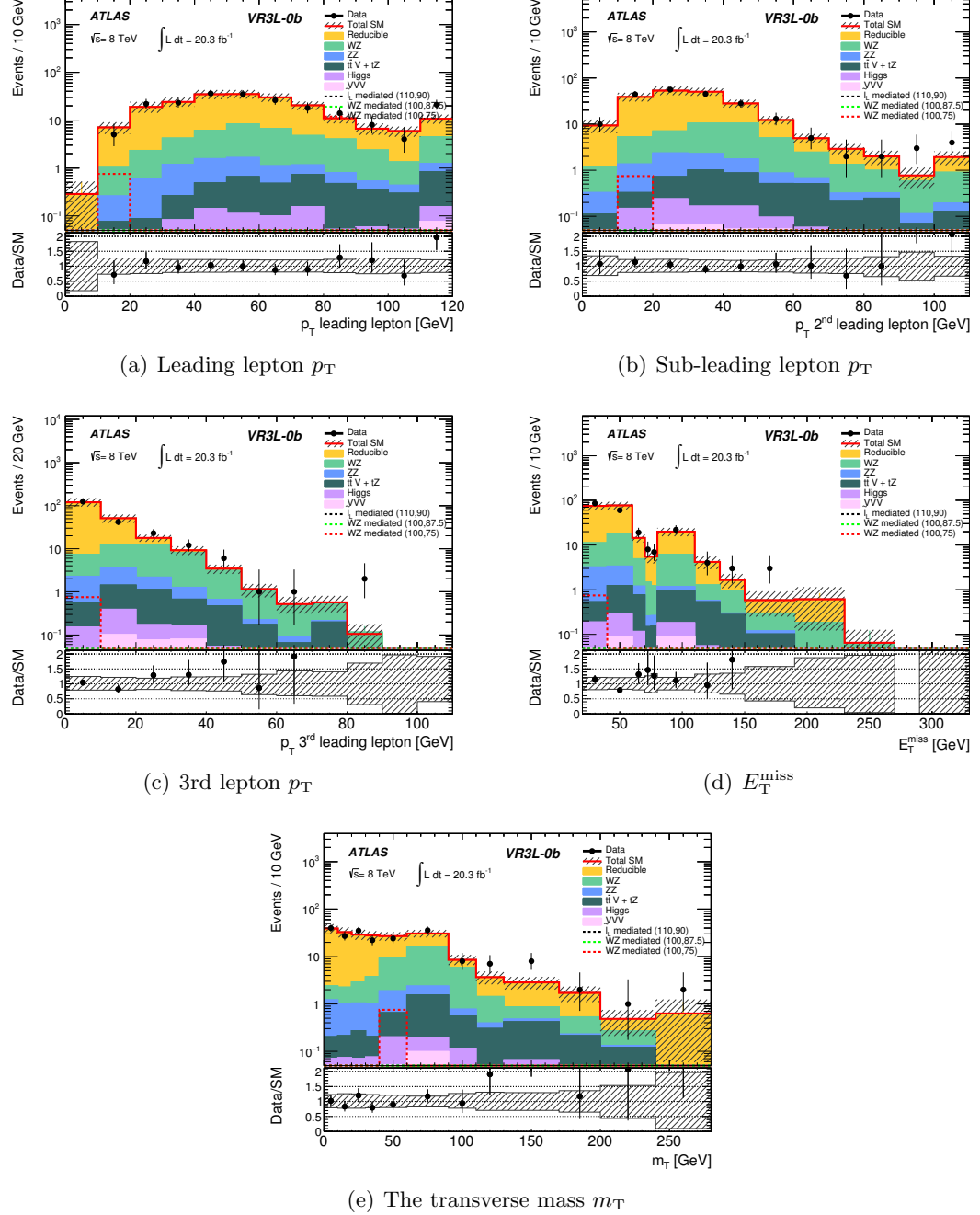


Figure 6.30: Kinematic distributions in VR3L-0b (Produced by another analyser, taken from [136]).

6.7 Systematic Uncertainties

Several sources of uncertainty arise in the analysis, due to the MC background estimate and data driven fake estimate.

6.7.1 MC Statistics

Since MC statistics is limited, it is a source of systematic uncertainty. This uncertainty is one of the dominating uncertainties for the signal regions as they have stringent cuts that limit the MC events to the order of 5 events. It is treated as uncorrelated between regions and MC samples.

6.7.2 MC Cross Section

Each cross section for a given background process has an uncertainty provided centrally by ATLAS, together with the generated MC samples. These are estimated by varying the renormalisation and factorisation scales. The cross-section uncertainties for the irreducible backgrounds used are 30% for $t\bar{t}+Z/W/WW$ [137] [113], 50% for tZ , 5% for ZZ [138], 7% for WZ [138]: these are recommended by ATLAS and found by comparing the results of calculations with the MCFM and MC@NLO generators and MSTW and CTEQ PDF sets. The uncertainty for triboson production is set to 100%. For the Higgs boson samples, a 20% uncertainty is used for VH and vector boson fusion (VBF) production [121], while a 100% uncertainty is assigned to $t\bar{t}H$ and Higgs boson production via gluon fusion [121].

6.7.3 PDF

The PDF uncertainties for the SHERPA WZ and ZZ samples were calculated using the PDF4LHC recommendations [139] [140] on the full eigenset of the PDF set CT10 [141]. The PDF set was provided by the CTEQ collaboration. The CTEQ PDF set is based on 26 free parameters and the resulting 90% confidence level upper and lower variations in these parameters form the “error set” for the PDF. The asymmetric positive and negative uncertainties of the PDFs (f_i) are computed as

$$\sigma_+[f] = \frac{1}{C_{90}} \sqrt{\sum_{i=1}^{26} (\max[(f_i^+ - f_0), (f_i^- - f_0), 0])^2},$$

$$\sigma_-[f] = \frac{1}{C_{90}} \sqrt{\sum_{i=1}^{26} (\max[(f_0 - f_i^+), (f_0 - f_i^-), 0])^2}.$$

Where $C_{90} = 1.64485$ is a re-scaling factor to convert the 90% CL variations into 1σ variations and f_0 is the nominal eigenvector value. The impact of the PDF uncertainties on the acceptance was found to be negligible ($<3\%$).

6.7.4 MC Background Uncertainties

Backgrounds which produce three prompt leptons are modeled by MC simulation and as such are subject to statistical and systematic uncertainties. These uncertainties are detailed in the following.

6.7.5 Electrons

Two sources of uncertainty arise on the electron energy, the electron energy scale (EES) and the electron energy resolution (EER). EES is the uncertainty arising from any mis-calibration of the electron energy using MC. EER considers the resolution of the ECAL sub-detector. Both uncertainties are calculated using an E_T and η dependent function with $Z \rightarrow ee$ and $W \rightarrow e\nu$ events in data. $J/\Psi \rightarrow ee$ events are used to estimate these uncertainties for low- p_T electrons [84]. The resulting uncertainties are applied to both the electrons and their associated components in the E_T^{miss} calculation. The electron scale factor (ESF) accounts for uncertainty in reconstruction and identification efficiency of electrons. This scale factor is also E_T and η dependent and is calculated by the ATLAS electron working group using W and Z events.

6.7.6 Muons

The muon energy scale (MES) uncertainty is composed of energy scale uncertainties from the inner detector track, known as Muon Inner Detector (MID), and the muon spectrometer track, known as the Muon Muon Spectrometer (MMS). These are calculated using data events for $J/\Psi \rightarrow \mu\mu$, $Z \rightarrow \mu\mu$ and $\Upsilon \rightarrow \mu\mu$ compared to MC [88]. The resulting uncertainties are applied to both muons and their associated components in the E_T^{miss} calculation. The muon scale factor (MSF) accounts for the uncertainty in muon reconstruction and is calculated as a function of muon p_T [88].

6.7.7 Jets

The Jet Energy Scale (JES) uncertainty is estimated by using a combination of *in situ* techniques exploiting the transverse momentum balance between a jet and a reference object such as a photon or Z boson for $20 \leq p_T^{\text{jet}} < 1000$ GeV. The uncertainty is applied

to jets with $p_T > 15$ GeV and $|\eta| < 4.5$ and their corresponding E_T^{miss} components [142]. The jet energy resolution (JER) uncertainty is estimated by smearing the p_T of each jet to a Gaussian distribution with unit mean. The resolution is dependent on the jet p_T and η [143].

6.7.8 Missing Transverse Energy

The pileup-suppressed soft term in the $E_{x(y)}^{softjets}$ in Equation 4.6 has an associated uncertainty which can be estimated by adjusting the energy scale and the resolution, and using these adjustments to recalculate the total resulting E_T^{miss} . The uncertainty in the other contributions to the E_T^{miss} are accounted for by the uncertainties of the objects associated with them as detailed above.

6.7.9 B-tagging Efficiency

The b -tagging algorithm performance was evaluated by the ATLAS flavour-tagging performance group using light and heavy jet samples. The associated uncertainty on the real efficiency and mis-tag rates for the 2011 and 2012 algorithms (JetFitterCombNN and MV1) was then propagated as an overall scale factor.

6.7.10 Trigger

An uncertainty of 5% is applied to MC samples to cover differences in efficiency observed for the leptonic triggers between data and the MC trigger simulation.

6.7.11 Luminosity

An uncertainty of 2.8% is prescribed for the ATLAS 2012 dataset based on preliminary calibration of the luminosity scale using beam separation scans in 2012 [144].

6.7.12 Pile-up

The uncertainty due to the modelling of the pileup in the MC simulation samples is estimated by varying the distribution of the number of interaction per bunch crossing overlaid in the MC samples by $\pm 10\%$.

6.7.13 Signal

The systematic uncertainties on the SUSY signal processes include theoretical uncertainties on the calculated NLO cross sections. This includes cross-section predictions using different PDF sets and factorisation and renormalisation scales. These theoretical systematic uncertainties on all signal processes are evaluated by varying the factorisation and re-normalisation scales in PROSPINO and are calculated using the method described in [145]. For $\tilde{\chi}_1^\pm \tilde{\chi}_2^0$ signal simulations that are sensitive to ISR, the impact of the choice of renormalisation scales, factorisation scales, the scale for the first emission in the so-called MLM matching scale [146] are evaluated by varying these individually between 0.5 and 2 times the nominal values in MADGRAPH.

6.7.14 MC Generator Systematic Uncertainties

Typically to assess the modelling of the SM processes by MC, two generators would be compared in particular regions enriched in the processes being assessed. As a consequence of the analysis exploring compressed scenarios, the p_T thresholds on the leptons were lowered from 10 to 7 GeV for electrons and from 10 to 5 GeV for muon. Also, the m_{SFOS} threshold was lowered from 12 to 4 GeV, meaning only one generator, POWHEG, with the correct lepton p_T filters could be used for the simulation of the WZ and ZZ processes, which are the dominant irreducible backgrounds in all signal regions. In order to place an uncertainty on the modelling, the MC distributions were compared with the data in dedicated control regions, to assess the agreement. A conservative uncertainty of 20% was assumed, based on the differences between data and MC in the control regions. The control regions are defined to be enriched in the WZ and ZZ processes. The definitions are summarised in Sections 6.7.14.1 and 6.7.14.2.

6.7.14.1 WZ Control Region

The definition of the WZ control region requires exactly three light leptons. b -jets are vetoed to reduce contributions from $t\bar{t}$. There is an ISR request in order to make the control region signal like, as the dominant background in the signal regions is WZ , correct modelling of signal like WZ events is crucial. The p_T on all the leptons is greater than 30 GeV in order for the control region to remain orthogonal to the signal regions. The E_T^{miss} is greater than 30 GeV and less than 50 GeV to target the peak of the E_T^{miss} distribution, where better agreement is observed between data and MC. At least one possible pair of

leptons in the event must be SFOS as there should be a Z boson decay in the event. In addition, a dilepton and trilepton Z veto, where the invariant mass of the system is outside of the 10 GeV window of the on shell Z boson mass. This cut is designed to target off-shell Z mass decays. The full list of definitions are shown in Table 6.5. Kinematic distributions in Figure 6.31 show the agreement between data and MC: jet multiplicity, E_T^{miss} , leading jet p_T , leading lepton p_T , m_T and the ratio between the leading lepton p_T and leading jet p_T . The data and MC is shown to agree within an uncertainty of 15%. The MC-based and MM estimates are shown in Table 6.6.

Variable	WZ Control Region Selection	ZZ Control Region Selection
ℓ flavour/sign	$\ell^\pm \ell^\mp \ell$	$\ell^\pm \ell^\mp \ell^\pm \ell^\mp$
b -jet	veto	veto
jets	≥ 1	-
$m_{\text{SFOS}}/m_{\ell\ell\ell}$	veto [81.2-101.2]	m_{SFOS} request [81.2-101.2]
E_T^{miss}	30 – 50	< 50 GeV
$p_T^{1^{st}l}$	> 30	> 10 GeV

Table 6.5: WZ and ZZ control region definition. Units are in GeV

6.7.14.2 ZZ Control Region

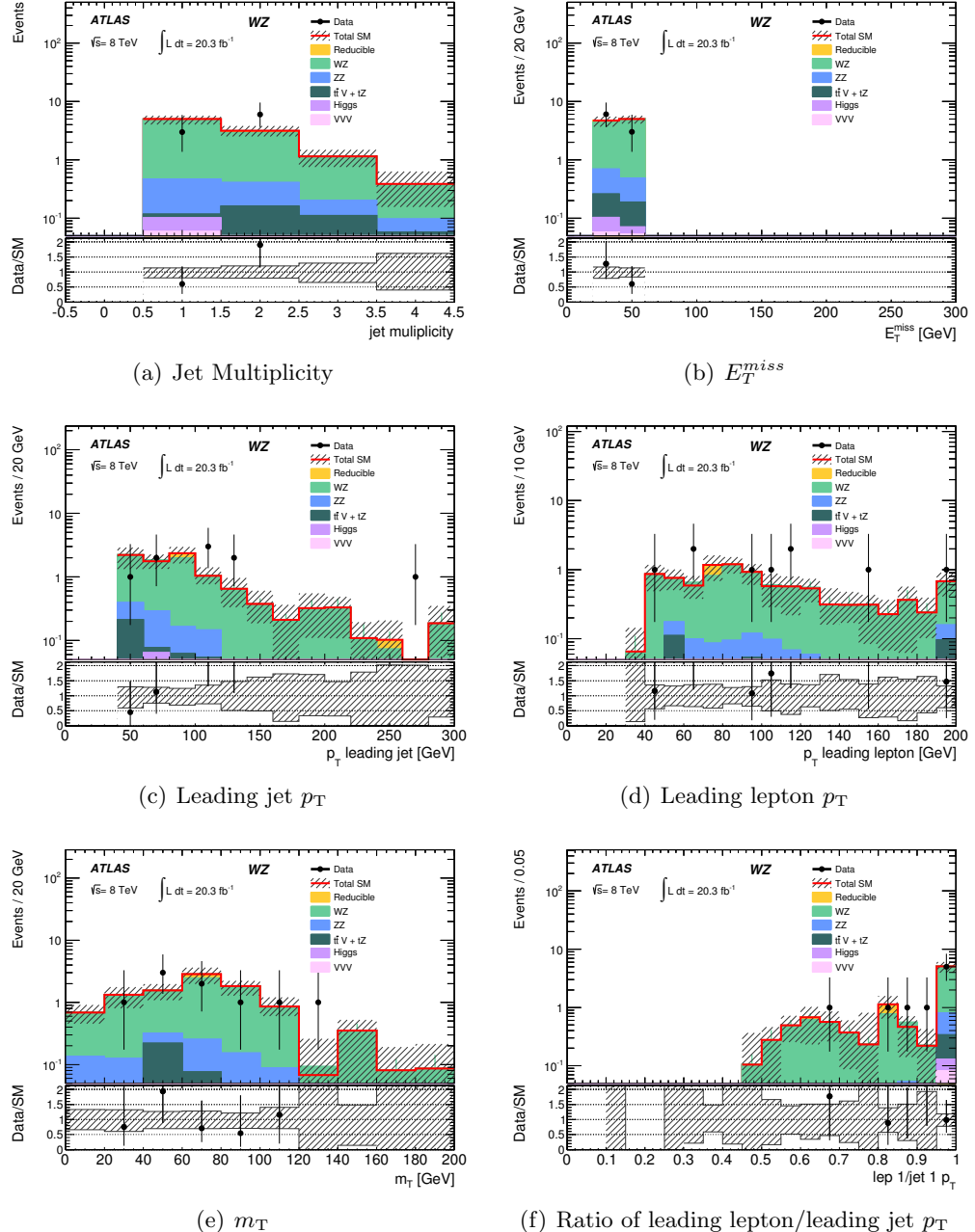
The definition of the ZZ control region requires exactly four leptons as both Z -bosons are expected to decay leptonically. The p_T of all leptons is greater than 10 GeV to remove low p_T contributions from $Z+jets$ processes. The E_T^{miss} is required to be less than 50 GeV as there is no expected E_T^{miss} from the Z -boson decays.. There is a request for two same flavour-opposite sign pairs, with both pairs having an invariant mass within 10 GeV of the on-shell Z -boson ($m_z = 91.2$ GeV), this is to target two on-shell Z -boson decays. The full list of definitions are shown in Table 6.5. Kinematic distributions in Figure 6.32 show the agreement between data and MC. Specifically these distributions are: jet multiplicity, E_T^{miss} , leading jet p_T , leading lepton p_T , $m_{\ell\ell\ell}$ and the ratio of the leading lepton to the leading jet p_T . The MC-based and MM estimates are shown in Table 6.7. Due to the request for four leptons, the WZ process is treated as a reducible process. The typical reducible processes described in Section 6.5 are reduced to zero due to the request for four leptons as these processes produce three leptons or less in the final state. The data and MC are found to agree within an uncertainty of 15%.

	WZ	ZZ	$t\bar{t} + V$	$VV V$	Higgs	Reducible	Σ SM	Data
CRWZ	$8.2^{+1.1}_{-1.3}$	$0.73^{+0.08}_{-0.10}$	$0.27^{+0.18}_{-0.18}$	$0.11^{+0.11}_{-0.11}$	$0.06^{+0.04}_{-0.04}$	$0.33^{+0.39}_{-0.40}$	$9.7^{+1.2}_{-1.4}$	9

Table 6.6: WZ control region yields. The uncertainties quoted are combined statistical and systematic.

	ZZ	$t\bar{t} + V$	$VV V$	Higgs	Reducible (incl. WZ)	Σ SM	Data
CRZZ	140^{+11}_{-11}	$0.18^{+0.08}_{-0.07}$	$0.14^{+0.15}_{-0.15}$	$0.35^{+0.09}_{-0.10}$	$0.0^{+0.0}_{-0.0}$	141^{+11}_{-11}	141

Table 6.7: MC-only estimated yields in the ZZ control region. The uncertainties quoted are combined statistical and systematic.

Figure 6.31: Kinematic distributions for the WZ control region.

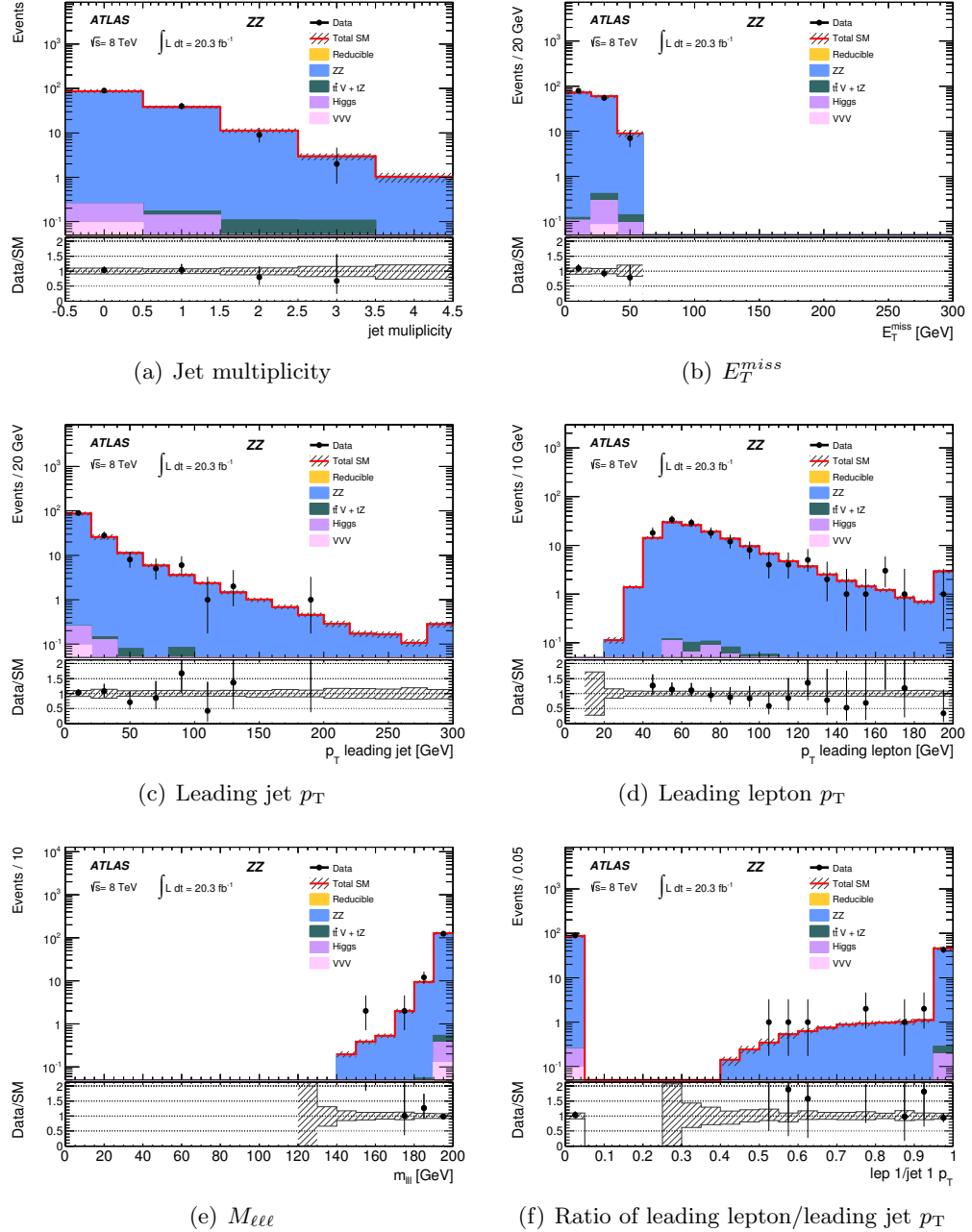


Figure 6.32: Kinematic distributions for the ZZ control region.

6.7.15 Systematic uncertainties on the reducible background

Systematic uncertainties on the reducible background estimated with the matrix method are assessed. The uncertainties can be categorised into the systematics arising from the input components of the weighted average fake rates defined in Equation 6.7: the fake rate and real lepton efficiencies (f and ϵ respectively), the scale factors (sf) and the fake fractions (R), defined in Section 6.5.3. The following will discuss these sources of systematic uncertainties affecting the final data driven estimate of the reducible background.

Fake Rate and Real Lepton Efficiencies (f,ϵ) The measured fake rate and real lepton efficiencies are taken from MC-simulated events which are corrected for any discrepancies with respect to data. These efficiencies showed a dependence on p_T and η and are therefore parameterised in these variables. The dependency of these efficiencies on variables used in the event selection of the signal regions were thoroughly investigated by the analysis team and found to be very similar to those taken into account for the previous 3ℓ analysis [132].

Fake Rate Scale Factors (sf) The measurement of the fake rate scale factors for the different fake sources showed no strong dependence in p_T , $|\eta|$ and number of good vertices. The central values for the scale factors were calculated without parameterisation on any variable and the differences with respect to the results of the fit in these considered variables are assigned as a systematic uncertainty of the order of 5%.

Fake Fractions (R) The uncertainty on the fake fractions originates from a potential lack of knowledge of the relative contributions of certain types of SM physics processes in a given signal or validation region. To account for this uncertainty, the yields of the physics processes are varied by the following amounts: diboson processes by 50%, top processes by 50% and V+jets processes by 30%. In addition to these systematic uncertainties, the statistical uncertainty on the data events is included. This is used to apply the matrix equation. The statistical uncertainty on the fake rates is measured in simulation.

6.7.16 Systematic Uncertainties Summary

The dominating systematic sources are summarised in Table 6.8. In SR 3ℓ -0 and SR 3ℓ -1 the dominant systematic uncertainties are the statistical uncertainty and the muon misidentification probability. The former arises due to the very low statistics in all signal

regions. The latter arises due to the low muon p_T threshold, which introduces muons which are harder to identify due to the likelihood of having increased jet activity around the reconstructed muon object. The systematic uncertainties are presented graphically for each signal region in Appendix B.

Table 6.8: Breakdown of the dominant systematic uncertainties on background estimates in the three-lepton signal regions. The percentages show the size of the uncertainty relative to the total expected background. Taken from [3].

Source of uncertainty	SR3 ℓ -0a	SR3 ℓ -0b	SR3 ℓ -1a	SR3 ℓ -1b
Reducible background				
- statistical uncertainty	34%	14%	11%	30%
- muon misidentification probability	30%	11%	< 1%	11%
- electron misidentification probability	21%	10%	2%	9%
- heavy-flavor relative contribution	22%	5%	< 1%	2%
- light-flavor relative contribution	23%	4%	n/a	< 1%
- conversion relative contribution	2%	6%	< 1%	10%
E_T^{miss} soft-term scale	12%	7%	< 1%	1%
Statistical uncertainty on MC samples	4%	3%	25%	10%
Theoretical modeling of WZ	2%	5%	12%	8%
Cross-section	2%	2%	6%	4%
Total	59%	25%	33%	39%

Chapter 7

Results and Interpretations for Run-1 Compressed Spectra SUSY Analysis

In Chapter 6, the analysis strategy for the search for compressed SUSY events with three-lepton final states with Run-1 data has been described. This chapter presents the interpretation of the results obtained in data, beginning with an introduction into the statistical approach to interpretation used, followed by an assessment of the compatibility between the expected SM background and the observed events in data in all signal regions. Lastly the statistical interpretation of the results for each SUSY model considered is presented.

7.1 Statistical Procedure

7.1.1 The CL_s Method

A p -value is defined as the probability of an experiment to get a certain outcome or one that is more unlikely than the one that was observed, i.e. the p -value is calculated as the integral over the probability density function, integrated from the observed value to infinity,

$$\int_{q_{obs}}^{\infty} f(q) dq, \quad (7.1)$$

where q is the test statistic, which is a scalar quantity representative of the experiment. The p -value is defined to represent the two hypotheses and determine which best describes the observed data. Therefore, to assess the statistical significance of the number of events

in data with respect to the expected background, the probability that the observation agrees with the background-only hypothesis (H_0) or the signal plus background hypothesis (H_1). The p -values for H_0 and H_1 are defined as:

$$p_0 = P(q \leq q_{obs}|H_0) = \int_{-\infty}^{q_{obs}} f(q|b)dq$$

$$p_1 = P(q \geq q_{obs}|H_1) = \int_{q_{obs}}^{\infty} f(q|s+b)dq,$$

where $f(q|b)$ and $f(q|s+b)$ are the probability density functions of the test statistic, q and q_{obs} is the observed result.

A given “signal” hypothesis, which would correspond to a particular SUSY model in this case, can be considered to be excluded if $p_1 \leq 0.05$, this means the probability of rejecting the hypothesis given the hypothesis is true is 5%. This is equivalent to saying the hypothesis is excluded at 95% Confidence Level (CL). However, it is possible that this can lead to a signal being incorrectly excluded in the case that the analysis does not expect a large ratio of signal to background events in the observed region - i.e. the analysis has a low sensitivity to the considered signal. To protect against this, a variation of the CL method, the CL_s method [147] [148], takes the ratio of p -values and is defined as:

$$CL_s = \frac{CL_{s+b}}{CL_b}, \quad (7.2)$$

where s is the expected signal, and

$$CL_{s+b} = P(q \geq q_{obs}|s+b), \quad (7.3)$$

and

$$CL_b = P(q \geq q_{obs}|b). \quad (7.4)$$

Using this method, a signal hypothesis is said to be excluded at 95% CL if the condition:

$$CL_s \leq 0.05 \quad (7.5)$$

is satisfied.

This analysis uses a profile log-likelihood ratio [149] formalism to define the test statistic q , which is used to obtain the relevant p -values and the CL_s . The likelihood is given by:

$$L(n_{obs}|\mu S, B, \eta) = \text{Pois}(n_{obs}|\mu S + B) \times \prod_{\eta} G_{syst}(\eta^0, \eta), \quad (7.6)$$

where S is the number of expected signal events, B is the number of expected background events, μ is the SUSY signal strength to be tested, and η and η_0 are the various systematics, described as nuisance parameters. $\text{Pois}(n_{obs}|\mu S + B)$ is the Poisson distribution for the expected events in a signal region, given the expected signal and background, and $G_{syst}(\eta^0, \eta)$ is a Gaussian, which is centered on the nominal value η^0 , around which the nuisance parameters can be varied when maximising the likelihood. Each nuisance parameter is described as a separate Gaussian, with $\mu=1$, and the product of these is then taken.

The likelihood can be concisely rewritten as $L(\mu, \nu(\mu))$, where ν represents the full signal plus background model, which is a function of the signal strength μ . Given this notation, the profile likelihood ratio $\lambda_p(\mu)$ is given by:

$$\lambda_p(\mu) = \frac{L(\mu, \hat{\nu}(\mu))}{L(\hat{\mu}, \hat{\nu}(\hat{\mu}))}. \quad (7.7)$$

In this definition, $\hat{\nu}$ represents using an “unconditional” likelihood fit to maximise the likelihood, which means that μ and ν are both varied simultaneously, whilst $\hat{\nu}$ represents a “conditional” maximisation of the likelihood, which involves fixing μ whilst ν is varied. The dependence on the nuisance parameters is removed by maximising likelihood or “profiling” procedure. The profile likelihood ratio tends to unity if the observation is compatible with the hypothesised value of μ .

The test statistic, q , is defined as a function of the log likelihood ratio $\lambda_p(\mu)$ given by:

$$q = \begin{cases} -2 \ln \lambda_p(\mu) & \hat{\mu} \leq \mu \\ 0 & \hat{\mu} > \mu, \end{cases} \quad (7.8)$$

where $\hat{\mu}$ is an estimator of the signal strength μ . The probability of observing the number of events predicted by the signal hypothesis or more given the signal strength is used to define the discovery p -value. This can be expressed as the integral of the probability distribution function of the test statistic for a given μ value, $f(q|\mu)$. The integral is calculated between the limits of the test statistic using the observed values q_{obs} and infinity in order to evaluate the total probability of obtaining a higher number of events than those observed. This gives the definition of the discovery p -value in terms of the log-likelihood ratio $\lambda_p(\mu)$:

$$p_\mu = \int_{q_{obs}}^{\infty} f(q|\mu) dq \quad (7.9)$$

The p -value is said to be “one-sided” [135], as an excess of events constitutes a signal observation, but an underfluctuation does not. The modelling of the likelihood, calculation of the CL_s and p -values, were performed using the ATLAS HistFitter package [148] [150], a tool able to perform likelihood fits and their statistical interpretation.

7.1.2 Combination of Signal Regions

All signal regions considered in this analysis (see Section 6.4) are orthogonal and in turn can be statistically combined for overall improvement in signal sensitivity. The method involves a combined likelihood, defined as:

$$L(\mu, \nu) = \prod_i^N L_i(\mu, \nu_i), \quad (7.10)$$

for N signal regions. If a signal region has no sensitivity to a given signal, the corresponding likelihood will not be a function of μ , and therefore it will not contribute to the combined likelihood for that signal scenario.

7.2 Observations in 8 TeV Data

The data events observed in the signal regions with the background yields are displayed in Table 7.1. No excess in the number of events is observed when comparing to the expected SM background. There is good agreement between the data and the SM background within systematic uncertainties. The quantitative analysis of the differences between the number of expected and observed events is discussed in Section 7.3. The main kinematic variables used to define the ISR signal regions SR3 ℓ -1 are shown in this section not only highlighting the agreement with data and MC but also the shape and kinematic features of the ISR signal.

Table 7.1: Expected and observed yields in the three-lepton signal regions. The uncertainties shown include both statistical and systematic components. The “Others” background category includes $t\bar{t}V$, VVV and SM Higgs boson production [3].

	SR3 ℓ -0a	SR3 ℓ -0b	SR3 ℓ -1a	SR3 ℓ -1b
WZ	$0.59^{+0.47}_{-0.32}$	$5.0^{+1.5}_{-1.2}$	$0.54^{+0.20}_{-0.19}$	1.6 ± 0.4
ZZ	$0.23^{+0.09}_{-0.07}$	0.66 ± 0.16	0.024 ± 0.013	$0.10^{+0.05}_{-0.04}$
Reducible	$2.8^{+1.5}_{-2.2}$	$9.7^{+3.1}_{-3.6}$	0.09 ± 0.08	$1.4^{+1.0}_{-1.1}$
Others	$0.0033^{+0.0036}_{-0.0033}$	0.07 ± 0.05	0.013 ± 0.010	0.038 ± 0.021
Total SM	$3.7^{+1.6}_{-2.2}$	$15.4^{+3.5}_{-3.9}$	$0.67^{+0.22}_{-0.21}$	$3.1^{+1.1}_{-1.2}$
Data	4	15	1	3

7.2.1 Kinematic Distributions

Figures 7.1 and 7.2 shows the SM expectations and the observations in data in the SR3 ℓ -1a and SR3 ℓ -1b signal regions respectively. For illustration purposes, the distributions are also shown for two $\tilde{\chi}_1^\pm \tilde{\chi}_2^0$ via WZ and one $\tilde{\chi}_1^\pm \tilde{\chi}_2^0$ via $\tilde{\ell}_L$ benchmark points with $m(\tilde{\chi}_1^\pm \tilde{\chi}_2^0, \tilde{\chi}_1) = (100, 87.5), (100, 75)$ and $(110, 90)$ GeV. These are points are chosen to show the sensitivity for varying mass differences in the signal regions for WZ-mediated and $\tilde{\ell}_L$ -mediated simplified models. Figures 7.3 and 7.4 shows the SM expectations and the observations in data in the SR3 ℓ -0 signal regions.

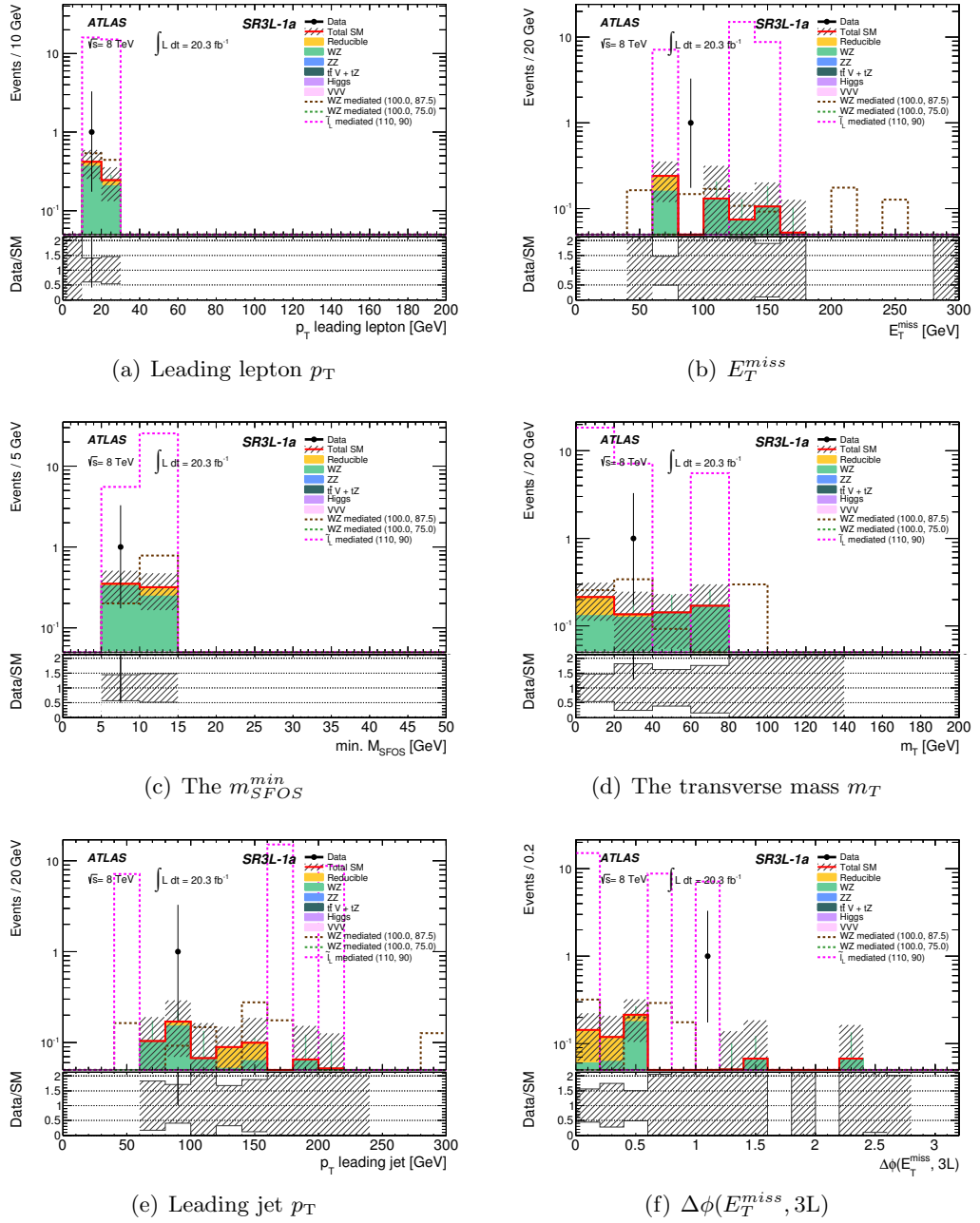


Figure 7.1: Kinematic distributions in SR3L-1a. (a) $p_T^{1^{\text{st}}\ell}$, (b) E_T^{miss} , (c) $m_{\text{SFOS}}^{\text{min}}$, (d) m_T , (e) $p_T^{1^{\text{st}}j}$, (f) $\Delta\phi(E_T^{\text{miss}}, 3\ell)$. The uncertainty band covers systematic and statistical uncertainties. The plots also show the distributions for signal hypotheses, where the parentheses following the simplified model denote the mass parameters in GeV as $(m(\tilde{\chi}_1^\pm/\tilde{\chi}_2^0), m(\tilde{\chi}_1^0))$.

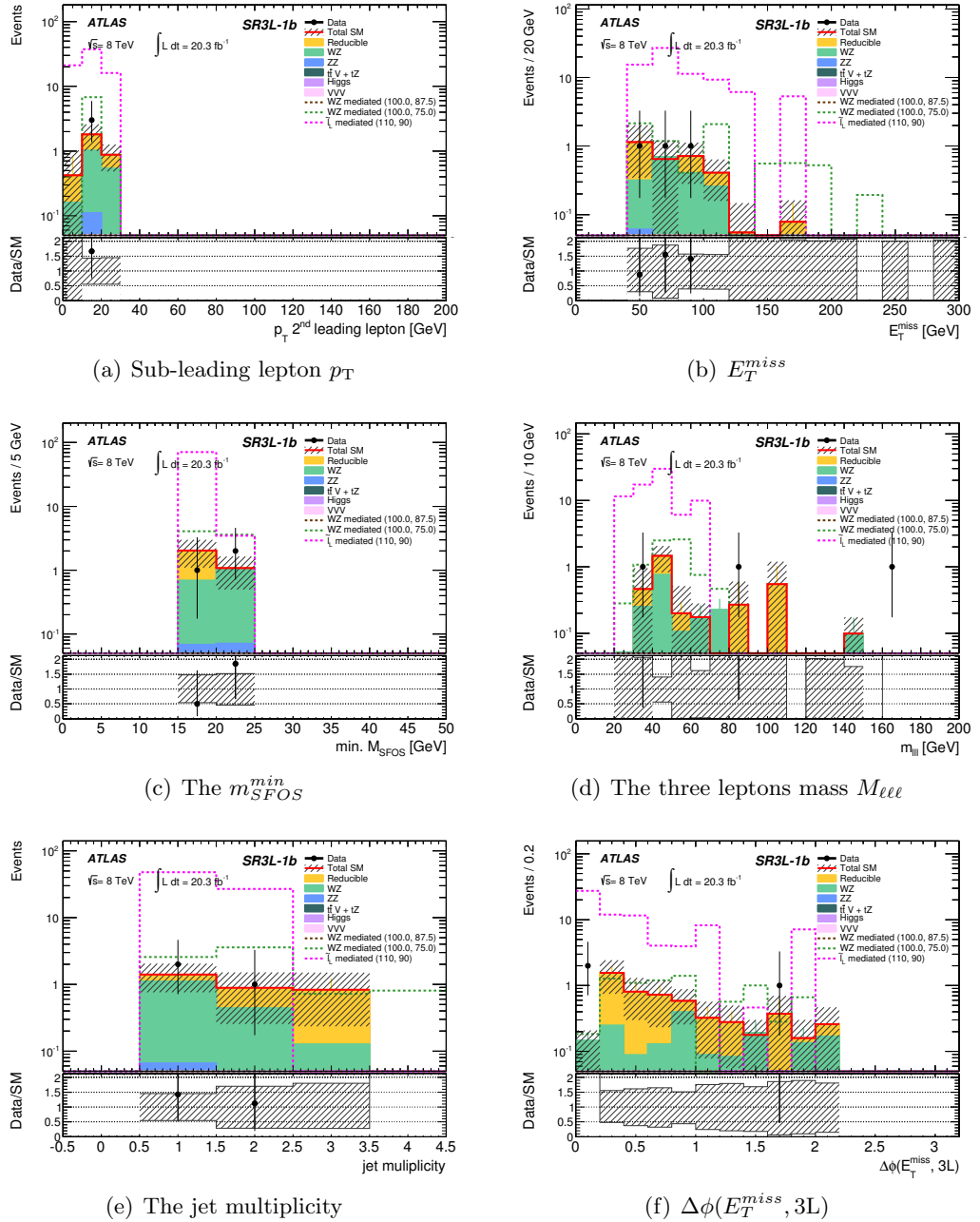


Figure 7.2: Kinematic distributions in SR3L-1b. (a) $p_T^{2\text{nd}\ell}$, (b) E_T^{miss} , (c) m_{SFOS}^{\min} , (d) $M_{\ell\ell\ell}$, (e) Jet multiplicity, (f) $\Delta\phi(E_T^{\text{miss}}, 3\ell)$. The uncertainty band covers systematic and statistical uncertainties. The plots also show the distributions for signal hypotheses, where the parentheses following the simplified model denote the mass parameters in GeV as $(m(\tilde{\chi}_1^\pm/\tilde{\chi}_2^0), m(\tilde{\chi}_1^0))$.

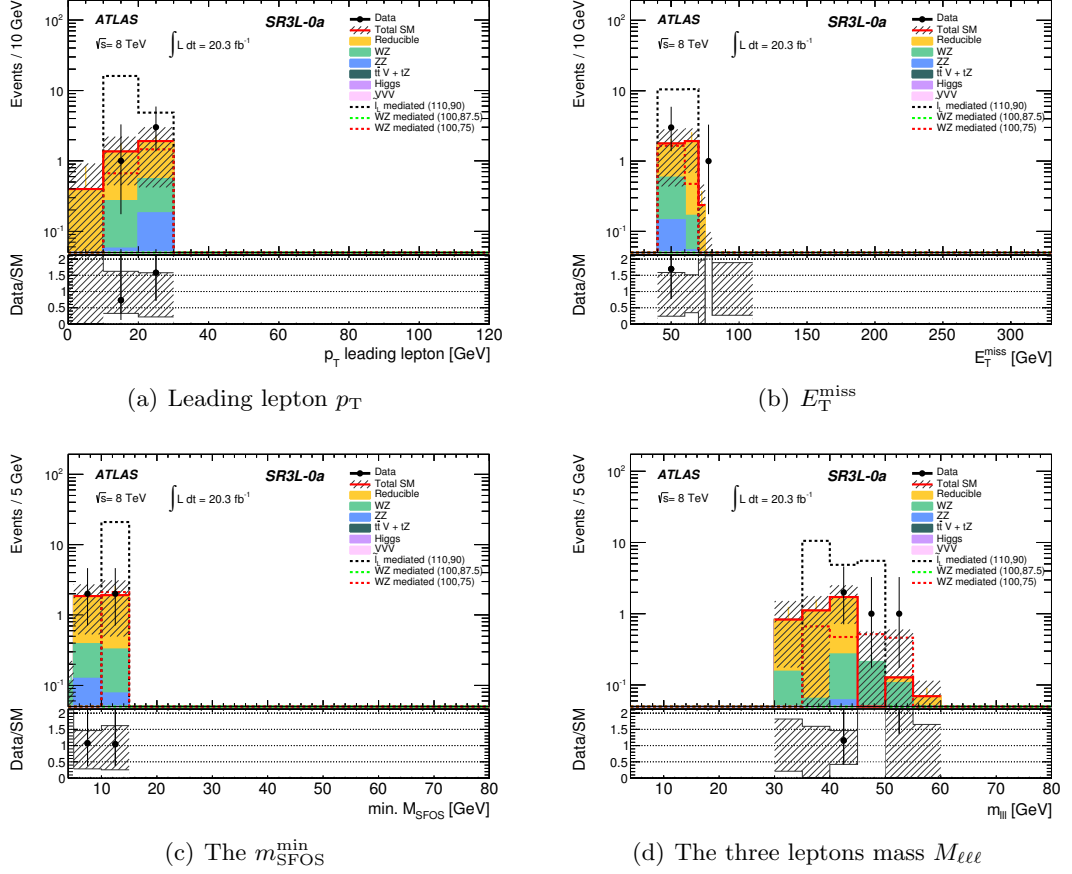


Figure 7.3: Kinematic distributions in SR3L-0a. (a) $p_T^{1^{\text{st}}\ell}$, (b) E_T^{miss} , (c) $m_{\text{SFOS}}^{\text{min}}$, (d) $M_{\ell\ell\ell}$. The uncertainty band covers systematic and statistical uncertainties. The plots also show the distributions for signal hypotheses, where the parentheses following the simplified model denote the mass parameters in GeV as $(m(\tilde{\chi}_1^\pm/\tilde{\chi}_2^0), m(\tilde{\chi}_1^0))$ (Produced by another analyser, taken from [136]).

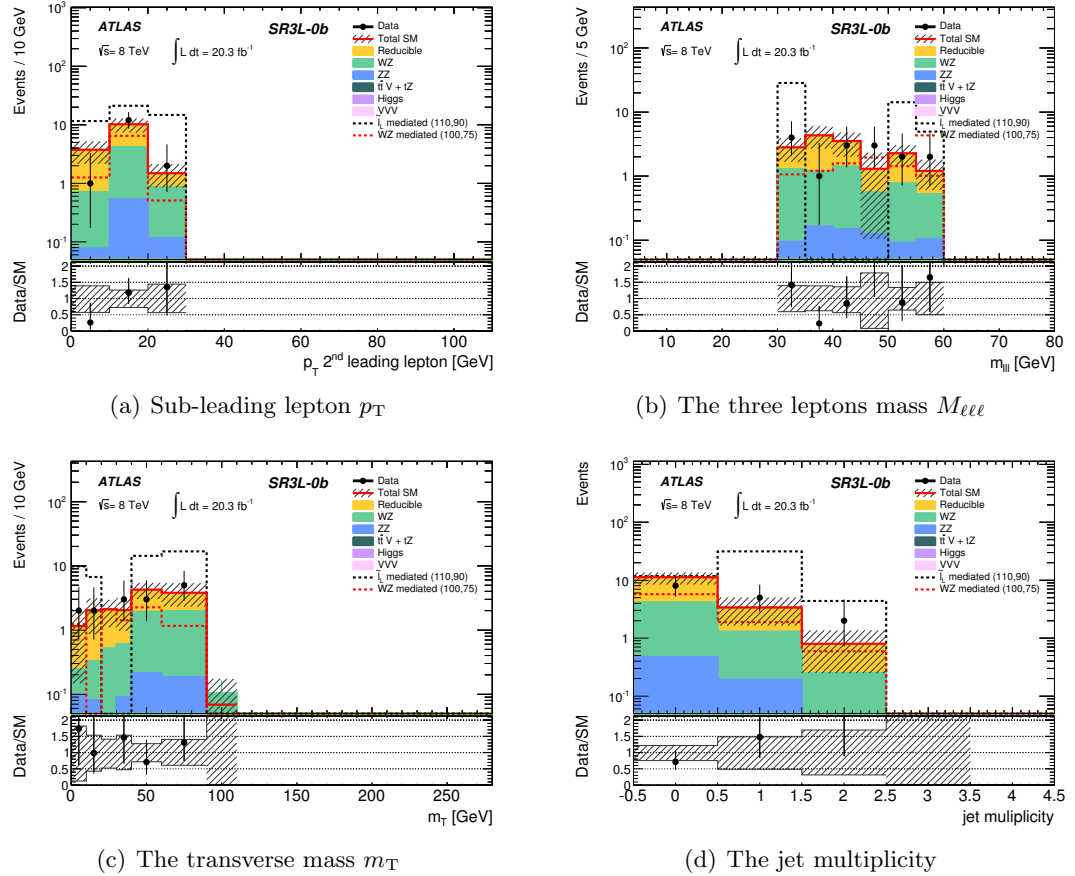


Figure 7.4: Kinematic distributions in SR3L-0b. (a) $p_T^{2nd\ell}$, (b) $M_{\ell\ell\ell}$, (c) m_T , (d) Jet multiplicity. The uncertainty band covers systematic and statistical uncertainties. The plots also show the distributions for signal hypotheses, where the parentheses following the simplified model denote the mass parameters in GeV as $(m(\tilde{\chi}_1^\pm/\tilde{\chi}_2^0), m(\tilde{\chi}_1^0))$ (Produced by another analyser, taken from [136]).

7.3 Statistical Interpretation of Results

7.3.1 Model Independent Limits

In addition to considering the interpretation for the specific SUSY scenarios this analysis was optimised for, the compatibility of the observed data with the background-only hypothesis b can be assessed. This corresponds to signal strength $\mu = 0$. In order to quantify the probability of the background-only hypothesis to fluctuate to the number of observed events or higher, the one-sided p_0 -value is calculated and truncated to 0.5 for $p_0 > 0.5$. The upper limits at 95% CL on the expected and observed number of beyond the SM event (S_{exp}^{95} , S_{obs}^{95}) for each signal region are calculated using the CL_s method. For both of these calculations the profile likelihood ratio is used as a test-statistic. The p_0 and CL_s values are calculated using pseudo-experiments. The upper limit on the visible cross-section is

set for any new physics scenarios. It is defined as the cross section times the branching ratio times acceptance times efficiency ($\sigma \times BR \times A \times \epsilon$) of new physics processes satisfying the signal region requirements. Upper limits are derived by evaluating p_μ at a large (and hence easily excluded) starting value of μ until p_μ exceeds 0.5. This visible cross-section can be used to test scenarios not considered in this work using the observed data in the SRs. The model-independent limits are shown in Table 7.2.

	SR3 ℓ -0a	SR3 ℓ -0b	SR3 ℓ -1a	SR3 ℓ -1b
Total SM	$3.7^{+1.6}_{-2.2}$	$15.4^{+3.5}_{-3.9}$	$0.67^{+0.22}_{-0.21}$	$3.1^{+1.1}_{-1.2}$
Data	4	15	1	3
p_0	0.47	0.50	0.36	0.50
S_{obs}^{95}	8.3	12.6	4.0	6.1
S_{exp}^{95}	$8.2^{+1.7}_{-2.2}$	$12.6^{+5.2}_{-3.0}$	$3.8^{+0.6}_{-0.3}$	$6.0^{+2.1}_{-1.3}$
$\langle\epsilon\sigma\rangle_{\text{obs}}^{95} [\text{fb}]$	0.41	0.62	0.20	0.30
CL_b	0.59	0.50	0.69	0.54

Table 7.2: The model-independent limits are shown, calculated from the three-lepton signal region observations: the one-sided p_0 -values; the expected and observed upper limits at 95% CL on the number of beyond-the-SM events (S_{exp}^{95} and S_{obs}^{95}) for each signal region, calculated using pseudo-experiments and the CL_s prescription; the observed 95% CL upper limit on the signal cross-section times efficiency ($\langle\epsilon\sigma\rangle_{\text{obs}}^{95}$); and the CL_b value for the background-only hypothesis [3].

7.3.2 Model Dependent Limits: Simplified Models

Both the WZ- and $\tilde{\ell}_L$ -mediated simplified models are considered for limit setting. The observed and expected 95% CL limit contours are calculated using MC pseudo-experiments for each SUSY model point, taking into account the theoretical and experimental uncertainties on the SM background and the experimental uncertainties on the signal, σ_{exp} in addition to the Poissonian fluctuations on the number of observed events. The yellow bands in Figures 7.5- 7.7 show the impact of $\pm 1\sigma$ variations of σ_{exp} on the expected limit. The impact of the theoretical uncertainty on the signal cross section $\sigma_{\text{theory}}^{\text{SUSY}}$ are shown as $\pm 1\sigma$ variation bands (red dashed lines) on the observed limit. The combination of SR3 ℓ -0 and SR3 ℓ -1 showed no significant improvements in sensitivity to the WZ-mediated model compared to the limits produced in [132]. Only one compressed mass splitting point could be excluded. The 1D upper limit on the production cross-section for $\Delta m(\tilde{\chi}_1^\pm - \tilde{\chi}_1^0) = 25$ GeV is shown in Figures 7.5. The excluded point corresponds to $m(\tilde{\chi}_1^\pm) = 100$ GeV and $m(\tilde{\chi}_1^0) = 75$ GeV. The difficulty in improving sensitivity in this simplified model is largely due to the smaller production cross-sections compared to the via $\tilde{\ell}_L$ model.

Limits are set on the $\tilde{\chi}_1^\pm \tilde{\chi}_2^0$ scenarios with $\tilde{\ell}_L$ -mediated decays, with the $\tilde{\ell}_L$ masses set to the $\tilde{\chi}_1^0$ mass plus 50% or 95% of the difference between the $\tilde{\chi}_1^\pm$ and $\tilde{\chi}_1^0$ masses. Figure 7.6 shows the combination of the compressed scenario analyses and the previous published results, with $\tilde{\ell}_L$ halfway between $\tilde{\chi}_1^\pm/\tilde{\chi}_2^0$ and $\tilde{\chi}_1^0$ masses, with an improved sensitivity to compressed scenarios up to $\tilde{\chi}_1^\pm$ masses of 250 GeV. The results for the scenario where the $\tilde{\ell}_L$ mass is 95% between the $\tilde{\chi}_1^\pm$ and the $\tilde{\chi}_1^0$ masses is combined with the previous three-lepton results and the same-sign, two lepton analysis [3] and is shown in Figure 7.7. In scenarios with large mass splittings, $\tilde{\chi}_1^\pm$ masses are excluded up to 700 GeV. In the compressed area of the parameter space, where the $\tilde{\ell}_L$ mass is halfway between the $\tilde{\chi}_1^\pm$ and $\tilde{\chi}_1^0$ masses, the identification of three leptons in the final state is possible and so the three-lepton analysis has the strongest sensitivity. However, where the $\tilde{\ell}_L$ mass is 95% between the $\tilde{\chi}_1^\pm$ and $\tilde{\chi}_1^0$ masses, one of the leptons may have momentum too low to be reconstructed, as such the two same-sign lepton analysis, which was designed to compliment the three-lepton search shows the strongest sensitivity.

7.3.3 Summary of Electroweak SUSY Searches at 8 TeV

The ATLAS results for electroweakino searches at 8 TeV in the simplified models framework are summarised in Figure 7.8 in the $m(\tilde{\chi}_1^\pm, \tilde{\chi}_2^0) - m(\tilde{\chi}_1^0)$ plane. Each of the $\tilde{\chi}_1^\pm/\tilde{\chi}_2^0/\tilde{\chi}_3^0$ decays considered in the plot is assumed to have 100% branching fraction and the production cross-section is for pure wino $\tilde{\chi}_1^+ \tilde{\chi}_1^-$ and $\tilde{\chi}_1^\pm \tilde{\chi}_2^0$, and pure higgsino $\tilde{\chi}_2^0 \tilde{\chi}_3^0$. The limits for $\tilde{\chi}_1^+ \tilde{\chi}_1^-$ and $\tilde{\chi}_1^\pm \tilde{\chi}_2^0$ and $\tilde{\chi}_2^0 \tilde{\chi}_3^0$ production with $\tilde{\ell}_L$ -mediated decays combine the compressed spectra, same-sign, two-lepton analyses with the previously published analyses. It is observed that for $\tilde{\chi}_1^\pm \tilde{\chi}_2^0 \tilde{\chi}_3^0$ masses up to 740 GeV are excluded at the 95% CL for massless $\tilde{\chi}_1^0$. Improvements in sensitivity are also seen in the near $\tilde{\chi}_1^\pm, \tilde{\chi}_1^0$ mass degenerate region, which is due to the inclusion of the combined compressed 3ℓ analyses and the same-sign, two-lepton analysis. In the high mass region, with large mass differences between the $\tilde{\chi}_1^\pm$ and the $\tilde{\chi}_1^0$ the exclusion limit has increased by 20 GeV. In the compressed region, near the boundary where $m_{\tilde{\chi}_1^\pm} = m_{\tilde{\chi}_1^0}$, the exclusion limit has been extended closer to the mass degenerate boundary up to 200 GeV more with the inclusion of the compressed spectra analyses.

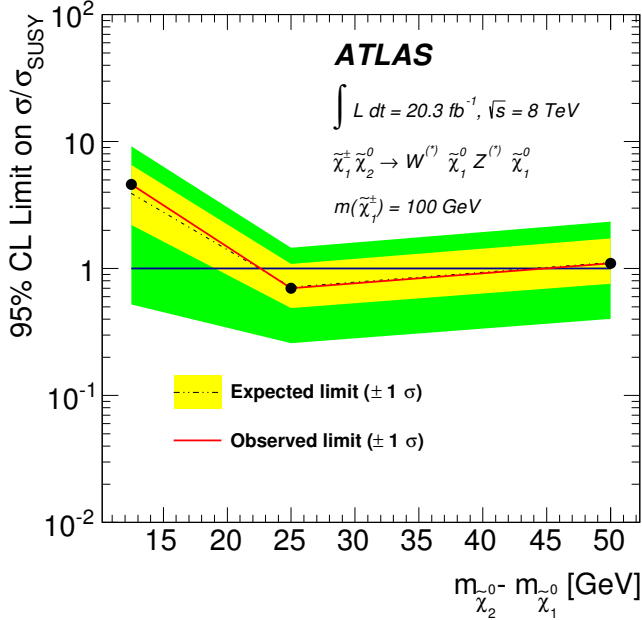


Figure 7.5: 95% CL upper limit on the cross section normalised to the SUSY production cross section for chargino and neutralino production in the WZ-mediated simplified models with $m(\tilde{\chi}_1^\pm) = 100$ GeV. The limits have been set with respect to the mass difference between $\tilde{\chi}_1^\pm - \tilde{\chi}_1^0$. Produced by other analyser, taken from [136].

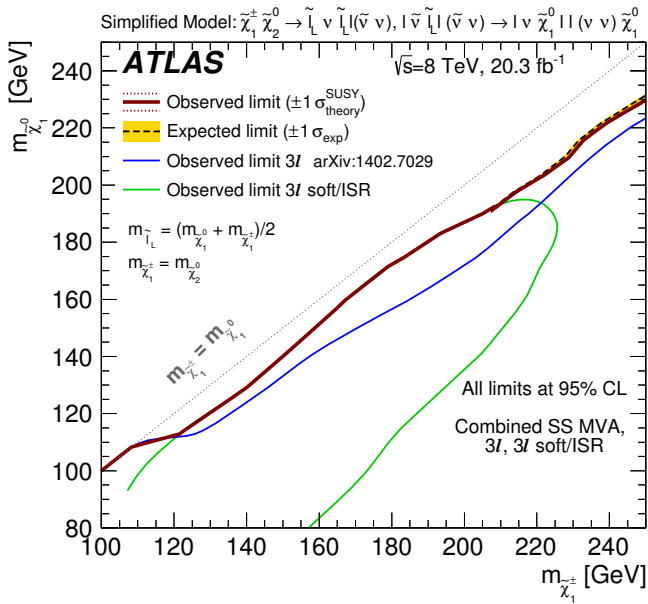


Figure 7.6: The 95% CL exclusion limits on $\tilde{\chi}_1^\pm \tilde{\chi}_2^0$ production with $\tilde{\ell}_L$ -mediated decays, as a function of the $\tilde{\chi}_1^\pm$ and $\tilde{\chi}_1^0$ masses, where the intermediate slepton mass is set to the $\tilde{\chi}_1^0$ mass plus 50% of the difference between the $\tilde{\chi}_1^\pm$ and the $\tilde{\chi}_1^0$ masses. The red contour corresponds to the limits set using a combination of the 3ℓ analysis from [132], the compressed scenario 3ℓ analysis and the same-sign, two lepton analysis [3]. The green contour corresponds to the combined SR 3ℓ -0 and SR 3ℓ -1 limits.

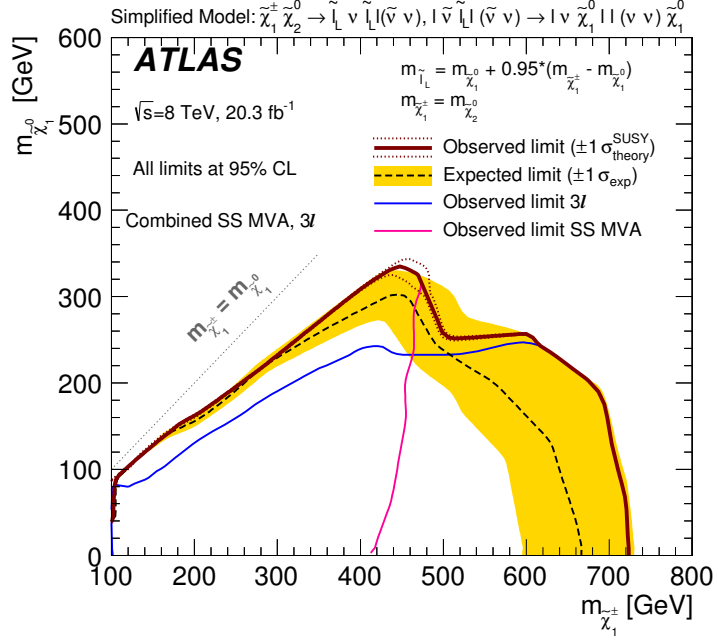
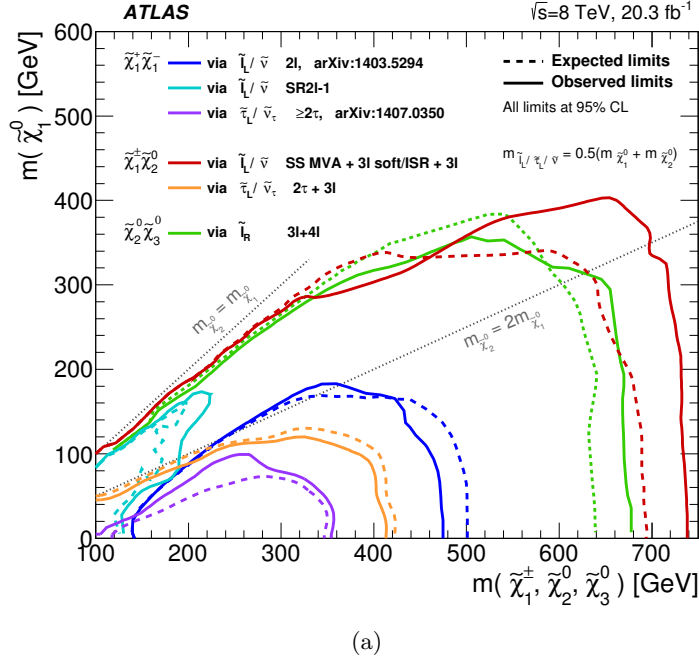


Figure 7.7: The 95% CL exclusion limits on $\tilde{\chi}_1^\pm \tilde{\chi}_2^0$ production with $\tilde{\ell}_L$ -mediated decays, as a function of the $\tilde{\chi}_1^\pm$ and $\tilde{\chi}_2^0$ masses, where the intermediate slepton mass is set to the $\tilde{\chi}_1^0$ mass plus 95% of the difference between the $\tilde{\chi}_1^\pm$ and the $\tilde{\chi}_1^0$ masses. The red contour corresponds to the combined limits for the 3ℓ analysis from [132], the compressed scenario 3ℓ analysis and the same-sign, two lepton analysis [3]. The blue contour corresponds to the combined limits of the 3ℓ analyses and the pink contour corresponds to the limits from the same-sign, two lepton analysis.



(a)

Figure 7.8: The 95% CL exclusion limits on $\tilde{\chi}_1^\pm \tilde{\chi}_1^-$, $\tilde{\chi}_1^\pm \tilde{\chi}_2^0$ and $\tilde{\chi}_2^0 \tilde{\chi}_3^0$ production with $\tilde{\ell}_L$ -mediated decays, as a function of the $\tilde{\chi}_1^\pm$, $\tilde{\chi}_2^0$ and $\tilde{\chi}_3^0$ masses. The production cross-section is for pure wino $\tilde{\chi}_1^\pm \tilde{\chi}_1^-$ and $\tilde{\chi}_1^\pm \tilde{\chi}_2^0$, and pure higgsino $\tilde{\chi}_2^0 \tilde{\chi}_3^0$ [3].

Chapter 8

Looking Into the Future: A First Optimisation for an Electroweak SUSY Search with Three-Lepton Final States at 13 TeV

8.1 Introduction

This chapter presents a search for electroweak SUSY, in particular direct $\tilde{\chi}_1^\pm \tilde{\chi}_2^0$ production with decay via intermediate left-handed sleptons, $\tilde{\ell}_L$. The search is simulation based, with Run-2 conditions i.e. $\sqrt{s} = 13$ TeV with a projected integrated luminosity of 10fb^{-1} of pp -collision simulated data. With higher beam energies and expected higher luminosities during Run-2, improved sensitivity to SUSY production is expected. This is shown in Figure 8.1, where the cross-section for gaugino pair-production is \sim four times greater at 14 TeV than 8 TeV for $m(\tilde{\chi}) = 500$ GeV. Electroweak SUSY production will not immediately benefit from the increase in beam energies due to the relatively small production cross-sections compared to strong production. However, electroweak SUSY production will benefit from the increase in luminosity. This analysis is designed to give a preliminary projection of the sensitivity to electroweak SUSY production with the expected Run-2 data to be collected from 2015-2016. The selections presented for the signal regions are not final and are likely to be subject to change by other analysers until publication.

This analysis targets two scenarios: where the $m_{\tilde{\chi}_1^\pm, \tilde{\chi}_2^0} = 600$ GeV - 1 TeV (heavy), or 100 - 600 GeV (intermediate). This region of the $m(\tilde{\chi}_1^\pm \tilde{\chi}_2^0 - \tilde{\chi}_1^0)$ parameter space is different

from the compressed scenarios discussed in Chapters 6 and 7, where the final state objects had relatively low p_T . Therefore the optimisation strategy utilises different variables, which highlight the larger E_T^{miss} , m_T and lepton $p_T^{1,2,3}$. The general analysis strategy is discussed in Section 8.2. The Run-2 trigger selection is shown in Section 8.4. The definitions of the physics objects used for this analysis are described in Section 8.5, where only differences to the Run-1 analysis are highlighted. The signal region optimisation strategy is described in Section 8.6. The expected signal sensitivity is discussed in Section 8.7.

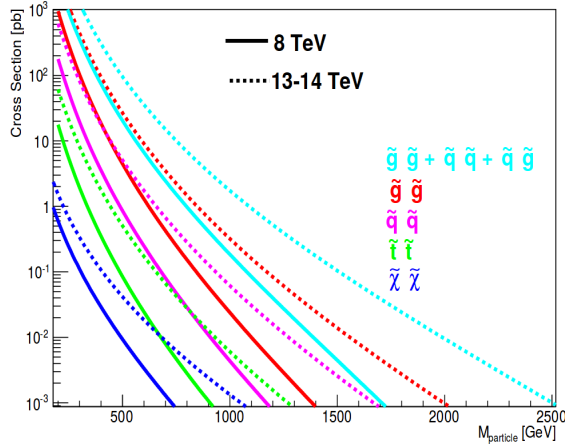


Figure 8.1: Cross-sections for SUSY particle production at $\sqrt{s} = 8$ TeV and 13-14 TeV. The coloured particle cross sections are from NLL-FAST [151] and evaluated at $\sqrt{s} = 8$ TeV and 13 TeV; the electroweak pure higgsino cross sections are from PROSPINO [152] and evaluated at $\sqrt{s} = 8$ TeV and 14 TeV. Taken from [153].

8.2 Analysis Overview

8.3 SUSY Simplified Models Considered

In this analysis, one $\tilde{\chi}_1^\pm \tilde{\chi}_2^0$ production mode is explored in the content of simplified models: direct $\tilde{\chi}_1^\pm \tilde{\chi}_2^0$ with intermediate sleptons leading to a final state of three leptons and E_T^{miss} as illustrated in Figure 2.3.

The $\tilde{\chi}_1^\pm$ and $\tilde{\chi}_2^0$ are considered purely wino and mass degenerate, the $\tilde{\ell}$ are assumed to be left-handed ($\tilde{\ell}_L$) and their masses are halfway between the $\tilde{\chi}_1^\pm, \tilde{\chi}_2^0$ and $\tilde{\chi}_1^0$. The $\tilde{\chi}_1^\pm$ and $\tilde{\chi}_2^0$ are allowed to decay only through $\tilde{\ell}_L$ with all the slepton flavours allowed with equal branching ratios.

This analysis is simulation based and was designed with an integrated luminosity of 10 fb^{-1} of data with $\sqrt{s} = 13$ TeV. The MC simulated samples are the same as those described in Section 4.6.4.

8.4 Trigger Selection

This analysis selects events with at least two leptons with $p_T > 25$ GeV in order to increase signal efficiency. Dileptonic triggers were chosen in the analysis instead of single lepton triggers, to provide uniformity with the Run-2 two-lepton analysis, which exclusively uses dileptonic triggers. The impact on signal acceptance was explored and found to be negligible.

Trigger Type	Trigger Name	Offline p_T threshold [GeV]
Double e	HLT_2e12_lhloose_L12EM10VH	14,14
Double μ	HLT_mu18_mu8noL1	20,10
Combined $e\mu$	HLT_e17_lhloose_mu14	19(e),16(μ)

Table 8.1: Summary of leptonic triggers used in this analysis and the offline threshold used ensuring that the lepton(s) triggering the event are in the plateau region of the trigger efficiency.

8.5 Object Selection

8.5.1 Electrons

Baseline electrons must have $p_T > 10$ GeV and satisfy the loose likelihood ID criteria (refer to likelihood based lepton identification in Section 5.3). Signal electrons must have $p_T > 25$ GeV, satisfy the medium likelihood ID criteria and be isolated with respect to other high- p_T charged particles, satisfying a loose isolation criteria [154]. Signal electron candidates must also satisfy the IP conditions $d_0/\sigma_{d_0} < 5$ and $z_0 \sin\theta < 0.5$ mm. The electron selection is summarised in Table 8.2.

8.5.2 Muons

Baseline muons must have $p_T > 10$ GeV. Signal muons must have $p_T > 25$ GeV, satisfy the medium likelihood ID criteria and be isolated with respect to other high- p_T charged particles, satisfying the loose criteria as assigned to signal electrons. Signal muon candidates must also satisfy the IP conditions $d_0/\sigma_{d_0} < 3$ and $z_0 \sin\theta < 0.5$ mm. The muon selection is summarised in Table 8.3.

Requirement	Value/description
Baseline Electron	
Acceptance	$p_T > 10 \text{ GeV}, \eta^{\text{clust}} < 2.47$
PID Quality	Loose likelihood
Signal Electron	
Acceptance	$p_T > 25 \text{ GeV}, \eta^{\text{cluster}} < 2.47$
PID Quality	Medium likelihood
Isolation	Loose
Impact parameter	$ z_0 \sin \theta < 0.5 \text{ mm}$ $ d_0/\sigma_{d_0} < 5$

Table 8.2: Summary of the electron selection criteria. The signal selection requirements are applied on top of the baseline selection and after overlap removal.

Requirement	Value/description
Baseline Muon	
Acceptance	$p_T > 10 \text{ GeV}, \eta < 2.4$
Signal Muon	
Acceptance	$p_T > 25 \text{ GeV}, \eta < 2.4$
PIDQuality	Medium likelihood
Isolation	Loose
Impact parameter	$ z_0 \sin \theta < 0.5 \text{ mm}$ $ d_0/\sigma_{d_0} < 3$

Table 8.3: Summary of the muon selection criteria. The signal selection requirements are applied on top of the baseline selection after overlap removal.

8.5.3 Jets

Baseline jets are required to have $p_T > 20 \text{ GeV}$ and are required to satisfy $|\eta| < 2.8$. Signal jets are required to pass a *JVT* cut of > 0.59 if the jet p_T is less than 60 GeV and it resides with $|\eta| < 2.4$. *B*-tagged jets are identified with the *b*-tagger algorithm (MV2c20) with an efficiency of 77% [155]. The jet selection is summarised in Table 8.4.

8.5.4 Missing Transverse Energy

The missing transverse energy (E_T^{miss}) definition uses selected analysis objects and tracks using an algorithm [156], which assigns topological clusters to reconstructed objects and calibrates according to the object. Calibrated baseline electrons, muons and jets, where the full η range is used for jets, are considered in the E_T^{miss} calculation.

Requirement	Value/description
Baseline jet	
Acceptance	$p_T > 20 \text{ GeV}, \eta < 2.8$
Signal jet	
JVT	$ JVT > 0.59$ for jets with $p_T < 60 \text{ GeV}$ and $ \eta < 2.4$
Signal b-jet	
b -tagger Algorithm	MV2c20
Efficiency	77 %

Table 8.4: Summary of the jet and b -jet selection criteria. The signal selection requirements are applied on top of the baseline requirements after Overlap Removal has been performed.

8.6 Signal Region Optimisation

This section motivates the signal optimisation strategy that offers sensitivity to the $\tilde{\chi}_1^\pm/\tilde{\chi}_2^0$ via intermediate $\tilde{\ell}_L$ scenario. The signal regions are optimised using the variable Z_N as described in Equation 6.2. Two signal regions are defined to target different regions of the $m(\tilde{\chi}_1^\pm/\tilde{\chi}_2^0) - m(\tilde{\chi}_1^0)$ parameter space: SR3 ℓ -H targets the high mass spectra, where the $\tilde{\chi}_1^\pm/\tilde{\chi}_2^0$ masses are above 600 GeV and the mass difference with the $\tilde{\chi}_1^0$ is greater than 100 GeV; SR3 ℓ -I targets intermediate mass spectra, where the $\tilde{\chi}_1^\pm/\tilde{\chi}_2^0$ masses are greater than 100 GeV and up to 600 GeV and the mass difference with the $\tilde{\chi}_1^0$ is up to 400 GeV. These signal regions require three leptons, one SFOS pair and veto all events with b -tagged jets. In the following, this selection is referred to as the baseline selection as motivated in Section 6.4.1.1.

Each cut used in this signal region will be defined and motivated using the event distributions for each variable in tandem with one-dimensional Z_N distributions. The distributions will be shown at the baseline and at the signal region definition with the cut for the corresponding variable removed, i.e. N-1 stage. For SR3 ℓ -H, four high mass signal points are chosen for optimisation, with the following masses for $m(\tilde{\chi}_1^\pm/\tilde{\chi}_2^0, \tilde{\chi}_1^0)$: (900,300), (800,0), (900,0), (800,200) GeV. For SR3 ℓ -I, four intermediate mass signal points are chosen for optimisation, with the following masses for $m(\tilde{\chi}_1^\pm/\tilde{\chi}_2^0, \tilde{\chi}_1^0)$: (300,200), (600,400), (400,200), (500,400) GeV. The high mass points were chosen because they were outside of the exclusion contour for the combined two and three-lepton analyses shown in Figure 7.8. The intermediate mass points were chosen because they were close to the mass-degenerate region of the parameter space or outside of the aforementioned exclusion contour.

8.6.1 High Mass Signal Region - SR3 ℓ -H

8.6.1.1 Transverse momentum of third-leading lepton

The event distribution for this variable at baseline is shown in Figure 8.2(a). The SM background dominates in values below 100 GeV with a short tail that drops off at approximately 250 GeV. The benchmark signal points display a flat distribution. Judging from the shapes of these distributions and the requirement for hard- p_T leptons in the high mass region of the parameter space, a cut above 50 GeV would be a good cut to discriminate against the SM background. Figure 8.2(b) shows the N-1 distribution, the magenta line highlights the optimal cut for this variable, which is above 90 GeV. With this cut, the majority of the diboson contribution, which is the dominant irreducible background is removed.

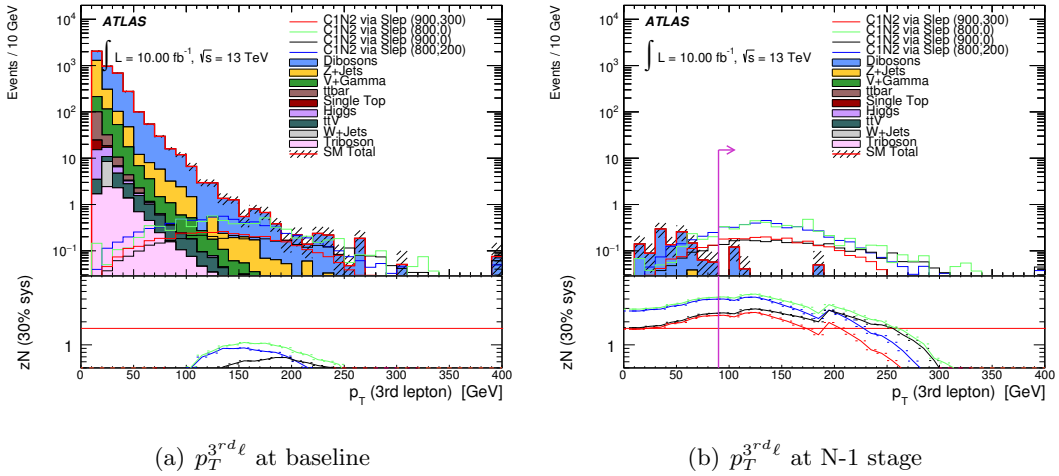


Figure 8.2: Baseline and N-1 distributions for the transverse momentum of the 3rd lepton. The Z_N curves are produced assuming a flat 30% relative uncertainty to account for systematic uncertainties.

8.6.1.2 Missing transverse momentum

The Z+jets SM process dominates the low E_T^{miss} values at below 100 GeV at baseline, as shown in Figure 8.3(a), whereas the signal distributions have large tails extending beyond 350 GeV, which is due to the expected heavy $\tilde{\chi}_1^0$ in the final state. This shows that the E_T^{miss} distribution is a good discriminator against the main reducible background. Figure 8.3(b) shows a possible cut is at 80 GeV, with most of the signal yields preserved in the tails of the distribution.

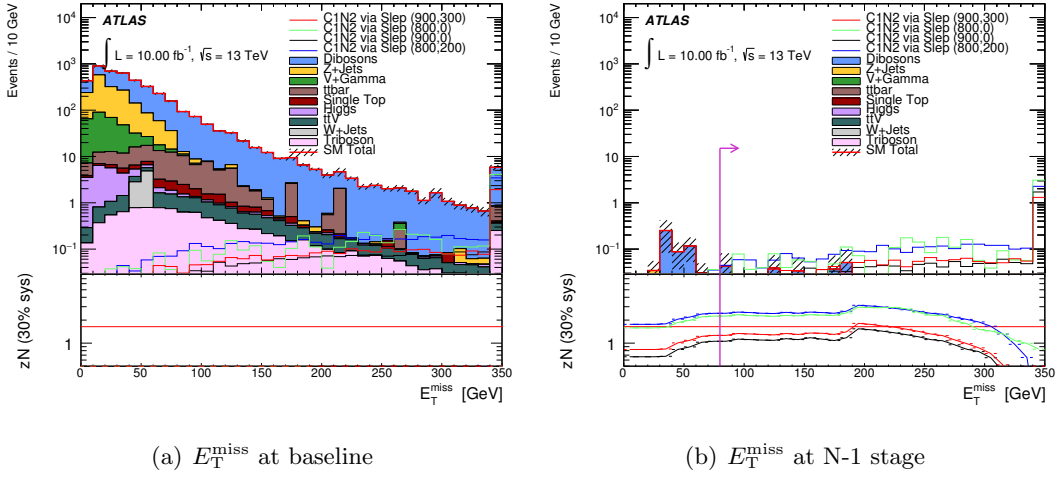


Figure 8.3: Baseline and N-1 distributions for the missing transverse momentum. The Z_N curves are produced assuming a flat 30% relative uncertainty to account for systematic uncertainties.

8.6.1.3 Transverse Mass

The transverse mass variable (refer to Section 6.4.3 for definition) is useful for targeting heavy decaying particles with invisible decay products in the final state. A large value of m_T discriminates against backgrounds containing W-bosons, such as WW or WZ , where the kinematic endpoint for these processes should be around the mass of the W-boson, 80.3 GeV. For the signal points where the $\tilde{\chi}_1^\pm \tilde{\chi}_2^0$ are expected to have masses to the order of several hundred GeV, their m_T distributions are flatter with a larger tail and a much higher kinematic endpoint, which is shown in Figure 8.4(a). Figure 8.4(b) shows the optimal cut at above 100 GeV indicated by the magenta line.

8.6.1.4 Invariant Mass of the SFOS leptons

The invariant mass of the SFOS pair of leptons is useful for discriminating for or against processes that contain an on-shell Z-boson which decays to a pair of SFOS leptons with an invariant mass close to the mass of the Z-boson. Processes that contain an on-shell Z-boson have a peak in their m_{SFOS} distribution around 91.2 GeV. The leptons originating from decays via intermediate sleptons do not exhibit this behaviour and show no distinct peak in the distribution. For high mass signal points, the leptons in the final state are hard- p_T and as such will have a large invariant mass, resulting in large tails as shown in Figure 8.5(a). Figure 8.5(b) shows that a cut above 101.2 GeV is effective at removing the Z-containing backgrounds, whilst having minimal effect on the signal yields.

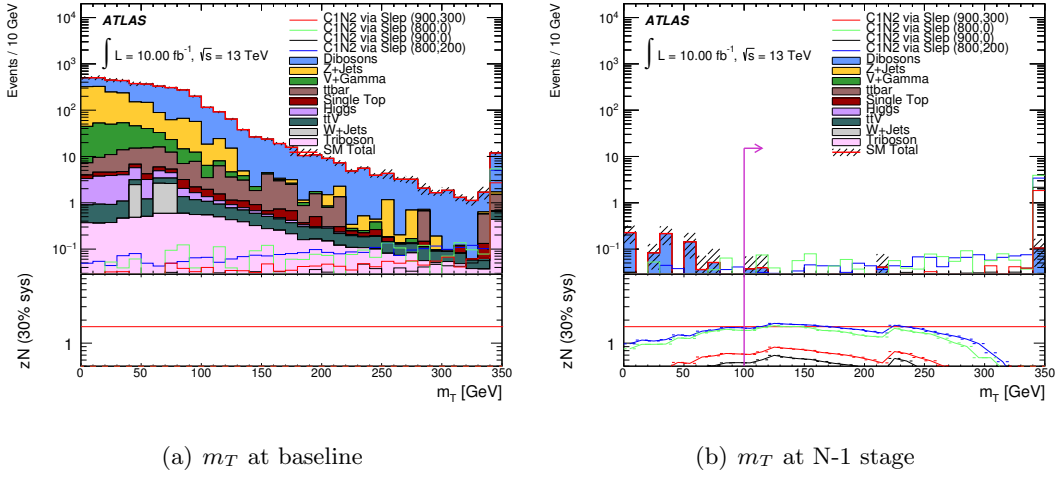


Figure 8.4: Baseline and N-1 distributions for the transverse mass. The Z_N curves are produced assuming a flat 30% relative uncertainty to account for systematic uncertainties.

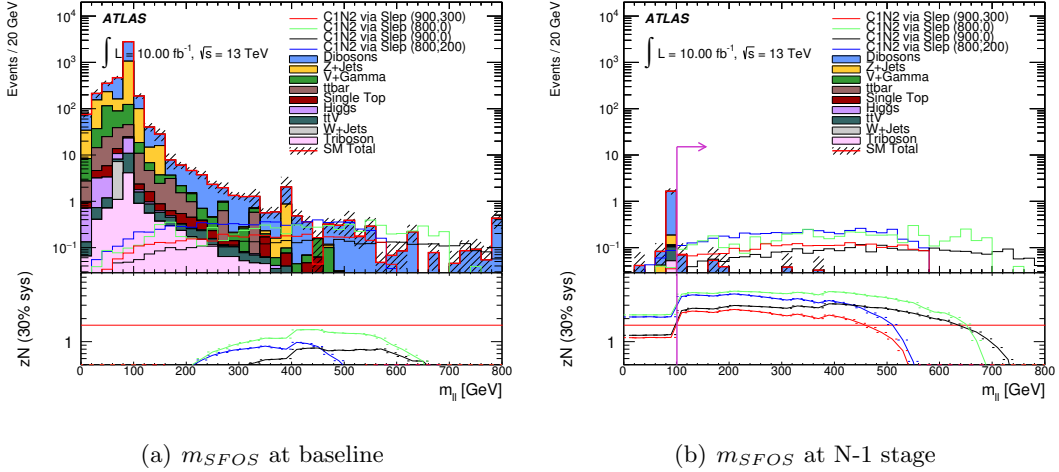


Figure 8.5: Baseline and N-1 distributions for the invariant mass of the SFOS lepton pair. The Z_N curves are produced assuming a flat 30% relative uncertainty to account for systematic uncertainties.

8.6.1.5 Sum of the transverse momentum of the three leptons

This variable is used to select the high- p_T leptons produced from high mass $\tilde{\chi}_1^\pm \tilde{\chi}_2^0$ decays. The benchmark signal point distributions start at ≈ 300 GeV, whereas the SM background starts at 20 GeV as shown in Figure 8.6(a). The N-1 distribution in Figure 8.6(b) shows that a cut of above 400 GeV is effective at maximising the significance for the high mass points and reducing the remaining diboson background contribution.

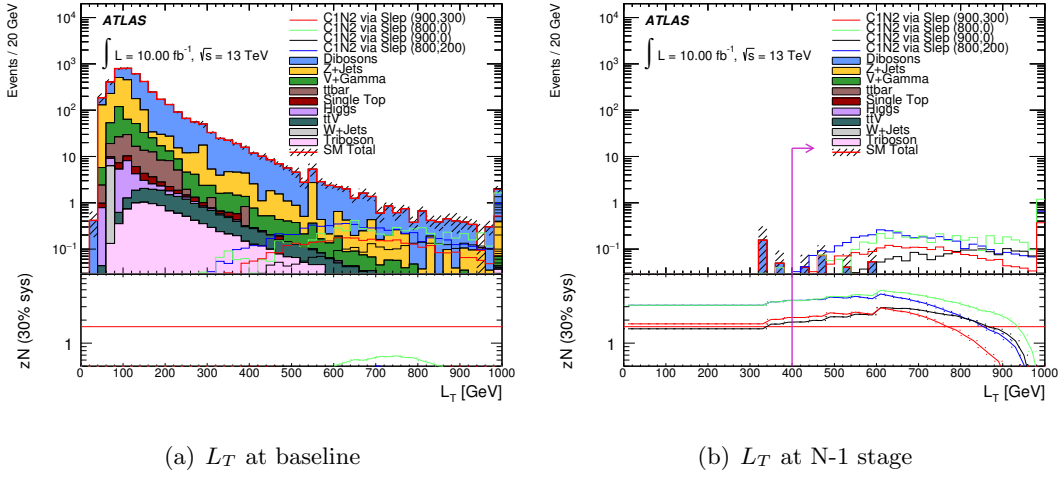


Figure 8.6: Baseline and N-1 distributions for the sum of the transverse momentum of the three leptons. The Z_N curves are produced assuming a flat 30% relative uncertainty to account for systematic uncertainties.

8.6.1.6 Polar angle between SFOS pair of leptons and the missing transverse momentum

The topology of the E_T^{miss} and the SFOS pair of leptons can be exploited as these final state objects are produced back-to-back in signal events due to the high p_T of the leptons and large E_T^{miss} from the invisible $\tilde{\chi}_1^0$ carrying the majority of the transverse momentum in the final state. This is shown in Figure 8.7(a), where the signal distributions dominate bins close to π , whereas the SM background distributions are comparatively flat. The

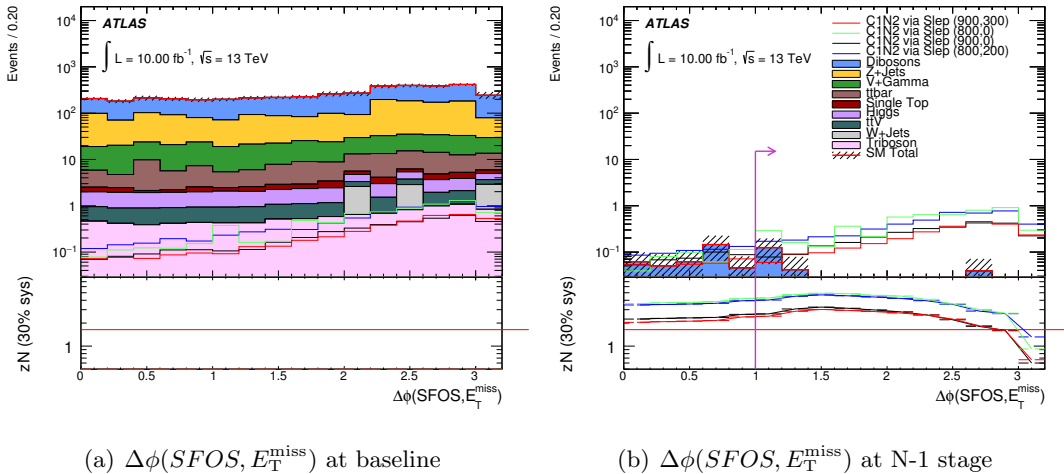


Figure 8.7: Baseline and N-1 distributions $\Delta\phi$ between the SFOS pair of leptons and missing transverse momentum. The Z_N curves are produced assuming a flat 30% relative uncertainty to account for systematic uncertainties.

N-1 distribution shown in Figure 8.7(b) shows an optimal cut placed at 1 is effective at

removing the remaining diboson background contribution.

8.6.2 Intermediate Mass Signal Region - SR3 ℓ -I

8.6.2.1 Transverse momentum of third-leading lepton

Unlike the high mass signal points, the distribution of the intermediate mass points in p_T is softer and more like the SM background, with similar peaks around 20-30 GeV as shown in Figure 8.8(a). Consequently, a softer cut on this variable is optimal, to preserve the signal yields. The N-1 distribution shown in Figure 8.8(b) shows the most optimal cut for the points considered is at 30 GeV.

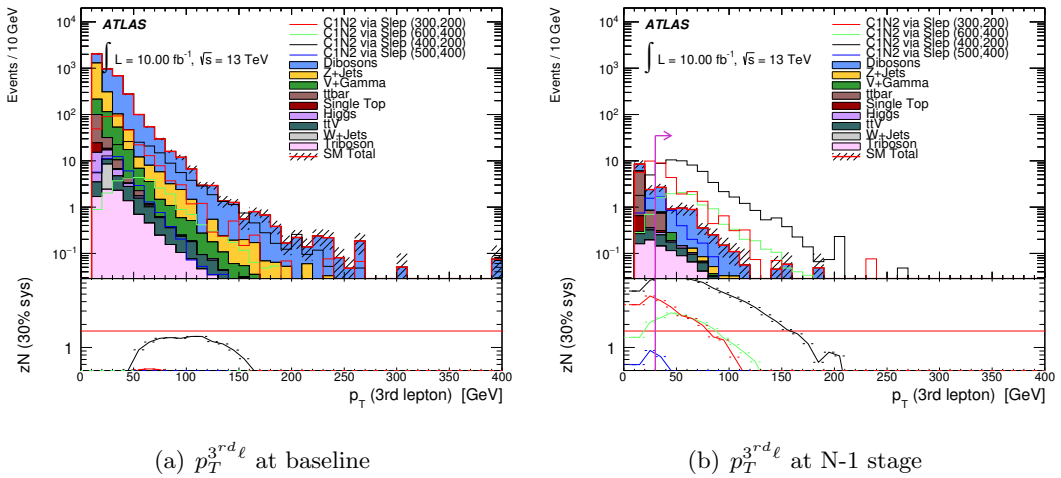


Figure 8.8: Baseline and N-1 distributions for the transverse momentum of the 3rd lepton. The Z_N curves are produced assuming a flat 30% relative uncertainty to account for systematic uncertainties.

8.6.2.2 Missing Transverse Energy

Similar to the high mass signal points, the E_T^{miss} distribution of the intermediate mass points are flatter than the SM background with large tails, due to the heavy neutralinos produced in the final state. As the requirement on the p_T of the third lepton is softer, the E_T^{miss} cut can be tighter to remove the Z+jets and diboson contributions, as shown in Figure 8.9(b), a cut of above 120 GeV is optimal.

8.6.2.3 Transverse Mass

The transverse mass is strongly correlated to the E_T^{miss} in an event, as the mass of the decaying particles increases, the amount of energy available to the final state particles increases. Consequently, the distribution of m_T shows similar behaviour to E_T^{miss} for the

intermediate mass points. A similar cut of above 110 GeV is used to discriminate against the diboson SM background process, as shown in Figure 8.10(b).

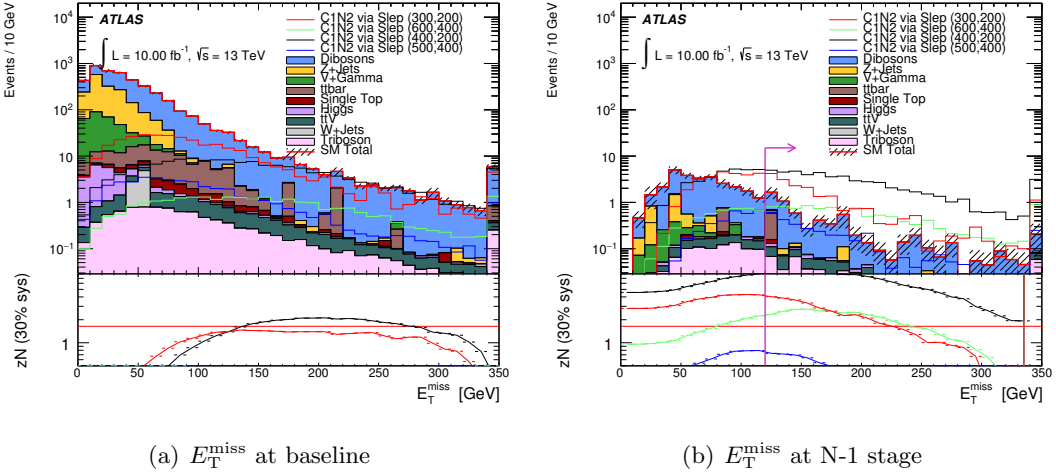


Figure 8.9: Baseline and N-1 distributions for the missing transverse momentum. The Z_N curves are produced assuming a flat 30% relative uncertainty to account for systematic uncertainties.

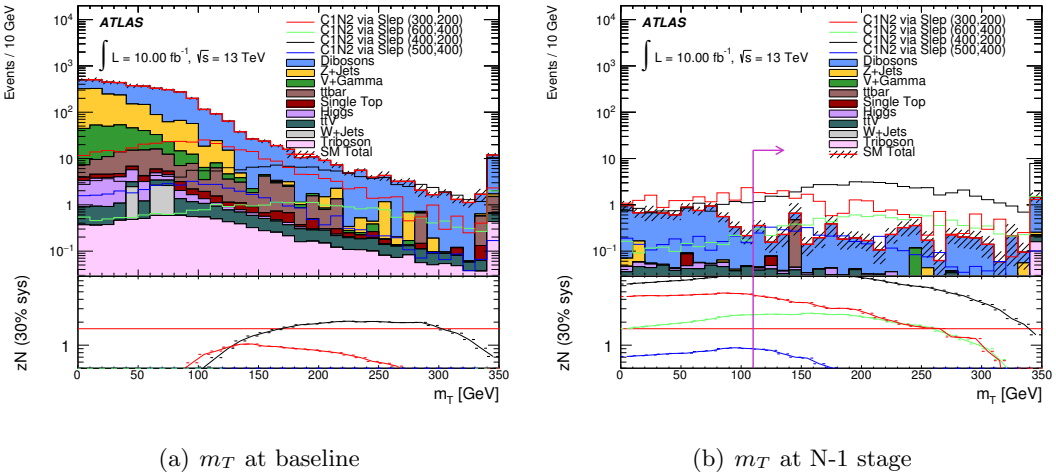


Figure 8.10: Baseline and N-1 distributions for the transverse mass. The Z_N curves are produced assuming a flat 30% relative uncertainty to account for systematic uncertainties.

8.6.2.4 Invariant Mass of the SFOS leptons

The leptons produced in the final state are significantly softer for the intermediate mass points than the high mass points. The m_{SFOS} spectrum is softer and the signal yields are concentrated in a much smaller range of up to 200 GeV as shown in Figure 8.11(a). In order to discriminate against the Z-containing backgrounds, events with a SFOS pair of leptons with an invariant mass within 10 GeV of on-shell Z-boson mass are vetoed.

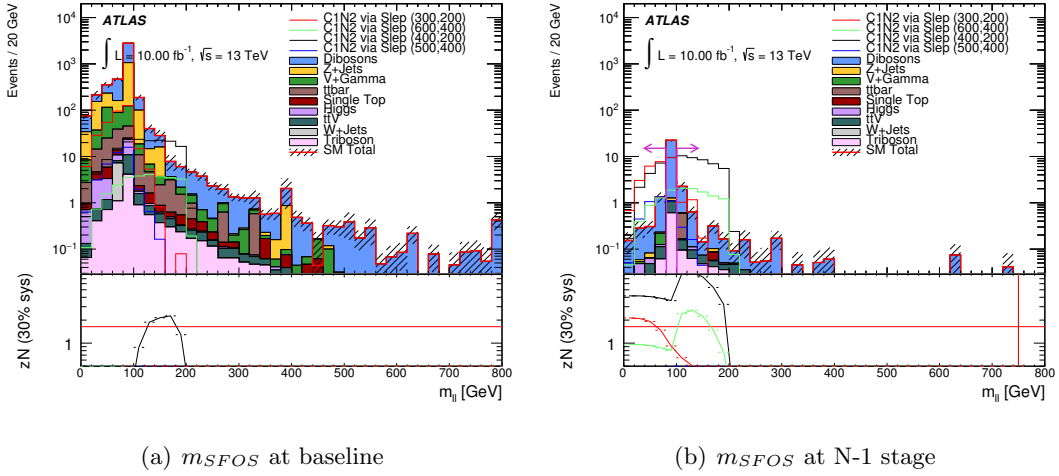


Figure 8.11: Baseline and N-1 distributions for the invariant mass of the SFOS lepton pair. The Z_N curves are produced assuming a flat 30% relative uncertainty to account for systematic uncertainties.

8.6.3 Signal Region Summary

The preliminary signal regions developed for an early 13 TeV analysis are defined in Table 8.5. The cut-by-cut yields for SR3 ℓ -H and SR3 ℓ -I are given in Tables 8.6 and 8.7 respectively. Table 8.6 shows the cut selection in the high mass SR reduces the total SM background from ≈ 4000 events to < 1 event. The dominating background in this SR is the diboson processes, which consist of ZZ, WZ and WW. Considering the benchmark signal points yields, the SR3 ℓ -H signal acceptance is $\approx 60\%$ with respect to baseline yields. This shows that this signal region is effective at preserving the high mass signal points, by targeting the tails of the distributions of the cut variables, where these signal points dominate.

Table 8.7 shows the cut selection in the intermediate mass SR reduces the total SM background from ≈ 4000 events to 6.5 events. The dominating background in this SR are the diboson and triboson processes. Considering the benchmark signal point yields, the SR3 ℓ -I signal acceptance varies from 10-35%. Although the signal acceptance for this region is lower than for SR3 ℓ -H, the production cross-section for the light mass points are higher, leading to overall higher yields than the high mass points.

8.7 Significance in Signal Regions

An estimation of the performance of each signal region for the chosen SUSY scenarios made by calculating the significance Z_N for each mass point and filling a three dimensional

Table 8.5: Three lepton Signal Regions. Units are in GeV.

Variable	SR3 ℓ -I	SR2 ℓ -H
lepton $p_T >$	30	90
$E_T^{\text{miss}} >$	120	80
$m_T >$	110	100
$m_{SFOS} >$	81.2 (< 101.2)	101.2
$L_T >$	–	400
$\Delta\phi(SFOS, E_T^{\text{miss}}) >$	–	1

histogram with the significance as a function of the parameter space. The x axis displays the $\tilde{\chi}_1^\pm \tilde{\chi}_2^0$ masses, the y axis displays the $\tilde{\chi}_1^0$ mass and the z axis displays the significance. A significance value of 1.64 or greater corresponds to an exclusion of the SUSY scenario considered with 95% confidence level [147] [148].

8.7.1 Significance in Intermediate Mass Signal Region

Figure 8.12 displays the two-dimensional histogram for the SR3 ℓ -I scenario where a flat 30% relative uncertainty is considered in the Z_N calculation. This signal region provides sensitivity to the intermediate mass signal points. $\tilde{\chi}_1^\pm \tilde{\chi}_2^0$ masses up to 700 GeV with $\tilde{\chi}_1^0$ masses ≤ 400 GeV are excluded. There is sensitivity to the near mass-degenerate region with $\tilde{\chi}_1^\pm \tilde{\chi}_2^0$ masses up to 400 GeV excluded with a mass splitting of 50 GeV. The gain in sensitivity to the low mass points is achieved by having less stringent cuts on the p_T of the leptons and vetoing events with two leptons close to the Z-mass, as the leptons from this scenario originate from sleptons. As the Z-mass window is small - 20 GeV - the majority of the signal event yields are retained.

Sample	Baseline	$p_T^{3rd\ell} > 90$	$m_T > 100$	$E_T^{\text{miss}} > 80$	$m_{SFOS} > 101.2$	$L_T > 400$	$\Delta\phi(SFOS, E_T^{\text{miss}}) > 1$
$t\bar{t}$	93.69 ± 6.77	0.0 ± 0.0	0.0 ± 0.0	0.0 ± 0.0	0.0 ± 0.0	0.0 ± 0.0	0.0 ± 0.0
Single top	11.48 ± 0.63	0.0 ± 0.0	0.0 ± 0.0	0.0 ± 0.0	0.0 ± 0.0	0.0 ± 0.0	0.0 ± 0.0
$Z + \text{jets}$	1370.83 ± 104.82	3.83 ± 1.53	0.97 ± 0.68	0.22 ± 0.08	0.02 ± 0.01	0.02 ± 0.01	0.0 ± 0.0
$W + \text{jets}$	6.01 ± 3.51	0.0 ± 0.0	0.0 ± 0.0	0.0 ± 0.0	0.0 ± 0.0	0.0 ± 0.0	0.0 ± 0.0
Diboson	2427.96 ± 18.5	25.17 ± 1.65	8.08 ± 0.81	3.87 ± 0.49	0.76 ± 0.22	0.49 ± 0.14	0.19 ± 0.09
$t\bar{t} + V$	10.41 ± 0.09	0.4 ± 0.02	0.19 ± 0.01	0.13 ± 0.01	0.04 ± 0.01	0.03 ± 0.01	0.02 ± 0.0
V/γ	261.65 ± 4.65	1.14 ± 0.09	0.34 ± 0.05	0.03 ± 0.02	0.0 ± 0.0	0.0 ± 0.0	0.0 ± 0.0
Higgs	20.4 ± 0.1	0.03 ± 0.01	0.01 ± 0.01	0.01 ± 0.01	0.0 ± 0.0	0.0 ± 0.0	0.0 ± 0.0
Triboson	9.64 ± 0.09	0.33 ± 0.02	0.22 ± 0.01	0.17 ± 0.01	0.09 ± 0.01	0.07 ± 0.01	0.04 ± 0.01
Total background	4212.06 ± 106.82	30.9 ± 2.25	9.82 ± 1.05	4.42 ± 0.49	0.92 ± 0.22	0.61 ± 0.14	0.25 ± 0.09
<hr/>							
via Slep (800,200)	7.72 ± 0.12	5.93 ± 0.11	5.57 ± 0.1	5.39 ± 0.1	5.17 ± 0.1	5.11 ± 0.1	4.58 ± 0.09
via Slep (900,0)	4.1 ± 0.06	3.36 ± 0.06	3.19 ± 0.06	3.12 ± 0.06	3.06 ± 0.06	3.05 ± 0.06	2.67 ± 0.05
via Slep (800 ,0)	7.59 ± 0.38	6.02 ± 0.34	5.73 ± 0.33	5.61 ± 0.33	5.48 ± 0.33	5.39 ± 0.32	5.0 ± 0.31
via Slep (900 , 300)	4.06 ± 0.06	3.15 ± 0.06	2.94 ± 0.05	2.85 ± 0.05	2.74 ± 0.05	2.72 ± 0.05	2.43 ± 0.05

Table 8.6: MC estimated yields per cut in high mass signal region SR3 ℓ -H. The uncertainties are statistical only.

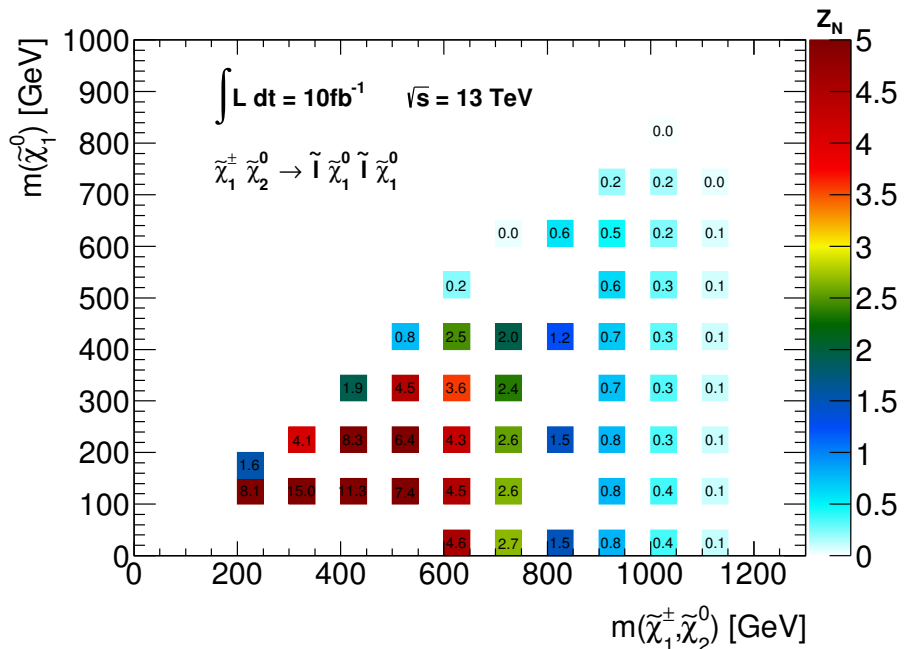
8.7.2 Significance in High Mass Signal Region

Figure 8.13(a) displays the two-dimensional histogram for the SR3 ℓ -H scenario where a flat 30% relative uncertainty is considered in the Z_N calculation. This signal region provides sensitivity to the high mass signal points, where $\tilde{\chi}_1^\pm \tilde{\chi}_2^0$ masses up to 1 TeV are excluded. The smallest mass splitting of 50 GeV, suffers in this region, with no sensitivity seen for the points closest to the mass-degenerate region. This is due to low p_T spectra of the final state products in this region, which are removed with the stringent cuts in the high mass SR. The decrease in significance with increasing $\tilde{\chi}_1^\pm \tilde{\chi}_2^0$ mass is caused by decreasing cross-section for the considered process. Figure 8.13(b) shows the sensitivity with 100% relative uncertainty considered in the Z_N calculation, this adjustment was considered due to the low statistics in this signal region, which would lead to large systematic uncertainties on the data driven fake estimation. Using 100% relative uncertainty gives a “worst case scenario” in terms of sensitivity. $\tilde{\chi}_1^\pm \tilde{\chi}_2^0$ masses can be excluded up to 900 GeV with this scenario, which corresponds to a 100 GeV worsening of exclusion reach compared to the conservative 30% relative uncertainty scenario.

8.7.3 Combined Significance in Signal Regions

The two signal regions offer sensitivity to different regions of the parameter space, the signal regions are not orthogonal and are can not be combined. To present the best case with the two signal regions, the best significance is shown per point, considering SR3 ℓ -H and SR3 ℓ -I in Figure 8.14(a). The best signal region per point is shown in Figure 8.14(b). This shows that SR3 ℓ -H dominates in providing sensitivity to $\tilde{\chi}_1^\pm \tilde{\chi}_2^0$ masses above 500 GeV and SR3 ℓ -I dominates in providing sensitivity to the $\tilde{\chi}_1^\pm \tilde{\chi}_2^0$ masses below 500 GeV and the near mass degenerate region.

Sensitivity to electroweak SUSY production profits from increasing luminosity, given the relatively low production cross-section compared to strong SUSY production. With the combination of increasing luminosity and variables such as E_T^{miss} and m_T , which offer more discriminatory power at higher beam energies, electroweak production of SUSY will continue to be well motivated and could provide an insight into BSM physics in future LHC data.

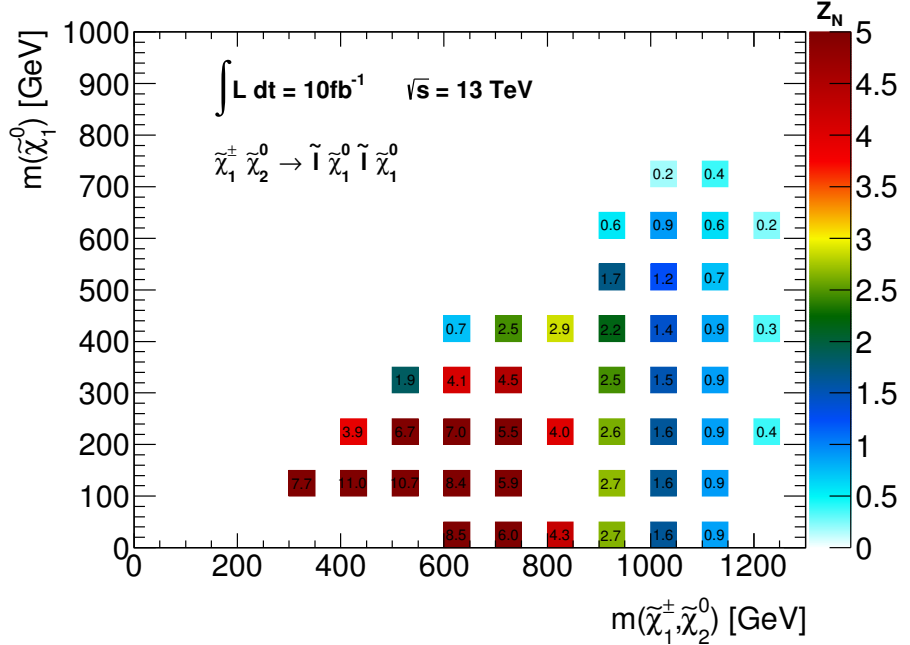


(a) Significance with MC-only estimates - 30% relative uncertainty.

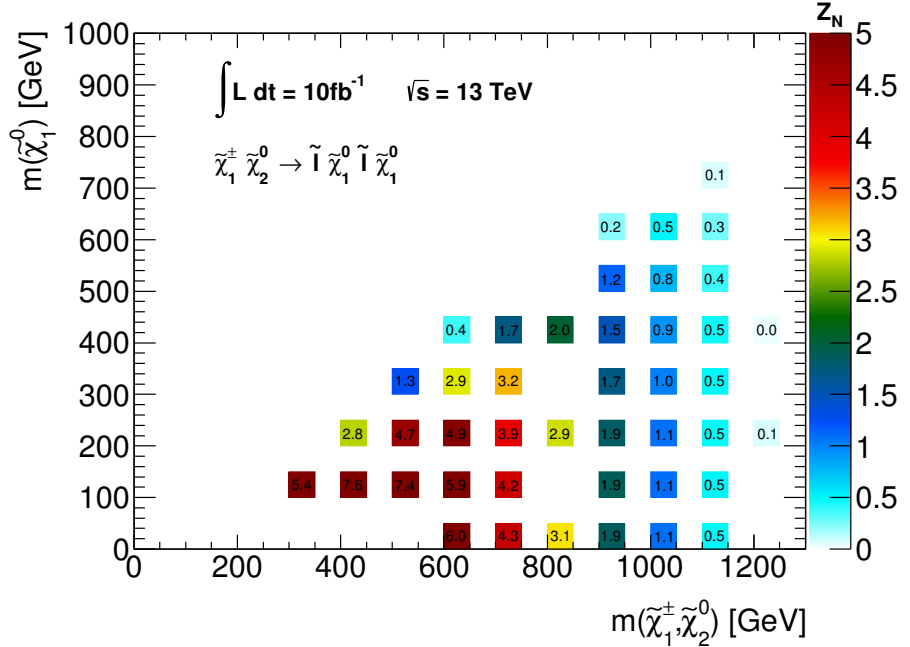
Figure 8.12: Significance in SR3 ℓ -I. The calculation of the significance values are based on MC-only for all SM backgrounds. The uncertainty in the MC background estimate is 30% flat uncertainty to cover systematic uncertainty.

Sample	Baseline	$p_T^{3^{rd}\ell} > 30$	$E_T^{\text{miss}} > 120$	$m_T > 110$	$ m_{SFOS} - m_Z > 10$
$t\bar{t}$	93.69 ± 6.77	5.2 ± 1.57	0.93 ± 0.66	0.42 ± 0.42	0.42 ± 0.42
Single top	11.48 ± 0.63	0.57 ± 0.14	0.07 ± 0.05	0.03 ± 0.03	0.03 ± 0.03
Z+jets	1370.83 ± 104.82	99.1 ± 15.46	-0.18 ± 0.89	0.23 ± 0.09	0.1 ± 0.07
W+jets	6.01 ± 3.51	0.0 ± 0.0	0.0 ± 0.0	0.0 ± 0.0	0.0 ± 0.0
Diboson	2427.96 ± 18.5	1009.66 ± 12.97	68.61 ± 1.78	25.88 ± 1.17	4.9 ± 0.55
$t\bar{t} + V$	10.41 ± 0.09	6.19 ± 0.07	1.54 ± 0.03	0.75 ± 0.02	0.3 ± 0.02
V/ γ	261.65 ± 4.65	65.55 ± 2.22	0.13 ± 0.09	0.12 ± 0.09	0.1 ± 0.09
Higgs	20.4 ± 0.1	2.51 ± 0.05	0.18 ± 0.02	0.1 ± 0.02	0.08 ± 0.02
Triboson	9.64 ± 0.09	5.53 ± 0.07	1.63 ± 0.03	1.14 ± 0.03	0.54 ± 0.02
Total background	4212.06 ± 106.82	1194.31 ± 20.37	72.91 ± 2.1	28.69 ± 1.25	6.48 ± 0.7
via Slep (500,400)	41.22 ± 0.6	24.17 ± 0.47	7.14 ± 0.26	4.48 ± 0.21	3.43 ± 0.18
via Slep (400,200)	155.47 ± 1.93	137.16 ± 1.82	75.5 ± 1.36	64.3 ± 1.25	54.76 ± 1.15
via Slep (600 ,400)	26.72 ± 0.33	23.81 ± 0.31	14.75 ± 0.25	12.98 ± 0.23	11.06 ± 0.21
via Slep (300, 200)	331.23 ± 4.96	192.17 ± 3.81	51.21 ± 2.01	29.31 ± 1.52	20.61 ± 1.27

Table 8.7: MC estimated yields per cut in intermediate mass signal region SR3 ℓ -I. The uncertainties are statistical only. Negative events for Z+jets due to negative weights at NLO assigned by SHERPA.

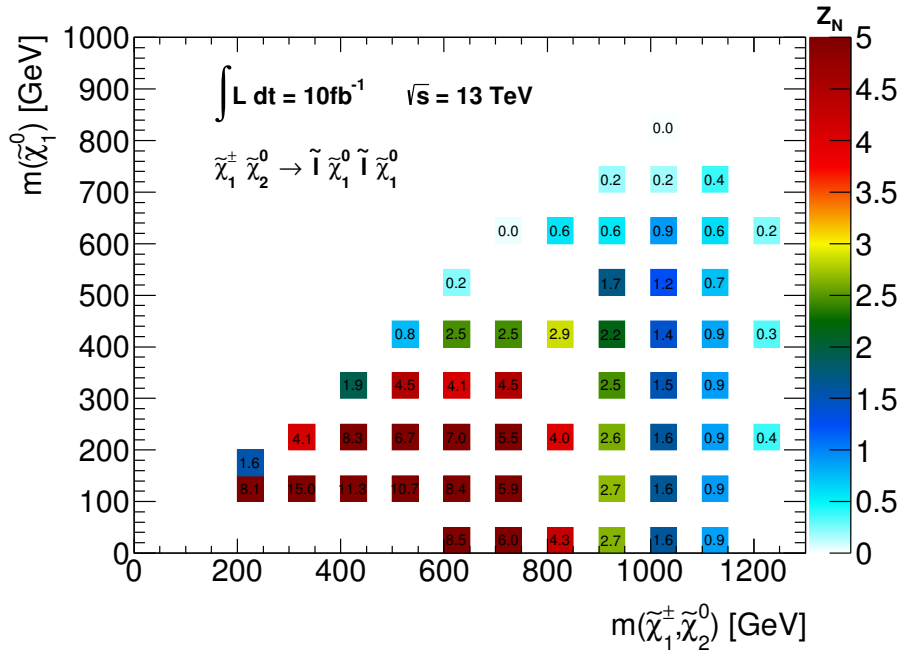


(a) Significance with MC-only estimates - 30% relative uncertainty.

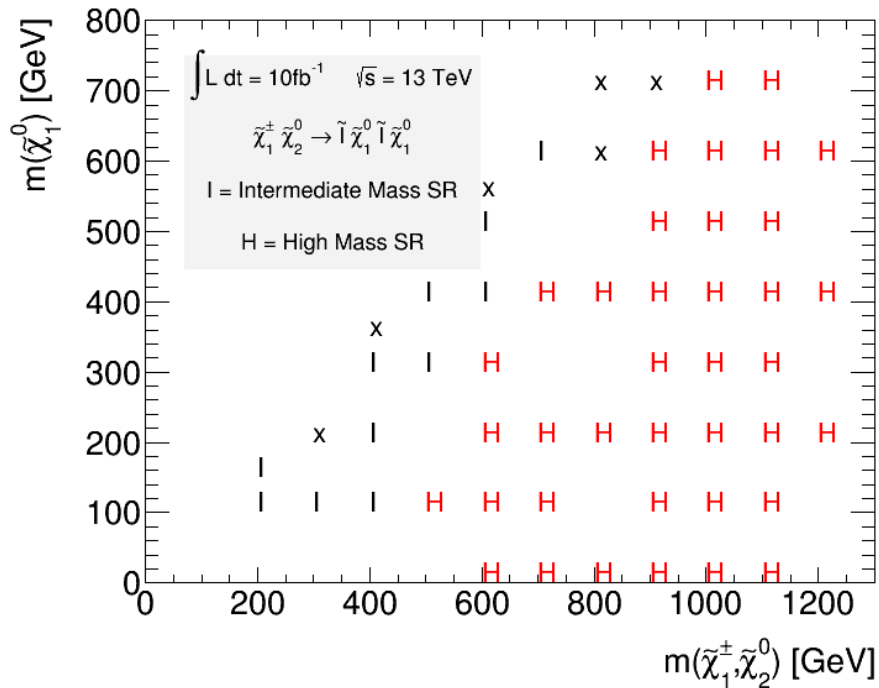


(b) Significance with MC-only estimates - 100% relative uncertainty.

Figure 8.13: Significance in SR3 ℓ -H. The calculation of the significance values are based on MC-only for all SM backgrounds. The uncertainty in the MC background estimate is (a) 30% or (b) 100% flat uncertainty to cover systematic uncertainty.



(a) Best Significance per point



(b) Best Signal Region per point

Figure 8.14: (a) Best expected significance and (b) best signal region per $\tilde{\chi}_1^\pm \tilde{\chi}_2^0$ production via $\tilde{\ell}$ point in SR3 ℓ . The calculation of the significance values are based on MC-only for all SM backgrounds. The uncertainty in the MC background estimate is a 30% flat uncertainty to cover systematic uncertainty. In (b) H refers to the SR3 ℓ -H signal region, I refers to the SR3 ℓ -I signal region and X indicates a zero Z_N value for both regions.

Chapter 9

Conclusions

This thesis presents results produced by ATLAS on the search for the electroweak production of supersymmetric particles in events with three leptons and missing transverse energy, with particular focus on compressed scenarios, using the full $\mathcal{L} = 20.3 \text{ fb}^{-1}$ dataset at $\sqrt{s} = 8 \text{ TeV}$.

R-parity conserving supersymmetric scenarios were targeted with optimised selection criteria applied to events containing three electrons or muons. For scenarios where the mass of the $\tilde{\chi}_1^\pm, \tilde{\chi}_2^0$ is near degenerate with the $\tilde{\chi}_1^0$, low- p_T leptons and an initial-state-radiation jet were required in the event selection. No significant deviation was seen between observed data and Standard Model expectations, within the statistical and systematic uncertainties. A statistical interpretation of the results was conducted in order to set 95% CL exclusion limits on the mass parameters of the models considered, as well as model-independent limits on the visible cross-section for relevant beyond-the-Standard Model scenarios.

Simplified models were considered where pure-wino $\tilde{\chi}_1^\pm \tilde{\chi}_2^0$, $\tilde{\chi}_1^\pm \tilde{\chi}_1^\mp$ and pure higgsino $\tilde{\chi}_2^0 \tilde{\chi}_3^0$ pairs are produced, which then decay with 100% branching fraction to three-lepton final states. Limits at 95% CL were extracted for chargino and neutralino decays via intermediate sleptons, by combining results from this (compressed spectra) analysis, the recent same-sign two-lepton analysis [3] and previously published analyses [132]. Chargino and heavy neutralino masses up to 740 GeV were excluded at 95% CL for massless $\tilde{\chi}_1^0$. This improves on existing mass limits by approximately 20 GeV. More significant improvements were seen in the region of the parameter space where the $\tilde{\chi}_1^\pm, \tilde{\chi}_2^0$ are nearly degenerate with the $\tilde{\chi}_1^0$. In this compressed region, the main improvements come from the analysis performed by the author and presented in this thesis.

Looking forward to Run-2, a first optimisation of an event selection for electroweak production of supersymmetric particles at 13 TeV was conducted. To that purpose, Monte

Carlo simulated events were used, based on a projected integrated luminosity of 10 fb^{-1} in 13 TeV data. The preliminary 13 TeV analysis targets two distinct scenarios, with different regimes for mass splittings between the $\tilde{\chi}_1^\pm \tilde{\chi}_2^0$ and $\tilde{\chi}_1^0$. At the time of writing, the signal region optimisation for $\tilde{\chi}_1^\pm \tilde{\chi}_2^0$ production with decays via intermediate sleptons was still ongoing, with improvements expected on the selection presented in the last chapter of this thesis. With sensitivity to electroweak SUSY production expected to improve with luminosity, the ATLAS detector will continue to probe SUSY beyond the limits set in Run-1.

Appendix A

Multilepton Trigger Results

A.1 Introduction

This section provides one-dimensional efficiencies and scale factors for the leptonic triggers used in the analysis described in Chapter 6. The efficiencies are for a given leptonic leg of the trigger chain are derived using the Tag and Probe method as described in Section 5.2. These are shown as a function of p_T , η and number of primary vertices. The scale factors are defined as:

$$sf_{trig} = \frac{\epsilon_{trig}^{Data}}{\epsilon_{trig}^{MC}}, \quad (\text{A.1})$$

and are shown for each trigger as a function of the aforementioned variables. The trigger efficiency scale factors are found to be 1 within a 29% uncertainty for the leptonic triggers, which are treated as a systematic in the analysis. These results are given for reference only.

A.2 Three-Lepton Trigger Efficiencies

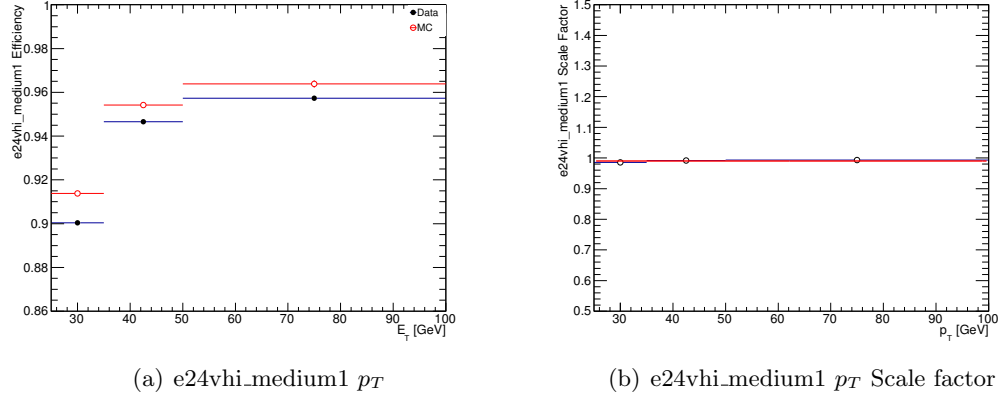


Figure A.1: Trigger efficiency for EFe24vhi_medium1 as a function of electron p_T in MC and data and efficiency scale factor. Uncertainties are statistical.

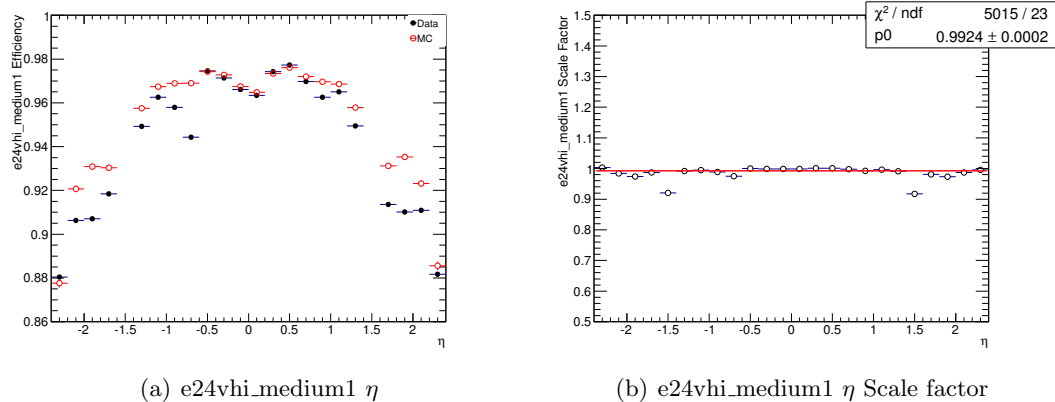


Figure A.2: Trigger efficiency for EFe24vhi_medium1 as a function of electron η in MC and data and efficiency scale factor. Uncertainties are statistical.

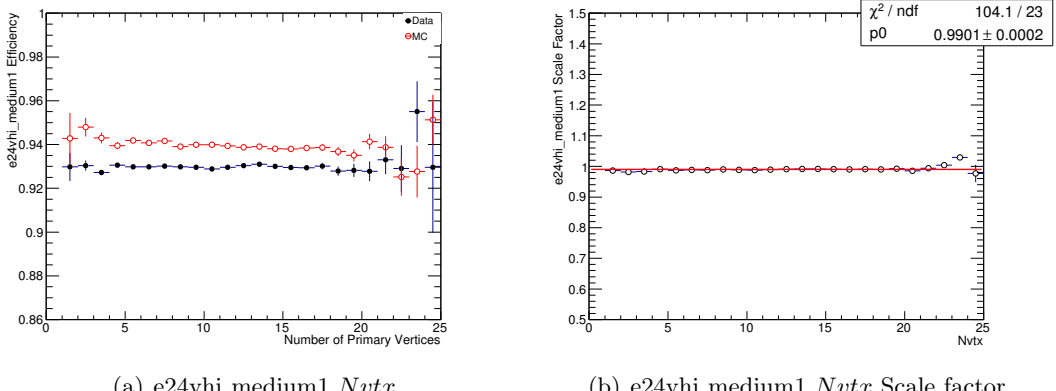


Figure A.3: Trigger efficiency for EFe24vhi_medium1 as a function of electron $Nvtx$ in MC and data and efficiency scale factor. Uncertainties are statistical.

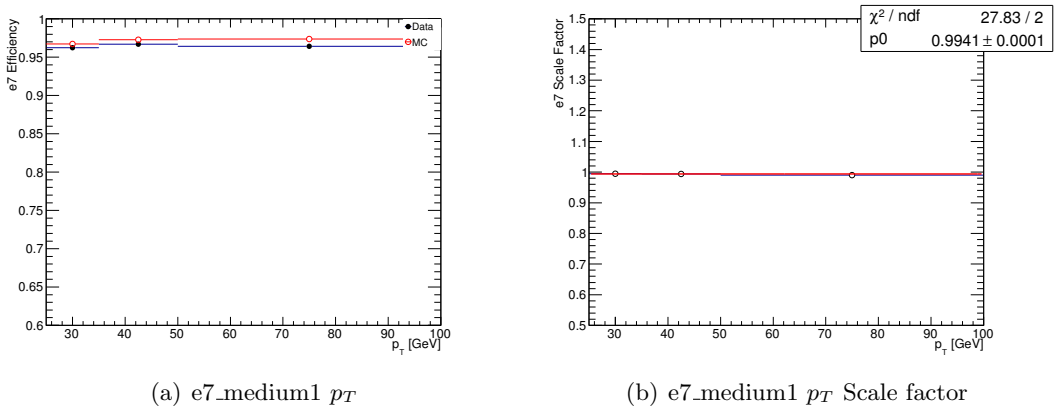


Figure A.4: Trigger efficiency for EFe7_medium1 as a function of electron p_T in MC and data and efficiency scale factor. Uncertainties are statistical.

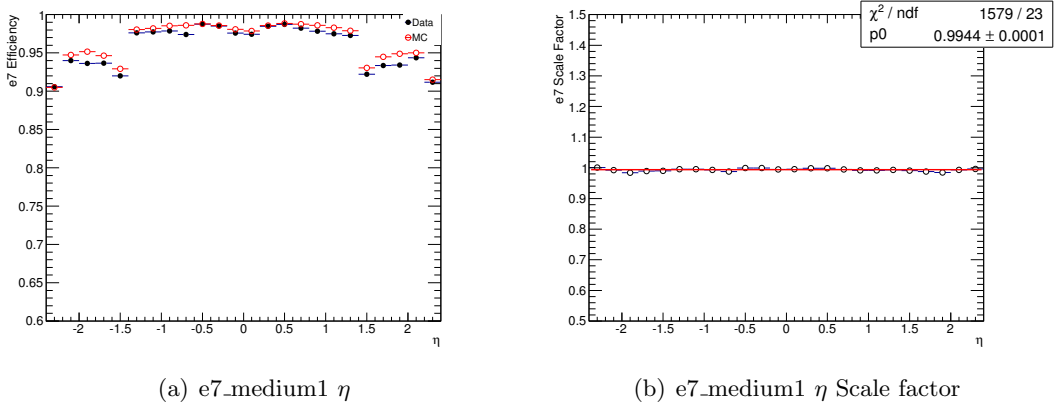


Figure A.5: Trigger efficiency for EFe7_medium1 as a function of electron η in MC and data and efficiency scale factor. Uncertainties are statistical.

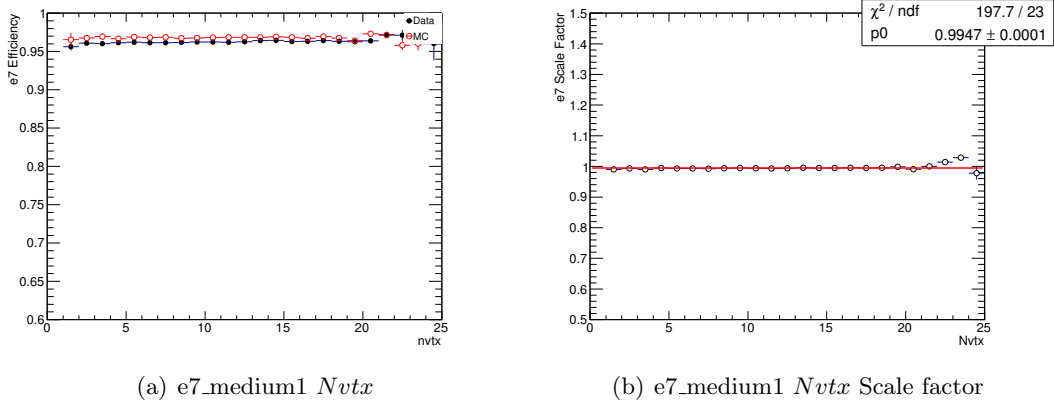


Figure A.6: Trigger efficiency for EFe7_medium1 as a function of electron N_{vtx} in MC and data and efficiency scale factor. Uncertainties are statistical.

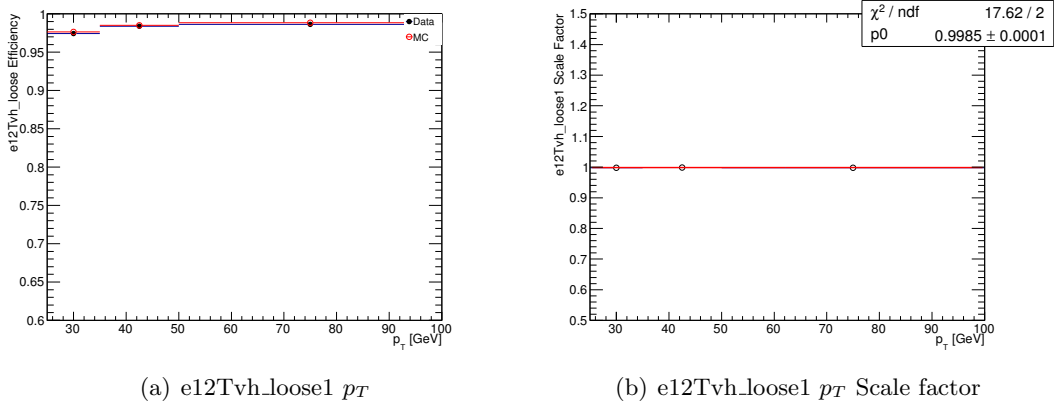


Figure A.7: Trigger efficiency for EFe12Tvh_loose1 as a function of electron p_T in MC and data and efficiency scale factor. Uncertainties are statistical.

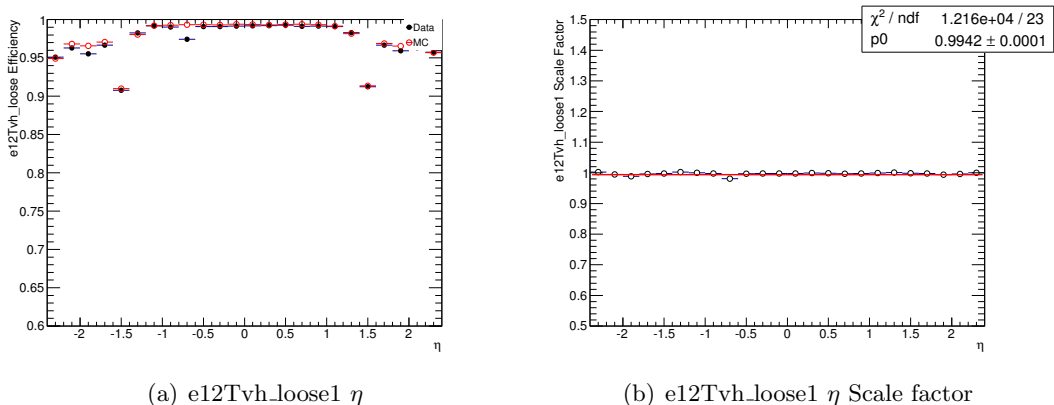


Figure A.8: Trigger efficiency for EFe12Tvh_loose1 as a function of electron η in MC and data and efficiency scale factor. Uncertainties are statistical.

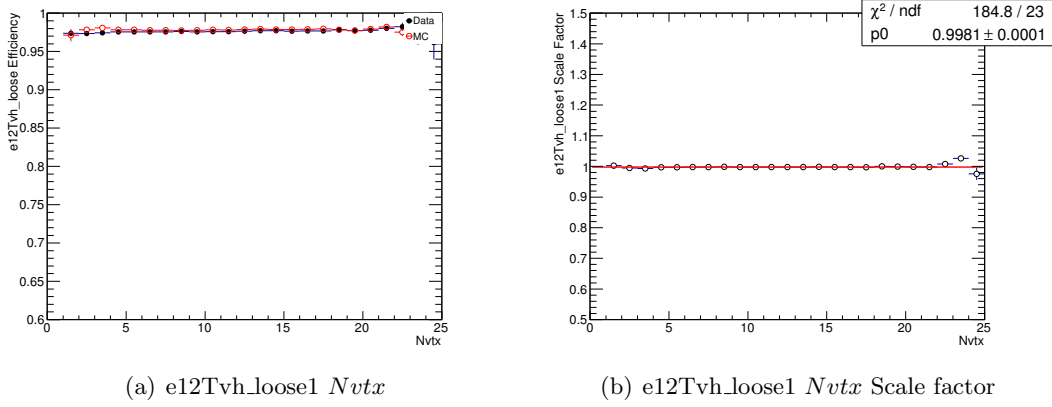


Figure A.9: Trigger efficiency for EFe12Tvh_loose1 as a function of electron $Nvtx$ in MC and data and efficiency scale factor. Uncertainties are statistical.

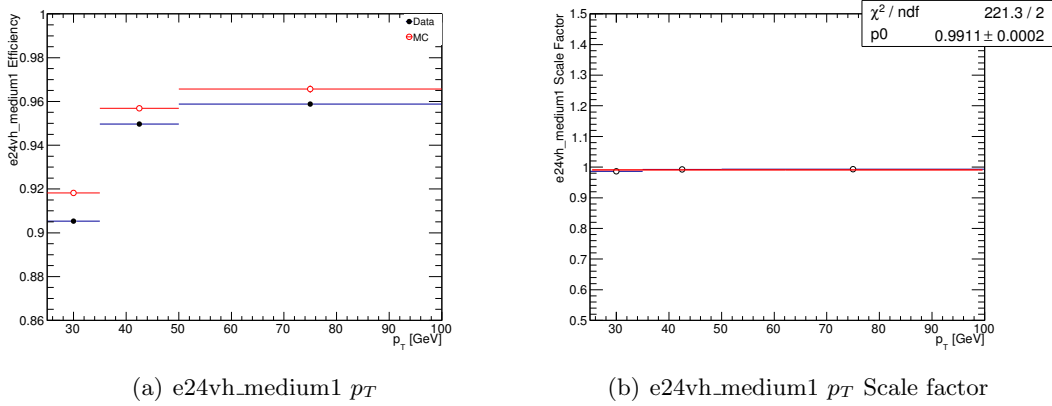


Figure A.10: Trigger efficiency for EFe24vh_medium1 as a function of electron p_T in MC and data and efficiency scale factor. Uncertainties are statistical.

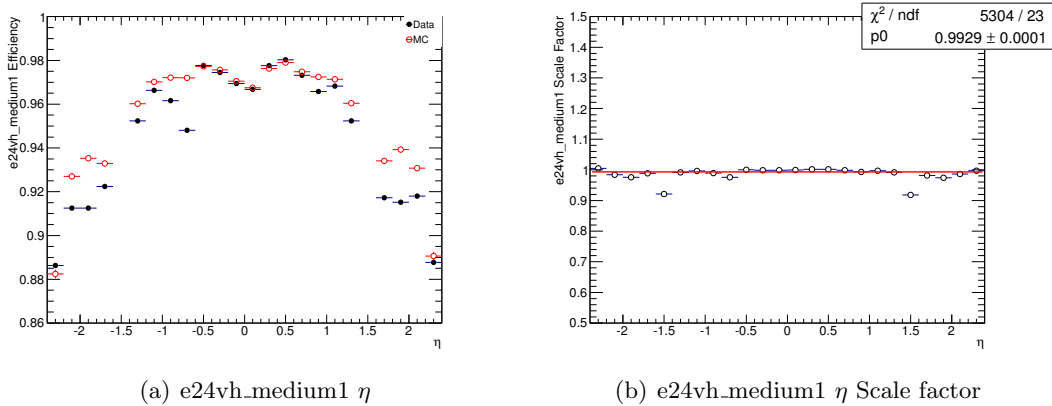


Figure A.11: Trigger efficiency for EFe24vh_medium1 as a function of electron η in MC and data and efficiency scale factor. Uncertainties are statistical.

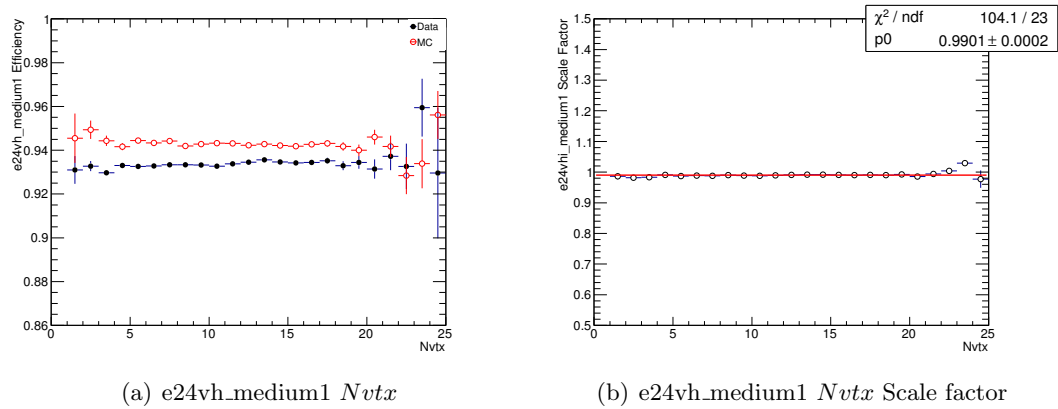


Figure A.12: Trigger efficiency for EFe24vh_medium1 as a function of electron N_{vtx} in MC and data and efficiency scale factor. Uncertainties are statistical.

A.2.0.1 Muon Trigger Efficiencies

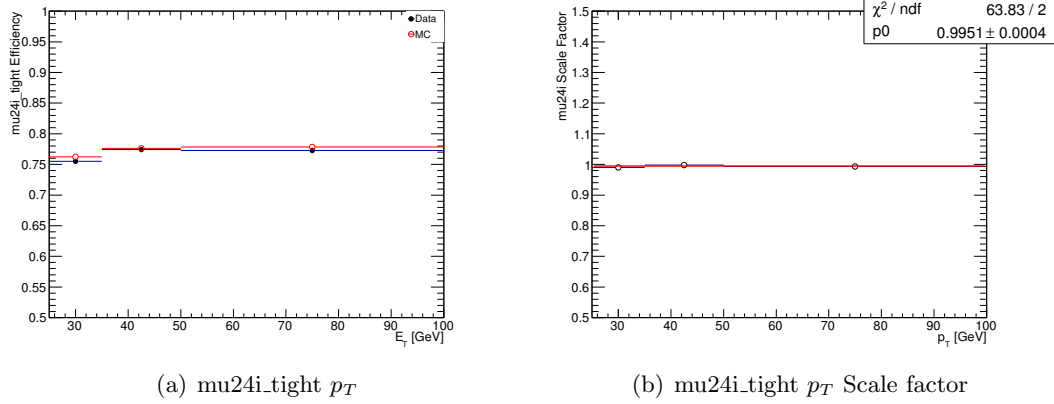


Figure A.13: Trigger efficiency for EFmu24i_tight as a function of muon p_T in MC and data and efficiency scale factor. Uncertainties are statistical.

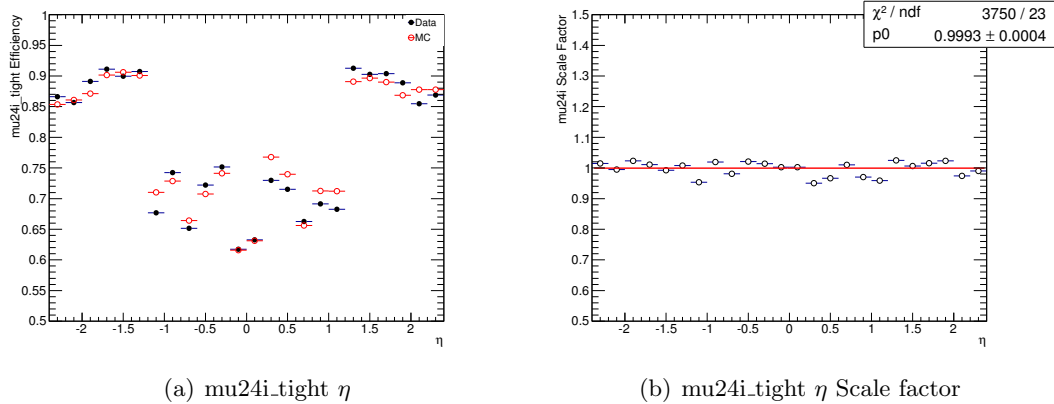


Figure A.14: Trigger efficiency for EFmu24i_tight as a function of muon η in MC and data and efficiency scale factor. Uncertainties are statistical.

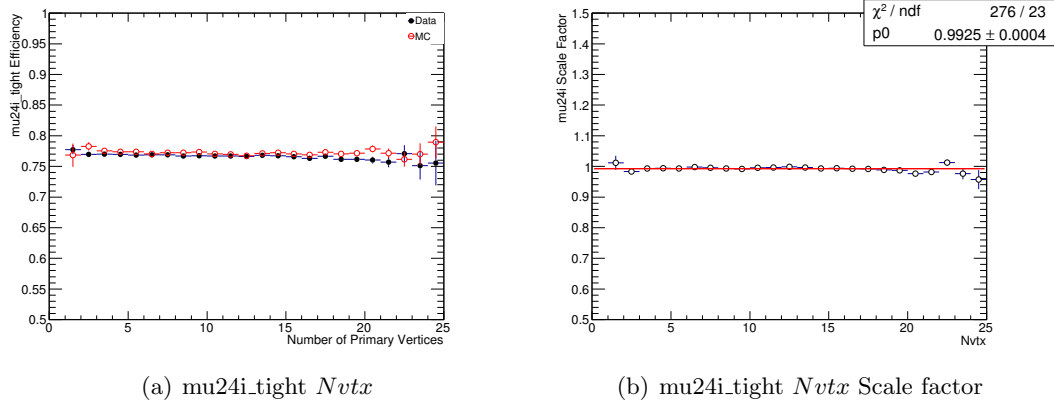


Figure A.15: Trigger efficiency for EFmu24i_tight as a function of muon $Nvtx$ in MC and data and efficiency scale factor. Uncertainties are statistical.

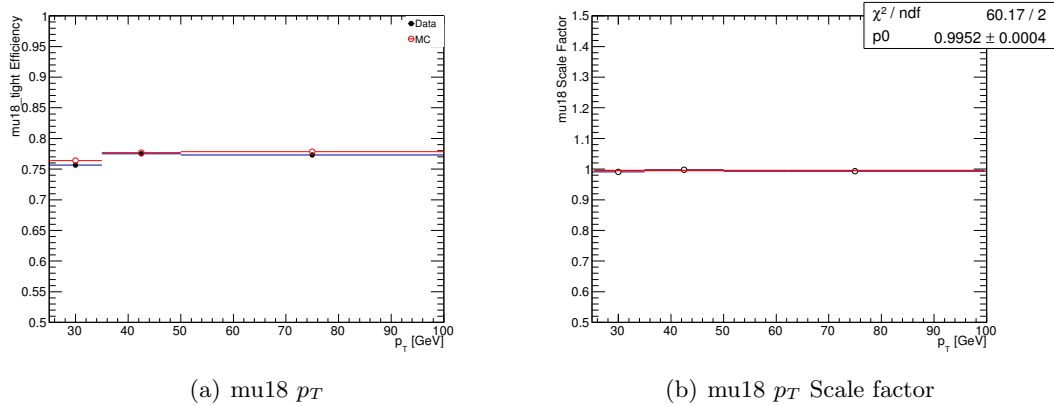


Figure A.16: Trigger efficiency for EFmu18 as a function of muon p_T in MC and data and efficiency scale factor. Uncertainties are statistical.

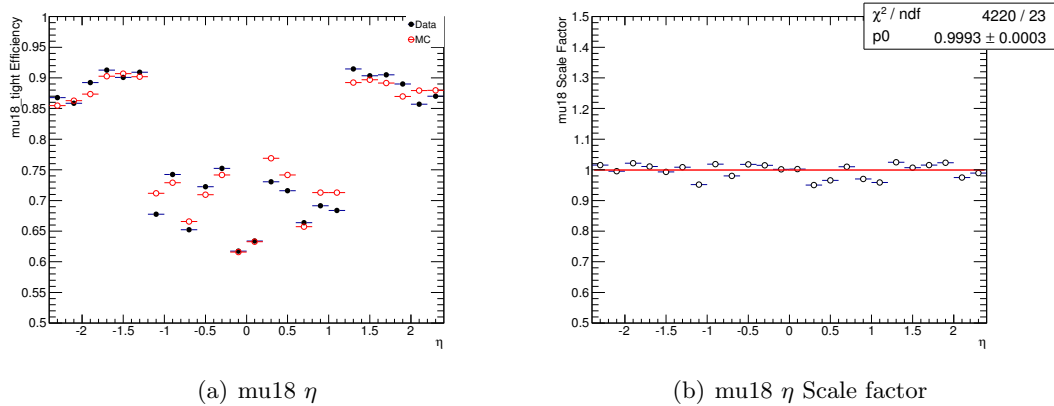


Figure A.17: Trigger efficiency for EFmu18 as a function of muon η in MC and data and efficiency scale factor. Uncertainties are statistical.

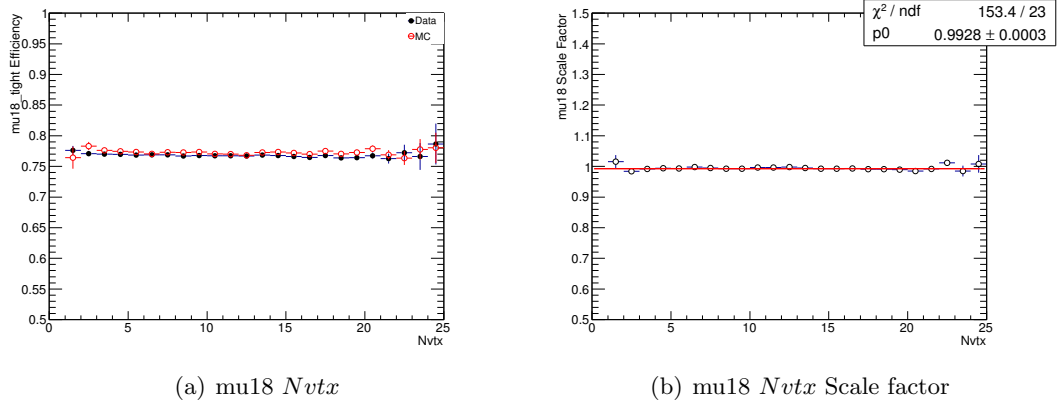


Figure A.18: Trigger efficiency for EFmu18 as a function of muon N_{vtx} in MC and data and efficiency scale factor. Uncertainties are statistical.

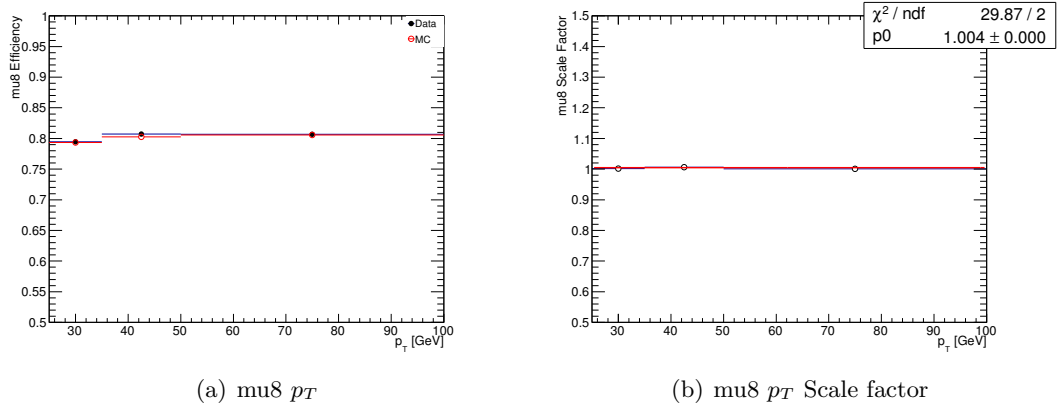


Figure A.19: Trigger efficiency for EFmu8 as a function of muon p_T in MC and data and efficiency scale factor. Uncertainties are statistical.

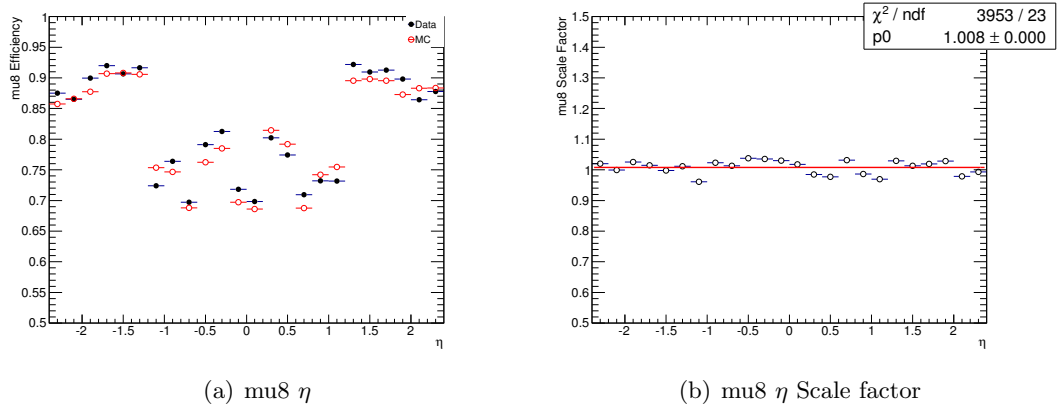


Figure A.20: Trigger efficiency for EFmu8 as a function of muon η in MC and data and efficiency scale factor. Uncertainties are statistical.

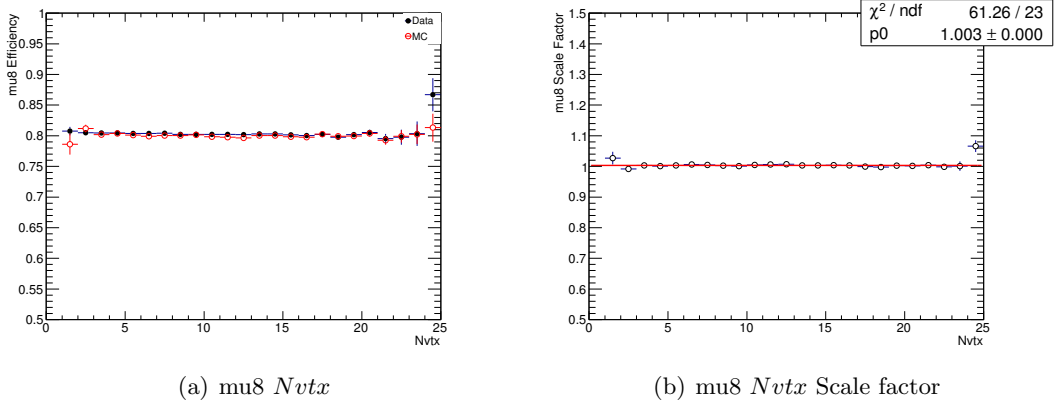


Figure A.21: Trigger efficiency for EFmu8 as a function of muon N_{vtx} in MC and data and efficiency scale factor. Uncertainties are statistical.

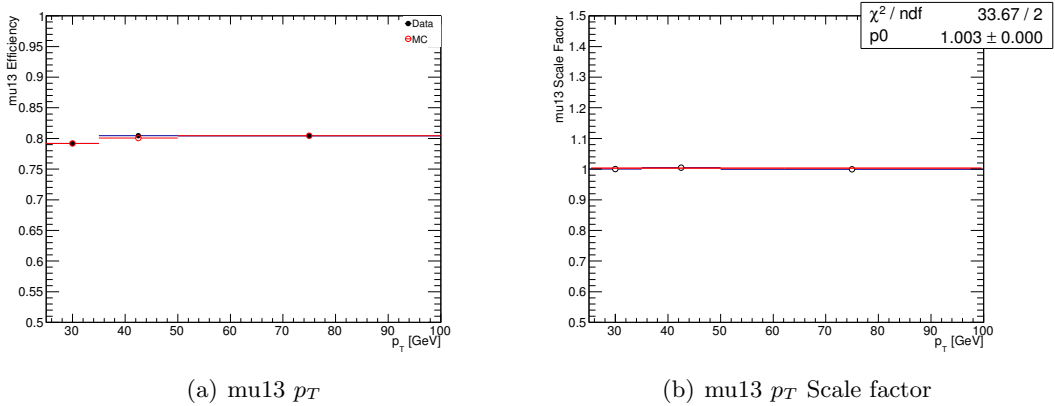


Figure A.22: Trigger efficiency for EFmu13 as a function of muon p_T in MC and data and efficiency scale factor. Uncertainties are statistical.

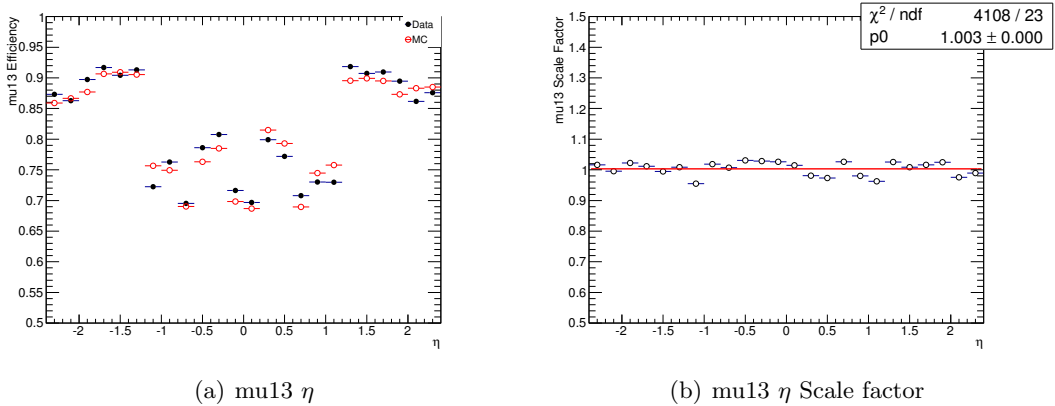


Figure A.23: Trigger efficiency for EFmu13 as a function of muon η in MC and data and efficiency scale factor. Uncertainties are statistical

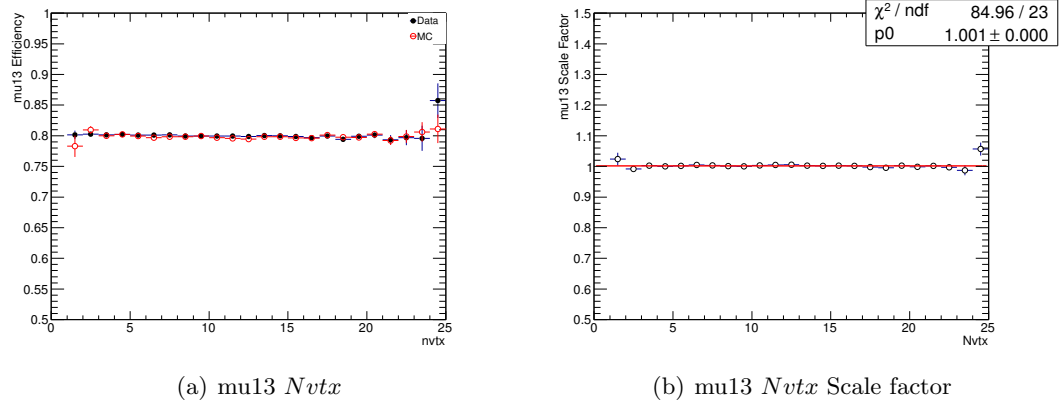


Figure A.24: Trigger efficiency for EFmu13 as a function of muon N_{vtx} in MC and data and efficiency scale factor. Uncertainties are statistical

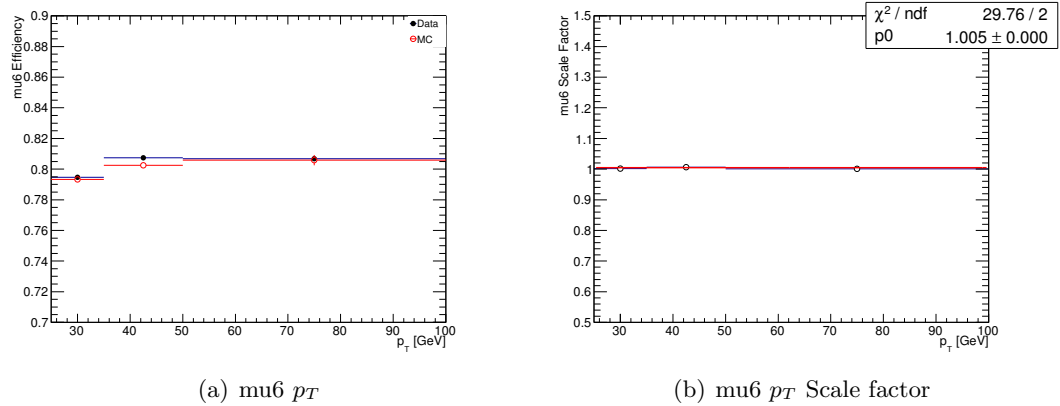


Figure A.25: Trigger efficiency for EFmu6 as a function of muon p_T in MC and data and efficiency scale factor. Uncertainties are statistical.

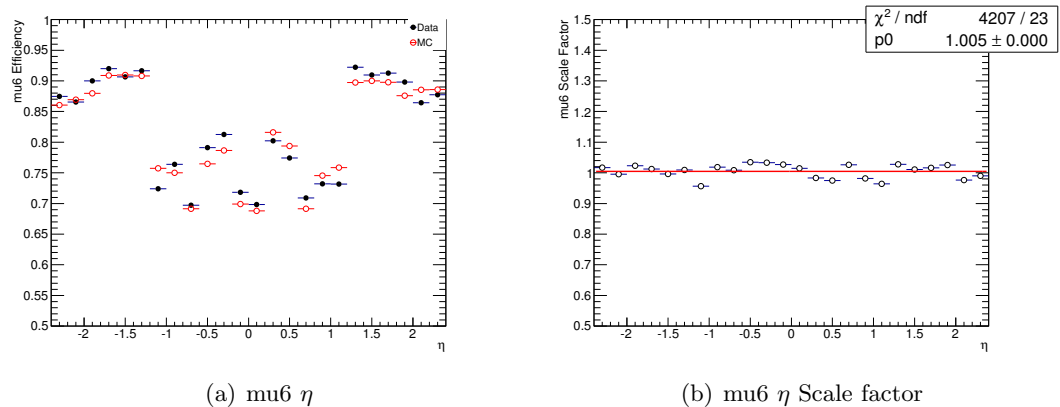


Figure A.26: Trigger efficiency for EFmu6 as a function of muon η in MC and data and efficiency scale factor. Uncertainties are statistical.

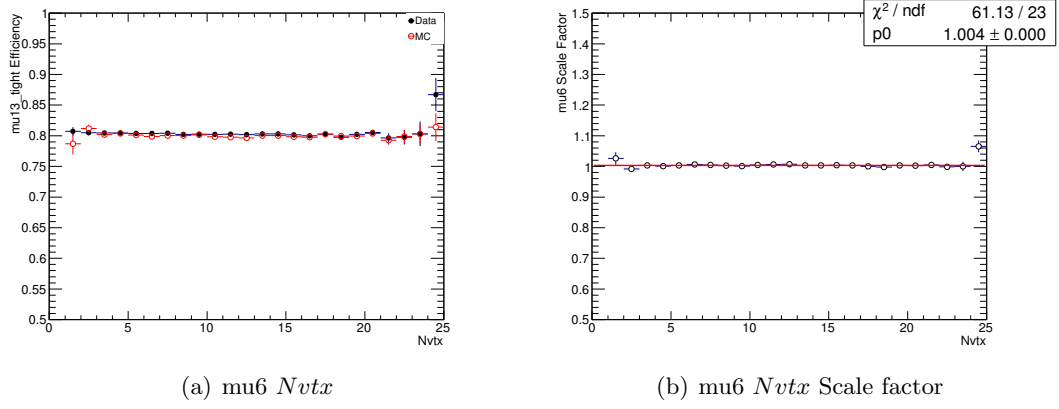


Figure A.27: Trigger efficiency for EFmu6 as a function of muon N_{vtx} in MC and data and efficiency scale factor. Uncertainties are statistical.

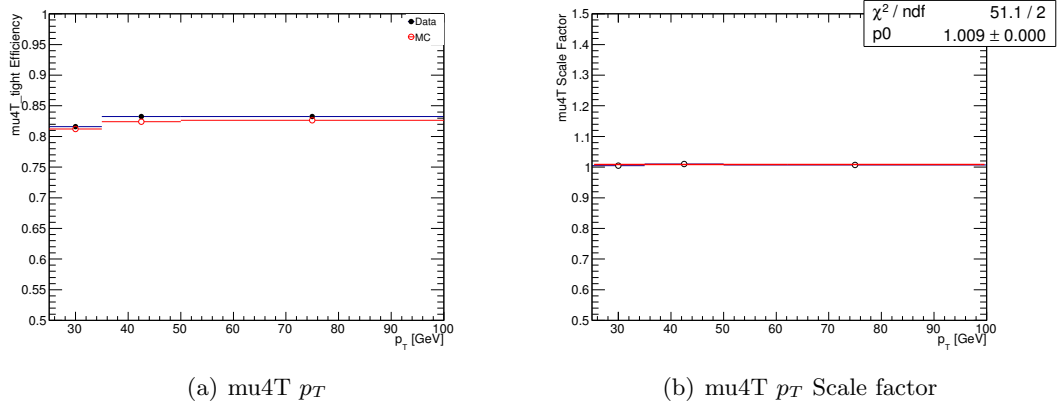


Figure A.28: Trigger efficiency for EFmu4T as a function of muon p_T in MC and data and efficiency scale factor. Uncertainties are statistical.

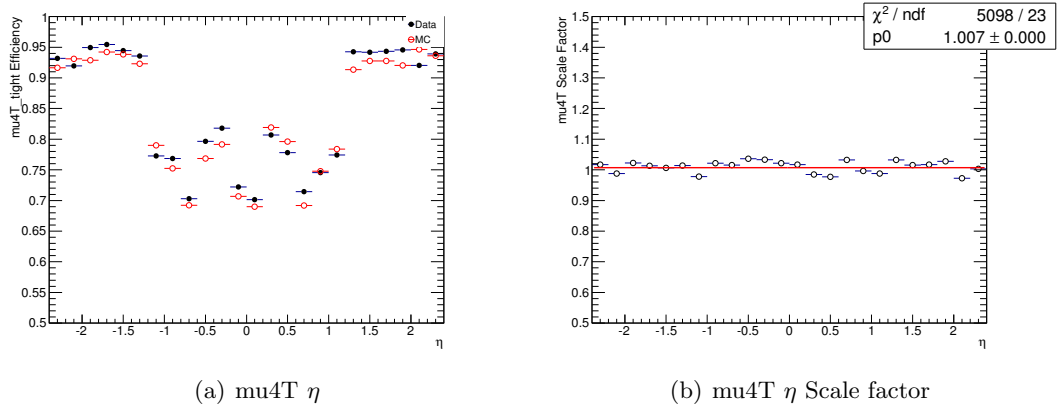


Figure A.29: Trigger efficiency for EFmu4T as a function of muon η in MC and data and efficiency scale factor. Uncertainties are statistical

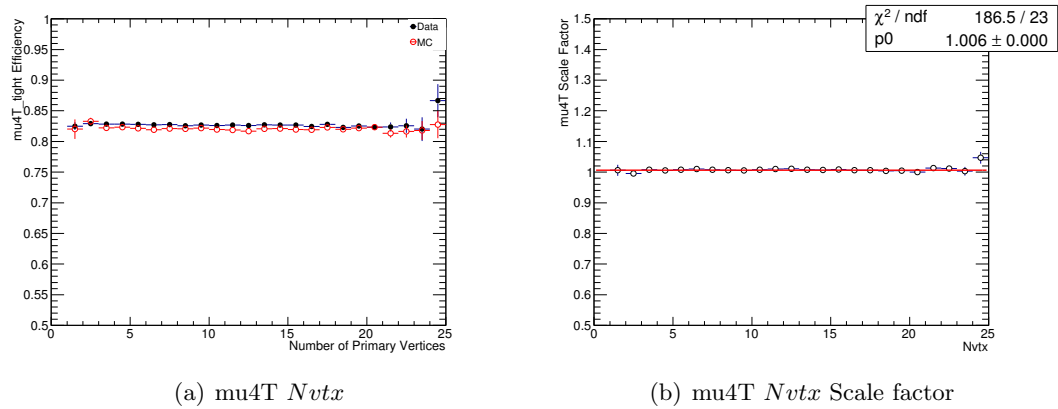


Figure A.30: Trigger efficiency for EFmu4T as a function of muon N_{vtx} in MC and data and efficiency scale factor. Uncertainties are statistical

Appendix B

Appendix B Systematic Uncertainties

B.1 Introduction

An overview of the systematic uncertainties is given in Section 6.7. In this appendix, the systematic uncertainties in each bin are graphically represented in Figures B.1- B.2. The abbreviations in these figures are:

B.2 Glossary

Total the total uncertainty in each bin (red) and per sample. The different sources of uncertainties are added in quadrature for uncorrelated systematic uncertainties and added linearly for correlated systematics. The cross-section, the PDF and the generator uncertainties are treated as correlated between regions but uncorrelated between background processes. All other uncertainties are treated as correlated between regions and between samples, except the uncertainty from limited MC statistics which is not correlated. Due to technical limitations, a systematic uncertainty is always treated as either fully correlated or fully uncorrelated.

MC Stat Monte Carlo statistics

MM Stat Matrix Method statistics

JES Jet energy scale

JER Jet energy resolution

JVF Jet vertex fraction

ESF Electron identification efficiency (electron scale factor)

MEFF Muon identification efficiency

BJET b -tagging

CJET c -tagging

BMISTAGJET l -tagging (b -mistagging)

TauID SF Tau identification efficiency

EES low Electron energy scale for low- p_{T} electrons

EES mat Electron energy scale due to additional material

EES ps Electron energy scale in presampler

EES Z electron energy scale in $Z \rightarrow ee$ measurement

EER Electron energy resolution

MID Muon track resolution in inner detector

MMS Muon track resolution in muon spectrometer

TES Tau energy scale

Scale ST $E_{\mathrm{T}}^{\mathrm{miss}}$ energy scale

Reso ST $E_{\mathrm{T}}^{\mathrm{miss}}$ energy resolution

Lumi Luminosity

MM elec eff Matrix Method electron real efficiency

MM muon eff Matrix Method muon real efficiency

MM elec fr Matrix method electron fake rate

MM muon fr Matrix method muon fake rate

TIDSF Tau identification scale factor

TES Tau scale factor

B.3 Systematic Uncertainty Figures

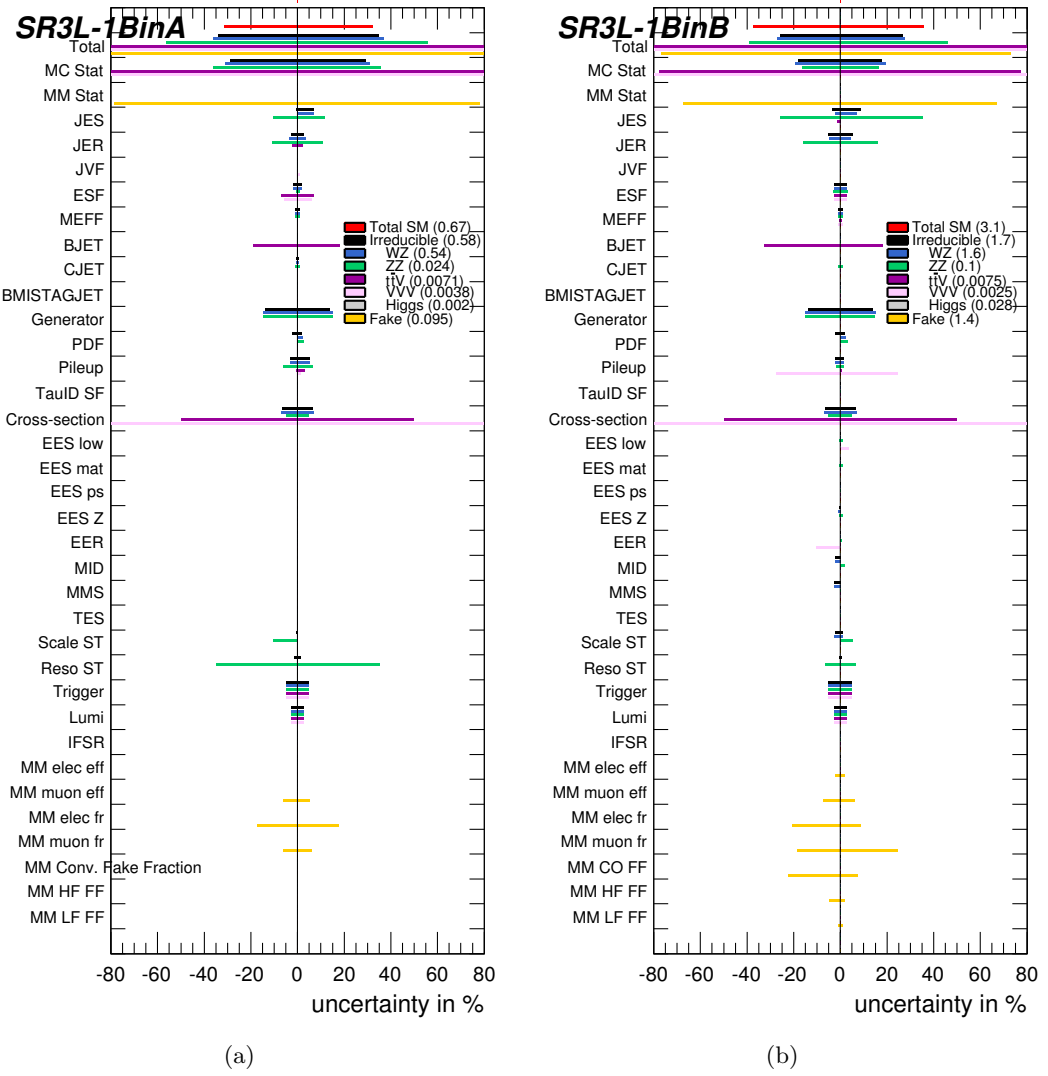
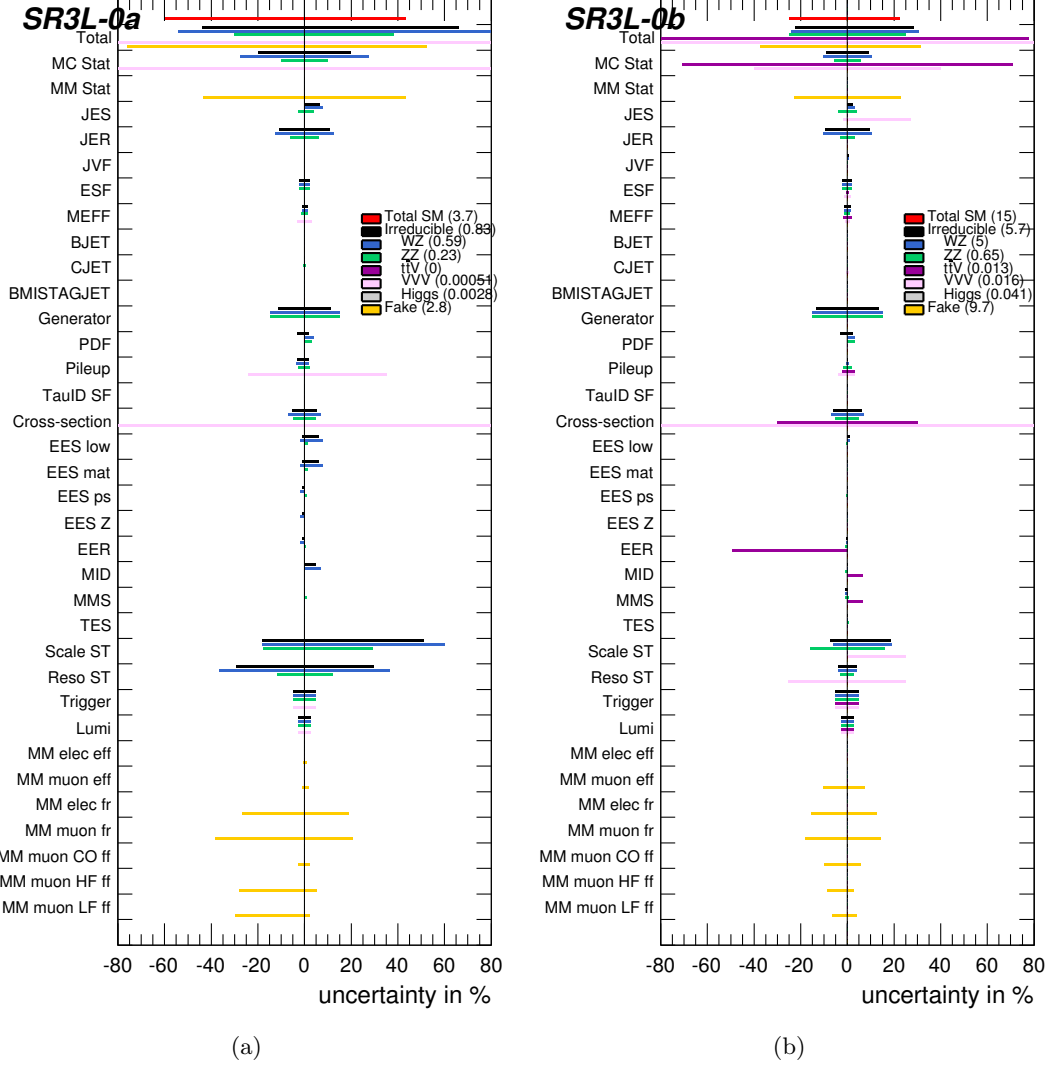


Figure B.1: Systematic uncertainties in Bin A and Bin B of SR3 ℓ -1

Figure B.2: Systematic uncertainties in Bin A and Bin B of SR3 ℓ -0

Bibliography

- [1] ATLAS Collaboration, *The ATLAS experiment at the CERN Large Hadron Collider*, Journal of Instrumentation **3** no. 08, (2008) S08003.
<http://stacks.iop.org/1748-0221/3/i=08/a=S08003>. 1, 27, 30, 33, 34, 35, 36, 37, 38
- [2] O. S. Brüuning, P. Collier, P. Lebrun, S. Myers, R. Ostojic, J. Poole and P. Proudlock, *LHC Design Report*, <https://cds.cern.ch/record/782076>. 1
- [3] ATLAS Collaboration, *Search for the electroweak production of supersymmetric particles in $\sqrt{s} = 8$ TeV pp collisions with the ATLAS detector*,
[arXiv:1509.07152 \[hep-ex\]](https://arxiv.org/abs/1509.07152). 1, 133, 138, 143, 144, 145, 146, 166
- [4] W. N. Cottingham and D. A. Greenwood, *An introduction to the standard model*. Cambridge, 1998. 2
- [5] M. Herrero, *The Standard Model*, <https://arxiv.org/abs/hep-ph/9812242>. 3, 6
- [6] ATLAS Collaboration, *Observation of a New Particle in the Search for the Standard Model Higgs Boson with the ATLAS Detector at the LHC*, *Phys.Lett.* **B716** (2012), [arXiv:1207.7214 \[hep-ex\]](https://arxiv.org/abs/1207.7214). 3
- [7] CMS Collaboration, *Observation of a new boson at a mass of 125 GeV with the CMS experiment at the LHC*, *Phys.Lett.* **B716** (2012), [arXiv:1207.7235 \[hep-ex\]](https://arxiv.org/abs/1207.7235). 3
- [8] ATLAS, CMS Collaborations, *Combined Measurement of the Higgs Boson Mass in pp Collisions at $\sqrt{s} = 7$ and 8 TeV with the ATLAS and CMS Experiments*, *Phys. Rev. Lett.* **114** (2015), [arXiv:1503.07589 \[hep-ex\]](https://arxiv.org/abs/1503.07589). 3
- [9] J. H. Schwarz, *The Early History of String Theory and Supersymmetry*, [arXiv:1201.0981 \[physics.hist-ph\]](https://arxiv.org/abs/1201.0981). 3
- [10] A. Pich, *The Standard Model of Electroweak Interactions*, [arXiv:1201.0537 \[hep-ph\]](https://arxiv.org/abs/1201.0537). 4
- [11] K. A. Olive et al. (Particle Data Group), *Review of Particle Physics*, *Chin.Phys. C*

38(9) (2014). 5, 6, 20

- [12] M. E. Peskin, D. V. Schroeder, *An Introduction to Quantum Field Theory*. Westview Press, 1995. 6
- [13] F. Englert and R. Brout, *Broken Symmetry and the Mass of Gauge Vector Bosons*, Phys. Rev. Lett. **13** (1964) 321–323. 8
- [14] P. W. Higgs, *Broken Symmetries and the Masses of Gauge Bosons*, Phys. Rev. Lett. **13** (1964) 508–509. 8
- [15] T. W. B. Kibble, *Symmetry Breaking in Non-Abelian Gauge Theories*, Phys. Rev. **155** (1967) 1554–1561. <http://link.aps.org/doi/10.1103/PhysRev.155.1554>. 8
- [16] J. Goldstone, A. Salam and S. Weinberg, *Broken Symmetries*, Phys. Rev. **127** (1962) 965–970. 8
- [17] S. Weinberg, *Implications of Dynamical Symmetry Breaking*, Phys. Rev. **D19** (1976) 1277–1280. 10
- [18] M. C. Gonzalez-Garcia and M. Maltoni, *Phenomenology with massive neutrinos*, Physics Reports **460** no. 1-3, (2008) 1 – 129. 10
- [19] E. Kh. Akhmedov, et. al, *Seesaw mechanism and structure of neutrino mass matrix*, Phys. Lett. **B478** (1999). 10
- [20] V. C. Rubin and W. K. Ford, Jr., *Rotation of the Andromeda Nebula from a Spectroscopic Survey of Emission Regions*, Astrophysical Journal **159** (1970) 379. 11
- [21] R. Massey, T. Kitching, and J. Richard, *The dark matter of gravitational lensing*, Reports on Progress in Physics **73** no. 8, (2010) 086901. <http://arxiv.org/abs/1001.1739>. 11
- [22] A. Challinor, *CMB anisotropy science: a review*, arXiv:1210.6008 [astro-ph.CO]. 11
- [23] B. Novosyadlyj, V. Pelykh, Yu. Shtanov, A. Zhuk, *Dark Energy: Observational Evidence and Theoretical Models*, arXiv:1502.04177 [astro-ph.CO]. 11
- [24] S. P. Martin, *A Supersymmetry Primer*, arXiv:hep-ph/9709356. 12, 16, 20
- [25] M. Dine, W. Fischler, and M. Srednicki, *Supersymmetric Technicolor*, Nucl. Phys. **B187** (1981). 16
- [26] L. J. Hall, J. D. Lykken and S. Weinberg, *Supergravity as the Messenger of Supersymmetry Breaking*, Phys. Rev. **D27** (1983) 2359–2378. 16
- [27] L. Randall and R. Sundrum, *A Large mass hierarchy from a small extra*

- dimension*, Phys. Rev. Lett. **83** (1999) 3370–3373, [arXiv:9905221 \[hep-ph\]](https://arxiv.org/abs/hep-ph/9905221). 16
- [28] L. Randall and R. Sundrum, *Out of this world supersymmetry breaking*, Nucl. Phys. **B557** (1999), [arXiv:hep-th/9810155 \[hep-th\]](https://arxiv.org/abs/hep-th/9810155). 16
- [29] L. J. Hall, D. Pinner, and J. T. Ruderman, *A natural SUSY Higgs near 125 GeV*, Journal of High Energy Physics **2012** no. 4, (2012) 1–25.
[http://dx.doi.org/10.1007/JHEP04\(2012\)131](http://dx.doi.org/10.1007/JHEP04(2012)131). 17
- [30] J. A. Casas, et. al, *What is a Natural SUSY Scenario*, [arXiv:1407.6966 \[hep-ph\]](https://arxiv.org/abs/1407.6966). 19
- [31] M. Papucci, et. al, *Natural SUSY Endures*, [arXiv:1110.6926 \[hep-ph\]](https://arxiv.org/abs/1110.6926). 19
- [32] ATLAS Collaboration, *Search for squarks and gluinos with the ATLAS detector in final states with jets and missing transverse momentum and 20.3 fb^{-1} of $\sqrt{s} = 8 \text{ TeV}$ proton-proton collisions*, <https://cds.cern.ch/record/1547563>. 21
- [33] Johan Alwall, Philip C. Schuster and Natalia Toro, *Simplified models for a first characterization of new physics at the LHC*, Phys. Rev. D **D79** (2009). 22
- [34] <https://atlas.web.cern.ch/Atlas/GROUPS/PHYSICS/SUSY/FeynmanGraphs/C1N2-lllvN1N1-sls1.png>. 23
- [35] <https://atlas.web.cern.ch/Atlas/GROUPS/PHYSICS/SUSY/FeynmanGraphs/C1N2-lllvN1N1-WZ.png>. 23
- [36] <https://atlas.web.cern.ch/Atlas/GROUPS/PHYSICS/SUSY/FeynmanGraphs/C1N2-lllvN1N1g-WZ.png>. 24
- [37] D. Barducci, et. al, *Uncovering Natural Supersymmetry via the interplay between the LHC and Direct Dark Matter Detection*, [arXiv:1504.02472v2 \[hep-ph\]](https://arxiv.org/abs/1504.02472v2). 24
- [38] G. Hinshaw, et. al, *Nine-Year Wilkinson Microwave Anisotropy Probe (WMAP) Observations: Cosmological Parameter Results*, [arXiv:1212.5226 \[astro-ph.CO\]](https://arxiv.org/abs/1212.5226). 24
- [39] Planck Collaboration, *Planck 2013 results. XVI. Cosmological parameters*, A&A **571** **A16** (2014), [arXiv:1303.5076](https://arxiv.org/abs/1303.5076). 24
- [40] P. Schwaller, J. Zurita, *Compressed electroweakino spectra at the LHC*, [arXiv:1312.7350 \[hep-ph\]](https://arxiv.org/abs/1312.7350). 24
- [41] S. Gori, S. Jung, L. Wang, *Cornering electroweakinos at the LHC*, [arXiv:1307.5952 \[hep-ph\]](https://arxiv.org/abs/1307.5952). 24
- [42] A. Barr, J. Scoville, *A boost for the EW SUSY hunt: monojet-like search for compressed sleptons at LHC14 with 100fb^{-1}* , [arXiv:1501.02511 \[hep-ph\]](https://arxiv.org/abs/1501.02511). 24
- [43] CERN. Geneva, *LEP Design Report*, <https://cds.cern.ch/record/102083>. 25

- [44] Berndt Muller, Jurgen Schukraft, Bolek Wyslouch, *First Results from Pb+Pb collisions at the LHC*, [arXiv:1202.3233 \[hep-ex\]](https://arxiv.org/abs/1202.3233). 26
- [45] C. Lefèvre, *The CERN accelerator complex*,
<http://cds.cern.ch/record/1260465>. 26
- [46] CMS Collaboration, *The CMS experiment at the CERN LHC*, Journal of Instrumentation **3** no. 08, (2008) S08004.
<http://stacks.iop.org/1748-0221/3/i=08/a=S08004>. 27
- [47] LHCb Collaboration, et. al, *The LHCb Detector at the LHC*, JINST (2008). 27, 46
- [48] ALICE Collaboration, *The ALICE experiment at the CERN LHC*, Journal of Instrumentation **3** no. 08, (2008) S08002.
<http://stacks.iop.org/1748-0221/3/i=08/a=S08002>. 27
- [49] ATLAS Collaboration, *The ATLAS Inner Detector commissioning and calibration*, Eur. Phys. JC**70** , [arXiv:1004.5293](https://arxiv.org/abs/1004.5293). 30
- [50] ATLAS Collaboration, *Alignment of the ATLAS Inner Detector Upgraded for the LHC Run II*, Journal of Physics: Conference Series **664** no. 7, (2015) 072025.
<http://stacks.iop.org/1742-6596/664/i=7/a=072025>. 30
- [51] A. Bingl, *The ATLAS TRT and its Performance at LHC*, Journal of Physics: Conference Series **347** no. 1, (2012) 012025. <http://iopscience.iop.org/article/10.1088/1742-6596/347/1/012025/meta>. 32
- [52] ATLAS Collaboration, *ATLAS liquid-argon calorimeter: Technical Design Report*,
<http://cds.cern.ch/record/331061>. 34
- [53] ATLAS Collaboration, *ATLAS muon spectrometer: Technical design report*,
<http://cds.cern.ch/record/331068>. 36
- [54] ATLAS Collaboration, *Performance of the ATLAS Trigger System in 2010*, Eur. Phys. J **C72** (2012), [arXiv:1110.1530 \[hep-ex\]](https://arxiv.org/abs/1110.1530). 40, 42
- [55] Monika Grothe (on behalf of the ATLAS High Level Trigger Group), *Architecture of the ATLAS High Level Trigger Event Selection Software*, [arXiv:physics/0306097 \[physics.comp-ph\]](https://arxiv.org/abs/physics/0306097). 41
- [56] R. Frühwirth, *Application of Kalman filtering to track and vertex filtering*, Nucl.Instrum.Meth. **A262** (1987). 41, 53
- [57] ATLAS Collaboration, *ATLAS Insertable B-Layer Technical Design Report*,
<http://cds.cern.ch/record/1291633>. 43
- [58] S. T. A. Salzburger and M. Wolter, *The ATLAS Tracking Geometry Description*,
<http://cds.cern.ch/record/1038098>. 43

- [59] E. Simoni, *The Topological Processor for the future ATLAS Level-1 Trigger: from design to commissioning*, [arXiv:1406.4316](https://arxiv.org/abs/1406.4316). 44
- [60] ATLAS Collaboration, *Fast TracKer (FTK) Technical Design Report*,
<https://cds.cern.ch/record/1552953>. 44
- [61] ATLAS Collaboration, *ATLAS Computing : technical design report*,
<https://cds.cern.ch/record/837738>. 46
- [62] G. Barrand, et. al, *GAUDI - A software architecture and framework for building HEP data processing applications*,
[http://dx.doi.org/10.1016/S0010-4655\(01\)00254-5](http://dx.doi.org/10.1016/S0010-4655(01)00254-5). 46
- [63] A. Buckley, J. Butterworth, S. Gieseke, D. Grellscheid, S. Hoche, et al.,
General-purpose event generators for LHC physics, Phys.Rept. **504** (2011).
<http://arXiv.org/abs/1101.2599>. 46
- [64] J. M. Butterworth, et. al, *Hard Processes in Proton-Proton Collisions at the Large Hadron Collider*, Annual Review of Nuclear and Particle Science **62** (2012). 48
- [65] J. M. Campbell, J. Houston and W. Stirling, *Hard Interactions of Quarks and Gluons: A Primer of LHC Physics*, Rept. Prog. Phys. **70** no. 1, (2007). 48
- [66] I. W. Stewart, F. J. Tackmann and W. J. Waalewijn, *Factorization at the LHC: From PDFs to Initial State Jets*, Phys.Rev. **D81** (2010).
<http://arXiv.org/abs/0910.0467>. 48
- [67] A. D. Martin, *Proton structure, Partons, QCD, DGLAP and beyond*, Acta Phys. Polon. **B39** (2008). <http://arXiv.org/abs/0802.0161>. 48
- [68] G. Corcella, et al., *HERWIG 6: an event generator of hadron emission reactions with interfering gluons (including supersymmetric processes)*, J. High Energy Phys. **JHEP(2001)** (2001).
<http://iopscience.iop.org/article/10.1088/1126-6708/2001/01/010/meta>.
49, 69, 72
- [69] T.S., et al., *PYTHIA 6.4 physics and manual*, J. High Energy Phys. **JHEP(2006)** (2006).
<http://iopscience.iop.org/article/10.1088/1126-6708/2006/05/026/meta>.
49, 69
- [70] T. Gleisberg, et al., *Event generation with SHERPA 1.1*, J. High Energy Phys. **JHEP(2009)** (2009).
<http://iopscience.iop.org/article/10.1088/1126-6708/2009/02/007/meta>.
49

- [71] Bernd A. Berg, *Introduction to Markov Chain Monte Carlo Simulations and their Statistical Analysis*, [arXiv:cond-mat/0410490 \[cond-mat\]](https://arxiv.org/abs/cond-mat/0410490). 49
- [72] S. Catani, F. Krauss, R. Kuhn and B. Webber, *QCD Matrix Elements + Parton Showers*, JHEP 0111 (2001), [arXiv:hep-ph/0109231 \[hep-ph\]](https://arxiv.org/abs/hep-ph/0109231). 49
- [73] M. L. Mangano, M. Moretti and R. Pittau, *Multijet Matrix Elements and Shower Evolution in Hadronic Collisions: $Wb\bar{b} + n$ Jets as a Case Study*, Nucl.Phys **B632** (2001), [arXiv:0108069 \[hep-ph\]](https://arxiv.org/abs/0108069). 49
- [74] B. Andersson, S. Mohanty and F. Soderberg, *Recent Developments in the Lund Model*, [arXiv:hep-ph/0212122 \[hep-ph\]](https://arxiv.org/abs/hep-ph/0212122). 49
- [75] A. Kupco , *Cluster Hadronization in HERWIG 5.9*, [arXiv:hep-ph/9906412 \[hep-ph\]](https://arxiv.org/abs/hep-ph/9906412). 49
- [76] R. D. Field, *The Underlying Event in Hard Scattering Processes*, [arXiv:hep-ph/0201192 \[hep-ph\]](https://arxiv.org/abs/hep-ph/0201192). 50
- [77] J. M. Butterworth, J. R. Forshaw, M. H. Seymour Z. Phys. C **72** (1996).
<http://arxiv.org/abs/hep-ph/9601371>. 50, 69
- [78] GEANT4 Collaboration, *Geant4 a simulation toolkit*, Nucl. Instrum. Meth. A **506** (2003). 50
- [79] W. Lukas, *Fast Simulation for ATLAS: Atlfast-II and ISF*, J. Phys.: Conf. Ser **396** no. 022031, (2012). 50
- [80] ATLAS Collaboration, *The simulation principle and performance of the ATLAS fast calorimeter simulation FastCaloSim*,
<https://cds.cern.ch/record/1300517>. 50
- [81] L. Evans and P. Bryant, *LHC Machine*, JINST **3** (2008). 52
- [82] ATLAS Collaboration, *Luminosity Determination in pp Collisions at $\sqrt{s} = 7$ TeV Using the ATLAS Detector at the LHC*, Eur. Phys. J **C71** (2011), [arXiv:1101.2185 \[hep-ex\]](https://arxiv.org/abs/1101.2185). 52
- [83] W. Lampl, et al., *Calorimeter Clustering Algorithms: Description and Performance*, <https://cds.cern.ch/record/1099735>. 54, 60
- [84] ATLAS Collaboration, *Electron performance measurements with the ATLAS detector using the 2010 LHC proton-proton collision data*, Eur. Phys. J. **C72** (2012). <http://arxiv.org/abs/1110.3174>. 55, 125
- [85] ATLAS Collaboration, *Electron reconstruction and identification efficiency measurements with the ATLAS detector using the 2011 LHC proton-proton collision data*, Eur. Phys. J. **74** no. 7, (2014), [arXiv:1404.2240 \[hep-ex\]](https://arxiv.org/abs/1404.2240). 56, 57

- [86] ATLAS Collaboration, *Electron Efficiency measurements with the ATLAS detector using the 2012 LHC proton-proton collision data.,*
<http://cds.cern.ch/record/1706245>. 57, 81, 112
- [87] R. Nicolaïdou, L. Chevalier, S. Hassani, J. F. Laporte, E. L. Menedeu, and A. Ouraou, *Muon identification procedure for the ATLAS detector at the LHC using Muonboy reconstruction package and tests of its performance using cosmic rays and single beam data*, Journal of Physics: Conference Series **219** no. 3, (2010) 032052.
<http://stacks.iop.org/1742-6596/219/i=3/a=032052>. 58
- [88] ATLAS Collaboration, *Measurement of the muon reconstruction performance of the ATLAS detector using 2011 and 2012 LHC proton-proton collision data*, *Eur. Phys. J. C* **74** (2014). 59, 112, 125
- [89] ATLAS Collaboration, *Properties of Jets and Inputs to Jet Reconstruction and Calibration with the ATLAS Detector Using Proton-Proton Collisions at $\sqrt{s} = 7$ TeV.*, <http://cds.cern.ch/record/1281310/files/ATLAS-CONF-2010-053.pdf>. 60
- [90] G. S. M. Cacciari, G. P. Salam, *The Anti- $k(t)$ jet clustering algorithm*, *JHEP* **0804** (2008), [arXiv:0802.1189 \[hep-ph\]](https://arxiv.org/abs/0802.1189). 60
- [91] ATLAS Collaboration, *Jet energy scale and its systematic uncertainty in proton-proton collisions at $\sqrt{s} = 7$ TeV with ATLAS 2011 data.,*
<https://cds.cern.ch/record/1509552>. 61
- [92] ATLAS Collaboration, *Pile-up corrections for jets from proton-proton collisions at $\sqrt{s} = 7$ TeV in ATLAS in 2011.*, <https://cds.cern.ch/record/1459529>. 61
- [93] ATLAS Collaboration, *Commissioning of the ATLAS high-performance b-tagging algorithms in the 7 TeV collision data.,* <https://cds.cern.ch/record/1369219>. 61
- [94] ATLAS Collaboration, *Identification and energy calibration of hadronically decaying tau leptons with the ATLAS experiment in pp collisions at $\sqrt{s} = 8$ TeV*, *Eur. Phys. J. C* **75:303** (2015). 61, 63
- [95] ATLAS Collaboration, *Performance of the Reconstruction and Identification of Hadronic Tau Decays with ATLAS.*, <https://cds.cern.ch/record/1398195>. 62
- [96] ATLAS Collaboration, *Performance of missing transverse momentum reconstruction in proton-proton collisions at $\sqrt{s} = 7$ TeV with ATLAS*, *Eur. Phys. J. C* **75** no. 1844, (2012). 63, 64
- [97] ATLAS Collaboration, *Performance of Missing Transverse Momentum*

- Reconstruction in ATLAS studied in Proton-Proton Collisions recorded in 2012 at $\sqrt{s} = 8 \text{ TeV}$.*, <https://cds.cern.ch/record/1570993>. 64
- [98] M. Bahr, S. Gieseke, M. Gigg, D. Grellscheid, K. Hamilton, et al., *Herwig++ Physics and Manual*, *Eur.Phys.J C* **58** (2008). 69
- [99] T. Gleisberg et al., *Event generation with SHERPA 1.1*, *JHEP* **02** (2009) 007. 69
- [100] M. L. Mangano et al., *ALPGEN, a generator for hard multiparton processes in hadronic collisions*, *JHEP* **07** (2003) 001. 69
- [101] J. Alwall, et al, *MadGraph/MadEvent v4: The New Web Generation*, *JHEP* **09** (2007). 69, 72
- [102] B. P. Kersevan and E. Richter-Was, *The Monte Carlo event generator AcerMC versions 2.0 to 3.8 with interfaces to PYTHIA 6.4, HERWIG 6.5 and ARIADNE 4.1*, *Comput. Phys. Commun.* **184** (2013) 919 – 985. 69
- [103] S. Frixione, and P. Nason, and C. Oleari, *Matching NLO QCD computations with Parton Shower simulations: the POWHEG method*, *JHEP* **11** (2007) 070. 69
- [104] P. Nason, *A New method for combining NLO QCD with shower Monte Carlo algorithms*, *JHEP* **11** (2004) 040. 69
- [105] ATLAS Collaboration, *ATLAS tunes of PYTHIA 6 and Pythia 8 for MC11*, <https://cds.cern.ch/record/1363300>. 71
- [106] H. L. Lai, et al., *New parton distributions for collider physics*, *Phys. Rev.* **D82** (2010). 71
- [107] M. S. W. Beenakker, R. Hopker and P. Zerwas, *Squark and gluino production at hadron colliders*, *Nucl.Phys* **B492** (1997). 72
- [108] S. P. Leif Lonnblad, *Merging Multi-leg NLO Matrix Elements with Parton Showers*, [arXiv:1211.7278](https://arxiv.org/abs/1211.7278). 72
- [109] W. Beenakker, et al., *The Production of Charginos/Neutralinos and Sleptons at Hadron Colliders*, *Phys.Rev.Lett* **83** (1999). 72
- [110] C. Borschensky, et al., *Squark and gluino production cross sections in pp collisions at $\sqrt{s} = 13, 14, 33$ and 100 TeV*, *European Physical Journal C* **74** no. 12, . 73
- [111] R. E. J. Campbell and C. Williams, *Vector boson pair production at the LHC*, *JHEP* **07** (2011). 73
- [112] J. Campbell and R. Ellis, *An Update on vector boson pair production at hadron colliders*, *Phys.Rev.* **D60** (1999). 73
- [113] A. Kardos, and Z. Trocsanyi, and C.G. Papadopoulos, *Top quark pair production in association with a Z-boson at next-to-leading order accuracy*, *Phys. Rev. D* **85**

- (2012). 73, 124
- [114] J. M. Campbell and R. K. Ellis, *$t\bar{t}W^{+-}$ production and decay at NLO*, **JHEP** **07** (2012) 052. 73
- [115] J. Campbell, R. K. Ellis, and R. Rontsch, *Single top production in association with a Z boson at the LHC*, **Phys. Rev.** **D87** (2013) 114006. 73
- [116] M. Aliev, et al., *HATHOR - HAdronic Top and Heavy quarks crOss section calculatoR*, **Computer Physics Communications** **182** (2011). 73
- [117] N. Kidonakis, *Next-to-next-to-leading-order collinear and soft gluon corrections for t-channel single top quark production*, **Phys. Rev.** **D** **83** (2011) 091503. 73
- [118] N. Kidonakis, *NNLL resummation for s-channel single top quark production*, **Phys. Rev.** **D** **81** (2010) 054028. 73
- [119] N. Kidonakis, *Two-loop soft anomalous dimensions for single top quark associated production with a W- or H-*, **Phys. Rev.** **D** **82** (2010) 054018. 73
- [120] S. Catani et al., *Vector boson production at hadron colliders: A Fully exclusive QCD calculation at NNLO*, **Phys. Rev. Lett.** **103** (2009) 082001. 73
- [121] S. Dittmaier, et al., *Handbook of LHC Higgs Cross Sections: 2. Differential Distributions*, **CERN-2012-002** (2012). 73, 124
- [122] ATLAS Collaboration, *Measurement of the low-mass Drell-Yan differential cross section at $\sqrt{s} = 7$ TeV using the ATLAS detector*, **JHEP** **06** (2014). 73
- [123] J. P. Lansberg, *Total J/Psi and Upsilon production cross section at the LHC: theory vs. experiment*, [arXiv:1012.2815 \[hep-ph\]](https://arxiv.org/abs/1012.2815). 73
- [124] ATLAS Collaboration, *Multi-Boson Simulation for 13 TeV ATLAS Analyses*, <https://cds.cern.ch/record/2119986>. 74
- [125] ATLAS Collaboration, *Modelling of the $t\bar{t}H$ and $t\bar{t}V$ ($V = W, Z$) processes for $\sqrt{s} = 13$ TeV ATLAS analyses*, <https://cds.cern.ch/record/2120826>. 74
- [126] ATLAS Collaboration, *Simulation of top quark production for the ATLAS experiment at $\sqrt{s} = 13$ TeV*, <https://cds.cern.ch/record/2120417>. 74
- [127] ATLAS Collaboration, *Monte Carlo Generators for the Production of a W or Z/ γ^* Boson in Association with Jets at ATLAS in Run 2*, <https://cds.cern.ch/record/2120133>. 74
- [128] ATLAS Collaboration, *Studies of Monte Carlo generators in Higgs boson production for ATLAS Run 2*, <https://cds.cern.ch/record/1978192>. 74
- [129] ATLAS Collaboration, *Expected Performance of the ATLAS Experiment - Detector, Trigger and Physics*, [arXiv:0901.0512 \[hep-ex\]](https://arxiv.org/abs/0901.0512). 77

- [130] ATLAS Collaboration, *Performance of the ATLAS muon trigger in pp collisions at $\sqrt{s} = 8 \text{ TeV}$* , *Eur. Phys. J. C* **75** no. 3, (2015). 79
- [131] J. Reichert, on behalf of the ATLAS Collaboration, *The Upgrade and Performance of the ATLAS Electron and Photon Triggers Towards Run 2.*,
<https://cds.cern.ch/record/2058100>. 82
- [132] ATLAS Collaboration, *Search for the electroweak production of supersymmetric particles in $\sqrt{s} = 8 \text{ TeV}$ pp collisions with the ATLAS detector*, [arXiv:1402.7029 \[hep-ex\]](https://arxiv.org/abs/1402.7029). 86, 105, 113, 132, 143, 145, 146, 166
- [133] <https://twiki.cern.ch/twiki/bin/view/Sandbox/StevenScrammBCHSsandbox>. 90
- [134] M. Shamos, F. Preparata, *Computational Geometry: Algorithms and Applications*. Springer-Verlag, 2008. 102
- [135] G. Cowan, *Statistical Data Analysis*. Clarendon Press, 1998. 102, 137
- [136] ATLAS Collaboration, *Search for supersymmetry in compressed scenarios with two and three leptons and missing transverse momentum in the final state in 20.3 fb^{-1} pp collisions at $\sqrt{s} = 8 \text{ TeV}$ with the ATLAS detector*,
<https://cds.cern.ch/record/2004862>. 103, 107, 109, 110, 122, 123, 141, 142, 145
- [137] J. Campbell and R. Ellis, *$t\bar{t}W +$ production and decay at NLO*, *JHEP* **1207** (2012). 124
- [138] J. Butterworth, et al., *Single Boson and Diboson Production Cross Sections in pp collisions at $\sqrt{s} = 7 \text{ TeV}$* , Tech. Rep. ATL-COM-PHYS-2010-695 (2010). 124
- [139] http://www.hep.ucl.ac.uk/pdf4lhc/PDF4LHC_practical_guide.pdf. 124
- [140] S. Alekhin, et al., *The PDF4LHC Working Group Interim Report*,
[arXiv:1101.0536](https://arxiv.org/abs/1101.0536). 124
- [141] P. M. Nadolsky, et al., *Implications of CTEQ global analysis for collider observables*, *Phys. Rev. D* **78** no. 013004, (2008). 124
- [142] ATLAS Collaboration, *Jet energy scale and its systematic uncertainty in proton-proton collisions at $\sqrt{s} = 7 \text{ TeV}$ with ATLAS 2011 data*,
<https://cds.cern.ch/record/1509552>. 126
- [143] ATLAS Collaboration, *Jet energy resolution and selection efficiency relative to track jets from in-situ techniques with the ATLAS detector using proton-proton collisions at a centre of mass energy $\sqrt{s} = 7 \text{ TeV}$* ,
<https://inspirehep.net/record/1204034>. 126

- [144] ATLAS Collaboration, *Improved luminosity determination in pp collisions in $\sqrt{s} = 7$ TeV using the ATLAS detector at the LHC*, *Eur. Phys. J.* **C73** no. 8, (2013) 2518, [arXiv:1302.4393 \[hep-ex\]](https://arxiv.org/abs/1302.4393). 126
- [145] Krämer, et. al, *Supersymmetry production cross sections in pp collisions at $\sqrt{s} = 7$ TeV*, [arXiv:1206.2892v1 \[hep-ph\]](https://arxiv.org/abs/1206.2892v1). 127
- [146] J. Alwall, et. al, *Comparative study of various algorithms for the merging of parton showers and matrix elements in hadronic collisions*, *Eur. Phys. J.* **C53** (2007). 127
- [147] A. L. Read, *Presentation of search results: the CL_s technique*, *Journal of Physics G: Nuclear and Particle Physics* **28** no. 10, (2002) 2693.
<http://stacks.iop.org/0954-3899/28/i=10/a=313>. 135, 159
- [148] A. L. Read, *Modified frequentist analysis of search results (the CL_s method),*
<https://cds.cern.ch/record/451614>. 135, 137, 159
- [149] E. Gross, *LHC Statistics for Pedestrians*,
<https://cds.cern.ch/record/1099994>. 135
- [150] G. Cowan, et al., *Asymptotic formulae for likelihood-based tests of new physics*, *Eur. Phys. J.* **C71** (2011), [arXiv:1007.1727 \[physics.data-an\]](https://arxiv.org/abs/1007.1727). 137
- [151] W. Beenakker, et al., *Squark and Gluino Hadroproduction*, *Int. J. Mod. Phys.* **A26** (2011). 148
- [152] W.Beenakker, R.Hoepker, M.Spira, *PROSPINO: A Program for the Production of Supersymmetric Particles in Next-to-leading Order QCD*, [arXiv:hep-ph/9611232 \[hep-ph\]](https://arxiv.org/abs/hep-ph/9611232). 148
- [153] Eva Halkiadakis, George Redlinger and David Shih, *Status and Implications of Beyond-the-Standard-Model Searches at the LHC*, *Annual Review of Nuclear and Particle Science* **64** (2014) 319–342, [arXiv:1411.1427 \[hep-ex\]](https://arxiv.org/abs/1411.1427). 148
- [154] ATLAS Collaboration, *Muon reconstruction performance in early $\sqrt{s} = 13$ TeV data*,
<https://cds.cern.ch/record/2047831>. 149
- [155] ATLAS Collaboration, *Expected performance of the ATLAS b-jet trigger in Run-2*,
<https://cds.cern.ch/record/2032280/>. 150
- [156] ATLAS Collaboration, *Performance of the Missing Transverse Energy Reconstruction and Calibration in Proton-Proton Collisions at a Centre-of-Mass Energy of 7 TeV with the ATLAS Detector*,
<https://cds.cern.ch/record/1281330>. 150